

Università degli Studi di Padova
Centro Ricerche Fusione (**CRF**)

Universidade de Lisboa
Instituto Superior Técnico **(IST)**

Università degli Studi di Napoli Federico II

JOINT RESEARCH DOCTORATE IN FUSION SCIENCE AND ENGINEERING
Cycle XXXII

MODELING OF MHD INSTABILITIES IN EXISTING AND FUTURE FUSION DEVICES IN VIEW OF CONTROL

Coordinator: Prof. Paolo Bettini

Supervisor: Prof. Fabio Villone

Ph.D. Student: Matteo Bonotto

Padova, 02/12/2019

A voi che avete creduto in me.

Abstract

In this thesis, an improved version of the CarMa code is presented, called CarMa-D, for the analysis of Resistive Wall Modes (RWMs) in thermonuclear fusion devices, simultaneously considering the effects of volumetric three-dimensional conducting structures and in presence of the effects associated with plasma dynamics, toroidal rotation or drift-kinetic damping.

The CarMa-D code is the result of the coupling of the CARIDDI code, for the eddy current analysis in the conducting structures, with the MARS-K code, for MHD stability computations. The strength point behind CarMa-D is that the new coupling strategy does not rely on the simplifying assumptions of neglecting the plasma mass, toroidal rotation and kinetic damping physics, assumptions on which relies the CarMa code. Under these hypothesis, the plasma response to external perturbations depends on the dynamic of the perturbation itself: this behaviour is modelled through a matrix-based Padé rational function. The approximated plasma response is then combined with the equation for the eddy current induced in the metallic structures, in order to obtain a linear system of differential equations as the original CarMa version, but with a higher number of degrees of freedom to model the dynamics of the plasma. The new version overcomes the main limitations of the original computational model, in particular: (i) the massless assumption for the plasma is removed, allowing modeling of global modes growing on ideal-kink time scales; (ii) the effects of toroidal plasma flow and drift kinetic damping can be rigorously included into the new model, providing a powerful tool to study macroscopic phenomena where both plasma dynamics and 3-D conducting structures play important roles. The mathematical model has been also generalized to take into account multiple toroidal mode numbers (*multi-modal* CarMa-D). The code has been successfully tested with a reference equilibrium of a plasma with circular cross-section, and then used to study RWM stability analysis of the modes $n = 1$ and $n = 2$ on JT-60SA Scenario 5.

Finally, additional effort has been made to write the CarMa-D mathematical model in a way suitable for a state-space representation, in order to exploit its features in a model-based feedback control strategy to actively suppress RWMs.

Sommario

In questo lavoro viene presentata una versione migliorata del codice CarMa, chiamato CarMa-D, per lo studio di Resistive Wall Modes (RWMs) nei reattori a fusione termonucleare. Tale codice è in grado di rappresentare accuratamente le strutture conduttrici tridimensionali della macchina, e considerare simultaneamente nel modello gli effetti dovuti alla dinamica del plasma, alla toroidal rotation e agli effetti drift-cinetici.

CarMa-D è il risultato dell'accoppiamento dei codici CARIDDI, per lo studio delle correnti indotte nelle strutture conduttrici, e MARS-K per analisi di stabilità MHD nel plasma. Punto di forza della strategia di accoppiamento alla base di CarMa-D è che non si basa sulle ipotesi semplificative su cui si basa la versione statica di CarMa, ovvero non vengono trascurati la massa del plasma, toroidal rotation e l'effetto del damping cinetico. In questo modo la risposta del plasma a perturbazioni esterne dipende dall'andamento temporale della perturbazione stessa: questo andamento viene approssimato per mezzo di funzioni razionali di Padé a coefficienti matriciali. Il passo successivo è dato dalla combinazione della risposta di plasma approssimata con l'equazione delle correnti indotte nelle strutture passive, per ottenere un modello matematico desctitto come un sistema di equazioni differenziali lineari formalmente uguale alla versione statica di CarMa, ma con un numero maggiori di gradi di libertà per tener conto della dinamica di plasma. La nuova versione del codice supera le principali limitazioni del modello originale, in particolare: (i) considerando la massa del plasma è possibile modellare modi con dinamiche molto veloci, come l'external-kink ideale, (ii) il modello è in grado di tener conto rigorosamente di toroidal rotation e damping cinetico. Questi vantaggi rendono CarMa-D uno strumento potente, in grado di studiare fenomeni macroscopici in cui sia la dinamica del plasma, che gli effetti 3-D delle strutture, sono marcati. Inoltre, il modello matematico risultate è stato generalizzato per tener conto della simulazione più armoniche toroidali simultaneamente (*multi-modal* CarMa-D). Il codice è stato poi testato con successo su un equilibrio di riferimento dato da un plasma a sezione circolare, e successivamente per lo studio di stabilità per i modi $n = 1$ e $n = 2$ su JT-60SA, Scenario 5.

Infine, si è dimostrato come il modello matematico di CarMa-D possa essere scritto in una formulazione state-space, in vista di un successivo impiego nella progettazione di un controllo in retoazione per la stabilizzazione attiva dei RWMs.

Resumo

Esta tese apresenta uma versão aprimorada do código CarMa, chamado CarMa-D, para o estudo de Resistive Wall Modes (RWMs) em reatores de fusão termonuclear. Este código é capaz de representar com precisão as estruturas condutoras tridimensionais da máquina e considerar simultaneamente no modelo os efeitos devidos à dinâmica do plasma, à toroidal rotation e aos efeitos cinéticos da deriva.

CarMa-D é o resultado do acoplamento dos códigos CARIDDI, para o estudo das correntes induzidas nas estruturas condutoras, e MARS-K, para análise da estabilidade da MHD no plasma. A força da estratégia de acoplamento na base do CarMa-D é que ela não se baseia nas hipóteses simplificadoras nas quais a versão estática do CarMa se baseia, ou seja, a massa plasmática, a rotação toroidal e o efeito do amortecimento cinético não são negligenciados. Dessa forma, a resposta do plasma a perturbações externas depende do curso temporal da própria perturbação: essa tendência é aproximada por meio de funções racionais de Padé com coeficientes de matriz. O próximo passo é a combinação da resposta do plasma aproximada com a equação das correntes induzidas nas estruturas passivas, para obter um modelo matemático descrito como um sistema de equações diferenciais lineares formalmente iguais à versão estática do CarMa, mas com um número maior que graus de liberdade para levar em consideração a dinâmica do plasma. A nova versão do código supera as principais limitações do modelo original, em particular: (i) considerando a massa do plasma, é possível modelar modos com dinâmica muito rápida, como a torção externa ideal, (ii) o modelo é capaz de leve em consideração a rotação toroidal e o amortecimento cinético. Essas vantagens tornam o CarMa-D uma ferramenta poderosa, capaz de estudar fenômenos macroscópicos nos quais são marcadas a dinâmica do plasma e os efeitos 3-D das estruturas. Além disso, o modelo matemático resultante p foi generalizado para levar em consideração a simulação de múltiplas harmônicas toroidais simultaneamente (emph multimodal CarMa-D). O código foi então testado com sucesso em uma balança de referência e posteriormente para o estudo de estabilidade para os modos $n = 1$ e $n = 2$ no JT-60SA, Cenário 5.

Finalmente, foi demonstrado como o modelo matemático do CarMa-D pode ser escrito em uma formulação state-space, em vista de um uso subsequente no projeto de um controle de retenção para a estabilização ativa de RWMs.

Foreword

The work presented in this thesis has been carried out during these three years of Ph.D in Fusion Science and Engineering, under the title *Modeling of MHD instabilities in existing and future fusion devices in view of control*. The title of the work underlines how the modeling activity has meant to be oriented to control purposes, in order to develop an accurate and reliable mathematical model viable to be the starting point for control activities. For this reason, keeping in mind the aim of the work, the author has tried to conciliate different points of view from different multi-physical problems, but being mainly bound to an engineering approach.

Within the broad topic of MHD instabilities, this work focuses on the Resistive Wall Modes. This kind of instabilities arise if the plasma pressure exceeds a certain threshold, causing a kink deformation of the outer part of the plasma. The Resistive Wall Modes pose a strong limit to increase the plasma pressure and pursuit steady state economic production of thermonuclear fusion energy.

The dynamic of RWMs is strongly influenced by the resistive wall geometry. Many computational tools have been developed to deal with RWMs, all of them sharing the strategy of coupling a MHD solver to a eddy current code. To get rid of this coupling problem, some simplifying assumption must be made, both on the MHD and on the electromagnetic point of view. This work is focused on the coupling strategy behind one of this codes, the well-known CarMa code, obtained from the coupling of CARIDDI and MARS. On one hand, unique feature of CarMa is being able to rigorously model the actual conducting structures geometry, including the thickness of the resistive wall. On the other hand, some simplifying assumptions are made, such as disregarding the plasma mass, no toroidal flow is present and no kinetic damping is taken into account. Within these assumptions, CarMa has been used extensively to study the stability of RWMs.

However, if the instability is close to the ideal wall beta limit, or when the toroidal flow and the kinetics effects are taken into account, CarMa is no longer a reliable tool. The accurate modelling of these effects is desirable for several reason. At first, for realistic machines the range of growth rates that can be expected for a RWM can vary in a quite broad range between the slow RWMs and the ideal MHD modes, thus the inertia effects cannot simply be neglected. In addition to this, toroidal rotation and kinetic damping physics are key features for RWMs stability problem, because it has been proved that plasma rotation, combined with magnetic feedback, can lead to

a complete stabilization of RWMs. Furthermore, recent results show that for modes faster than the conventional RWMs, but slower than the ideal MHD modes, the thin wall approximation made in almost every computational tools, except CarMa, lead to a complete neglect of the non linear energy storage in the resistive wall, effect which can contribute to the stabilization. It follows that improving the coupling strategy behind the CarMa code to take into account all the previous features could provide a computational tool which is ideally the state of the art of the RWMs modelling for stability analysis and active stabilization in presence of 3-D conducting structures.

The first part of work has the aim to develop a new coupling strategy between CARIDDI and MARS, named CarMa-*Dynamic* (CarMa-D), without relying on the aforementioned assumptions. If the plasma inertia is considered, the relation between the magnetic field perturbation as input and the plasma response as output is no longer static, as the previous case, but depends on the (complex) frequency of the perturbation itself. The plasma response to external perturbation is a key step in the coupling strategy, because it is necessary to describe the reaction of the plasma to the eddy current induced inside the resistive wall by the RWM. The key point of this formulation is the following one: instead of searching a closed relation to model the frequency dependent plasma response, a numerical approach is exploited, describing the response by means of a *matrix-based Padé rational function*. This means that we are dealing with an interpolation of the plasma response, which depends on the choice of the basis points. Starting from this point, the coupling strategy is completely reformulated, finally leading to a modified RL equation formally equivalent to the static CarMa, but able to take into account the plasma dynamics in the RWMs stability analysis. In addition to this, the mathematical model is further generalized to take into account an arbitrary amount of toroidal mode numbers (*multi-modal* CarMa-D).

CarMa-D is then extensively tested against a tokamak plasma with a circular cross-section, and surrounded by an axisymmetric resistive wall with a coherent shape. The testing activity follows different steps, in order to assess CarMa-D reliability and robustness. Two different damping physics models have been considered, (i) the parallel sound wave damping and (ii) the self-consistent, full toroidal drift kinetic model; moreover, different values of toroidal rotation have been considered for both the cases. For the analyzed situations, it has been shown that the Padé rational function is able to model the plasma dynamics in a very accurate way, and the resulting CarMa-D successfully deals with equilibria where the simultaneous effects of plasma dynamics, toroidal flow and kinetic damping are prominent.

In the second part of the work CarMa-D is used for a RWM stability

analysis on the JT-60SA, since many complications would arise when considering a realistic device. For example, realistic plasma configurations are characterized to be highly elongated, and the geometry of the passive conductors are expected to be less stabilizing. A detailed study of the effects of this 3-D geometry on the stability of both the toroidal modes $n = 1$ and $n = 2$ has been performed, and it has turned out that the modes growth rates increase of one order of magnitude if the realistic 3-D geometry of the stabilizing plates is considered, if compared to an axi-symmetric poloidally continuous conducting structure. In addition to this, a noticeable toroidal mode coupling appears due to the holes and ports present in the real geometry. These results provide further motivation regarding the need of an effective stabilization.

Finally, additional effort is made to write the CarMa-D mathematical model in a way suitable to be casted as a state-space representation. This is a crucial step needed to exploit CarMa-D features in a model-based feedback control strategy. Unlikely the original CarMa, CarMa-D cannot be written straightforwardly in a state-space form, due to the new matrix-based coupling strategy. This can be done rigorously, only by algebraic manipulation of the system matrices without any simplifying assumption.

Further work will concern the application of CarMa-D to several cases of interest, such as, for example, additional work related to JT-60SA and the application to ITER, both concerning the stability analysis as well as the design and the implementation of a model-based feedback controller.

Contents

List of Figures

List of Tables

List of tables

1 | Controlled thermonuclear fusion

Contents

1.1 The issue of energy supplying

> *The Stone Age didn't end for lack of stone, and the oil age will end long before the world runs out of oil.*

These words have been credited to Ahmed Zaki Yamani, former Minister of Oil for and Mineral Resources of Saudi Arabia, who was in charge for more than twenty years. The meaning of this sentence is clearly related to the fact that, at some point of the world's history, the Oil supplying will no longer be viable, with respect of other energy sources. Obviously, the same statement can be clearly extended to the other fossil fuels, underlying the need of other solutions.

The word *viable* here is meant broadly speaking. Of course, there are economic issues, related to the fact that the discovery and exploitation of new sites will be more and more expensive if compared to other kinds of fuels, up to the point that it will not worth the trouble. On the other hand, together with these economic issues, there are alarming and undeniable environmental problems related to the extensive consumption of fossil fuels. We cannot burn all of the remaining fossil fuel resources (oil, gas and coal) without catastrophic global warming [1]. For this reasons, environmental considerations are for sure more important than the aforementioned economical reasons, and this further stresses the need of a progressive reduction of the use of fossil fuels. Our society requires environmentally friendly solutions

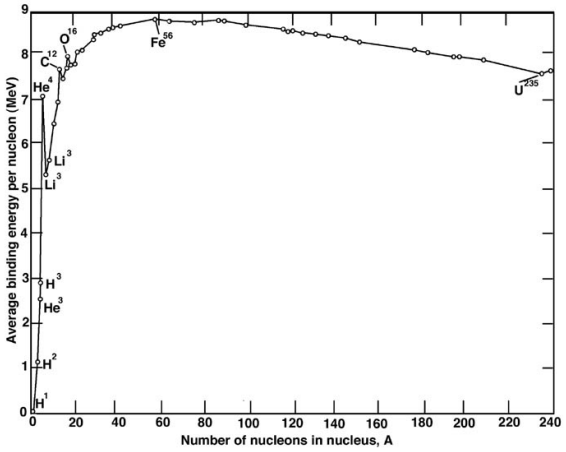

Figure 1.1: *Nuclear binding energy curve.*

for energy production, and nuclear fusion seems to be the best candidate to satisfy this task.

Nuclear fusion consists in the combination of two (or more) atomic nuclei, giving rise to one or more different subatomic particles. The difference in mass (*mass defect*) between the reactants and products is manifested as the release of energy. The mass defect arises due to the different atomic *binding energy* of the nuclei before and after the reaction. Any nucleons with low binding energy, if suitably triggered, can change its configuration to a more stable one through the release of a certain amount of energy. Thus, the more the binding energy is, the more the atomic configuration is stable. The binding energy of the fusion reactions is reported in Fig. 1.1. As can be seen, the elements with the smallest mass per nucleon (candidates for fusion) have also the smallest binding energy per nucleon, meaning that they can release more energy if compared to the largest mass nucleons (candidates for fission). For this reason, fusion reactions have an energy density many times greater than nuclear fission, making, from the point of view of energy per unit of mass, fusion much more appealing than fission [2].

Among the many possible fusion reactions, by far the easiest to initiate are the reactions between deuterium (^{2}D) and tritium (^{3}T). These nucleons are isotopes of hydrogen, respectively with one and two additional neutrons. Specifically, four different nuclear reactions are considered relevant for fusion purposes:

$$^2\mathrm{D} + {}^2\mathrm{D} \longrightarrow {}^3\mathrm{He}\,(0.8\,\mathrm{MeV}) + n\,(2.5\,\mathrm{MeV})$$
$$^2\mathrm{D} + {}^2\mathrm{D} \longrightarrow {}^3\mathrm{T}\,(1\,\mathrm{MeV}) + p\,(3\,\mathrm{MeV})$$

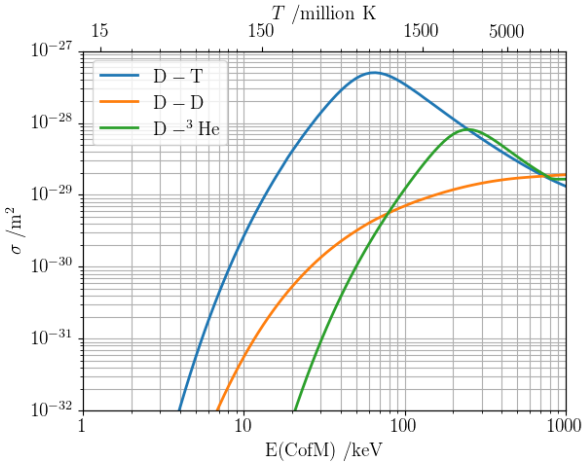

Figure 1.2: *Nuclear fusion cross-sections for reactions* ${}^2D + {}^2D$, ${}^2D + {}^3T$ *and* ${}^2D + {}^3He$.

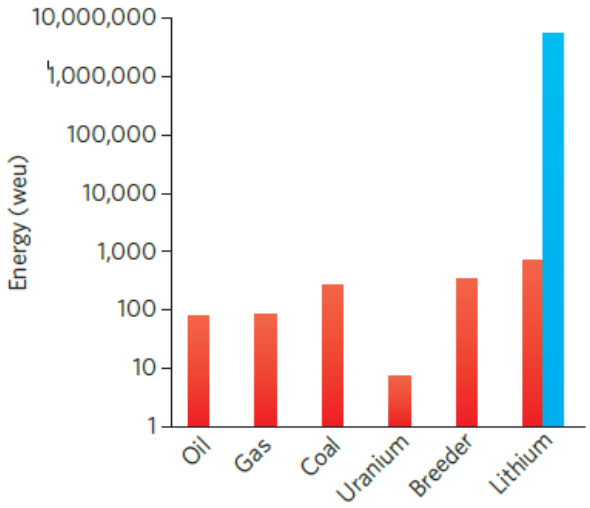

Figure 1.3: *approximate amounts of remaining fuel resources given in world energy units (1 weu = 2.4 terawatt years) [3], existing resource at current prices (red) and resource of lithium from seawater (blue) .*

$$^2\mathrm{D} + {}^3\mathrm{T} \longrightarrow {}^4\mathrm{He}\,(3.5\,\mathrm{MeV}) + n\,(14.1\,\mathrm{MeV})$$
$$^2\mathrm{D} + {}^3\mathrm{He} \longrightarrow {}^4\mathrm{He}\,(3.7\,\mathrm{MeV}) + n\,(14.6\,\mathrm{MeV})$$

where p, n are respectively proton and neutron. The energy is released by means of kinetic energy of the reaction results, and divided among these particles depending on the inverse of their mass, following the momentum conservation. The cross-section for these reaction, which gives measure of the probability of a fusion reaction as a function of the relative velocity of the two reactant nuclei, is reported in Fig. 1.2. As can be seen, the reaction $^2\mathrm{D} + {}^3\mathrm{T}$ is the easiest to obtain.

The first reactions occur with an equal probability and at the same time. In addition, deuterium is widespread in nature and can be found in seawater with a percentage of 0.0115% [4]. On the other hand, tritium is almost not available in nature, because it is a radioactive $\beta-$unstable isotope of the hydrogen, with a half-life of ≈ 12.3 years [5], making any storage in long term facilities not feasible. A possible solution can be the breeding of tritium directly inside the reactors from lithium (^{6}L), through the so-called *breeding blankets*, where a lithium mantle interacts with the slowed down neutrons to produce tritium [6]. Lithium can be found in seawater with a concentration of ≈ 0.02 ppm [7], giving a total amount of 230 billion tonnes of lithium supply. This is clear if Fig. 1.3 is considered, where the approximate amounts of remaining fuel resources is shown [3]. The x-axis uses *weu* as unit, the world's current electricity production in a year as a unit of energy (1 weu = 2.4 terawatt years). The lithium availability is shown both for current world reserves (red, $\approx 10^3$ weu) and if the lithium present in seawater is considered, which can be extracted in minimal cost and can be guessed $\approx 25 \times 10^6$ weu (blue stripe in Fig. 1.3). Moreover, the aforementioned abundance of natural widespread deuterium can be considered, in terms of weu, of more or less 5×10^{10} weu, making fusion even more appealing. This solutions opens the possibility of exploiting the $^2\mathrm{D} + {}^3\mathrm{T}$ reaction, which is, as already mentioned, the easiest to initiate.

The environmental impact of fusion is expected to be low, making this solution definitely more attractive than fission. The net result of the D-T fusion is a small amount of helium, a inert gas. On the other hand, it si true that the neutrons produced in the D-T reactions would cause the activations of the structural materials of fusion reactors, such as steel, tungsten and so on, but the use of specific low activation materials (i.e. EUROFER [8], a reduced-activation steel) ensures short-lived radionuclides, making the activation of structures decays to recyclable levels in less than 200 years [9]. This is a negligible amount of time if compared to the $\approx 10^6$ years of typical

nuclear fission products [10].

Fusion power plants are expected to be also safe and reliable to faults during operations, because, if the conditions necessary to obtain the D-T reactions are not fulfilled, the process simply extinguishes in few microseconds so there are no runaway scenarios to consider [3]. Such sudden termination of the operation would be clearly dangerous for the health of the reactor, but there are no other issues for the operators or the population. Some activation could be releases in case of mechanical failure, but the analysis of worst case accidents reveals that a design in which the evacuation is never necessary is achievable [9].

However, the extreme conditions needed to obtain the fusion reactions are very challenging to be reproduced, because the nucleons have to be maintained (*confined*) to extremely high levels of pressure and temperature. In these conditions, nuclei are accelerated to high enough speed to overcome their mutual electrostatic repulsion, and are brought close each other enough such that the attractive nuclear force overcomes the repulsive Coulomb force. Up to now, two are the most attracting confinement solutions developed by scientists: magnetic and inertial confinement. The first exploits magnetic field to confine the hot plasma, a fully ionized gas, inside the fusion chamber. In the latter, fuel pellets are heated and compressed by means of a sufficiently powerful set of shock waves, typically obtained with high-energy beams of laser light. Both the solution ensures promising results; however, in this work the attention will be focused on the magnetic confinement only.

1.2 Introduction to magnetic confinement

Extremely high temperatures, well above the ionization energies, are needed to reach a significative cross-section. At these temperatures, the fusion reactants exist in a plasma state. Being the plasma a fully ionized gas, its charged particles can be bound, as a result of the Lorentz force, to the magnetic field lines so that they are confined in certain region of space [11]. This is the principle of magnetic confinement nuclear fusion, in which strong magnetic fields are used to confine the hot plasma in order to generate thermonuclear fusion power. In general, a fusion plasma is said to be confined when it is maintained, through a suitable configuration of magnetic fields, in a desired position and shape. The most important task is to keep the hot plasma at a certain distance from the wall, to avoid both the wall to be damaged and the plasma to be cooled down.

The simplest magnetic field geometry that can be used is the straight cylinder. However, this kind of configuration is not viable for the purpose of

fusion energy production, because the plasma would escape from both the ends of the cylinder. A possible solution to achieve a certain confinement even in straight cylinder configuration is to exploit the so-called magnetic mirrors, in which the field strength is increased at both ends using additional magnetic coils. However, a sufficiently good confinement can never been achieved with this configuration, mainly because of the instabilities generated by end losses. For this reason, the magnetic-mirror approach was studied until mid 80s, when it was finally abandoned.

To prevent losses, the obvious solution is to bend the straight cylinder onto a toroidal shape. This can be easily done simply by winding coils (toroidal field coils) around the toroidal vacuum chamber. On one hand, this would avoid the typical losses of the magnetic mirror machines, but further issues on the confinement arise. Indeed, having a toroidal geometry would make the problem of confinement hard to deal with, because expansion forces in the radial direction would arise. This is due to purely geometrical reasons: giving a net radial expansion force due to the pressure (the so-called *tire tube* force [12]). In addition, the field on the outer side of the torus is lower than the field on the inner side. Such asymmetry would cause the ions and electrons to drift across the field, eventually hitting the wall of the torus. A possible solution would be not only to bend the magnetic field line into a torus, but also to twist them around in an helical shape [13].

To implement these solutions, different configurations have been proposed and developed in last decades. The main are the tokamak [13], the Reverse Field Pinch (RFP) [14], the stellarator [15], and many others, all of them with different particularities and features. Due to its relation with the work carried out in this thesis, only the tokamak device is briefly introduced in the next part of the chapter.

1.2.1 The tokamak device

Among the different concepts of fusion devices, tokamak has been the leader for many years in terms of overall performance, making this type of reactor to serve as the reference configuration against which all other concepts are compared [12]. A schematic view of a tokamak device can be seen in Fig. 1.4.

The tokamak is an axisymmetric device with strong toroidal magnetic field and significant toroidal current. This concept has been developed by Soviet researchers in the late 1950s, when they noted that the plasma would be more stable with an helical configuration of the magnetic field lines in the toroidal direction. This particular features was achieved by adding a DC

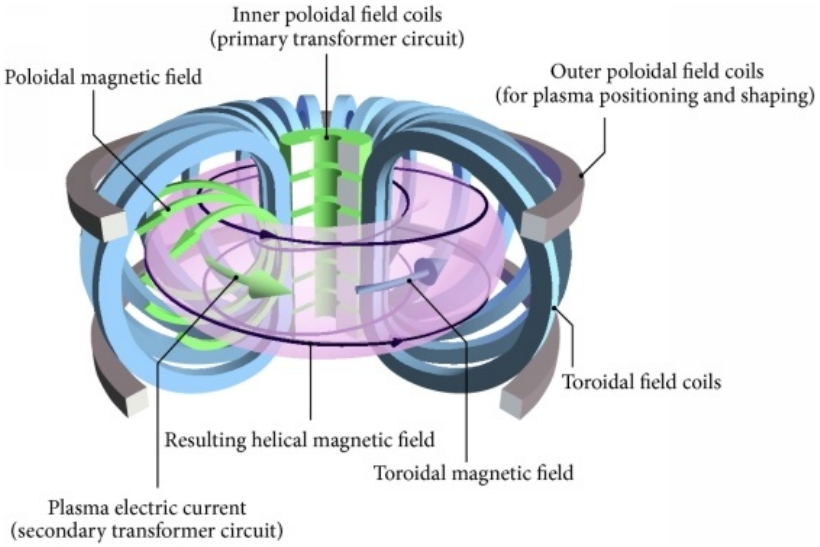

Figure 1.4: *Schematic view of a tokamak device.*

toroidal current, because the superposition of the resulting poloidal field with the already present toroidal field would give twisted field lines, increasing the stability of order of magnitudes.

In the classical tokamak devices, the needed DC toroidal plasma current is given by the central solenoid through a time varying current. These coils work as the primary element of a transformer, inducing a toroidal current in the plasma column (transformer coil in Fig. 1.4). The toroidal field is provided by the toroidal field coils instead (red in Fig. 1.4). Additional coils needed for plasma shaping are present, responsible for the vertical magnetic field needed to counteract the radial expansion forces (B_v if Fig. 1.4).

Even if tokamak reactors have achieved many goals from both technological and physical point of view, there are still many open issues. At first, an important technological problem facing the tokamak is the large toroidal field needed to provide MHD stability, requiring a set of high-B toroidal field magnets. Such high magnetic field cannot be easily obtained simply by means of conventional resistive magnets, due to the extreme heat loads caused by the Joule effect, but super-conducting magnets are often required. This would rise both the complexity of the problem, as well as the cost. Other technological issues are related to the extremely harsh conditions due to the tremendous level of heat loads and irradiations to which the inner walls are subjected, requiring the development of special ad-hoc materials.

As was already said, there are still open problems from the physical point of view as well. Future tokamaks are expected to be steady state devices,

to be a viable option for energy production [16, 17]. To achieve this goal, clearly the major problem is related to the strong poloidal current, which cannot be induced by the central solenoid any more, being this solution not feasible for steady state operation. Fortunately, there is a naturally occurring transport driven current, known as the *bootstrap current*, due to the collisions between trapped and passing particles [18]. One method to address this problem involves a new type of tokamak operation, known as *advanced tokamak* (AT) [19]. The combination of feedback stabilization and the control of current and pressure profiles would produce a large bootstrap current, with the aim of sustaining fully non-inductive discharges. However, improving the fraction of bootstrap current would require the rise of plasma pressure beyond the MHD beta limit, causing severe MHD instabilities to occur. The need of some kind of stabilization of the arising MHD instabilities is crucial. Specifically, this particular problem will be discussed extensively in the next part of the work.

Bibliography

[1] Core Writing Team and R. K. Pachauri and L. A. Meyer (eds.), *IPCC, 2014: Climate Change 2014: Synthesis Report. Contribution of Working Groups I, II and III to the Fifth Assessment Report of the Intergovernmental Panel on Climate Change*. IPCC, Geneva, Switzerland: INTERNATIONAL ATOMIC ENERGY AGENCY.

[2] *Fusion Physics*. Non-serial Publications, Vienna: INTERNATIONAL ATOMIC ENERGY AGENCY, 2012.

[3] S. C. Cowley, "The quest for fusion power," *Nature Physics*, vol. 12, pp. 384–386, 2016.

[4] `http://www.nndc.bnl.gov/chart/reCenter.jsp?z=1&n=1`.

[5] L. L. Lucas and M. P. Unterweger, "Comprehensive review and critical evaluation of the half-life of tritium," *Journal of Research of the National Institute of Standards and Technology*, vol. 105, 07 2000.

[6] R. Andreani, E. Diegele, W. Gulden, R. Lässer, D. Maisonnier, D. Murdoch, M. Pick, and Y. Poitevin, "Overview of the european union fusion nuclear technologies development and essential elements on the way to demo," *Fusion Engineering and Design*, vol. 81, no. 1, pp. 25 – 32, 2006. Proceedings of the Seventh International Symposium on Fusion Nuclear Technology.

[7] Institute of Ocean Energy, *Lithium Occurrence*. Japan: Saga University. Archived from the original on 2 May 2009. Retrieved 13 March 2009.

[8] B. Van der Schaaf, F. Tavassoli, C. Fazio, E. Rigal, E. Diegele, R. Lindau, and G. LeMarois, "The development of eurofer reduced activation steel," *Fusion Engineering and Design*, vol. 69, pp. 197 – 203, 9 2003.

[9] D. Maisonnier, D. Campbell, I. Cook, L. Di Pace, L. Giancarli, J. Hayward, A. Li Puma, M. Medrano, P. Norajitra, M. Roccella, P. Sardain, M. Tran, and D. Ward, "Power plant conceptual studies in europe," *Nuclear Fusion*, vol. 47, no. 11, pp. 1524 – 1532, 2007.

[10] J. Walker, "Barely radioactive elements," `www.fourmilab.ch`, Retrieved 2018-03-09.

[11] J. Ongena, R. Koch, R. Wolf, and H. Zohm, "Magnetic-confinement fusion," *Nature Physics*, vol. 12, pp. 398–410, 2016.

[12] J. Freidberg, *Plasma Physics and Fusion Energy*. Cambridge University Press, 2008.

[13] J. Wesson and D. Campbell, *Tokamaks*. International Series of Monogr, OUP Oxford, 2011.

[14] H. A. B. Bodin and A. A. Newton, "Reversed-field-pinch research," *Nuclear Fusion*, vol. 20, pp. 1255–1324, Oct. 1980.

[15] A. H. Boozer, "Physics of magnetically confined plasmas," *Rev. Mod. Phys.*, vol. 76, pp. 1071–1141, Jan 2005.

[16] P. Kaw, "Steady state operation of tokamaks," *Nuclear Fusion*, vol. 39, pp. 1605–1607, nov 1999.

[17] R. J. Buttery, B. Covele, J. Ferron, A. Garofalo, C. T. Holcomb, T. Leonard, J. M. Park, T. Petrie, C. Petty, G. Staebler, E. J. Strait, and M. Van Zeeland, "DIII-D research to prepare for steady state advanced tokamak power plants," *Journal of Fusion Energy*, vol. 38, pp. 72–111, Feb 2019.

[18] R. Bickerton, J. Connor, and J. Taylor, "Diffusion-driven plasma currents and bootstrap tokamak," *Nature (London). Phys. Sci. 229: 110-12(25 Jan 1971).*

[19] A. D. Turnbull, T. S. Taylor, Y. R. Lin-Liu, and H. S. John, "High beta and enhanced confinement in a second stable core VH-mode advanced tokamak," *Phys. Rev. Lett.*, vol. 74, pp. 718–721, Jan 1995.

2 Introduction to Plasma equilibrium and stability

Contents

The first part of this chapter is devoted to a brief introduction of the equilibrium and stability properties of magnetically confined fusion plasmas. The mathematical formulation is carried out in the framework of a fluid theory, the so-called Magnetohydrodynamic (MHD), with the aim of deriving the single fluid, ideal MHD equations, and discuss some of their basic properties, regarding in particular the equilibrium and stability of a plasma configuration in toroidal geometry. The second part is focused on a particular MHD instability which can occur in toroidal devices, the external kink, imposing a strong limit to the achievable performances. The derivation follows the discussions of Refs. [1, 2, 3, 4, 5].

2.1 Introduction to ideal MHD theory

The ideal MHD equations give the simplest fluid model to describe the macroscopic properties of equilibrium and stability in magnetized plasmas. Even though the description of many important plasma phenomena goes

beyond the ideal MHD (such as, for example, radiation, RF heating and current drive, resonant particle effects and many others), this model is still very useful to provide an accurate description of macroscopic plasma behavior, such as equilibrium and stability. In particular, ideal MHD helps to answer to basic questions as: How does a given magnetic geometry provide forces to hold a plasma in equilibrium? Why are certain magnetic geometries more stable against macroscopic disturbances than others? Why do fusion configurations have such technologically undesirable shapes as a torus or a toroidal-helix?

2.1.1 Ideal MHD equations

A rigorous and formal derivation of ideal MHD equations should start from the fundamental and inclusive kinetic description of the plasma [2]. Within this formulation, plasma is described by means of electron and ion distribution functions $f_\alpha(\vec{\boldsymbol{r}}, \vec{\boldsymbol{v}}, t)$ (where α is the species):

$$\left(\frac{\partial f_\alpha}{\partial t}\right)_c = \frac{\partial f_a}{\partial t} + \vec{\boldsymbol{v}} \cdot \nabla f_\alpha + \frac{Z_\alpha e}{m_\alpha}(\vec{\boldsymbol{E}} + \vec{\boldsymbol{v}} \times \vec{\boldsymbol{B}}) \cdot \nabla_v f_\alpha \tag{2.1}$$

where the left-hand side is the collision operator, $\vec{\boldsymbol{v}}$ the particles velocity, e the electric charge of the electron, m_α the mass for each species, $Z_\alpha = 1$ for ions and $Z_\alpha = -1$ for electrons, $\vec{\boldsymbol{E}}$ the electric field and $\vec{\boldsymbol{B}}$ the magnetic field. It is assumed that the plasma is fully ionized and consists of two species, electrons and singly charged ions.

The Maxwell's equations in vacuum are then considered:

$$\nabla \times \vec{\boldsymbol{E}} = -\frac{\partial \vec{\boldsymbol{B}}}{\partial t} \tag{2.2}$$

$$\nabla \times \vec{\boldsymbol{B}} = \mu_0 \vec{\boldsymbol{J}} + \frac{1}{c^2}\frac{\partial \vec{\boldsymbol{E}}}{\partial t} \tag{2.3}$$

$$\nabla \cdot \vec{\boldsymbol{E}} = \frac{\sigma}{\epsilon_0} \tag{2.4}$$

$$\nabla \cdot \vec{\boldsymbol{B}} = 0 \tag{2.5}$$

where $\vec{\boldsymbol{J}}$ the current density, σ the electric charge density, μ_0 and ϵ_0 respectively magnetic permeability and electric permittivity of vacuum, and c the speed of light. The full set of kinetic-Maxwell equations are then considered together. This model provides a detailed and complete description of plasma behavior; however, the complexity of the model makes it impossible to be solved, even numerically, for any non-trivial geometry.

The macroscopic behavior of plasma can be described by averaging Eq.

(2.1) over a sufficiently large number of particles. This averaging is done taking the appropriate *moments* of the kinetic equation [3]. The arising model is no longer written in terms of distribution functions, but of fluid equations both for the ion and the electron species (the so-called two-fluid equations), in which physical variables such as density, velocity, and pressure are considered.

However, these equations are still not useful since there is no prescription for closing the system, being more unknowns than equations. For this purpose, the plasma is considered *ideal*, meaning that we are neglecting the electrical resistivity, the viscosity, and the heat flux through the boundary. In addition to this, further simplification can be made through the following asymptotic assumptions:

1. neglect high frequency, short-wavelength information from the Maxwell's equations by letting $\epsilon_0 \to 0$. This means that the displacement current $\epsilon_0 \partial \vec{\boldsymbol{E}}/\partial t$ and the net charge $\epsilon_0 \nabla \cdot \vec{\boldsymbol{E}}$ are neglected in Eqs. (2.3) and (2.4).

2. neglect electron inertia by letting $m_e \to 0$. This means that the electron have and infinitely fast response with respect to ions.

Under these assumptions, the combinations of fluid equations with Maxwell's equations gives the *ideal MHD system*:

$$\frac{\partial \rho}{\partial t} + \nabla \cdot \rho \vec{\boldsymbol{v}} = 0 \tag{2.6}$$

$$\rho\left(\frac{\partial \vec{\boldsymbol{v}}}{\partial t} + \vec{\boldsymbol{v}} \cdot \nabla \vec{\boldsymbol{v}}\right) = -\nabla p + \vec{\boldsymbol{J}} \times \vec{\boldsymbol{B}} \tag{2.7}$$

$$\frac{\partial p}{\partial t} + \vec{\boldsymbol{v}} \cdot \nabla p = -\Gamma p \nabla \cdot \vec{\boldsymbol{v}} \tag{2.8}$$

$$\frac{\partial \vec{\boldsymbol{B}}}{\partial t} = \nabla \times \left(\vec{\boldsymbol{v}} \times \vec{\boldsymbol{B}}\right) \tag{2.9}$$

$$\nabla \times \vec{\boldsymbol{B}} = \mu_0 \vec{\boldsymbol{J}} \tag{2.10}$$

$$\nabla \cdot \vec{\boldsymbol{B}} = 0 \tag{2.11}$$

where Γ is the specific heat ratio. The Ohm's law for ideally conducting plasma $\vec{\boldsymbol{E}} + \vec{\boldsymbol{v}} \times \vec{\boldsymbol{B}} = 0$ has been implicitly used.

2.1.2 Equilibrium in toroidal configurations

The first goal in order to obtain suitable conditions to reach fusion is to confine the hot plasma, in order to keep it isolated from the wall. The task

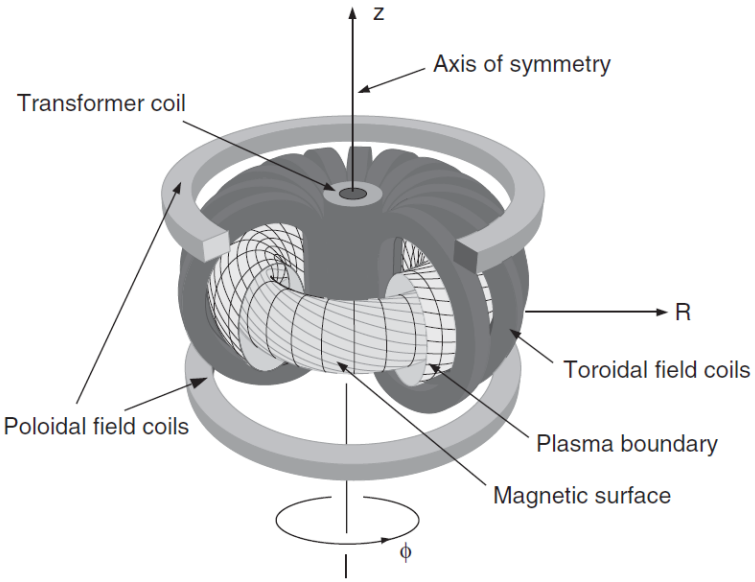

Figure 2.1: *Schematic layout of a tokamak geometry and the coordinate system used in the derivation of equilibrium equation.*

of finding magnetic geometries suitable for this purpose is one of the goal of MHD equilibrium theory. Research from the last 70 years has lead to the discovery of many different configurations such MHD equilibrium properties. As was already said in the previous chapter, the most common feature of the current fusion concepts is that almost each device is constructed in the shape of a torus, to obtain magnetic configurations with closed magnetic field lines. In this subsection, the problem of toroidal force balanced is addressed for such configurations which are symmetric with respect to an axis, known as axi-symmetric configurations. A schematic view of an axi-symmetric toroidal geometry for a tokamak device, as well as the coordinate system used in the discussion, can be seen in Fig. 2.1.

The MHD system of equations (2.6) - (2.11) can lead to the equations governing the plasma equilibrium. Since the aim is the derivation of an equilibrium equation, it is natural to assume zero velocity, and constant quantities; therefore:

$$\frac{\partial}{\partial t} = 0 \tag{2.12}$$

an additional hypothesis is assuming zero velocity $\vec{\boldsymbol{v}} = 0$. In this case, the system of equations (2.6) - (2.11) reduces to:

$$\vec{\boldsymbol{J}} \times \vec{\boldsymbol{B}} = \nabla p \tag{2.13}$$

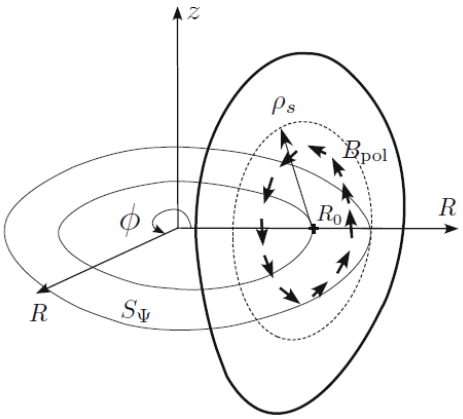

Figure 2.2: *Definition of S_ψ for the computation of the poloidal flux $\psi(r,z)$.*

$$\nabla \times \vec{\boldsymbol{B}} = \mu_0 \vec{\boldsymbol{J}} \tag{2.14}$$

$$\nabla \cdot \vec{\boldsymbol{B}} = 0 \tag{2.15}$$

Two important properties follow from the force balance equation (2.13), and can be obtained multiplying the left-hand side by respectively $\vec{\boldsymbol{J}}$ and $\vec{\boldsymbol{B}}$ to obtain:

$$\vec{\boldsymbol{J}} \cdot \nabla p = 0 \tag{2.16}$$

$$\vec{\boldsymbol{B}} \cdot \nabla p = 0 \tag{2.17}$$

This means that both the magnetic field and the current field lines lie on constant pressure surfaces, without any component along the direction of the pressure gradient. The magnetic field lines cannot intersect these surface of constant pressure, which have therefore also constant values of magnetic flux (the so-called iso-flux surfaces).

We define at this point two scalar functions related to the total surface integrals of the magnetic and current density vector fields through the poloidal area element:

$$\psi = \frac{1}{2\pi} \int_{S_\psi} \vec{\boldsymbol{B}} \cdot \hat{\boldsymbol{n}} \; dS_\psi \tag{2.18}$$

$$F = \frac{1}{2\pi} \int_{S_\psi} \vec{\boldsymbol{J}} \cdot \hat{\boldsymbol{n}} \; dS_\psi \tag{2.19}$$

where the poloidal area element is defined as shown in Fig. 2.2, and $\hat{\boldsymbol{n}}$ is the unit vector normal to S_ψ.

These quantities are used to recombine the Eqs. (2.13) - (2.15), which

are vector equations, to obtain the Grad-Shafranov equation, a single partial differential equation for the normalized poloidal flux $\psi = \psi(r, z)$ and describing the equilibrium of an axi-symmetric toroidal configuration:

$$\Delta^* \psi = -\mu_0 r^2 \frac{dp}{d\psi} - \frac{1}{2} \frac{dF^2}{d\psi} \tag{2.20}$$

where the elliptic operator Δ^* is called Shafranov operator, and is defined as:

$$\Delta^* = r \frac{\partial}{\partial r} \left(\frac{1}{r} \frac{\partial}{\partial r} \right) + \frac{\partial^2}{\partial t^2} \tag{2.21}$$

The solution of Eq. (2.20) provides the constant flux (and pressure) surfaces in real axi-symmetric tokamak geometry. The functions $p(\psi), F(\psi)$ are completely arbitrary, and must be determined from considerations different than the simple toroidal force balance, such as determined experimentally, or from a transport calculation, or using some suitable parametrization functions [6].

2.1.3 Stability

In this section, the MHD equations are assumed to be solved, and the resulting equilibrium calculated. The fact that the equilibrium exists means that the sum of all the forces acting on the plasma is zero. Such equilibrium can be either stable or unstable. The task of stability analysis consists, given an infinitesimal perturbation, in understanding if the arising perturbed forces tend to restore the plasma to its original equilibrium state, or otherwise to increase the perturbation itself.

Linearization of MHD equations for small displacements

The most common technique used to deal with the stability problem is the study of the *linear* stability. To do this, all the quantities of interest in the set of ideal MHD equations (2.6) - (2.11) are linearized around their equilibrium point:

$$f(\vec{\boldsymbol{r}}, t) = f_0(\vec{\boldsymbol{r}}) + f_1(\vec{\boldsymbol{r}}, t) \tag{2.22}$$

where f_0 is the zeroth order value (equilibrium), and f_1 the first order perturbation, assumed such as $|f_1/f_0| \ll 1$.

Equations (2.6) - (2.11) are then written in terms of def. (2.22), neglecting the higher order terms, to obtain:

$$\frac{\partial \rho_1}{\partial t} = -\nabla \cdot \rho_0 \vec{\boldsymbol{v}}_1 \tag{2.23}$$

$$\rho_0 \frac{\partial \vec{\boldsymbol{v}}_1}{\partial t} = -\nabla p_1 + \vec{\boldsymbol{J}}_0 \times \vec{\boldsymbol{B}}_1 + \vec{\boldsymbol{J}}_1 \times \vec{\boldsymbol{B}}_0 \tag{2.24}$$

$$\frac{\partial p_1}{\partial t} = -\vec{\boldsymbol{v}}_1 \cdot \nabla p_0 - \Gamma p_0 \nabla \cdot \vec{\boldsymbol{v}}_1 \tag{2.25}$$

$$\frac{\partial \vec{\boldsymbol{B}}_1}{\partial t} = \nabla \times \left(\vec{\boldsymbol{v}}_1 \times \vec{\boldsymbol{B}}_0\right) \tag{2.26}$$

in addition, for Eqs. (2.10) - (2.10) we have:

$$\nabla \times \vec{\boldsymbol{B}}_0 = \mu_0 \vec{\boldsymbol{J}}_0 \qquad \nabla \cdot \vec{\boldsymbol{B}}_0 = 0 \tag{2.27}$$

$$\nabla \times \vec{\boldsymbol{B}}_1 = \mu_0 \vec{\boldsymbol{J}}_1 \qquad \nabla \cdot \vec{\boldsymbol{B}}_1 = 0 \tag{2.28}$$

At this point, it is useful to define the quantity $\vec{\boldsymbol{\xi}}$ such as:

$$\vec{\boldsymbol{v}}_1 = \frac{\partial \vec{\boldsymbol{\xi}}}{\partial t} \tag{2.29}$$

it follows that $\vec{\boldsymbol{\xi}}$ represents the infinitesimal displacement of the plasma from its equilibrium state. Equations (2.23), (2.24) and (2.25) can be written in terms of $\vec{\boldsymbol{\xi}}$ as an initial value problem:

$$\rho_1 = -\vec{\boldsymbol{\xi}} \cdot \nabla \rho_0 - \rho_0 \nabla \cdot \vec{\boldsymbol{\xi}} \tag{2.30}$$

$$p_1 = -\vec{\boldsymbol{\xi}} \cdot \nabla p_0 - \Gamma p_0 \nabla \cdot \vec{\boldsymbol{\xi}} \tag{2.31}$$

$$\vec{\boldsymbol{B}}_1 = \nabla \times \left(\vec{\boldsymbol{\xi}} \times \vec{\boldsymbol{B}}_0\right) \tag{2.32}$$

here vanishing initial conditions have been assumed, corresponding to the situation where the plasma is, at the time $t = 0$, in its equilibrium point.

Equations (2.30) and (2.32) are than put into Eq. (2.24) to obtain:

$$\begin{aligned} \rho_0 \frac{\partial^2 \vec{\boldsymbol{\xi}}}{\partial^2 t} &= \vec{\boldsymbol{J}}_0 \times \left[\nabla \times \left(\vec{\boldsymbol{\xi}} \times \vec{\boldsymbol{B}}_0\right)\right] + \frac{1}{\mu_0}\left\{\nabla \times \left[\nabla \times \left(\vec{\boldsymbol{\xi}} \times \vec{\boldsymbol{B}}_0\right)\right]\right\} + \\ &\quad + \nabla\left(\vec{\boldsymbol{\xi}} \cdot \nabla p_0\right) + \Gamma \nabla\left(p_0 \nabla \cdot \vec{\boldsymbol{\xi}}\right) \qquad (2.33) \\ &= \boldsymbol{F}(\vec{\boldsymbol{\xi}}) \qquad (2.34) \end{aligned}$$

where $\boldsymbol{F}(\vec{\boldsymbol{\xi}})$ is the so-called *force operator*. This is a wave equation that can be directly used to compute, through integral over the whole system volume, the change in potential energy of the plasma due to the perturbation.

The equations can be further simplified recalling the *normal mode expansion*, which gives a more efficient way to investigate the problem. This can be done by considering in Eq. (2.22) perturbed quantities of the following

form:

$$f_1(\vec{\boldsymbol{r}}, t) = f_1(\vec{\boldsymbol{r}})e^{-i\omega t} \tag{2.35}$$

under this assumption, the momentum equation (2.34) becomes:

$$-\rho_0\omega^2\vec{\boldsymbol{\xi}} = \boldsymbol{F}(\vec{\boldsymbol{\xi}}) \tag{2.36}$$

which has clearly the form of an eigenvalue problem, being $\vec{\boldsymbol{\xi}}$ the eigenfunction and ω^2 the related eigenvalue.

The energy principle

If compared to the initial value problem, the normal mode approach is more suitable to the analysis of the stability property, and less numerically heavy from the computational point of view. However, it is still not the most efficient way to just determine a "yes or no" answer with respect to plasma stability, and investigate the marginal stability. To this purpose, in this subsection at first some details on the force operator are given, to present then the Energy Principle, which is the most efficient way to investigate marginal stability.

An important mathematical property of the MHD force operator defined as Eq. (2.33), is its being a *self-adjoint* operator. Formally, this means that, given two vector fields $\vec{\boldsymbol{\xi}}$ and $\vec{\boldsymbol{\eta}}$, it holds that:

$$\int \vec{\boldsymbol{\eta}} \cdot \boldsymbol{F}(\vec{\boldsymbol{\xi}})\ dV = \int \vec{\boldsymbol{\xi}} \cdot \boldsymbol{F}(\vec{\boldsymbol{\eta}})\ dV \tag{2.37}$$

This property can be proved writing the right-hand side of the integral (2.37) of $\boldsymbol{F}(\vec{\boldsymbol{\xi}})$ eo Eq. (2.33), and arranging the resulting relation by a series of algebraic manipulations and integrations by parts. Here, the proof of the fact that $\boldsymbol{F}(\vec{\boldsymbol{\xi}})$ is self-adjoint is not reported; a detailed explanation can be found in Ref. [2].

The self-adjoint property of $\boldsymbol{F}(\vec{\boldsymbol{\xi}})$ suggests that the stability problem can be casted into a variational form, without solving the differential equation (2.33). Without going into details, this can be exploited by taking the dot product of $\bar{\vec{\boldsymbol{\xi}}}$, which is the complex conjugate of $\vec{\boldsymbol{\xi}}$, to both the sides of Eq. (2.36), and then integrating over the plasma volume to obtain the relation:

$$\omega^2\{\vec{\boldsymbol{\xi}}\} = \frac{\delta W\{\bar{\vec{\boldsymbol{\xi}}}, \vec{\boldsymbol{\xi}}\}}{K\{\bar{\vec{\boldsymbol{\xi}}}, \vec{\boldsymbol{\xi}}\}} \tag{2.38}$$

where δW represent the change in potential energy associated with the per-

turbation and K the kinetic energy of the system. These quantities are defined as:

$$\delta W\{\bar{\vec{\boldsymbol{\xi}}}, \vec{\boldsymbol{\xi}}\} = -\frac{1}{2}\int \bar{\vec{\boldsymbol{\xi}}} \cdot \boldsymbol{F}(\vec{\boldsymbol{\xi}})\, dV \tag{2.39}$$

$$K\{\bar{\vec{\boldsymbol{\xi}}}, \vec{\boldsymbol{\xi}}\} = \frac{1}{2}\int \rho \bar{\vec{\boldsymbol{\xi}}} \cdot \vec{\boldsymbol{\xi}}\, dV \tag{2.40}$$

Since $\omega^2\{\vec{\boldsymbol{\xi}}\}$ is a functional of $\vec{\boldsymbol{\xi}}$, it follows that any allowable trial function $\vec{\boldsymbol{\xi}}$ producing an extremum in the value of ω^2 is an actual eigenfunction of the ideal MHD normal mode equation, with eigenvalue ω^2 equal to Eq. (2.38).

Equation (2.38) states that for any displacement $\vec{\boldsymbol{\xi}}$ such that $\delta W < 0$, then $\omega^2 < 0$, and the system is unstable. This leads to the *ideal MHD Energy Principle*: if $\delta W \geq 0$ for *all* allowable displacements, then the system is stable; if at least one displacement is found to give $\delta W < 0$, then the system is unstable. The physical basis for the Energy Principle is the fact that the energy is exactly conserved in an ideal MHD system. It follows that the most negative eigenvalue ω^2 is related to the absolute minimum in potential energy δW. For this reason, any study of stability/instability of the system can be determined only by examining the sign of δW through the sign of ω^2.

The change in potential energy δW defined as (2.39) can be formulated, through a suitable sequence of integrations by parts, in different forms depending on how these integrations are performed. The first is the so-called *standard form* of δW, particularly useful because a boundary term appears by appropriate integrations by parts, which can be used to evaluate the contribution to the stability of the vacuum region between the plasma and the conducting wall. Conversely, one can obtain the "intuitive form" of δW, in wich the boundary term is no longer present, but the form is more suitable for providing physical insight into the nature of the various occurring MHD instabilities.

The previous discussion, which can be considered the traditional derivation of the Energy Principle, was carried out considering the plasma surrounded by a perfectly conducting wall, exactly enclosing the plasma boundary and without a vacuum region in between. Therefore, this formulation does not allow any local displacement on the plasma boundary. This description can be further generalized to this case, giving so-called *Extended Energy Principle*. Such formulation is of particular interest and usefulness because the most dangerous MHD instabilities involve the perturbation of the plasma surface, not allowed for the previous case.

The derivation of the Extended Energy Principle requires that $\boldsymbol{F}(\vec{\boldsymbol{\xi}})$ has to remain self-adjoint when also the vacuum region is considered. This can be

done through a suitable manipulation of the boundary therm which arises in the integral (2.37) and takes into account the energy associated to the vacuum region [2]. In this framework, the total potential energy of the perturbed system can be written as:

$$\delta W = \delta W_F + \delta W_S + \delta W_V \tag{2.41}$$

where δW_F is the contribution from the plasma (fluid), δW_S from the interface between plasma and vacuum, and δW_V is the contribution from the vacuum region. More specifically:

$$\begin{aligned}
\delta W_F &= \frac{1}{2}\int_{V_F}\left[\frac{|\delta\vec{\boldsymbol{B}}|^2}{\mu_0} - \vec{\boldsymbol{\xi}}_\perp\cdot(\vec{\boldsymbol{J}}\times\vec{\boldsymbol{B}}) + \Gamma\rho_0|\nabla\cdot\vec{\boldsymbol{\xi}}|^2 + \right.\\
&\qquad\left. + (\vec{\boldsymbol{\xi}}_\perp\cdot\nabla p_0)\nabla\cdot\bar{\vec{\boldsymbol{\xi}}}_\perp\right]\,dV\\
\delta W_S &= \frac{1}{2}\oint_S |\hat{\boldsymbol{n}}\cdot\vec{\boldsymbol{\xi}}_\perp|^2\hat{\boldsymbol{n}}\cdot\nabla\left[\!\left[p + \frac{B^2}{2\mu_0}\right]\!\right]\,dS\\
\delta W_V &= \frac{1}{2}\int_V \frac{|\delta\vec{\boldsymbol{B}}|^2}{\mu_0}\,dV
\end{aligned}$$

where $\vec{\boldsymbol{\xi}}_\perp$ is the component of the displacement perpendicular to the equilibrium magnetic field and the brackets $[\![]\!]$ mean the jump condition at the plasma–vacuum interface. The extended energy principle forms the basis for much of linear stability theory, especially for fusion plasmas.

2.1.4 Note on the inertia-free approximation

Before going on, it is useful to spend some words about the so called *inertia-free* approximation, being relevant in the next chapters.

Depending on the possibility of neglecting the plasma inertia, two different models to describe the MHD problem arise [7]. Let us consider the momentum equation (2.7), here written in term of the convective derivative:

$$\rho\frac{d\vec{\boldsymbol{v}}}{dt} = -\nabla p + \vec{\boldsymbol{J}}\times\vec{\boldsymbol{B}} \tag{2.42}$$

this equation describes the behavior of a plasma under the action of electrodynamic forces. On the right-hand side of the equation, both the pressure gradient forces and the electrodynamic forces can be seen. A look at this equation is sufficient to see that two extreme cases are possible, each characterizing a large group of confinement methods.

If the inertia term on the left-hand side of the equation is small if com-

pared to the terms on the right hand side, it can be disregarded as well:

$$\nabla p = \vec{\boldsymbol{J}} \times \vec{\boldsymbol{B}} \tag{2.43}$$

in this case, the gas-kinetic and magnetic pressures permanently balance each other.

Conversely, for the other case, the timescale of the phenomena is compared to the Alfvén time τ_A, defined as the inverse of the Alfvén frequency ω_A:

$$\tau_A = \frac{1}{\omega_A} = \frac{\sqrt{\mu_0 n_i m_i}}{BR_0} \tag{2.44}$$

where n_i is the ion number density, m_i is the ion mass and R_0 is the machine major radius. If the timescale of interest has the same order of magnitude of the Alfvén time, the electrodynamic force will be balanced by "inertial forces", giving rise to:

$$\rho \frac{d\vec{\boldsymbol{v}}}{dt} = \vec{\boldsymbol{J}} \times \vec{\boldsymbol{B}} \tag{2.45}$$

Characteristic of this type of plasma-magnetic field interaction is the short duration of the process, characterized by order of magnitude equal to a/v, where a is the distance traversed by the plasma under the action of the accelerating forces, and v is the velocity attained. In cases of practical interest, the duration of this acceleration process should be of the order of 10^{-6} to 10^{-5} sec, which is comparable with the timescale of the Alfvén phenomena. It follows that, if such "fast" phenomena have to be considered, the assumption of inertia-free is not suitable.

2.2 External kink instabilities and Resistive Wall Modes

Extensive theoretical and experimental analysis in fusion devices has lead, among decades, to further and deeper understanding in the ideal MHD stability properties of fusion plasmas, allowing the identification of the external kink instabilities as the major obstacle to increase the plasma pressure and pursue steady state economic production of fusion energy. Substantial improvements have been achieved in the field of stabilization of these instabilities, partly because of the deeper awareness gained in the passive stabilizing mechanism proper to the plasma under certain operational conditions, and for the continuous improvement of the modelling activity and the active control strategies. In the following part of the section, at first a brief introduction on the historical background of the RWMs problem is reported,

followed by a discussion on the different stabilization mechanisms.

2.2.1 Background

The energy production is one of the main goals for the magnetically confined thermonuclear fusion. To this purpose, extensive effort has been spent in order to optimize plasma configurations to increase as much as possible the fusion power and achieve steady state operation. Since the fusion density scales roughly as $\langle p \rangle^2$ [8, 9], high performance in producing fusion energy implies high values of:

$$\beta_T = \frac{2\mu_0 \langle p \rangle}{B_T^2}$$

where $\langle p \rangle$ is the average plasma pressure, and B_T the strength of the toroidal magnetic field.

Plasma with high pressure is more likely to operate close to one (or more) stability limit(s) related to ideal MHD instabilities. Among these, the ideal kink has been considered for a long time the major limitation to achieve high performances. However, even though a lot of experiments were terminated by instabilities growing slower than Alfvén timescales, there were no experimental evidence to relate these instabilities to external kinks. Important advantages in the understanding of these phenomena comes from the theoretical investigation of the stability properties of the MHD model, in particular through the MHD Energy Principle already presented in subsection 2.1.3. These properties have been studied analytically at first by Shafranov in 1970 [10], then followed by many further improvements.

However, the most prominent advancements in understanding MHD stability properties was carried out with the development of large ideals MHD stability codes (ERATO [11], KINX [12], PEST [13], and many others [8]). Extensive analysis were carried out with these computational tools, and one of the most remarkable result was the so-called Troyon's scaling limit: specifically, the maximum value of achievable β_N was:

$$\beta_N^{Troyon} = \beta_{T,max} \frac{aB_T}{I} \approx 2.8$$

where I is the toroidal plasma current and a is the minor radius. This value was found to be the same for a wide variety of current and pressure profiles. This result was obtained assuming that no external conducting wall was present. In addition to this, neither dissipation nor rotation was considered for the plasma.

The effect of a finite-conducting wall surrounding the plasma was inves-

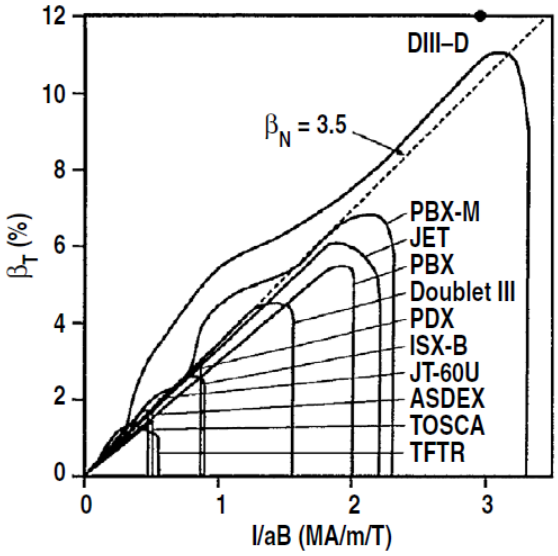

Figure 2.3: *Comparison of experimental achieved β_T as function of the normalized current I/aB_T for major tokamaks until 1994 [15].*

tigated by Pfirsch and Tasso [14]. In particular, their work showed that replacing an ideally conducting wall with a resistive wall cannot stabilize an unstable plasma. The effect of the wall was to significantly reduce the instability growth rate, from the Alfvénic timescale, to the characteristic decay time of the eddy current induced in the wall. Such instabilities were then called Resistive Wall Modes.

Experimental studies have been carried out to validate the Troyon's limit. In particular, some results previous to 1994 and reviewed in Ref. [15] are reported in Fig. 2.3, where the experimental achieved values of β_T are plotted as function of the normalized current I/aB_T (here I is the total plasma current and a the minor radius). It is clear that the value of β_T achievable in tokamaks is bounded by a straight line corresponding to $\beta_N = 3.5$. But, also $\beta_N > \beta_N^{Troyon}$, meaning a higher maximum value of β_N is achievable. Further investigation has lead to find out that the reason was the stabilizing effect of the conducting wall, which was not included in the computation of Troyon's limit.

Further requirements to operate with higher values of β_N was imposed with the development of the so-called Advanced Tokamak (AT) scenarios [16]. The aim was to reach fully non inductive steady-state operations, maximizing the fraction of the self-generated bootstrap current [17]. Specifically, the plasma bootstrap current was verified to be proportional to the plasma

poloidal beta:

$$\beta_P = \frac{\langle p \rangle 2\mu_0}{\langle B_P^2 \rangle} \tag{2.46}$$

where $\langle B_P^2 \rangle$ is the averaged value of the poloidal magnetic field. The high values of β_P and β_T require consequently a high β_N [8], leading to the need of stabilize the external kinks.

In the early 1990s, higher β_T discharges was obtained by an extensive use of Neutral Beam Injection (NBI). The MHD instabilities arising in that situations were found to be less unstable than what was predicted, being the growth time smaller than the characteristic wall time. The explanation of this effect was given by Bondeson and Ward [18], who correlate the momentum injection provided by NBI to the more stable modes. In particular, it was explained that low n external kinks, where n is the toroidal mode number(i.e. the periodicity along the toroidal direction), could be fully stabilized in presence of a resistive wall if the plasma rotates with at a certain fraction of the sound speed. This study has paved the way to the investigation of *passive* stabilization mechanism, called in such way in contraposition to the *active* (feedback) stabilization. These methods are exploited in a synergic way in present machines, and are expected to be so also in future devices.

2.2.2 Stabilization of resistive wall mode

When $\beta_N > \beta_N^{no-wall}$, i.e. the *no-wall* stability threshold, the plasma is expected to be unstable to the RWM. In this case, some stabilization mechanisms are required to maintain the plasma stable and avoid sudden and abrupt loss of confinement. The stabilization mechanisms can be both passive and active: the first comes from the combination of the plasma rotation with the energy dissipation inherent to the plasma and already presented in the previous subsection, while the latter can be achieve through an active feedback control system. A brief description of both of them will follow in the next part of the discussion.

Rotational stabilization

If a NBI system is used for plasma heating, not only energy, but also toroidal angular momentum, is injected into the plasma. The mode couples with the rotation through a dissipation mechanism, causing the plasma to slowly rotate with respect to the conducting wall. If the toroidal angular momentum is prominent, the low n, pressure driven, external kink can be completely stabilized by the resulting rotation of the plasma with respect to the resistive wall. In their explanation, Bondeson and Ward [18], have considered that the

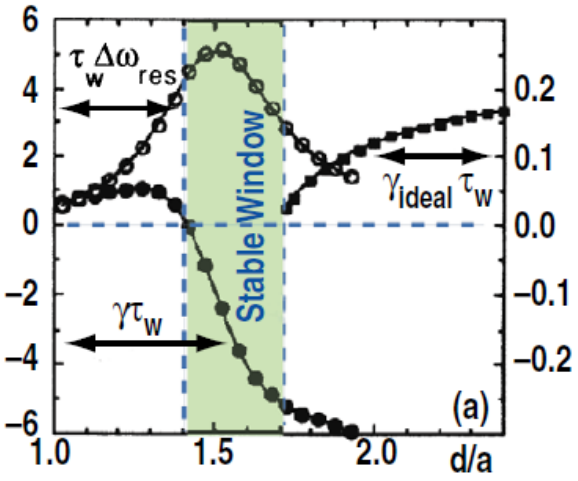

Figure 2.4: *Growth rate γ and slip frequency $\Delta\omega = \omega_{rot} - \omega$, normalized by the wall time τ_W, as a function of the resistive wall position. Also the no-wall external kink growth rate is reported [18].*

momentum transfer from the plasma to the mode occurred by the Landau damping mechanism, showing that a critical rotation value of a fraction of Alfvén speed was sufficient to fully stabilize the mode, opening a stability window from low β_N to the ideal-wall limit.

The nature of this stabilizing effect can be seen in Fig. 2.4, where the mode growth rate γ and slip frequency $\Delta\omega = \omega_{rot} - \omega$, normalized by the wall time τ_W, are computed for different position of the wall location (here d is the radius of the wall and a of the plasma). The rotation of the plasma with respect to the resistive wall is modelled through a fake rotation of the wall with angular velocity ω_{rot}. The ideal kink mode is stable with $d/a < 1.7$. If the resistivity of the wall is taken into account, the resulting RWM occurs, which is stable when the slip frequency $\omega\tau_W$ of RWM is large with respect to the wall, due to the momentum transfer from the plasma to the mode. Note the shaded region of $1.4 < d/a < 1.7$ in which both γ_{RWM} and the extended γ_{ideal} are expected to be negative.

Theoretical, numerical, and experimental studies have been carried out to further understand these passive stabilization mechanisms. In particular, from the numerical point of view it is worth mentioning the development of the stability code MARS-K, based on the drift-kinetic approach to compute the complete RWM eigenfunction with the self-consistent inclusion of diamagnetic and magnetic drifts [19]. This code has been extensively used to study the critical rotation and damping mechanisms for RWMs, giving a strong improvement to the knowledge on passive stabilization.

Present and further effort are oriented to the combination of this beneficial passive stabilizing effect with the active feedback control, in order to reach operational regimes at higher values of β_N.

Feedback stabilization

The slowing down effect provided by the resistive wall on the external kink growth rate opens to the possibility of the use of active feedback strategy, to obtain a synergic effect with both active and passive stabilization.

Following the results reported in [18], Bondeson suggested that a rotating plasma would cause the current induced into the wall to rotate with respect to the wall itself, avoiding the wall current and the mode perturbed current to grow in phase, and thus leading to stabilization. Following this idea, the concept of rotating real or virtual walls was proposed and developed [20].

Bishop proposed to use a feedback coils system covering the entire surface of the torus, to artificially reproduce the effect of the ideally conducting structures, replenish the flux leakage though wall [21]. This is the so-called *intelligent shell concept*, and requires, in principle, a high number of saddle coils supplied and driven with a degree of freedom suitable to ensure that the replenish of the flux leakage is ensured locally.

The toroidal calculations the RWM feedback control was were first presented by Liu and Bondeson [22], with a simple arrangement of actuator and sensor coils, and considering thin axi-symmetric conducting structures. This analysis, carried out with the MARS-F code, shows that the mode can be fully stabilized with a simple set of coils and one array of sensor coils located at one poloidal location, in contraposition to original configuration proposed by Bishop [21]. In order to characterize the effectiveness of different sensor and feedback configurations, further studies have been done using a lumped parameters model in terms of fluxes produced by the plasma and the feedback coils, considering into the computation also the response of the conducting structures, but modelled as a thin shell [23]. It has turned out that better performance can be obtained with poloidal field sensors rather than the radial sensors.

Since both the feedback coils and the plasma interact with every passive conductors close to them, it is clear that a reliable model of such structures should be consider fundamental in the study the plasma stability during feedback. This modelling activity should be devoted to take into account the real geometry of the system, in which specifically the 3-D features of the stabilizing wall can play a crucial role [24, 25, 26, 27]. For this reason, many computational tools have been developed in recent years, such as KINX [12],

VALEN, [28, 29], STARWALL [30, 31] and CarMa [32, 33]. These codes have been extensively used to design new (and optimum) feedback systems, as well as for the interpretation of experimental results.

In this work, particular attention will be focused specifically on the CarMa code, in order to overcome some of these weaknesses can be too limiting in some particular cases.

Bibliography

[1] D. Schnack, *Lectures in Magnetohydrodynamics: With an Appendix on Extended MHD*. Lecture Notes in Physics, Springer Berlin Heidelberg, 2009.

[2] J. P. Freidberg, *Ideal MHD*. Cambridge University Press, 2014.

[3] H. Zohm, *Magnetohydrodynamic Stability of Tokamaks*. 01 2015.

[4] J. Wesson and D. Campbell, *Tokamaks*. International Series of Monogr, OUP Oxford, 2011.

[5] V. Igochine, *Active Control of Magneto-hydrodynamic Instabilities in Hot Plasmas*. Springer Series on Atomic, Optical, and Plasma Physics, Springer Berlin Heidelberg, 2014.

[6] J. Blum, *Numerical simulation and optimal control in plasma physics: with applications to Tokamaks*. Gauthier-Villars, 1989.

[7] L. Artsimovich, "Research on controlled thermonuclear reactions in the physics-uspekhiussr," *Physics-Uspekhi*, vol. 1, no. 2, pp. 191–207, 1958.

[8] M. S. Chu and M. Okabayashi, "Stabilization of the external kink and the resistive wall mode," *Plasma Physics and Controlled Fusion*, vol. 52, p. 123001, oct 2010.

[9] ITER Physics Basis Editors and ITER Physics Expert Group Chairs an Co-Chairs and ITER Joint Central Team and Physics Unit, "Chapter 1: Overview and summary," *Nuclear Fusion*, vol. 39, pp. 2137–2174, dec 1999.

[10] V. D. Shafranov, "Hydromagnetic Stability of a Current-Carrying Pinch in a Strong Longitudinal Magnetic Field," *Soviet Physics Technical Physics*, vol. 15, p. 175, Aug 1970.

[11] R. Gruber, F. Troyon, D. Berger, L. Bernard, S. Rousset, R. Schreiber, W. Kerner, W. Schneider, and K. Roberts, "Erato stability code," *Computer Physics Communications*, vol. 21, no. 3, pp. 323 – 371, 1981.

[12] L. Degtyarev, A. Martynov, S. Medvedev, F. Troyon, L. Villard, and R. Gruber, "The KINX ideal MHD stability code for axisymmetric plasmas with separatrix," *Computer Physics Communications*, vol. 103, no. 1, pp. 10 – 27, 1997.

[13] R. Grimm, R. Dewar, and J. Manickam, "Ideal MHD stability calculations in axisymmetric toroidal coordinate systems," *Journal of Computational Physics*, vol. 49, no. 1, pp. 94 – 117, 1983.

[14] D. Pfirsch and H. Tasso, "A theorem on MHD-instability of plasmas with resistive walls," *Nuclear Fusion*, vol. 11, pp. 259–260, may 1971.

[15] E. J. Strait, "Stability of high beta tokamak plasmas*," *Physics of Plasmas*, vol. 1, no. 5, pp. 1415–1431, 1994.

[16] A. D. Turnbull, T. S. Taylor, Y. R. Lin-Liu, and H. S. John, "High beta and enhanced confinement in a second stable core VH-mode advanced tokamak," *Phys. Rev. Lett.*, vol. 74, pp. 718–721, Jan 1995.

[17] R. Bickerton, J. Connor, and J. Taylor, "Diffusion-driven plasma currents and bootstrap tokamak," *Nature (London). Phys. Sci. 229: 110-12(25 Jan 1971).*

[18] A. Bondeson and D. J. Ward, "Stabilization of external modes in tokamaks by resistive walls and plasma rotation," *Phys. Rev. Lett.*, vol. 72, pp. 2709–2712, Apr 1994.

[19] Y. Q. Liu, M. S. Chu, I. T. Chapman, and T. C. Hender, "Toroidal self-consistent modeling of drift kinetic effects on the resistive wall mode," *Physics of Plasmas*, vol. 15, no. 11, p. 112503, 2008.

[20] R. Fitzpatrick and T. H. Jensen, "Stabilization of the resistive wall mode using a fake rotating shell," *Physics of Plasmas*, vol. 3, no. 7, pp. 2641–2652, 1996.

[21] C. M. Bishop, "An intelligent shell for the toroidal pinch," *Plasma Physics and Controlled Fusion*, vol. 31, pp. 1179–1189, jun 1989.

[22] Y. Q. Liu and A. Bondeson, "Active feedback stabilization of toroidal external modes in tokamaks," *Phys. Rev. Lett.*, vol. 84, pp. 907–910, Jan 2000.

[23] E. Strait, J. Bialek, N. Bogatu, M. Chance, M. Chu, D. Edgell, A. Garofalo, G. Jackson, T. Jensen, L. Johnson, J. Kim, R. L. Haye, G. Navratil, M. Okabayashi, H. Reimerdes, J. Scoville, A. Turnbull, M. Walker, and the DIII–D Team, "Resistive wall stabilization of high-beta plasmas in DIII–D," *Nuclear Fusion*, vol. 43, pp. 430–440, may 2003.

[24] F. Villone, R. Albanese, Y. Q. Liu, A. Portone, and G. Rubinacci, "3D effects of conducting structures on RWMs control in ITER," *34th EPS Conference on Plasma Physics 2007, EPS 2007 - Europhysics Conference Abstracts*, vol. 31, 01 2007.

[25] F. Villone, Y. Q. Liu, P. Roberto, T. Bolzonella, and G. Rubinacci, "Effects of three-dimensional electromagnetic structures on resistive-wall-mode stability of reversed field pinches," *Phys. Rev. Lett.*, vol. 100, p. 255005, 06 2008.

[26] F. Villone, Y. Q. Liu, G. Rubinacci, and S. Ventre, "Effects of thick blanket modules on the resistive wall modes stability in ITER," *Nuclear Fusion*, vol. 50, p. 125011, nov 2010.

[27] V. D. Pustovitov, "Plasma stability theory including the resistive wall effects," *Journal of Plasma Physics*, vol. 81, no. 6, 2015.

[28] J. Bialek, A. H. Boozer, M. E. Mauel, and G. A. Navratil, "Modeling of active control of external magnetohydrodynamic instabilities," *Physics of Plasmas*, vol. 8, no. 5, pp. 2170–2180, 2001.

[29] A. H. Boozer, "Perturbed plasma equilibria," *Physics of Plasmas*, vol. 6, no. 3, pp. 831–836, 1999.

[30] E. Strumberger, S. Günter, P. Merkel, S. Riondato, E. Schwarz, C. Tichmann, and H. Zehrfeld, "Numerical MHD stability studies: toroidal rotation, viscosity, resistive walls and current holes," *Nuclear Fusion*, vol. 45, pp. 1156–1167, sep 2005.

[31] E. Strumberger, P. Merkel, M. Sempf, and S. Günter, "On fully three-dimensional resistive wall mode and feedback stabilization computations," *Physics of Plasmas*, vol. 15, no. 5, p. 056110, 2008.

[32] A. Portone, F. Villone, Y. Q. Liu, R. Albanese, and G. Rubinacci, "Linearly perturbed MHD equilibria and 3D eddy current coupling via the control surface method," *Plasma Physics and Controlled Fusion*, vol. 50, no. 8, p. 085004, 2008.

[33] R. Albanese, Y. Q. Liu, A. Portone, G. Rubinacci, and F. Villone, "Coupling between a 3-D integral eddy current formulation and a linearized MHD model for the analysis of resistive wall modes," *IEEE Transactions on Magnetics*, vol. 44, June 2008.

3 RWMs analysis with full 3-D geometry: the CarMa code

Contents

3.1 Introduction

As was already said in the previous chapter, one of the most stringent limitations to reach high performances in toroidal fusion devices is given by external ideal MHD modes of low toroidal mode number n [1, 2], driven either by the plasma current or pressure. These instabilities produce magnetic field perturbations, which induce stabilizing image currents in the metallic structures placed around the plasma. Such image currents, flowing inside the resistive wall, reduce the mode growth rate from the Alfvén time scale (microseconds) to the characteristic time of the passive structures (the so called *wall time*), that is the penetration time of the perturbed magnetic field. This fact motivates the name of Resistive Wall Modes (RWMs) for these instabilities. This time ranges go from several milliseconds for the existing devices to about 0.3s for ITER [3, 4]. Since RWMs typically grow on millisecond timescale, it is hence possible to get stabilization with magnetic feedback. Many different strategies have been applied to tackle active control of RWMs. Both experimental and modelling examples can be found on a variety of Tokamak devices [5, 6, 7], and extensions of the virtual shell

concept for stabilization of multiple RWMs have been applied to Reversed Field Pinch experiments as well [8, 9, 10, 11].

It is well known that the three-dimensional characteristics of conducting structures, as well as the geometry of the feedback coil system, play an important role in determining the mode dynamics. It is therefore important to implement modelling tools that allow to take these characteristics into account.

The CarMa code [12, 13] is a computational tool developed for the purpose of studying RWM instabilities coupled with conducting structures [14]. CarMa takes rigorously into account the real geometry of conducting structures, such as the thickness of the conductors. Many other tools have been developed with the same purpose [15, 16, 17, 18, 19], all of them using a *thin-wall* approximation [20] for the passive conductors. This approximation, however, has been found valid only for relatively slow modes. As reported in [21] and [22], when the instability is faster than the conventional RWM ($\gamma\tau_w >> 1$, where γ is the mode growth rate and τ_w the wall characteristic time) the skin effect of the induced wall current can make the thin-wall approximation unacceptable, because the magnetic energy stored inside the wall is coupled in a non-linear way with the RWM growth rate. The CarMa code can overcome this approximation, taking advantage of a volume integral solution of the eddy current problem.

CarMa has been successfully used in existing devices, such as JET [23] and RFX-mod [24], with applications to RWM control modelling [25] and control system optimization [26]. Predictive simulations have been carried out for future devices as well, such as JT-60SA [27] and ITER [28, 29].

However, the coupling strategy behind CarMa code suffers of some limitations: the main one is the assumption of static plasma response to external magnetic field perturbation, the so-called *massless approximation*. This means that the plasma inertia and any associated Alfvén-wave-like phenomena can be neglected on the time scale of interest [30].

This chapter is devoted to a brief presentation of the CarMa code, paying particular attention to the decoupling problem of the plasma response computations.

3.2 Decoupling in the problem of plasma response computation

Analysis of the resistive wall mode (RWM) feedback stabilization in tokamaks requires knowledge of the plasma reaction to the slowly varying exter-

nal helical perturbations [31].

The time scale of the RWM dynamics is determined by the *wall time*, which is the decay time of the mirror current on the wall. In all cases, the timescale is much longer than the force balance equilibration time inside the plasma, therefore the plasma can be considered in equilibrium at each moment. This mean that, during the RWM evolution, the plasma can be considered in an equilibrium configuration perturbed by the RWM (or, generally, any slow instability) and evolving with the mode developing. Tokamak reactors usually operate with equilibrium where the normalized kinetic to magnetic pressure exceed the so-called *no-wall limit* [4, 32, 33]: this is a operational region where the RWMs become danger, and can lead to the sudden and abrupt loss of confinement.

The key step on the calculation of the perturbed equilibrium is the separation of the magnetic field produced by the plasma from the total magnetic field found from the perturbed equilibrium calculations. This is clearly indispensable to find the external field (due to currents flowing both in active and in passive conductors) necessary to maintain the plasma configuration in equilibrium. To this purpose, a closed control surface S_e, placed between the plasma region and the vacuum vessel [34], is chosen: that surface splits the space in two regions: the plasma region and the external environment. The magnetic field normal to the control surface is the boundary condition required to make the magnetic field unique in regions. The control surface allows one to completely separate the formulation of the interaction between RWM and conducting structures into two simpler problems: (1) a MHD problem of the linear plasma response computation to external perturbations, and (2) the electromagnetic field problem of the calculation of the eddy current induced inside the conducting structures that surround the plasma.

Once the coupling surface has been identified, the decoupling problem can be written considering the contributions to the total perturbed magnetic field on the coupling surface. The total perturbed magnetic field is given by:

$$\vec{\boldsymbol{B}} = \vec{\boldsymbol{B}}^{pl} + \vec{\boldsymbol{B}}^{ex} \tag{3.1}$$

therefore, to find the external field it is necessary to find the contribution $\vec{\boldsymbol{B}}^{pl}$, that is the plasma response.

In the next section, the coupling strategy used for the CarMa code will be described, which is a numerical procedure developed to decouple the plasma contribution from the total magnetic field perturbation.

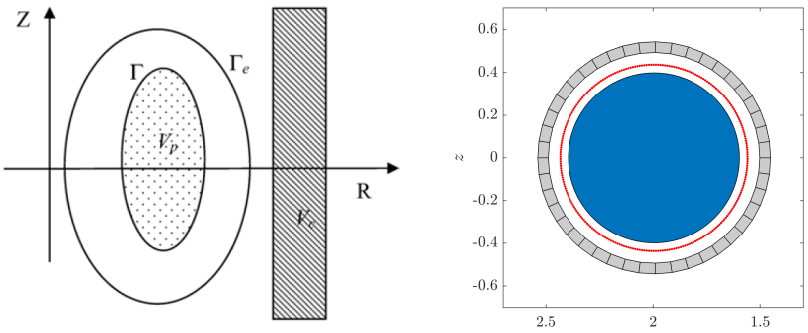

Figure 3.1: *Cross section: sample (a) and circular cross section (b).*

3.3 Plasma response with the Mars code

The procedure at the basis of the CarMa code aims to couple self consistently the computation of the eddy currents in the metallic structures surrounding the plasma to the solution of the plasma ideal MHD equations in their linear approximation. The coupling procedure, which is an extension of the $n = 0$ presented in [35], is described in details in [12, 36].

In the following description, the upper case letters are referred to equilibrium quantities, while the lower case letters to their first order variations with respect to the reference equilibrium. The coordinate system is toroidal (R, ϕ, Z), and (ρ, θ) are the minor radius and the poloidal angle with respect to a given pole (R_0, Z_0) on the poloidal plane

The equilibrium is assumed to be toroidally symmetric: the region of space occupied by the plasma in its reference equilibrium, called V_p, has trace Γ in the poloidal plane. The plasma is assumed not to be in contact with the wall, therefore a coupling surface S_e with trace Γ_e can always be defined between the plasma and the conducting wall, without any intersection with them. In fig. 3.1a a schematic overview of the problem can be seen, while in fig. 3.1b a more realistic case for a plasma with circular cross-section is reported. In particular, the trace of the coupling surface (red) can be seen between the cross-section (blue) and the conducting wall, which have been deliberately drown thicker for the sake of clearness.

The most important assumption behind the following coupling procedure is that the plasma is assumed to be static: since the focus is to capture the slow branch part of the plasma dynamic response, it is suitable to assume that the plasma inertia, for the timescale of interest, is negligible (*mass-less*

approximation). Under this assumption, the plasma mass is neglected, no toroidal flow is considered and the plasma equilibrium fluid velocity $\vec{\boldsymbol{v}} = 0$: the governing equations inside the volume V_p are the single fluid, linearized MHD linear system obtained from the combination of Eqs (2.24), (2.31), (2.32) and (2.28):

$$0 \approx -\nabla p_1 + \vec{\boldsymbol{J}}_1 \times \vec{\boldsymbol{B}}_0 + \vec{\boldsymbol{B}}_1 \times \vec{\boldsymbol{J}}_0 \tag{3.2}$$

$$p_1 = -\vec{\boldsymbol{\xi}} \cdot \nabla P_0 - \Gamma P_0 \nabla \cdot \vec{\boldsymbol{\xi}} \tag{3.3}$$

$$\vec{\boldsymbol{B}}_1 = \nabla \times (\vec{\boldsymbol{\xi}} \times \vec{\boldsymbol{B}}_0) \tag{3.4}$$

$$\mu_0 \vec{\boldsymbol{J}}_1 = \nabla \times \vec{\boldsymbol{B}}_1 \tag{3.5}$$

$$0 = \nabla \cdot \vec{\boldsymbol{B}}_1 \tag{3.6}$$

where the involved quantities have been presented in subsection 2.1.3.

For the study of Resistive Wall Modes stability, the mass-less approximation is justified because the evolution of such instabilities is normally determined by the wall eddy current dynamics, thus the plasma mass plays a minor role. For this reason the plasma mass can be neglected, leading to a plasma response to external magnetic perturbation which is static. However, there are cases when the plasma inertia cannot be neglected, for instance when the plasma is close to the ideal-wall beta limit, or when the plasma flow effects are important [37]. In these cases, in principle, CarMa cannot be used to study these instabilities, because the assumptions behind the coupling strategy are no longer valid.

Before going on, it is useful to remember that the original version of the coupling strategy was developed involving the MARS-F code, presented in [38], which solves the set single-fluid MHD equations (3.2)-(3.6). Recently, newer version of the MARS code have been presented, called MARS-K, able to self consistently model the drift kinetic effects, toroidal plasma flow and flow shear on global MHD modes [39]: however, the description of the coupling strategy refers to the fluid MHD equations (3.2)-(3.6), as was for the original version of the code.

The equation for the vacuum region outside V_p and bounded by the surface S_e are:

$$\nabla \times \vec{\boldsymbol{B}}_1 = 0 \tag{3.7}$$

$$\nabla \cdot \vec{\boldsymbol{B}}_1 = 0 \tag{3.8}$$

At this point, the components of the perturbed magnetic field normal and tangential to the coupling surface S_e are expanded in poloidal and toroidal

Fourier harmonics. Since in the next part of the work only perturbed quantities will be considered, unless specified, the quantities will be written neglecting the subscript 1. Thus:

$$\vec{\boldsymbol{B}} \cdot \hat{\boldsymbol{n}}|_{S_e} = B_N(\rho, \theta, \phi) \mid_{S_e} = B_N(\rho(\theta), \theta, \phi) = \sum_n \sum_m b_N^{n,m} e^{i(n\phi + m\theta)} \quad (3.9)$$

$$\vec{\boldsymbol{B}} \times \hat{\boldsymbol{n}}|_{S_e} = B_T(\rho, \theta, \phi) \mid_{S_e} = B_T(\rho(\theta), \theta, \phi) = \sum_n \sum_m b_T^{n,m} e^{i(n\phi + m\theta)} \quad (3.10)$$

where $\hat{\boldsymbol{n}}$ is the normal unit vector outgoing from S_e. For the mode analysis, only one specific toroidal harmonic component n and a suitable spectrum of poloidal harmonics $m = [M_1, M_2]$ is considered. It is clear that, in principle, an infinite number M of poloidal harmonics are required: for a realistic implementation only a finite number M, high enough to ensure the desired accuracy, is chosen.

For a fixed toroidal harmonic n and a chosen spectrum of M poloidal harmonics, what we aim is to find a *linear* mapping between the components of the perturbed magnetic field normal and tangential to the coupling surface, such as:

$$\boldsymbol{b}_T = \boldsymbol{K}\boldsymbol{b}_N \quad (3.11)$$

This is done in a numerical way solving the set of MHD equations (3.2)-(3.6) M times in the domain bounded by S_e. For each computation, a set of boundary conditions on normal component $\boldsymbol{b}_N$ of the total magnetic field is imposed, and the solution of each computation would give the tangential component $\boldsymbol{b}_T$ on S_e. In particular, for each computation, the boundary conditions are linearly independent. A set of used boundary conditions can be seen in figure 3.2.

The single toroidal mode description can be easily justified noting that, since the MHD equations are linear and the computational boundary axisymmetric, imposing a set of boundary conditions whit a single toroidal mode n would give a computed $\boldsymbol{b}$ on S_e exhibiting only the same single toroidal mode n.

The sufficiency of the normal magnetic field as a boundary condition can be understood from the properties of Laplace's equation [34]. The control surface lies in the vacuum region just outside the plasma boundary and concatenates the plasma. Assuming that there is no net perturbed plasma current, which is the case of helical perturbations, the perturbed magnetic field $\boldsymbol{b}$ is curl free on either side of the control surface. Thus $\boldsymbol{b} = \nabla\varphi$, with φ a suitable Laplacian-free scalar potential $\nabla^2\varphi = 0$. The Laplace's equation gives a unique answer for $\boldsymbol{b}$ if $\hat{\boldsymbol{n}} \cdot \nabla\varphi$ is given on a closed surface with $\hat{\boldsymbol{n}}$ the

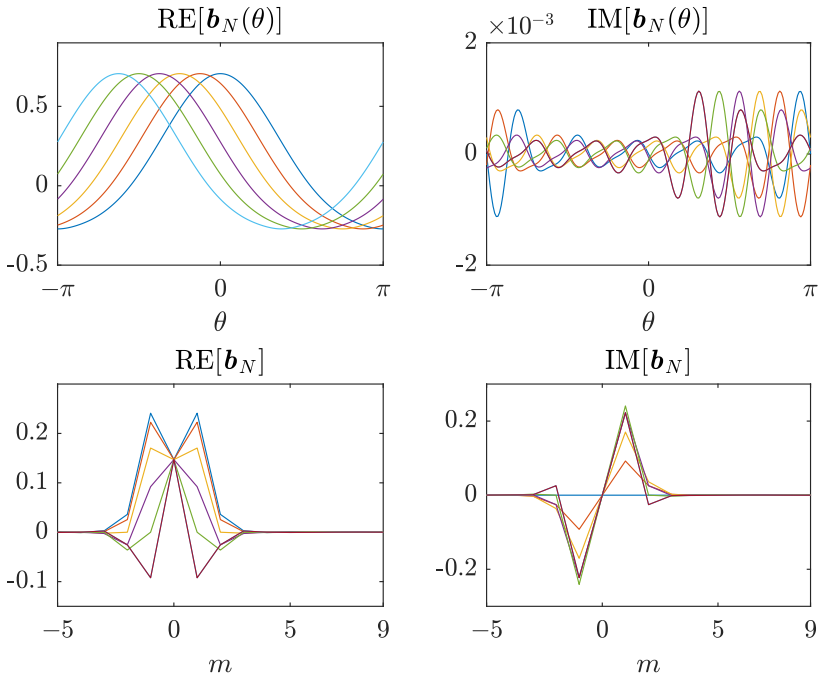

Figure 3.2: *Some of the M linearly independent boundary conditions on the normal field for the problem* (3.2)-(3.6)*. Both real and imaginary part of the spatial distribution $\boldsymbol{b}_N(\theta)$ and the related Fourier harmonics $\boldsymbol{b}_N$.*

surface normal.

Starting from M linearly independent boundary conditions we can obtain M independent solutions of the MHD equations:

$$\begin{aligned} \text{sol. 1} \qquad & \boldsymbol{b}_T^{(1)} = k_{1,1}\boldsymbol{b}_N^{(1)} + ... + k_{1,M}\boldsymbol{b}_N^{(M)} \\ & \vdots \\ \text{sol. M} \qquad & \boldsymbol{b}_T^{(M)} = k_{M,1}\boldsymbol{b}_N^{(M)} + ... + k_{M,M}\boldsymbol{b}_N^{(M)} \end{aligned} \tag{3.12}$$

where $\boldsymbol{b}_T^{(m)}$ is the vector of M Fourier coefficient for the tangential component of the magnetic field, referred to the *mth* set of boundary conditions. Writing the problem in a matricial form we obtain:

$$\underbrace{\left[\boldsymbol{b}_T^{(1)} \mid \boldsymbol{b}_T^{(2)} \mid ... \mid \boldsymbol{b}_T^{(M)}\right]}_{\boldsymbol{B}_T} = \boldsymbol{K}\underbrace{\left[\boldsymbol{b}_N^{(1)} \mid \boldsymbol{b}_N^{(2)} \mid ... \mid \boldsymbol{b}_N^{(M)}\right]}_{\boldsymbol{B}_N} \tag{3.13}$$

and finally:

$$\boldsymbol{K} = \boldsymbol{B}_T\boldsymbol{B}_N^{-1} \tag{3.14}$$

For large poloidal spectra, the matrix $\boldsymbol{B}_N$ of Fourier coefficient could be

ill-conditioned, leading to a inaccurate computation of the inverse $\boldsymbol{B}_N^{-1}$: in this case, a suitable regularization technique could be required to compute $\boldsymbol{B}_N^{-1}$. An example will be analyzed later in the next chapters.

The same procedure is repeated for vacuum equations (3.7),(3.8), still imposing the same boundary conditions on S_e. This gives the *vacuum solution* inside S_e, meaning that no plasma is present. We obtain:

$$\tilde{\boldsymbol{K}} = \tilde{\boldsymbol{B}}_T \boldsymbol{B}_N^{-1} \tag{3.15}$$

The computation of $\tilde{\boldsymbol{K}}$ is shortly justified: with simple electromagnetic reasoning, the quantity [40, 31]:

$$\boldsymbol{j}_{eq} = \frac{1}{\mu_0} \hat{\boldsymbol{n}} \times (\boldsymbol{b} - \tilde{\boldsymbol{b}}) \tag{3.16}$$

$$= \frac{1}{\mu_0} (\boldsymbol{b}_T - \tilde{\boldsymbol{b}}_T) \tag{3.17}$$

is an equivalent surface current density flowing on S_e and producing, outside S_e, the same magnetic field as the plasma for each imposed normal field boundary conditions. Relation (3.17) can be written as:

$$\boldsymbol{j}_{eq} = \mu_0^{-1} (\boldsymbol{K} - \tilde{\boldsymbol{K}}) \boldsymbol{b}_N = \boldsymbol{F} \boldsymbol{b}_N \tag{3.18}$$

defining the matrix $\boldsymbol{F}$ that maps the poloidal harmonics of the total perturbed magnetic field, normal to S_e, onto the harmonics of the equivalent current density on S_e.

It is important to note that the magnetic field tangential to the coupling surface has two components, poloidal $\boldsymbol{b}_{T,\theta}$ and toroidal $\boldsymbol{b}_{T,\phi}$. The previous computations should be performed for both $\boldsymbol{b}_{T,\theta}$ and $\boldsymbol{b}_{T,\phi}$ exactly in the same way, to have a complete description of the tangential magnetic field, and giving rise to both the poloidal and toroidal components of the equivalent current density.

The second step in the decoupling problem is to link $\boldsymbol{b}_N^{ex}$, harmonics of the external perturbed fields normal to S_e, to the total field $\boldsymbol{b}_N$. Here *external* refers generally to any magnetic field provided by the external environment to keep the plasma in equilibrium: since the aim of this work is at first to study the dynamic of RWMs in the presence of three dimensional conducting structures and in view of control, here we are going to consider as *external* field both the eddy current effect plus the contribution of any feedback control circuit.

Since $\boldsymbol{b}_N^{pl} = \boldsymbol{H} \boldsymbol{j}_{eq}$, where $\boldsymbol{H}$ is a $M \times M$ matrix computed from the

Biot-Savart integral, it follows that:

$$\boldsymbol{b}_N^{pl} = \boldsymbol{H}\boldsymbol{F}\boldsymbol{b}_N = \boldsymbol{G}\boldsymbol{b}_N \tag{3.19}$$

and then:

$$\begin{aligned} \boldsymbol{b}_N^{ex} &= \boldsymbol{b}_N - \boldsymbol{b}_N^{pl} && (3.20)\\ &= \boldsymbol{b}_N - \boldsymbol{G}\boldsymbol{b}_N && (3.21)\\ &= (\boldsymbol{E} - \boldsymbol{G})\boldsymbol{b}_N && (3.22) \end{aligned}$$

where $\boldsymbol{E}$ is the identity matrix, and $\boldsymbol{b}_N^{ex}$ is the vector of poloidal harmonics associated with the normal field on S_e due to external currents that, for the given excitation in the total field $\boldsymbol{b}_N$, complement the plasma reaction in producing the total field normal component $\boldsymbol{b}_N$. The final relation is:

$$\begin{aligned} \boldsymbol{b}_N &= (\boldsymbol{E} - \boldsymbol{G})^{-1}\boldsymbol{b}_N^{ex} && (3.23)\\ &= \boldsymbol{W}\boldsymbol{b}_N^{ex} && (3.24) \end{aligned}$$

In equation (3.23) the matrix $(\boldsymbol{E} - \boldsymbol{G})$ is assumed to be invertible: detailed considerations about the physical meaning of possible rank deficiency can be found in [12].

Equation (3.23) is a key relation in the decoupling problem, because it gives the normal component of the *total* magnetic field on S_e, including also the plasma response, for a given normal component of the *external* field acting as excitation. It is a $M \times M$ matrix which can be viewed as a permeability matrix, first introduced in [34]. The main difference with [34] is that the computations to obtain $\boldsymbol{W}$ involves all the Fourier harmonics of the truncated poloidal spectrum, rather than the no-wall kink eigenfunction [41].

3.4 Coupling strategy

In this section, the coupling problem between the current outside the coupling surface and the plasma response to such external perturbation will be discussed. In particular, since we are interested in the study of the RWMs stabilization, the external perturbations come from both the current from excitation coils and the eddy current induced inside the conducting structure by the mode evolution.

The computational electromagnetic problem is treated through an integral formulation [42] which assumes as primary unknown the current density

in conducting structures: with this formulation, only the conducting domain V_c (see Fig. 3.1) must be discretized, and the regularity conditions at infinity are automatically taken into account. This formalism allows to treat self consistently the three-dimensional volumetric geometry, without falling into any thin-plate approximation of the conductors, like for instance in [16, 43].

The first variation of electric field is expressed as:

$$\vec{\boldsymbol{e}} = -\frac{\partial \vec{\boldsymbol{a}}}{\partial t} - \nabla\varphi \tag{3.25}$$

where $\vec{\boldsymbol{a}}$ is the corresponding first order variation of the magnetic vector potential such that $\vec{\boldsymbol{B}}_1 = \nabla \times \vec{\boldsymbol{a}}$ and it is computed from the current density $\vec{\boldsymbol{j}}$ via the Biot–Savart law. The Ohm's law $\vec{\boldsymbol{e}} = \boldsymbol{\Theta} \cdot \vec{\boldsymbol{j}}$, where $\boldsymbol{\Theta}$ is the resistivity tensor of the conducting structures, can be written using the weighted residual approach to obtain the *weak form* of the problem [44]:

$$\int_{V_c} \vec{\boldsymbol{w}} \cdot (\boldsymbol{\Theta} \cdot \vec{\boldsymbol{j}} - \vec{\boldsymbol{e}})\ dV_c = 0 \tag{3.26}$$

for every test function $\vec{\boldsymbol{w}}$.

The current density is defined through the following linear combination of the basis functions:

$$\vec{\boldsymbol{j}} = \sum_i I_i \boldsymbol{J}_i \tag{3.27}$$

and divergence free condition on $\vec{\boldsymbol{j}}$ is imposed by introducing the electric vector potential $\vec{\boldsymbol{t}}$, such as $\vec{\boldsymbol{j}} = \nabla \times \vec{\boldsymbol{t}}$, adopting edge element shape functions $\boldsymbol{t}_k$ for the discretization of the domain V_c, and imposing the gauge condition $\vec{\boldsymbol{t}} \cdot \vec{\boldsymbol{w}} = 0$ for the uniqueness of $\vec{\boldsymbol{t}}$. This gauge is conveniently imposed directly on the basis functions, introducing the tree-cotree decomposition of the mesh and eliminating the degrees of freedom associated to tree edges. An automatic and self-consistent treatment is performed for topologically complex domains and for conductors with electrodes to be coupled with external circuits [45].

At this point, recalling the definition (3.27), it follows that:

$$\vec{\boldsymbol{j}} = \sum_i I_i \nabla \times \boldsymbol{t}_i \tag{3.28}$$

and using Galerking method we can write equation (3.26) in a finite element approach, which reduces to a linear system of ordinary differential equations in the unknown $\boldsymbol{i}$, i.e. the vector of discrete currents induced in the

conducting structures, of dimension N_{3D}. The problem can be written as:

$$\boldsymbol{L}\frac{d\boldsymbol{i}}{dt} + \boldsymbol{R}\boldsymbol{i} = -\frac{d\boldsymbol{u}}{dt} + \boldsymbol{D}\boldsymbol{v} \tag{3.29}$$

and can be solved using a suitable stepping integration method. Here $\boldsymbol{v}$ is the vector of voltages applied to externally fed electrodes Σ_i, and:

$$L_{ij} = \frac{\mu_0}{4\pi}\int_{V_c}\int_{V_c'}\frac{\nabla\times\boldsymbol{t}_i(\vec{\boldsymbol{r}})\cdot\nabla\times\boldsymbol{t}_j(\vec{\boldsymbol{r}}')}{|\vec{\boldsymbol{r}}-\vec{\boldsymbol{r}}'|}dV'dV \tag{3.30}$$

$$R_{ij} = \int_{V_c}\nabla\times\boldsymbol{t}_i\cdot\boldsymbol{\Theta}\cdot\nabla\times\boldsymbol{t}_j dV \tag{3.31}$$

$$u_i = -\frac{\mu_0}{4\pi}\int_{V_c}\nabla\times\boldsymbol{t}_i\cdot\vec{\boldsymbol{a}}_s dV \tag{3.32}$$

$$D_{i,j} = -\int_{\Sigma_i}\nabla\times\boldsymbol{t}_i\cdot\hat{\boldsymbol{n}}dS \tag{3.33}$$

Here $\vec{\boldsymbol{a}}_s$ is the contribution to the magnetic vector potential by the current densities *external* to the conducting structures, in particular of the plasma. To take into account the plasma contribution we define, for the coupling surface S_e discretized in N_e points in the poloidal plane, the following matrices:

- the mutual inductance matrix $\boldsymbol{M}$, of dimension $N_{3D}\times N_e$, linking the 3D conducting structures and the equivalent surface currents on S_e;
- the matrix $\boldsymbol{Q}$, of dimension $N_e\times N_{3D}$, that maps each set of discrete currents $\boldsymbol{i}$ into the magnetic field component normal to the coupling surface S_e.

Relations (3.18), (3.23) can be rearranged to obtain:

$$\begin{aligned}\boldsymbol{j}_{eq} &= \boldsymbol{F}\boldsymbol{b}_N &(3.34)\\ &= \boldsymbol{F}\big(\boldsymbol{E}-\boldsymbol{G}\big)^{-1}\boldsymbol{b}_N^{ex} &(3.35)\\ &= \boldsymbol{F}(\boldsymbol{E}-\boldsymbol{G})^{-1}\boldsymbol{Q}\boldsymbol{i} &(3.36)\\ &= \boldsymbol{F}\boldsymbol{W}\boldsymbol{Q}\boldsymbol{i} &(3.37)\end{aligned}$$

As was already said, relations are computed for a single toroidal mode number n. However, the complex Fourier series in (m,n) used by MARS and reported in Eqs (3.9) - (3.10) requires a symmetric choice of n, therefore any computation should be repeated for the coupled toroidal modes $(-n,n)$. Nevertheless, it can be proved that under suitable hypothesis, for the Fourier coefficients holds the equality $c^{(m,n)} = \overline{c}^{(-m,-n)}$, where $\overline{c}$ is the complex conjugate of c. For this reason, the plasma response can be computed with

MARS only for the mode n, taking advantage of the property of the complex Fourier series to have the information also for $-n$.

Taking advantage of the previous consideration, the perturbed magnetic flux $\boldsymbol{u}$ produced by the toroidal harmonics $(-n, n)$ of the plasma current is:

$$\boldsymbol{u} = \boldsymbol{M} \sum_{(n,-n)} \sum_{m} \boldsymbol{j}^{(m,n)} e^{i(n\phi + m\theta)} \tag{3.38}$$

$$= \boldsymbol{M} \sum_{(n,-n)} \boldsymbol{j}(\theta)^{(n)} \tag{3.39}$$

$$= \sum_{(n,-n)} \boldsymbol{M}^{(n)} \boldsymbol{j}(\theta)^{(n)} \tag{3.40}$$

$$= \boldsymbol{M}^{(n)} \boldsymbol{j}(\theta)_N^{(n)} + \overline{\boldsymbol{M}}^{(n)} \overline{\boldsymbol{j}}(\theta)^{(n)} \tag{3.41}$$

In particular, the fact that $\boldsymbol{j}(\theta)^{(-n)} = \overline{\boldsymbol{j}}(\theta)^{(n)}$ has been exploited.

The operator $\boldsymbol{M}$ in eq. (3.39) is the mutual inductance between the *total* (i.e. both toroidal components $(n, -n)$) current $\boldsymbol{j}(\theta)$ and the passive conductors, while $\boldsymbol{M}^{(n)}$ refers only to one single toroidal harmonic. However, since in the following part of the work only a single couple of toroidal mode number is considered, the superscript $^{(n)}$ will be dropped, and (3.41) will be performed implicitly to consider both n and $-n$).

It follows that the voltage therm $d\boldsymbol{u}/dt$ of equation (3.29) can be written as:

$$\frac{d\boldsymbol{u}}{dt} = \left(\sum_{(n,-n)} \underbrace{\boldsymbol{M}^{(n)} \boldsymbol{F}^{(n)} \boldsymbol{W}^{(n)}}_{\boldsymbol{S}^{(n)}} \boldsymbol{Q}^{(n)} \right) \frac{d\boldsymbol{i}}{dt} \tag{3.42}$$

$$= [\boldsymbol{SQ} + \overline{\boldsymbol{SQ}}] \frac{d\boldsymbol{i}}{dt} \tag{3.43}$$

$$= 2\mathrm{RE}\big[\boldsymbol{SQ}\big] \frac{d\boldsymbol{i}}{dt} \tag{3.44}$$

$$= \boldsymbol{X} \frac{d\boldsymbol{i}}{dt} \tag{3.45}$$

We will clarify shortly the reason for introducing matrix $\boldsymbol{S} = \boldsymbol{MFW}$, of dimension $N_{3D} \times M$ and mapping the external perturbed field $\boldsymbol{b}_N^{ex}$ to the perturbed magnetic flux $\boldsymbol{u}$ produced by the plasma reaction to this perturbation and linked to the passive structures. The matrix $\boldsymbol{X}$, whose dimensions are $N_{3D} \times N_{3D}$, is the *response matrix*, and describes the plasma response to external perturbations: this matrix takes into account consistently the plasma response and links this response to the eddy currents induced inside the passive structures. Since $rank(\boldsymbol{F}) = rank(\boldsymbol{W}) = M$, then $rank(\boldsymbol{SQ}) = M$, with M number of poloidal harmonics, and therefore $rank(\boldsymbol{SQ} + \overline{\boldsymbol{SQ}}) = 2M$,

and typically is $M << N_{3D}$. The fact that the rank of $\boldsymbol{X}$ is much lower than its dimensions can be used to improve the performance of the algorithm used for the computation of the mode eigenvalue [46].

This procedure let us to modify the eddy current problem (3.29):

$$\underbrace{(\boldsymbol{L}+\boldsymbol{X})}_{\boldsymbol{L^*}}\frac{d\boldsymbol{i}}{dt}+\boldsymbol{R}\boldsymbol{i}=\boldsymbol{D}\boldsymbol{v} \tag{3.46}$$

where $\boldsymbol{L^*}$ is the perturbed inductance operator that takes into account the plasma contribution. The mode growth/damping rate can be found looking for the unstable/stable mode of the modified eddy current equation (3.46).

Thanks to Eq. (3.44), it is clear that $\boldsymbol{X}$ has real entries, and so has $\boldsymbol{L^*}$. For this reason, the eigenvalues are expected to appear in complex conjugate pairs, referring to the pair of modes $(-n, n)$.

Moreover, the total perturbation of the magnetic field can be obtained, outside the coupling surface S_e,

$$\boldsymbol{b}=\big(\boldsymbol{C}_e+\boldsymbol{B}_s\boldsymbol{F}\boldsymbol{W}\boldsymbol{Q}\big)\boldsymbol{i}=\big(\boldsymbol{C}_e+\boldsymbol{Y}\big)\boldsymbol{i} \tag{3.47}$$

where $\boldsymbol{C}_e, \boldsymbol{B}_s$ are matrices that come from the discretization of Biot-Savart integral.

Equations (3.46) - (3.47) can be easily written in a state-space form:

$$\frac{d\boldsymbol{i}(t)}{dt}=\boldsymbol{A}\boldsymbol{i}(t)+\boldsymbol{B}\boldsymbol{u}(t) \tag{3.48}$$

$$\boldsymbol{b}(t)=\boldsymbol{C}\boldsymbol{i}(t) \tag{3.49}$$

a form particularly suitable for the design of an active control feedback stabilization.

It is important to note that $\boldsymbol{X}$ and $\boldsymbol{Y}$, respectively in (3.46) - (3.47) can be written with the same formalism to describe MHD instabilities occurring for any toroidal mode number n, where, for each, n, the symmetric $-n$ is automatically considered. In particular, we can expand $\boldsymbol{X}=\boldsymbol{X}^{(0)}+\boldsymbol{X}^{(1)}...$ in (3.46) to include a larger content of toroidal mode numbers:

$$\boldsymbol{L^*}=\boldsymbol{L}+\sum_n \boldsymbol{S}^{(n)}\boldsymbol{Q}^{(n)} \tag{3.50}$$

$$=\boldsymbol{L}+\sum_n \boldsymbol{X}^{(n)} \tag{3.51}$$

the contribution of each toroidal mode $n > 0$ is computed separately, as described above, thanks to the linearity of the model, and the contribution

of the symmetric modes $n < 0$ automatically kept into account following (3.44).

A particular feature of the CarMa code is the ability to take rigorously into account the coupling between modes with different n that occurs for non axisymmetric wall, even in case of linear MHD [47].

3.4.1 Some numerical considerations

In order to make such methods convenient for large-scale problems, "fast techniques" have been implemented in the CARIDDI code [46]. Firs of all, it is the use of an *inverse iteration scheme* for the computation of the mode eigenvalue. This scheme is widely used in Magneto-Hydrodynamic stability analysis, because it allows the computation of individual eigenvalues, with a fast convergence, starting from a sufficiently close initial guess. The implementation of this method in the CARIDDI code relies on the preconditioned GMRES iterative method for the efficient solutions of linear system required by the inverse iteration, since the use of a direct solver is unpractical for large-scale problems. In addition to this, the computations are further speeded-up both thanks to the peculiar features of this surface-based coupling between plasma and conductors, and to an efficient low-rank approximation of the sub-matrices of the inductance operator $\boldsymbol{L}$ representing interactions between far sources [48]: these sub-matrices are related to non-adjacent cells (sub-regions), and are described by a low-rank QR factorization [49] based on the full Modified Gram-Schmidt (MGR) to improve the computational efficiency [50]. It is worth noting that an ad-hoc strategy, based on the superposition of a regular grid to the finite element mesh, is used to identify well separated elements from adjacent ones.

Bibliography

[1] J. P. Freidberg, *Ideal MHD*. Cambridge University Press, 2014.

[2] G. Bateman, *MHD instabilities*. 1978.

[3] R. Aymar, P. Barabaschi, and Y. Shimomura, "The ITER design," *Plasma Physics and Controlled Fusion*, vol. 44, pp. 519–565, apr 2002.

[4] T.C. Hender et al., "Chapter 3: MHD stability, operational limits and disruptions," *Nuclear Fusion*, vol. 47, pp. S128–S202, jun 2007.

[5] V. D. Pustovitov, "Comparison of RWM feedback systems with differ-

ent input signals," *Plasma physics and controlled fusion*, vol. 44, no. 3, p. 295, 2002.

[6] S. A. Sabbagh et al., "Overview of physics results from the conclusive operation of the national spherical torus experiment," *Nuclear Fusion*, vol. 53, p. 104007, sep 2013.

[7] A. Garofalo, G. Jackson, R. L. Haye, M. Okabayashi, H. Reimerdes, E. Strait, J. Ferron, R. Groebner, Y. In, M. Lanctot, G. Matsunaga, G. Navratil, W. Solomon, H. Takahashi, M. Takechi, and A. Turnbull, "Stability and control of resistive wall modes in high beta, low rotation DIII-d plasmas," *Nuclear Fusion*, vol. 47, pp. 1121–1130, aug 2007.

[8] A. Setiadi, P. Brunsell, and L. Frassinetti, "Implementation of model predictive control for resistive wall mode stabilization on EXTRAP T2R," *Plasma Physics and Controlled Fusion*, vol. 57, p. 104005, 10 2015.

[9] P. Zanca, L. Marrelli, G. Manduchi, and G. Marchiori, "Beyond the intelligent shell concept: The clean-mode-control," *Nuclear Fusion*, vol. 47, p. 1425, 10 2007.

[10] T. Bolzonella, V. Igochine, S. Guo, D. Yadikin, M. Baruzzo, and H. Zohm, "Resistive-wall-mode active rotation in the RFX-Mod device," *Physical review letters*, vol. 101, p. 165003, 11 2008.

[11] T. Bolzonella, M. Cavinato, E. Gaio, L. Grando, A. Luchetta, G. Manduchi, G. Marchiori, L. Marrelli, P. Roberto, A. Soppelsa, and P. Zanca, "Feedback control of resistive wall modes by saddle coils in RFX-mod," *Fusion Engineering and Design*, vol. 82, pp. 1064–1072, 10 2007.

[12] A. Portone, F. Villone, Y. Q. Liu, R. Albanese, and G. Rubinacci, "Linearly perturbed MHD equilibria and 3D eddy current coupling via the control surface method," *Plasma Physics and Controlled Fusion*, vol. 50, no. 8, p. 085004, 2008.

[13] R. Albanese, Y. Q. Liu, A. Portone, G. Rubinacci, and F. Villone, "Coupling between a 3-D integral eddy current formulation and a linearized MHD model for the analysis of resistive wall modes," *IEEE Transactions on Magnetics*, vol. 44, June 2008.

[14] M. Ariola, G. D. Tommasi, A. Pironti, and F. Villone, "Control of resistive wall modes in tokamak plasmas," *Control Engineering Practice*, vol. 24, pp. 15 – 24, 2014.

[15] L. Degtyarev, A. Martynov, S. Medvedev, F. Troyon, L. Villard, and R. Gruber, "The KINX ideal MHD stability code for axisymmetric plasmas with separatrix," *Computer Physics Communications*, vol. 103, no. 1, pp. 10 – 27, 1997.

[16] J. Bialek, A. H. Boozer, M. E. Mauel, and G. A. Navratil, "Modeling of active control of external magnetohydrodynamic instabilities," *Physics of Plasmas*, vol. 8, no. 5, pp. 2170–2180, 2001.

[17] A. H. Boozer, "Perturbed plasma equilibria," *Physics of Plasmas*, vol. 6, no. 3, pp. 831–836, 1999.

[18] E. Strumberger, S. Günter, P. Merkel, S. Riondato, E. Schwarz, C. Tichmann, and H. Zehrfeld, "Numerical MHD stability studies: toroidal rotation, viscosity, resistive walls and current holes," *Nuclear Fusion*, vol. 45, pp. 1156–1167, sep 2005.

[19] E. Strumberger, P. Merkel, M. Sempf, and S. Günter, "On fully three-dimensional resistive wall mode and feedback stabilization computations," *Physics of Plasmas*, vol. 15, no. 5, p. 056110, 2008.

[20] V. D. Pustovitov, "Plasma stability theory including the resistive wall effects," *Journal of Plasma Physics*, vol. 81, no. 6, 2015.

[21] V. D. Pustovitov, "Thick-wall effects in the theory of resistive wall modes," *Physics of Plasmas*, vol. 19, no. 6, p. 062503, 2012.

[22] F. Villone and V. D. Pustovitov, "Skin effect modifications of the resistive wall mode dynamics in tokamaks," *Physics Letters A*, vol. 377, no. 39, pp. 2780 – 2784, 2013.

[23] G. Rubinacci, R. Albanese, G. Artaserse, T. Bellizio, R. Fresa, B. Viola, M. Furno Palumbo, F. Villone, and Y. Q. Liu, "Coupling plasmas and 3D passive structures in the jet tokamak," *International Journal of Applied Electromagnetics and Mechanics*, vol. 33, pp. 533–540, 01 2010.

[24] F. Villone, Y. Q. Liu, P. Roberto, T. Bolzonella, and G. Rubinacci, "Effects of three-dimensional electromagnetic structures on resistive-wall-mode stability of reversed field pinches," *Phys. Rev. Lett.*, vol. 100, p. 255005, 06 2008.

[25] G. Marchiori, M. Baruzzo, T. Bolzonella, Y. Q. Liu, A. Soppelsa, and F. Villone, "Dynamic simulator of RWM control for fusion devices: Modelling and experimental validation on RFX-mod," *Nuclear Fusion*, vol. 52, p. 023020, 01 2012.

[26] L. Pigatto, T. Bolzonella, G. Marchiori, and F. Villone, "Optimal strategies for real-time sparse actuator compensation in RFX-mod MHD control operations," *Fusion Engineering and Design*, vol. 96, 07 2015.

[27] L. Pigatto, T. Bolzonella, J. Garcia, S. C. Guo, Y. Q. Liu, and X. Xu, "Resistive wall mode stability in JT-60SA high β_n scenarios," *43rd EPS Conference on Plasma Physics (Leuven, Belgium)*, 2016.

[28] F. Villone, R. Albanese, Y. Q. Liu, A. Portone, and G. Rubinacci, "3D effects of conducting structures on RWMs control in ITER," *34th EPS Conference on Plasma Physics 2007, EPS 2007 - Europhysics Conference Abstracts*, vol. 31, 01 2007.

[29] F. Villone, Y. Q. Liu, G. Rubinacci, and S. Ventre, "Effects of thick blanket modules on the resistive wall modes stability in ITER," *Nuclear Fusion*, vol. 50, p. 125011, nov 2010.

[30] L. Artsimovich, "Research on controlled thermonuclear reactions in the physics-uspekhiussr," *Physics-Uspekhi*, vol. 1, no. 2, pp. 191–207, 1958.

[31] V. D. Pustovitov, "Decoupling in the problem of tokamak plasma response to asymmetric magnetic perturbations," *Plasma Physics and Controlled Fusion*, vol. 50, no. 10, p. 105001, 2008.

[32] F. Troyon, R. Gruber, H. Saurenmann, S. Semenzato, and S. Succi, "MHD-limits to plasma confinement," *Plasma Physics and Controlled Fusion*, vol. 26, pp. 209–215, jan 1984.

[33] ITER Physics Basis Editors and ITER Physics Expert Group Chairs an Co-Chairs and ITER Joint Central Team and Physics Unit, "Chapter 1: Overview and summary," *Nuclear Fusion*, vol. 39, pp. 2137–2174, dec 1999.

[34] A. H. Boozer, "Feedback equations for the wall modes of a rotating plasma," *Physics of Plasmas*, vol. 6, no. 8, pp. 3180–3187, 1999.

[35] A. Portone, "Perturbed solutions of fixed boundary MHD equilibria," *Nuclear Fusion*, vol. 44, pp. 265–278, jan 2004.

[36] Y. Q. Liu, R. Albanese, A. Portone, G. Rubinacci, and F. Villone, "An analytical demonstration of coupling schemes between magnetohydrodynamic codes and eddy current codes," *Physics of Plasmas*, vol. 15, no. 7, p. 072516, 2008.

[37] Y. Liu, M. S. Chu, W. F. Guo, F. Villone, R. Albanese, G. Ambrosino, M. Baruzzo, T. Bolzonella, I. T. Chapman, A. M. Garofalo, C. G. Gimblett, R. J. Hastie, T. C. Hender, G. L. Jackson, R. J. L. Haye, M. J. Lanctot, Y. In, G. Marchiori, M. Okabayashi, R. Paccagnella, M. F. Palumbo, A. Pironti, H. Reimerdes, G. Rubinacci, A. Soppelsa, E. J. Strait, S. Ventre, and D. Yadykin, "Resistive wall mode control code maturity: progress and specific examples," *Plasma Physics and Controlled Fusion*, vol. 52, p. 104002, sep 2010.

[38] Y. Q. Liu, A. Bondeson, C. M. Fransson, B. Lennartson, and C. Breitholtz, "Feedback stabilization of nonaxisymmetric resistive wall modes in tokamaks. I. electromagnetic model," *Physics of Plasmas*, vol. 7, no. 9, pp. 3681–3690, 2000.

[39] Y. Q. Liu, M. S. Chu, I. T. Chapman, and T. C. Hender, "Toroidal self-consistent modeling of drift kinetic effects on the resistive wall mode," *Physics of Plasmas*, vol. 15, no. 11, p. 112503, 2008.

[40] J. D. Jackson, *Classical electrodynamics*. New York, NY: Wiley, 3rd ed. ed., 1999.

[41] A. H. Boozer, "Equations for studies of feedback stabilization," *Physics of Plasmas*, vol. 5, no. 9, pp. 3350–3357, 1998.

[42] R. Albanese and G. Rubinacci, "Integral formulation for 3d eddy-current computation using edge elements," *IEEE Proceedings A - Physical Science, Measurement and Instrumentation, Management and Education - Reviews*, vol. 135, pp. 457–462, September 1988.

[43] P. Merkel and M. Sempf, "Feedback stabilization of resistive wall modes in the presence of multiply connected wall structures," *IAEA fusion energy conference*, 07 2006.

[44] R. Albanese and G. Rubinacci, "Finite element methods for the solution of 3D eddy current problems," vol. 102 of *Advances in Imaging and Electron Physics*, pp. 1 – 86, Elsevier, 1997.

[45] G. Rubinacci, A. Tamburrino, and F. Villone, "Circuits/fields coupling and multiply connected domains in integral formulations," *IEEE Transactions on Magnetics*, vol. 38, pp. 581–584, March 2002.

[46] G. Rubinacci, S. Ventre, F. Villone, and Y. Q. Liu, "A fast technique applied to the analysis of resistive wall modes with 3D conducting struc-

tures," *Journal of Computational Physics*, vol. 228, no. 5, pp. 1562 – 1572, 2009.

[47] R. Fitzpatrick, "Effect of a nonuniform resistive wall on the stability of tokamak plasmas," *Physics of Plasmas*, vol. 1, no. 9, pp. 2931–2939, 1994.

[48] D. Gope and V. Jandhyala, "Efficient solution of EFIE via low-rank compression of multilevel predetermined interactions," *IEEE Transactions on Antennas and Propagation*, vol. 53, pp. 3324–3333, Oct 2005.

[49] S. Kapur and D. E. Long, "N-body problems: Ies3: Efficient electrostatic and electromagnetic simulation," *IEEE Computational Science and Engineering*, vol. 5, pp. 60–67, Oct 1998.

[50] R. J. Burkholder and Jin-Fa Lee, "Fast dual-mgs block-factorization algorithm for dense MoM matrices," *IEEE Transactions on Antennas and Propagation*, vol. 52, pp. 1693–1699, July 2004.

4 CarMa-D: new coupling procedure based on dynamic plasma response

Contents

4.1 Why improving the static CarMa code?

It was already said in Chap. 3 that the CarMa code relies on some assumptions to couple self-consistently the codes MARS and CARIDDI: these assumptions are that the plasma mass is disregarded, no plasma flow is present and no kinetic damping is taken into account. Within these hypothesis, CarMa has been used extensively to study the stability of RWMs, which occur on timescales orders of magnitudes slower than Alvén-like phenomena. However, if the instability is close to the ideal wall beta limit, the mass-less plasma approximation is no longer valid. As was already pointed out in Ref. [1], for realistic machines the range of growth rates that can be expected for

a RWM can vary in a quite broad range between the slow RWMs and the ideal MHD modes, and it has been not properly explored yet in the theory [2, 3]. For this reason, a computational tool able to deal with broad range of external modes in a robust and accurate way seems to be necessary.

In addition to this, also toroidal rotation and kinetic damping physics are key features for the modelling or RWMs stability problem [4]. It has been demonstrated that plasma rotation, combined with magnetic feedback, can lead to a complete stabilization of RWMs [5, 6]. The stabilization comes from the combined effect of the inherent dissipation inside the plasma coupled with plasma rotation: this was first predicted in Ref. [7], and experimentally demonstrated conclusively in DIII-D experiments [8]. The stabilization process can be modelled by using MARS, relying on two different damping models and including non uniform plasma rotation: in particular, these models are the sound wave damping model [9] and the kinetic damping model [10]. The former damping model is implemented in the MARS-F code, already presented previously in this work and used as MHD solver for the static CarMa code, while the latter have been implemented in the MARS-K code [11]. MARS-K solves the nonlinear eigenvalue problem arising from the combination of the full set of single fluid linear MHD equations with the perturbed kinetic pressure tensor, analytically derived by solving the linearized drift kinetic equation [12, 13].

Furthermore, other considerations should be made on the contribution of the resistive wall for the modes faster than the conventional RWMs, but slower than the ideal magnetohydrodynamics modes. The vast majority of the models developed for the study of RWMs stability relies on the *thin wall* approximation, assuming the normal component of the magnetic perturbation to be constant across the wall. This means that the skin effect of the induced current is neglected, and this is reasonable for the case of slower modes, when the penetration depth of the induced current is much bigger than the wall thickness [1]. However, it has been recently demonstrated that, for the modes faster than the conventional RWMs, the skin effect makes the wall reaction nonlinear, and this energy exchange can contribute to the stabilization [14].

For all these reasons, the goal of coupling a *dynamic* plasma response model, able to take into account plasma rotation together with drift kinetic damping physics, with an eddy current code able to rigorously model 3D features, such as the thickness of the wall and the real geometry of the feedback coils, could provide a computational tool which is ideally the state of the art of the RWMs modelling for stability analysis and active stabilization.

The chapter is organized as follows: at first a set of Padé rational func-

tions is used to model the dynamic plasma response, then this rational interpolation is used to couple the plasma response equation to the eddy current equations, to obtain an improved version of the CarMa code, named CarMa-D (*dynamic*), formally equivalent to the static CarMa but able to take into account the plasma dynamics in the RWMs stability analysis. In addition to this, the mathematical model is then generalized to take into account an arbitrary amount of toroidal mode numbers (*multi-modal* CarMa-D). Additional considerations on the computational cost of the new procedure are also reported.

4.2 Dynamic plasma response and matrix-based rational approximation

The inertia-free approximation, from the point of view of the matrix $\boldsymbol{K}$ already introduced in Eq. (3.11), leads to a static relation between the normal and tangential components of the perturbed magnetic field on the coupling surface. When the plasma is close to the ideal-wall beta limit, or when the plasma flow effects are important, such assumption is no longer valid, and all the quantities involved in plasma response matrix computation in Sec. 3.3 should depend on the dynamics of the perturbation field, hence on the plasma dynamics. Thus, working in the Laplace domain, system (3.2) - (3.6) can be written as [15, 16, 17]:

$$\begin{aligned}
\rho\big(s+in\Omega\big)\vec{\boldsymbol{v}_1} &= -\nabla p_1 + \vec{\boldsymbol{J}_1}\times\vec{\boldsymbol{B}_0} + \vec{\boldsymbol{B}_1}\times\vec{\boldsymbol{J}_0} \\
&\qquad - \rho\big[2\Omega\hat{\boldsymbol{z}}\times\vec{\boldsymbol{v}_1} + (\vec{\boldsymbol{v}_1}\cdot\nabla\Omega)R^2\nabla\phi\big] && (4.1)\\
\big(s+in\Omega\big)p_1 &= -\vec{\boldsymbol{v}_1}\cdot\nabla P_0 - \Gamma P_0\nabla\cdot\vec{\boldsymbol{v}_1} && (4.2)\\
\big(s+in\Omega\big)\vec{\boldsymbol{B}_1} &= \nabla\times(\vec{\boldsymbol{v}_1}\times\vec{\boldsymbol{B}_0}) + (\vec{\boldsymbol{B}_1}\cdot\nabla\Omega)R^2\nabla\phi && (4.3)\\
\mu_0\vec{\boldsymbol{J}_1} &= \nabla\times\vec{\boldsymbol{B}_1} && (4.4)\\
0 &= \nabla\cdot\vec{\boldsymbol{B}_1} && (4.5)
\end{aligned}$$

where s is the complex Laplace variable, corrected by the Doppler shift $in\Omega$, Ω is the plasma rotation frequency along the toroidal direction $\hat{\boldsymbol{\phi}}$, R the plasma major radius, ρ is the unperturbed plasma density, and $\hat{\boldsymbol{z}}$ the unit vector in the vertical direction. Other quantities have already been defined in Chap. 3. The set of equations (4.1) - (4.5) are the full set of linearized MHD equations, written in term of perturbed velocity $\vec{\boldsymbol{v}}_1$, in which the plasma inertia is not neglected.

Drift-kinetic effects are included in the MHD model through the equation

involving the perturbed kinetic pressure tensors [11]:

$$\mathbf{p} = p_1\mathbf{I} + p_{\parallel}\hat{\boldsymbol{b}}\hat{\boldsymbol{b}} + p_{\perp}(\mathbf{I} - \hat{\boldsymbol{b}}\hat{\boldsymbol{b}}) \tag{4.6}$$

where $\mathbf{p}$ is the pressure tensor, p_1 is the scalar pressure perturbation, $p_{\parallel}$ and $p_{\perp}$ are respectively the components of the kinetic pressure perturbations parallel and perpendicular to the equilibrium magnetic field, $\mathbf{I}$ is the unit tensor and $\hat{\boldsymbol{b}} = \vec{\boldsymbol{B}}_0/|\vec{\boldsymbol{B}}_0|$. The full pressure tensor $\mathbf{p}$ is self-consistently included into the MHD formulation by replacing the term p_1 in the momentum equation (4.1).

From the aforementioned considerations it follows that, if the plasma mass is taken into account, a certain dependance of the matrix $\boldsymbol{K}$ on the complex Laplace variable s is expected, giving rise to a dynamic mapping $\boldsymbol{K}(s)$. From a formal point of view, the matrix $\boldsymbol{K}(s)$, which has now to be considered a matrix function, can be computed as done in Sec. 3.3. To this purpose, the system of equations (4.1) - (4.5) is written in a reformulated way [15], and solved for *frequency dependent* boundary conditions $\boldsymbol{b}_N(s)$ on the coupling surface:

$$\begin{cases} s\boldsymbol{D}\boldsymbol{x} = \boldsymbol{A}\boldsymbol{x} \\ \boldsymbol{b}_N\big|_{S_e} = \boldsymbol{b}_N(s) \end{cases} \tag{4.7}$$

where $\boldsymbol{x}$ is the vector of unknowns, and the matrices $\boldsymbol{D}$, $\boldsymbol{A}$ are obtained through numerical discretization of the differential equations (4.1) - (4.5) [18].

This means that Eq. (3.18) becomes:

$$\begin{cases} \boldsymbol{b}_T &= \boldsymbol{K}(s)\boldsymbol{b}_N \\ \tilde{\boldsymbol{b}}_T &= \tilde{\boldsymbol{K}}\boldsymbol{b}_N \end{cases} \quad \Rightarrow \quad \boldsymbol{j}_{eq} = \mu_0^{-1}(\boldsymbol{K}(s) - \tilde{\boldsymbol{K}})\boldsymbol{b}_N = \boldsymbol{F}(s)\boldsymbol{b}_N \tag{4.8}$$

where the vacuum matrix $\tilde{\boldsymbol{K}}$ clearly does not depend on the plasma dynamics. Equations (3.19) becomes:

$$\boldsymbol{b}_N^{pl} = \boldsymbol{H}\boldsymbol{F}(s)\boldsymbol{b}_N = \boldsymbol{G}(s)\boldsymbol{b}_N \tag{4.9}$$

then Eq. (3.22):

$$\boldsymbol{b}_N^{ex} = \big(\boldsymbol{E} - \boldsymbol{G}(s)\big)\boldsymbol{b}_N \tag{4.10}$$

and finally Eq. (3.23):

$$\boldsymbol{b}_N = \big(\boldsymbol{E} - \boldsymbol{G}(s)\big)^{-1}\boldsymbol{b}_N^{ex} \tag{4.11}$$

$$= \boldsymbol{W}(s)\boldsymbol{b}_N^{ex} \tag{4.12}$$

where $\boldsymbol{W}(s), \boldsymbol{F}(s)$ are now matrix functions that describe, together, the frequency dependent plasma response to externally applied magnetic field perturbation.

The arbitrary dependence of the plasma response with respect to the perturbation frequency can be treated as a dynamical linear system: equations (3.18), (3.23) and (3.29) are written showing the explicit dependence of the response matrices with the respect of s. Assuming vanishing initial conditions, we obtain:

$$\begin{cases} s\boldsymbol{L}\boldsymbol{i} + \boldsymbol{R}\boldsymbol{i} + s\boldsymbol{M}\boldsymbol{j}_{eq} = \boldsymbol{D}\boldsymbol{v} \\ \boldsymbol{b}_N = \boldsymbol{W}(s)\boldsymbol{b}_N^{ex} = \boldsymbol{W}(s)\boldsymbol{Q}\boldsymbol{i} \\ \boldsymbol{j}_{eq} = \boldsymbol{F}(s)\boldsymbol{b}_N \end{cases} \tag{4.13}$$

every entry of the matrices $\boldsymbol{F}(s)$ end $\boldsymbol{W}(s)$ is a scalar function of the variable s.

This system of equations describe the coupled problem of the plasma response to external field perturbation together with the eddy current equation, without any assumption of neglecting the plasma mass. It would be desirable to have an analytic relation for the matrix functions $\boldsymbol{W}(s)$, $\boldsymbol{F}(s)$. However, in this work, the problem is addressed in a numerical way, looking for a suitable set of matrix-based interpolating functions. For this purpose, we recall a result already proved in [19] for cylindrical geometry, stating that the plasma response is a rational function, also called Padé interpolation, of the complex variable s. The Padé approximation, which has been widely adopted in many fields as a model reduction technique, has been used also for representing the plasma response for feedback stabilization of RWMs [15, 20, 21, 22].

The Padé approximant for a *scalar* function is the rational function defined as [23]:

$$R(s) = \frac{\sum_{i=0}^{k_n} a_i s^i}{\sum_{i=1}^{k_d} b_i s^i + 1} \tag{4.14}$$

where k_n and k_d are the approximation degree and are not imposed to be equal. Here $R(s)$ is said to be the Padé approximant of order $[k_n/k_d]$. Indeed, since $\boldsymbol{F}(s), \boldsymbol{W}(s)$ are matrix-based functions of s, the relation (4.14) is generalized as:

$$\boldsymbol{F}(s) \quad = \frac{\sum_{i=0}^{k} \boldsymbol{A}_i s^i}{\sum_{i=1}^{k} \boldsymbol{B}_i s^i + \boldsymbol{E}} \tag{4.15}$$

$$\boldsymbol{W}(s) \quad = \frac{\sum_{i=0}^{k} \boldsymbol{C}_i s^i}{\sum_{i=1}^{k} \boldsymbol{D}_i s^i + \boldsymbol{E}}. \tag{4.16}$$

where $\boldsymbol{E}$ is the identity matrix, $\boldsymbol{A}_i, \boldsymbol{B}_i, \boldsymbol{C}_i, \boldsymbol{D}_i$ are the matrix coefficients of the interpolation. Here the same degree k, called *degree of the interpolation*, for both numerator and denominator is considered. Another possible solution can consider directly the product $\boldsymbol{P}(s) = \boldsymbol{F}(s)\boldsymbol{W}(s)$ for the rational interpolation:

$$\boldsymbol{P}(s) = \frac{\sum_{i=0}^{k} \boldsymbol{A}_{pi} s^i}{\sum_{i=1}^{k} \boldsymbol{B}_{pi} s^i + \boldsymbol{E}} \tag{4.17}$$

In general, since this Padé approximation is related to *matricial* functions, the denominators of (4.15)-(4.16)-(4.17) have to be intended as:

$$\boldsymbol{F}(s) = \frac{\boldsymbol{N}(s)}{\boldsymbol{D}(s)} = \left(\sum_{i=1}^{k} \boldsymbol{B}_i s^i + \boldsymbol{E} \right)^{-1} \left(\sum_{i=0}^{k} \boldsymbol{A}_i s^i \right) \tag{4.18}$$

and the domain of this rational function clearly does not allow a singular matrix function $\boldsymbol{D}(s)$. This point will be discussed later also from a physical point of view.

It is clear that, for a given degree k, the first approach with Eqs. (4.15)-(4.16) ensures a higher number of degrees of freedom (DoF) if compared to Eq. (4.17). Conversely, to have the same number of DoF of Eqs. (4.15)-(4.16), the choice of Eq.(4.17) requires a higher degree k. It is useful to stress the point that, as will be seen in the next section, the computations of the coefficients $\boldsymbol{A}_i, \boldsymbol{B}_i, \boldsymbol{C}_i, \boldsymbol{D}_i, \boldsymbol{A}_{pi}, \boldsymbol{B}_{pi}$ requires some matrix inversion operations, and this can be problematic in some cases, because the broad poloidal spectrum of Fourier harmonics required to model highly elongated equilibria can lead to very ill-conditioned response matrices. For this reason, the considerations on numerical accuracy of the strategy are as much important as physics-based considerations on the strategy itself, and will be kept in mind going through the discussion. On the other hand, choosing Eqs. (4.15)-(4.16) will require two inversions to compute the coefficients both of $\boldsymbol{F}(s)$ and $\boldsymbol{W}(s)$, rather than a single inversion required for the computation of $\boldsymbol{P}(s)$ coefficients. This means the propagation of a certain error both on $\boldsymbol{A}_i, \boldsymbol{B}_i$ and on $\boldsymbol{C}_i, \boldsymbol{D}_i$. For this reason, the choice of Eq. (4.15) and (4.16) over Eq. (4.17) is neither obvious nor a priori known. This aspect will be widely discussed in the next chapter.

Since the relations required to obtain the matrix coefficients are the same for (4.15), (4.16) and (4.17), in the following part of the section only the relations for $\boldsymbol{P}(s)$ are considered. For this reason, for simplicity the subscript

p of coefficients $\boldsymbol{A}_{ip}, \boldsymbol{B}_{ip}$ of Eq. (4.17) will be neglected.

To compute coefficients $\boldsymbol{A}_i, \boldsymbol{B}_i$ the rational function (4.17) is suitably manipulated. Equation (4.17) means:

$$\boldsymbol{P}(s) = \big(\boldsymbol{B}_k s^k + \ ... \ + \boldsymbol{E}\big)^{-1} \big(\boldsymbol{A}_k s^k + \ ... \ + \boldsymbol{A}_0\big) \tag{4.19}$$

therefore

$$\big(\boldsymbol{B}_k s^k + \ ... \ + \boldsymbol{E}\big)\boldsymbol{P}(s) = \big(\boldsymbol{A}_k s^k + \ ... \ + \boldsymbol{A}_0\big) \tag{4.20}$$

and so

$$\big(\boldsymbol{B}_k s^k + \ ... \ + \boldsymbol{B}_1 s\big)\boldsymbol{P}(s) - \big(\boldsymbol{A}_k s^k + \ ... \ + \boldsymbol{A}_0\big) = -\boldsymbol{P}(s) \tag{4.21}$$

With this approach, the plasma response is approximated through a matrix based rational interpolation of the reference one, computed starting from MHD equations (4.1) - (4.5). Dealing with an interpolation problem means that the coefficients $\boldsymbol{A}_i, \boldsymbol{B}_i$ have to be computed starting from the knowledge of the matrix function $\boldsymbol{P}(s)$, which has to be interpolated, on a certain number of frequencies s_i (the so-called *basis points*). For a given degree k, the coefficients of (4.17) require the choice of $2k+1$ basis points. These points consist in a suitable set of complex frequencies chosen along the complex plane, and used as input frequencies of the forcing problem (4.7): this means that, given $2k+1$ values of $s_i = \sigma_i + i\omega_i$ as complex excitation frequency, for each s_i the plasma response $\boldsymbol{P}(s_i)$ has to be computed solving the MHD kinetic-hybrid equations (4.1) - (4.5) running MARS-K. This is one of the main differences with the static CarMa code, in which the computation of the (static) plasma response has to be computed just once for vanishing excitation frequency $|s| \to 0$.

With this approach the problem of finding the interpolation coefficients is solved exactly, because $2k+1$ values are needed to find $2k+1$ degrees of freedom. Equation (4.21) is then written for these basis points in order to obtain a block-matrix linear system, where each unknown is a $M \times M$ matrix, being M the number of Fourier harmonics of the poloidal spectrum.

Among all possible sets of basis points, a desirable choice can be to force the function $\boldsymbol{P}(s)$ to pass over two particular points:

- $s = 0$, to match the *static response*:

$$\boldsymbol{A}_0 = \boldsymbol{P}(s = 0) \tag{4.22}$$

  this means that the coefficient $\boldsymbol{A}_0$ is exactly the same matrix of the static CarMa code;

- $|s| \to +\infty$, to match the *response at infinite frequency*:

$$\lim_{|s|\to+\infty} \boldsymbol{P}(s) = \boldsymbol{B}_k^{-1}\boldsymbol{A}_k = \boldsymbol{P}_\infty \tag{4.23}$$

whit this particular choice, equation (4.21) becomes

$$\boldsymbol{B}_k\big(\boldsymbol{P}(s) - \boldsymbol{P}_\infty\big)s^k + \sum_{i=1}^{k-1}\big(\boldsymbol{B}_i\boldsymbol{P}(s) - \boldsymbol{A}_i\big)s^i = \boldsymbol{P}_0 - \boldsymbol{P}(s) \tag{4.24}$$

the remaining $2k-1$ coefficients $\boldsymbol{A}_i, \boldsymbol{B}_i$ can be obtained performing $2k-1$ times the response computations with MARS-K for different value of s. Hence also the problem of choosing suitably the interpolation frequencies is very important.

Here follows the explicit procedure to compute coefficients $\boldsymbol{A}_i, \boldsymbol{B}_i$ for some of the lowest interpolation degrees k, as well as for the general kth order case. In the next part, the following redefinitions $\boldsymbol{\alpha}(s) = \boldsymbol{P}(s) - \boldsymbol{P}_\infty$, $\boldsymbol{\beta}(s) = \boldsymbol{P}_0 - \boldsymbol{P}(s)$ are used.

$\boldsymbol{k = 1}$: since $\boldsymbol{A}_0 = \boldsymbol{P}_0$, only the coefficients $\boldsymbol{A}_1, \boldsymbol{B}_1$ are needed, and one basis point because $\boldsymbol{A}_1$ follows directly from the knowledge of $\boldsymbol{P}_\infty$ as shown in (4.23). For this simple case, an analytical relation can be easily found:

$$\boldsymbol{B}_1 = \frac{1}{s}\boldsymbol{\beta}(s)\boldsymbol{\alpha}(s)^{-1} \tag{4.25}$$

$$\boldsymbol{A}_1 = \boldsymbol{B}_1\boldsymbol{P}_\infty \tag{4.26}$$

$\boldsymbol{k = 2}$: there are 3 DoF, respectively $\boldsymbol{A}_1, \boldsymbol{B}_2, \boldsymbol{B}_1$, therefore 3 basis points $(s, \boldsymbol{P}(s))$ are needed. The following linear system with matrix-valued unknowns can be obtained from (4.24):

$$\begin{bmatrix}\boldsymbol{B}_2 & \boldsymbol{B}_1 & \boldsymbol{A}_1\end{bmatrix}\begin{bmatrix} s_1^2\boldsymbol{\alpha}(s_1) & s_2^2\boldsymbol{\alpha}(s_2) & s_3^2\boldsymbol{\alpha}(s_3) \\ s_1\boldsymbol{P}(s_1) & s_2\boldsymbol{P}(s_2) & s_3\boldsymbol{P}(s_3) \\ -s_1\boldsymbol{E} & -s_2\boldsymbol{E} & -s_3\boldsymbol{E} \end{bmatrix} = \begin{bmatrix}\boldsymbol{\beta}(s_1) & \boldsymbol{\beta}(s_2) & \boldsymbol{\beta}(s_3)\end{bmatrix} \tag{4.27}$$

this leads to the computation of $\boldsymbol{A}_1, \boldsymbol{B}_2, \boldsymbol{B}_1$. The remaining coefficient $\boldsymbol{A}_2$ can be computed from (4.23):

$$\boldsymbol{A}_2 = \boldsymbol{B}_2\boldsymbol{P}_\infty \tag{4.28}$$

$\boldsymbol{k > 2}$: the number of DoF is $2k-1$, respectively $\boldsymbol{B}_k$, .., $\boldsymbol{B}_1$, $\boldsymbol{A}_{k-1}$, .., $\boldsymbol{A}_1$, and the same number of basis points is needed. From Eq. (4.24) we obtain the general relation:

$$\Big[\boldsymbol{B}_k \;..\; \boldsymbol{B}_1 \;\boldsymbol{A}_{k-1} \;..\; \boldsymbol{A}_1\Big] \underbrace{\begin{bmatrix} s_1^k\boldsymbol{\alpha}(s_1) & \dots & s_k^k\boldsymbol{\alpha}(s_k) \\ s_1^{k-1}\boldsymbol{P}(s_1) & \dots & s_k^{k-1}\boldsymbol{P}(s_k) \\ \vdots & \vdots & \vdots \\ s_1\boldsymbol{P}(s_1) & \dots & s_k\boldsymbol{P}(s_k) \\ -s_1^{k-1}\boldsymbol{E} & \dots & -s_k^{k-1}\boldsymbol{E} \\ \vdots & \vdots & \vdots \\ -s_1\boldsymbol{E} & \dots & -s_k\boldsymbol{E} \end{bmatrix}}_{\boldsymbol{Z}} = \underbrace{\Big[\boldsymbol{\beta}(s_1) \;\dots\; \boldsymbol{\beta}(s_k)\Big]}_{\boldsymbol{R}} \tag{4.29}$$

with the following solution:

$$\Big[\boldsymbol{B}_k \;..\; \boldsymbol{B}_1 \;\boldsymbol{A}_{k-1} \;..\; \boldsymbol{A}_1\Big] = \boldsymbol{R}\boldsymbol{Z}^{-1} \tag{4.30}$$

the remaining coefficient $\boldsymbol{A}_k$ can be computed from (4.23) as for the previous case. Matrix $\boldsymbol{Z}$ is square with dimension $M(2k-1) \times M(2k-1)$, while $\boldsymbol{R}$ has dimension $M \times (2k-1)$.

It is worth noting that the matrix $\boldsymbol{Z}$ can be very ill-conditioned, or even singular to machine working precision. This rank deficiency can happen because the information in the pairs $(s_i, \boldsymbol{P}(s_i))$ are linearly dependent, and this can be due to several reasons. One possible case is that the plasma response is almost constant for all the range of frequencies, and this is the case where the massless approximation holds and the static CarMa coupling strategy should be properly used. Another possible issue can be a non appropriate choice of the basis points for the interpolation, that could be erroneously placed in a "flat region" of the plasma response giving rise to a set of linearly dependent pairs $(s_i, \boldsymbol{P}(s_i))$.

On the other hand, even if the basis points are chosen correctly, in some cases it can happen that the matrix $\boldsymbol{Z}$ is ill-conditioned, requiring a special treatment. For example, in case of a broad poloidal spectrum needed to model highly elongated equilibria. This issue will be discussed in the following. The same drawback could be encountered when the interpolation degree k increases to have more DoF. Since Eq. (4.29) goes with the factor s^k, the matrix $\boldsymbol{Z}$ formally equivalent to a Vandermonde matrix typical of Vandermonde polynomial interpolation [24]. Normally, polynomial interpolation theory suggests the use of non-Vandermonde polynomials (for example Newton or Lagrange forms are suggested instead), but, for this spe-

cific case, a sufficiently low degree should be sufficient, because theoretical considerations shows that, for a cylindrical plasma, the system exhibits a second order dynamics [19]. In addition to this, the Vandermonde polynomials $\boldsymbol{N}(s), \boldsymbol{D}(s)$ in (4.18) are suitable to be coupled easily with the eddy current equation in the system (4.13).

It follows that these cases require a special treatment of the system (4.29), and a regularization technique can be used to find the solution. If the simple least-square method is not adequate to solve the linear system, the result can be obtain recalling the Truncated Singular Value Decomposition (TSVD) with truncation index t [25], which gives the factorization of the matrix $\boldsymbol{Z}$ as:

$$\boldsymbol{Z} = \boldsymbol{U}\boldsymbol{\Sigma}\boldsymbol{V}^T \tag{4.31}$$

where $\boldsymbol{\Sigma}$ is the diagonal matrix of the singular values $(\sigma_1, ..., \sigma_t)$, $\boldsymbol{U}, \boldsymbol{V}$ are orthogonal matrices ($\boldsymbol{U}^T = \boldsymbol{U}^{-1}$, same for $\boldsymbol{V}$), and t the desired truncation index. The solution is then obtained as:

$$\left[\boldsymbol{B}_k \; .. \; \boldsymbol{B}_1 \; \boldsymbol{A}_{k-1} \; .. \; \boldsymbol{A}_1\right] = \boldsymbol{R}\boldsymbol{U}^T\boldsymbol{\Sigma}^{-1}\boldsymbol{V} \tag{4.32}$$

the conputation of the inverse $\boldsymbol{\Sigma}^{-1}$ is not expensive because $\boldsymbol{\Sigma}$ is diagonal.

This strategy gives an exact relation to find the interpolation coefficients, because it requires $2k-1$ values, assuming to match the response at vanishing and infinite frequency, to obtain $2k+1$ unknowns: whit this approach the interpolated function is constrained to pass in the basis points, therefore the error is supposed to be zero in these points (in the limit of small condition number of $\boldsymbol{Z}$), but can be unacceptably high outside these points.

Another approach could be the use of a *lest-square* method to impose the trend of the interpolation function not starting from $2k-1$ points, but in a "global" way. Whit this approach, a certain number $N_i >> 2k+1$ of MHD simulations are performed with MARS-K to obtain $\boldsymbol{P}(s_i), \boldsymbol{\beta}(s_i)$: the matrices $\boldsymbol{Z}, \boldsymbol{R}$ of Eq.(4.29) have now respectively dimension $M(2k-1) \times MN_i$ and $M \times N_i$, giving rise to a over-determined linear system where the matrices have to be solved with a regularization technique, such as Truncated Singular Value Decomposition (TSVD) with a suitable truncation index.

4.3 Frequency dependent coupling scheme

The matrix-based rational interpolation functions, presented in the previous paragraph, are used to improve the static CarMa coupling scheme. The following description is carried out only for the case of interpolating directly

$\boldsymbol{P}(s)$, while the mathematical procedure needed in case of separate interpolation of $\boldsymbol{F}(s)$ and $\boldsymbol{W}(s)$ follows the same steps and can be found in details in Appendix A.

Using (4.17) in the system of Eq. (4.13) leads to:

$$\begin{cases} s\boldsymbol{L}\boldsymbol{i} + \boldsymbol{R}\boldsymbol{i} + s\boldsymbol{M}\boldsymbol{j}_{eq} = \boldsymbol{D}\boldsymbol{v} \\ \boldsymbol{j}_{eq} = \left(\sum_i s^i \boldsymbol{B}_i\right)^{-1} \left(\sum_i s^i \boldsymbol{A}_i\right) \boldsymbol{Q}\boldsymbol{i} \end{cases} \tag{4.33}$$

the second equation of the system can be written as:

$$\left(\sum_i s^i \boldsymbol{B}_i\right) \boldsymbol{j}_{eq} = \left(\sum_i s^i \boldsymbol{A}_i\right) \boldsymbol{Q}\boldsymbol{i} \tag{4.34}$$

therefore, system (4.33) becomes:

$$\begin{cases} s\boldsymbol{L}\boldsymbol{i} + \boldsymbol{R}\boldsymbol{i} + s\boldsymbol{M}\boldsymbol{j}_{eq} = \boldsymbol{D}\boldsymbol{v} \\ \left(\sum_i s^i \boldsymbol{B}_i\right) \boldsymbol{j}_{eq} - \left(\sum_i s^i \boldsymbol{A}_i\right) \boldsymbol{Q}\boldsymbol{i} = \boldsymbol{0} \end{cases} \tag{4.35}$$

This system can be written, through the definition of the block matrices $\boldsymbol{L}_{ia}, \boldsymbol{R}_a$, as a *kth* order system of differential equations in the Laplace domain for the vector of unknowns $\boldsymbol{x} = [\boldsymbol{i}\ \boldsymbol{j}_{eq}]$:

$$\begin{aligned} s^k \underbrace{\begin{bmatrix} \boldsymbol{0} & \boldsymbol{0} \\ -\boldsymbol{A}_k\boldsymbol{Q} & \boldsymbol{B}_k \end{bmatrix}}_{\boldsymbol{L}_{ak}} \underbrace{\begin{bmatrix} \boldsymbol{i} \\ \boldsymbol{j}_{eq} \end{bmatrix}}_{\boldsymbol{x}} + \ldots + s^i \underbrace{\begin{bmatrix} \boldsymbol{0} & \boldsymbol{0} \\ -\boldsymbol{A}_i\boldsymbol{Q} & \boldsymbol{B}_i \end{bmatrix}}_{\boldsymbol{L}_{ai}} \begin{bmatrix} \boldsymbol{i} \\ \boldsymbol{j}_{eq} \end{bmatrix} + \ldots \\ + s \underbrace{\begin{bmatrix} \boldsymbol{L} & \boldsymbol{M} \\ -\boldsymbol{A}_1\boldsymbol{Q} & \boldsymbol{B}_1 \end{bmatrix}}_{\boldsymbol{L}_{a1}} \begin{bmatrix} \boldsymbol{i} \\ \boldsymbol{j}_{eq} \end{bmatrix} + \underbrace{\begin{bmatrix} \boldsymbol{R} & \boldsymbol{0} \\ -\boldsymbol{P}_0\boldsymbol{Q} & \boldsymbol{E} \end{bmatrix}}_{\boldsymbol{R}_a} \begin{bmatrix} \boldsymbol{i} \\ \boldsymbol{j}_{eq} \end{bmatrix} = \underbrace{\begin{bmatrix} \boldsymbol{D}\boldsymbol{v} \\ \boldsymbol{0} \end{bmatrix}}_{\boldsymbol{u}} \end{aligned} \tag{4.36}$$

Here the fact that $\boldsymbol{A}_0 = \boldsymbol{P}_0$ and $\boldsymbol{B}_0 = \boldsymbol{E}$, already underlined in the previous paragraph, have been used. With a compact formalism we obtain:

$$\left(\sum_{i=1}^{k} s^i \boldsymbol{L}_{ai}\right) \boldsymbol{x} + \boldsymbol{R}_a \boldsymbol{x} = \boldsymbol{u} \tag{4.37}$$

where $\boldsymbol{u} = [\boldsymbol{D}\boldsymbol{v}\ \boldsymbol{0}]^T$ is the vector of the input quantities.

The *kth* order system of differential equations can be written as a first order system through the following change of variables [26]:

$$\begin{aligned} \boldsymbol{x} &= \boldsymbol{y}_1 \\ s\boldsymbol{y}_1 &= \boldsymbol{y}_2 \\ &\vdots \\ s\boldsymbol{y}_{k-1} &= \boldsymbol{y}_k \end{aligned} \tag{4.38}$$

and the new system of differential equations becomes

$$s \underbrace{\begin{bmatrix} \boldsymbol{E} & & & \\ & \boldsymbol{E} & & \\ & & \ddots & \\ & & & \boldsymbol{L}_k \end{bmatrix}}_{\boldsymbol{L}^*} \underbrace{\begin{bmatrix} \boldsymbol{x} \\ \boldsymbol{y}_1 \\ \vdots \\ \boldsymbol{y}_{k-1} \end{bmatrix}}_{\boldsymbol{y}^*} + \underbrace{\begin{bmatrix} \boldsymbol{0} & -\boldsymbol{E} & & \\ & \boldsymbol{0} & \ddots & \\ & & \ddots & -\boldsymbol{E} \\ \boldsymbol{R}_a & \boldsymbol{L}_1 & \cdots & \boldsymbol{L}_{ak-1} \end{bmatrix}}_{\boldsymbol{R}^*} \begin{bmatrix} \boldsymbol{x} \\ \boldsymbol{y}_1 \\ \vdots \\ \boldsymbol{y}_{k-1} \end{bmatrix} = \underbrace{\begin{bmatrix} \boldsymbol{u} \\ \boldsymbol{0} \\ \vdots \\ \boldsymbol{0} \end{bmatrix}}_{\boldsymbol{u}^*} \tag{4.39}$$

With obvious redefinitions, the systems is written as:

$$s\boldsymbol{L}^*\boldsymbol{y}^* + \boldsymbol{R}^*\boldsymbol{y}^* = \boldsymbol{u}^* \tag{4.40}$$

This is the CarMa-D system of differential equations, formally equivalent to Eq. (3.46), but with a higher number of states to take into account the higher order plasma dynamics. In particular, both $\boldsymbol{R}^*, \boldsymbol{L}^*$ are sparse matrices, and their dimensions are $k(M + N_{3D}) \times k(M + N_{3D})$, with N_{3D} the number of discrete unknown of the eddy current problem.

As was already discussed before, if the previous approach is used to study a resistive wall mode in the so called *typical RWM regime*, e.g. if the instability growth time has the same order of magnitude of wall time, the matrix $\boldsymbol{L}^*$ in Eq. (4.40) can be singular to the machine working precision. In the *static limit*, when the growth rate is small if compared to the wall time, the matrices $\boldsymbol{A}_i, \boldsymbol{B}_i$ in Eq. (4.36), with $i > 1$, are all zeros. This means that the matrix $\boldsymbol{L}^*$ is rank deficient, and the eigenvalue of the dynamical matrix of the system $-(\boldsymbol{L}^*)^{-1}\boldsymbol{R}^*$, which is the growth/damping rate of the RWM, can not be computed anymore because $\boldsymbol{L}^*$ is not invertible. On the other hand, the matrix $\boldsymbol{R}^*$ is always invertible, because it is the composition of the identity matrix with $\boldsymbol{R}_a$, which always has a full rank. A possible solution to this problem is to compute the eigenvalues of the system $-(\boldsymbol{R}^*)^{-1}\boldsymbol{L}^*$, to obtain the growth/damping *time* of the instability rather than the growth/damping rate: the growth rate then follows as the inverse of the growth time.

It can be proved that an analytical relation is available for the block inversion of $-(\boldsymbol{R}^*)^{-1}$, avoiding the numerical computation for the entire

matrix and limiting it to blocks $-(\boldsymbol{R}_a)^{-1}\boldsymbol{L}_{ai}$. This latter step is also not expensive, because matrix $\boldsymbol{R}_a$ is sparse. It follows that:

$$(\boldsymbol{R}^*)^{-1} = \begin{bmatrix} \boldsymbol{R}_a^{-1}\boldsymbol{L}_{a1} & \cdots & \boldsymbol{R}_a^{-1}\boldsymbol{L}_{ak-1} & \boldsymbol{R}_a^{-1} \\ -\boldsymbol{E} & & & \\ & \ddots & & \\ & & -\boldsymbol{E} & \end{bmatrix} \tag{4.41}$$

therefore, the matrix $-(\boldsymbol{R}^*)^{-1}\boldsymbol{L}^*$ becomes:

$$\begin{aligned} -(\boldsymbol{R}^*)^{-1}\boldsymbol{L}^* &= -\begin{bmatrix} \boldsymbol{R}_a^{-1}\boldsymbol{L}_{a1} & \cdots & \boldsymbol{R}_a^{-1}\boldsymbol{L}_{ak-1} & \boldsymbol{R}_a^{-1} \\ -\boldsymbol{E} & & & \\ & \ddots & & \\ & & -\boldsymbol{E} & \end{bmatrix} \begin{bmatrix} \boldsymbol{E} & & & \\ & \boldsymbol{E} & & \\ & & \ddots & \\ & & & \boldsymbol{L}_k \end{bmatrix} \\ &= -\begin{bmatrix} \boldsymbol{R}_a^{-1}\boldsymbol{L}_1 & \cdots & \boldsymbol{R}_a^{-1}\boldsymbol{L}_{ak-1} & \boldsymbol{R}_a^{-1}\boldsymbol{L}_k \\ -\boldsymbol{E} & & & \\ & \ddots & & \\ & & -\boldsymbol{E} & \end{bmatrix} \end{aligned} \tag{4.42}$$

The block matrix of (4.42) have the following structure:

$$\boldsymbol{R}_a^{-1}\boldsymbol{L}_{a1} = \begin{bmatrix} \boldsymbol{R}^{-1}\boldsymbol{L} & \boldsymbol{R}^{-1}\boldsymbol{M} \\ \boldsymbol{P}_0\boldsymbol{Q}\boldsymbol{R}^{-1}\boldsymbol{L} - \boldsymbol{A}_1\boldsymbol{Q} & \boldsymbol{P}_0\boldsymbol{Q}\boldsymbol{R}^{-1}\boldsymbol{M} - \boldsymbol{B}_1 \end{bmatrix} \tag{4.43}$$

$$\boldsymbol{R}_a^{-1}\boldsymbol{L}_{ai} = \begin{bmatrix} \boldsymbol{0} & \boldsymbol{0} \\ -\boldsymbol{A}_i\boldsymbol{Q} & -\boldsymbol{B}_i \end{bmatrix} \tag{4.44}$$

It is worth nothing that the ratio between CarMa and CarMa-D number of DoF scales almost linearly with the interpolation order k, being $N_{3D} >> M$:

$$\frac{DoF_{CarMa-D}}{DoF_{CarMa}} = \frac{k(M + N_{3D})}{N_{3D}} \approx k \tag{4.45}$$

However, the matrix $-(\boldsymbol{R}^*)^{-1}\boldsymbol{L}^*$ is sparse, with a dense square block on the upper left corner: this block is related to the $\boldsymbol{R}_a^{-1}\boldsymbol{L}_1$ in (4.42), which is exactly the static CarMa matrix. This means that the number of non-zeros of the system matrix is almost due to the passive block, and therefore:

$$\frac{nnz_{CarMa-D}}{nnz_{CarMa}} =\approx 1 \tag{4.46}$$

this will be shown in details in the next chapters. This means that, even if

the number of unknowns is much higher, if the problem is solved through a suitable sparse linear algebra toolbox, the computational effort to find the eigenvalues does not grow linearly with the interpolation degree .

4.3.1 Notes on the eigenvalues of CarMa-D for the static limit

We consider as *static limit* the case when the growth rate of the RWM is small if compared to the Alfvén time. In this case the static approximation for the plasma response holds, and, as mentioned in the previous subsection, the matrices $\boldsymbol{A}_i, \boldsymbol{B}_i$ in Eq. (4.36), with $i > 1$, are all zeros. It is useful to do some considerations on the rank of the matrix (4.43), as well as on its eigenvalues, to find some relation with static CarMa.

For this purpose, at first the simplest case of $2nd$ degree interpolation of $\boldsymbol{P}(s)$ is considered. For this case, the system matrix (4.42) is:

$$-(\boldsymbol{R}^*)^{-1}\boldsymbol{L}^* = -\begin{bmatrix} \boldsymbol{R}_a^{-1}\boldsymbol{L}_{a1} & \boldsymbol{R}_a^{-1}\boldsymbol{L}_{a2} \\ -\boldsymbol{E} & \boldsymbol{0} \end{bmatrix} \tag{4.47}$$

and, in the static limit, its blocks are equal to:

$$\boldsymbol{R}_a^{-1}\boldsymbol{L}_{a2} = \begin{bmatrix} \boldsymbol{0} & \boldsymbol{0} \\ -\cancel{\boldsymbol{A}_2\boldsymbol{Q}} & \cancel{\boldsymbol{B}_2} \end{bmatrix} = \begin{bmatrix} \boldsymbol{0} & \boldsymbol{0} \\ \boldsymbol{0} & \boldsymbol{0} \end{bmatrix} \tag{4.48}$$

and

$$-\boldsymbol{R}_a^{-1}\boldsymbol{L}_{a1} = -\begin{bmatrix} \boldsymbol{R}^{-1}\boldsymbol{L} & \boldsymbol{R}^{-1}\boldsymbol{M} \\ \boldsymbol{P}_0\boldsymbol{Q}\boldsymbol{R}^{-1}\boldsymbol{L} - \cancel{\boldsymbol{A}_1\boldsymbol{Q}} & \boldsymbol{P}_0\boldsymbol{Q}\boldsymbol{R}^{-1}\boldsymbol{M} - \cancel{\boldsymbol{B}_1} \end{bmatrix} \tag{4.49}$$

$$= -\begin{bmatrix} \boldsymbol{R}^{-1}\boldsymbol{L} & \boldsymbol{R}^{-1}\boldsymbol{M} \\ \boldsymbol{P}_0\boldsymbol{Q}\boldsymbol{R}^{-1}\boldsymbol{L} & \boldsymbol{P}_0\boldsymbol{Q}\boldsymbol{R}^{-1}\boldsymbol{M} \end{bmatrix} \tag{4.50}$$

$$= -\begin{bmatrix} \boldsymbol{E} \\ \boldsymbol{P}_0\boldsymbol{Q} \end{bmatrix} \begin{bmatrix} \boldsymbol{R}^{-1}\boldsymbol{L} & \boldsymbol{R}^{-1}\boldsymbol{M} \end{bmatrix} \tag{4.51}$$

$$= \boldsymbol{a}\boldsymbol{b}^T \tag{4.52}$$

from result (4.51), it follows that, in the static limit, the sub-matrix $-\boldsymbol{R}_a^{-1}\boldsymbol{L}_{a1}$ has dimension $(N_{3D} + M) \times (N_{3D} + M)$ and rank N_{3D}, while the system matrix $\boldsymbol{R}_a^{-1}\boldsymbol{L}_{a2}$ has dimension $2(N_{3D}+M)\times 2(N_{3D}+M)$ and rank $N_{3D}+M$.

To compute the eigenvalues of Eq. (4.47), the following relation for the

determinant of a 2×2 square block matrix is recalled [27]:

$$\det \begin{bmatrix} \boldsymbol{A}_{11} & \boldsymbol{A}_{12} \\ \boldsymbol{A}_{21} & \boldsymbol{A}_{22} \end{bmatrix} = \det\big(\boldsymbol{A}_{22}\big) \det\big(\boldsymbol{A}_{11} - \boldsymbol{A}_{12}\boldsymbol{A}_{22}^{-1}\boldsymbol{A}_{21}\big) \tag{4.53}$$

where $\boldsymbol{A}_{11} = \boldsymbol{R}_a^{-1}\boldsymbol{L}_{a1}, \boldsymbol{A}_{12} = \boldsymbol{R}_a^{-1}\boldsymbol{L}_{a2}, \boldsymbol{A}_{21} = -\boldsymbol{E}, \boldsymbol{A}_{22} = \boldsymbol{0}$. The eigenvalues of Eq. (4.47) can be computed solving the characteristic equation:

$$\det\big(-(\boldsymbol{R}^*)^{-1}\boldsymbol{L}^* - \lambda\boldsymbol{E}\big)\big|_{k=2} = 0 \tag{4.54}$$

where

$$\det\big(-(\boldsymbol{R}^*)^{-1}\boldsymbol{L}^* - \lambda\boldsymbol{E}\big)\big|_{k=2} = \det \begin{bmatrix} -\boldsymbol{R}_a^{-1}\boldsymbol{L}_{a1} - \lambda\boldsymbol{E} & \boldsymbol{0} \\ \boldsymbol{E} & -\lambda\boldsymbol{E} \end{bmatrix} \tag{4.55}$$

$$= \det\big(-\lambda\boldsymbol{E}\big) \det\big(\boldsymbol{R}_a^{-1}\boldsymbol{L}_{a1} - \lambda\boldsymbol{E}\big) \tag{4.56}$$

it follows from Eq. (4.56) that $-(\boldsymbol{R}^*)^{-1}\boldsymbol{L}^*$ has eigenvalue $\lambda = 0$ with multiplicity $N_{3D} + M$, plus other eigenvalues of the block $-\boldsymbol{R}_a^{-1}\boldsymbol{L}_{a1}$, whose rank is N_{3D} as shown in Eq. (4.51). Its eigenvalues are the eigenvalues of the matrix:

$$-\boldsymbol{a}^T\boldsymbol{b} = -\begin{bmatrix} \boldsymbol{R}^{-1}\boldsymbol{L} & \boldsymbol{R}^{-1}\boldsymbol{M} \end{bmatrix} \begin{bmatrix} \boldsymbol{E} \\ \boldsymbol{P}_0\boldsymbol{Q} \end{bmatrix} \tag{4.57}$$

$$= -\boldsymbol{R}^{-1}\boldsymbol{L} - \boldsymbol{R}^{-1}\boldsymbol{M}\boldsymbol{P}_0\boldsymbol{Q} \tag{4.58}$$

$$= -\boldsymbol{R}^{-1}\big[\boldsymbol{L} + \boldsymbol{M}\boldsymbol{P}_0\boldsymbol{Q}\big] \tag{4.59}$$

$$= -\boldsymbol{R}^{-1}\big[\boldsymbol{L} + \boldsymbol{X}\big] \tag{4.60}$$

where $\boldsymbol{X}$ has already been defined in Eq. (3.45) as the *static* plasma response matrix, meaning that Eq. (4.60) gives exactly the static CarMa system. For this reason, the block $-\boldsymbol{R}_a^{-1}\boldsymbol{L}_{a1}$ exhibits in total $N_{3D}+2M$ zeros eigenvalues corresponding to the zero growth times due to the instantaneous plasma response, and other N_{3D} non vanishing eigenvalues corresponding to the inverse of those obtained from the static CarMa system.

Thus, in the static limit $-(\boldsymbol{R}^*)^{-1}\boldsymbol{L}^*$ has, for $2nd$ degree interpolation, N_{3D} zero eigenvalues plus N_{3D} non-zero eigenvalues equal to those of the static CarMa model.

To generalize previous result for an arbitrary kth interpolation degree, at first the case $k = 3$ is considered. The system matrix from Eq. (4.42) is,

in the static limit:

$$-(\boldsymbol{R}^*)^{-1}\boldsymbol{L}^* = -\begin{bmatrix} \boldsymbol{R}_a^{-1}\boldsymbol{L}_{a1} & \boldsymbol{R}_a^{-1}\boldsymbol{L}_{a2} & \boldsymbol{R}_a^{-1}\boldsymbol{L}_{a3} \\ -\boldsymbol{E} & \boldsymbol{0} & \boldsymbol{0} \\ \boldsymbol{0} & -\boldsymbol{E} & \boldsymbol{0} \end{bmatrix} \tag{4.61}$$

$$= -\begin{bmatrix} \boldsymbol{R}_a^{-1}\boldsymbol{L}_{a1} & \boldsymbol{0} & \boldsymbol{0} \\ -\boldsymbol{E} & \boldsymbol{0} & \boldsymbol{0} \\ \boldsymbol{0} & -\boldsymbol{E} & \boldsymbol{0} \end{bmatrix} \tag{4.62}$$

and, for the eigenvalues:

$$\det\big(-(\boldsymbol{R}^*)^{-1}\boldsymbol{L}^* - \lambda\boldsymbol{E}\big)\big|_{k=3} = \det\left[\begin{array}{cc|c} \boldsymbol{R}_a^{-1}\boldsymbol{L}_{a1} - \lambda\boldsymbol{E} & \boldsymbol{0} & \boldsymbol{0} \\ \boldsymbol{E} & -\lambda\boldsymbol{E} & \boldsymbol{0} \\ \hline \boldsymbol{0} & \boldsymbol{E} & -\lambda\boldsymbol{E} \end{array}\right] \tag{4.63}$$

$$= \det\big(-\lambda\boldsymbol{E}\big)\det\big(-(\boldsymbol{R}^*)^{-1}\boldsymbol{L}^* - \lambda\boldsymbol{E}\big)\big|_{k=2} \tag{4.64}$$

which means that the eigenvalues of $-(\boldsymbol{R}^*)^{-1}\boldsymbol{L}^*$, for $k = 3$, are the same obtained for the case $k = 3$ plus N_{3D} zero eigenvalues.

It follows that, in the static limit, the matrix $-(\boldsymbol{R}^*)^{-1}\boldsymbol{L}^*$ of Eq. (4.42) has dimension $2k(N_{3D}+M)\times 2k(N_{3D}+M)$ and rank $k(N_{3D}+M)\times k(N_{3D}+M)$, with only N_{3D} non-zero eigenvalues due to the static CarMa block in Eq. (4.43).

4.4 Multi-modal analysis of RWMs based on dynamic plasma response

4.4.1 Considering the coupled modes $(n, -n)$

For a given toroidal mode number n, the aforementioned formulation does not consider directly the coupled $-n$, as was done with static CarMa trough Eq. (3.38). For this purpose, the system (4.13) is written showing explicitly the components of the modes $(n, -n)$:

$$\begin{cases} s\boldsymbol{L}\boldsymbol{i} + \boldsymbol{R}\boldsymbol{i} + s\boldsymbol{M}^{(n)}\boldsymbol{j}_{eq}^{(n)} + s\boldsymbol{M}^{(-n)}\boldsymbol{j}_{eq}^{(-n)} = \boldsymbol{D}\boldsymbol{v} \\ \boldsymbol{j}_{eq}^{(n)} = \boldsymbol{P}^{(n)}(s)\boldsymbol{Q}^{(n)}\boldsymbol{i} \\ \boldsymbol{j}_{eq}^{(-n)} = \boldsymbol{P}^{(-n)}(s)\boldsymbol{Q}^{(-n)}\boldsymbol{i} \end{cases} \tag{4.65}$$

in case of interpolating directly $\boldsymbol{P}(s)$.

In principle, system (4.65) shows that the frequency dependent plasma response, such as the rational interpolation procedure, should be performed both for the coupled toroidal modes $(\boldsymbol{j}_{eq}^{(n)}, \boldsymbol{j}_{eq}^{(-n)})$. This is actually not necessary, because from the property of the Fourier series that $c^{(m,n)} = \overline{c}^{(-m,-n)}$ follows that:

$$\boldsymbol{M}^{(-m,-n)}\boldsymbol{j}_{eq}^{(-m,-n)} = \overline{\boldsymbol{M}}^{(m,n)}\overline{\boldsymbol{j}}_{eq}^{(m,n)} \tag{4.66}$$

Therefore:

$$\begin{aligned}
\boldsymbol{j}_{eq}^{(-n)} &= \boldsymbol{P}^{(-n)}(s)\boldsymbol{Q}^{(-n)}\boldsymbol{i} && (4.67)\\
&= \left(\sum_{i=1}^{k} \boldsymbol{B}_i^{(-n)} s^i\right)^{-1} \left(\sum_{i=1}^{k} \boldsymbol{A}_i^{(-n)} s^i\right) \boldsymbol{Q}^{(-n)}\boldsymbol{i} && (4.68)\\
&= \left(\sum_{i=1}^{k} \overline{\boldsymbol{B}}_i^{(n)} s^i\right)^{-1} \left(\sum_{i=1}^{k} \overline{\boldsymbol{A}}_i^{(n)} s^i\right) \overline{\boldsymbol{Q}}^{(n)}\boldsymbol{i} && (4.69)\\
&= \overline{\boldsymbol{P}}^{(n)}(s)\overline{\boldsymbol{Q}}^{(n)}\boldsymbol{i} && (4.70)
\end{aligned}$$

System (4.65) can be written to obtain an analogous form of Eq. (4.36)

$$\underbrace{s^k \begin{bmatrix} \boldsymbol{0} & \boldsymbol{0} & \boldsymbol{0} \\ -\boldsymbol{A}_k^{(n)}\boldsymbol{Q}^{(n)} & \boldsymbol{B}_k^{(n)} & \boldsymbol{0} \\ -\overline{\boldsymbol{A}}_k^{(n)}\overline{\boldsymbol{Q}}^{(n)} & \boldsymbol{0} & \overline{\boldsymbol{B}}_k^{(n)} \end{bmatrix}}_{\boldsymbol{L}_{ak}} \boldsymbol{y}^* + \ldots + \underbrace{s \begin{bmatrix} \boldsymbol{L} & \boldsymbol{M}^{(n)} & \overline{\boldsymbol{M}}^{(n)} \\ -\boldsymbol{A}_1^{(n)}\boldsymbol{Q}^{(n)} & \boldsymbol{B}_1^{(n)} & \boldsymbol{0} \\ -\overline{\boldsymbol{A}}_1^{(n)}\overline{\boldsymbol{Q}}^{(n)} & \boldsymbol{0} & \overline{\boldsymbol{B}}_1^{(n)} \end{bmatrix}}_{\boldsymbol{L}_{a1}} \boldsymbol{y}^* + \underbrace{\begin{bmatrix} \boldsymbol{R} & \boldsymbol{0} & \boldsymbol{0} \\ -\boldsymbol{P}_0\boldsymbol{Q} & \boldsymbol{E} & \boldsymbol{0} \\ -\overline{\boldsymbol{P}}_0\overline{\boldsymbol{Q}} & \boldsymbol{0} & \boldsymbol{E} \end{bmatrix}}_{\boldsymbol{R}_a} \boldsymbol{y}^* = \boldsymbol{u}^* \tag{4.71}$$

where now $\boldsymbol{y}^* = [\boldsymbol{i}\ \boldsymbol{j}_{eq}^{(n)}\ \boldsymbol{j}_{eq}^{(-n)}]$ and $\boldsymbol{u}^* = [\boldsymbol{Dv}\ \boldsymbol{0}\ \boldsymbol{0}]$.

It is worth noting that, since the block system of equations (4.36) is considered, there is no explicit summation as Eq. (3.43). Therefore it is not possible to exploit step reported in Eq. (3.44) to compute the sum between complex conjugate terms, in order to have pure real quantities. The fact that these matrices have complex entries will be used in Chap. 6 to explain a small discrepancy on the imaginary parts of eigenvalues expected to be complex conjugate.

The matrices $\boldsymbol{L}_{ai}, \boldsymbol{R}_a$ have been redefined to include the effect of both the toroidal modes $(n, -n)$, but the *kth* order system of differential equation (4.71) is formally equivalent to the one in Eq. (4.36) for a single n. Thus

the discussion for the single mode already carried out in section 4.3 follows exactly the same steps, leading to the system block matrix $-(\boldsymbol{R^*})^{-1}\boldsymbol{L^*}$ of Eq. (4.42), but the block matrices $\boldsymbol{R}_a^{-1}\boldsymbol{L}_{a1}$, $\boldsymbol{R}_a^{-1}\boldsymbol{L}_{ai}$ of Eqs. (4.43)-(4.44) have been modified to take into account both the toroidal modes $(n, -n)$:

$$\boldsymbol{R}_a^{-1}\boldsymbol{L}_{a1} =$$
$$\begin{bmatrix} \boldsymbol{R}^{-1}\boldsymbol{L} & \boldsymbol{R}^{-1}\boldsymbol{M}^n & \boldsymbol{R}^{-1}\overline{\boldsymbol{M}}^n \\ \boldsymbol{P}_0^n\boldsymbol{Q}^n\boldsymbol{R}^{-1}\boldsymbol{L} - \boldsymbol{A}_1^n\boldsymbol{Q}^n & \boldsymbol{P}_0^n\boldsymbol{Q}^n\boldsymbol{R}^{-1}\boldsymbol{M}^n - \boldsymbol{B}_1^n & \boldsymbol{P}_0^n\boldsymbol{Q}^n\boldsymbol{R}^{-1}\overline{\boldsymbol{M}}^n \\ \overline{\boldsymbol{P}}_0^n\overline{\boldsymbol{Q}}^n\boldsymbol{R}^{-1}\boldsymbol{L} - \overline{\boldsymbol{A}}_1^n\overline{\boldsymbol{Q}}^n & \overline{\boldsymbol{P}}_0^n\overline{\boldsymbol{Q}}^n\boldsymbol{R}^{-1}\boldsymbol{M}^n & \overline{\boldsymbol{P}}_0^n\overline{\boldsymbol{Q}}^n\boldsymbol{R}^{-1}\overline{\boldsymbol{M}}^n - \overline{\boldsymbol{B}}_1^n \end{bmatrix}$$
$$\boldsymbol{R}_a^{-1}\boldsymbol{L}_{ai} =$$
$$\begin{bmatrix} \boldsymbol{0} & \boldsymbol{0} & \boldsymbol{0} \\ -\boldsymbol{A}_i^n\boldsymbol{Q}^n & \boldsymbol{B}_i^n & \boldsymbol{0} \\ -\overline{\boldsymbol{A}}_i^n\overline{\boldsymbol{Q}}^n & \boldsymbol{0} & \overline{\boldsymbol{B}}_i^n \end{bmatrix}$$

The analysis of the coupled modes $(n, -n)$ was possible, wit static CarMa, keeping the dimensions of the system matrix unchanged. This was due to the mass-less approximation, which leads to a static plasma response. Therefore the plasma equivalent current density $\boldsymbol{j}_{eq}$, which is the plasma reaction to external perturbation, is linear with respect to such perturbation, allowing the contributions of the modes $(n, -n)$ to be directly added. On the other hand, the CarMa-D coupling strategy is based on the rational interpolation of plasma response matrix: for this reason, the plasma response is no longer linear with respect to the perturbation, and the direct sum of the two contributions is no longer usable. For this reason, modelling of the symmetric modes $(n, -n)$ requires two different equations for the harmonics of the current density $(\boldsymbol{j}_{eq}^{(n)}, \boldsymbol{j}_{eq}^{(-n)})$ in the system (4.13).

4.4.2 Frequency dependent coupling scheme for multiple toroidal modes

It has already mentioned in paragraph 3.4 that one of the features of static Carma is the capability of take into account several toroidal modes at once, thanks to the linearity of the system. This property follows directly from the inertia-free approximation, as described in the previous subsection, and the plasma response matrices $\boldsymbol{X}^{(n)}$ for different toroidal modes can be computed with MARS for several toroidal modes and just added together, as done in Eq. (3.50). The toroidal mode coupling is then self-consistently taken into account from CARIDDI, because of the full 3D computational capabilities. It is worth noting that the aforementioned strategy for static CarMa does not require additional equations, thus the total number of DoF is independent

from the number of toroidal modes considered.

With the mathematical formulation used to derive CarMa-D model, the rational approximation is involved requiring a further manipulation of the system (4.33) to include additional toroidal modes. The following description will be carried out only for the case of interpolating directly $\boldsymbol{P}(s)$.

In principle, the distribution of the equivalent current density $\boldsymbol{j}_{eq}$ on the coupling surface is given for a desired number of toroidal modes:

$$\boldsymbol{j}_{eq}(\theta,\phi) = \sum_n \sum_m \boldsymbol{j}_{eq}^{(n,m)} e^{i(m\theta+n\phi)} \tag{4.72}$$

$$= \sum_n \boldsymbol{j}_{eq}^{(n)}(\theta,\phi) \tag{4.73}$$

where n is the toroidal mode number. The term $\boldsymbol{j}_{eq}^{(n)}(\theta,\phi)$ is the spatial distribution of the equivalent surface current density already defined in (3.16), and computed through (3.18) for the single toroidal mode number n.

For a toroidal spectrum $n \in [n_1, n_2]$, the voltage induced by the mode evolution of Eq.(4.33) is written in terms of eq. (4.72):

$$\boldsymbol{u} = s\boldsymbol{M}\boldsymbol{j}_{eq} \tag{4.74}$$

$$= s \sum_{n=n_1}^{n_2} \left[\boldsymbol{M}^{(n)} \boldsymbol{j}_{eq}^{(n)} + \overline{\boldsymbol{M}}^{(n)} \boldsymbol{j}_{eq}^{(-n)} \right] \tag{4.75}$$

and the system (4.65) becomes, writing explicitly the toroidal modes:

$$\begin{cases} s\boldsymbol{L}\boldsymbol{i} + \boldsymbol{R}\boldsymbol{i} + s \sum_{n=n_1}^{n_2} \left[\boldsymbol{M}^{(n)} \boldsymbol{j}_{eq}^{(n)} + \overline{\boldsymbol{M}}^{(n)} \boldsymbol{j}_{eq}^{(-n)} \right] = \boldsymbol{D}\boldsymbol{v} \\ \boldsymbol{j}_{eq}^{(n_1)} = \left(\sum_i s^i \boldsymbol{B}_i^{(n_1)}\right)^{-1} \left(\sum_i s^i \boldsymbol{A}_i^{(n_1)}\right) \boldsymbol{Q}^{(n_1)} \boldsymbol{i} \\ \boldsymbol{j}_{eq}^{(-n_1)} = \left(\sum_i s^i \overline{\boldsymbol{B}}_i^{(n_1)}\right)^{-1} \left(\sum_i s^i \overline{\boldsymbol{A}}_i^{(n_1)}\right) \overline{\boldsymbol{Q}}^{(n_1)} \boldsymbol{i} \\ \qquad \vdots \\ \boldsymbol{j}_{eq}^{(n_2)} = \left(\sum_i s^i \boldsymbol{B}_i^{(n_2)}\right)^{-1} \left(\sum_i s^i \boldsymbol{A}_i^{(n_2)}\right) \boldsymbol{Q}^{(n_2)} \boldsymbol{i} \\ \boldsymbol{j}_{eq}^{(-n_2)} = \left(\sum_i s^i \overline{\boldsymbol{B}}_i^{(n_2)}\right)^{-1} \left(\sum_i s^i \overline{\boldsymbol{A}}_i^{(n_2)}\right) \overline{\boldsymbol{Q}}^{(n_2)} \boldsymbol{i} \end{cases} \tag{4.76}$$

If we now follow, for this new system of equations, the same steps made in section 4.3 for Eqs. (4.33), (4.36), we can obtain a system of differential equations which is formally equivalent to (4.37), but with $\boldsymbol{L}_{ai}, \boldsymbol{R}_a$ defined as

follows to include different toroidal modes:

$$\boldsymbol{L}_{ai} = \begin{bmatrix} \mathbf{0} & \dots & & & & \\ -\boldsymbol{A}_i^{n_1}\boldsymbol{Q}^{n_1} & \boldsymbol{B}_i^{n_1} & & & & \\ -\overline{\boldsymbol{A}}_i^{n_1}\overline{\boldsymbol{Q}}^{n_1} & & \overline{\boldsymbol{B}}_i^{n_1} & & & \\ \vdots & & & \ddots & & \\ -\boldsymbol{A}_i^{n_2}\boldsymbol{Q}^{n_2} & & & & \boldsymbol{B}_i^{n_2} & \\ -\overline{\boldsymbol{A}}_i^{n_2}\overline{\boldsymbol{Q}}^{n_2} & & & & & \overline{\boldsymbol{B}}_i^{n_2} \end{bmatrix} \tag{4.77}$$

$$\boldsymbol{L}_{a1} = \begin{bmatrix} \boldsymbol{L} & \boldsymbol{M}^{n_1} & \overline{\boldsymbol{M}}^{n_1} & \dots & \boldsymbol{M}^{n_2} & \overline{\boldsymbol{M}}^{n_2} \\ -\boldsymbol{A}_1^{n_1}\boldsymbol{Q}^{n_1} & \boldsymbol{B}_1^{n_1} & & & & \\ -\overline{\boldsymbol{A}}_1^{n_1}\overline{\boldsymbol{Q}}^{n_1} & & \overline{\boldsymbol{B}}_1^{n_1} & & & \\ \vdots & & & \ddots & & \\ -\boldsymbol{A}_1^{n_2}\boldsymbol{Q}^{n_2} & & & & \boldsymbol{B}_1^{n_2} & \\ -\overline{\boldsymbol{A}}_1^{n_2}\overline{\boldsymbol{Q}}^{n_2} & & & & & \overline{\boldsymbol{B}}_1^{n_2} \end{bmatrix} \tag{4.78}$$

$$\boldsymbol{R}_a = \begin{bmatrix} \boldsymbol{R} & \mathbf{0} & \dots & & & \\ -\boldsymbol{A}_0^{n_1}\boldsymbol{Q}^{n_1} & \boldsymbol{B}_0^{n_1} & & & & \\ -\overline{\boldsymbol{A}}_0^{n_1}\overline{\boldsymbol{Q}}^{n_1} & & \overline{\boldsymbol{B}}_0^{n_1} & & & \\ \vdots & & & \ddots & & \\ -\boldsymbol{A}_0^{n_2}\boldsymbol{Q}^{n_2} & & & & \boldsymbol{B}_0^{n_2} & \\ -\overline{\boldsymbol{A}}_0^{n_2}\overline{\boldsymbol{Q}}^{n_2} & & & & & \overline{\boldsymbol{B}}_0^{n_2} \end{bmatrix} \tag{4.79}$$

Since formulation (4.76) leads to Eq. (4.37), also the changing of variables (4.38) can be adopted, giving straightforwardly the first order system of differential equations (4.40). Also the considerations on the rank-deficiency of the operator $\boldsymbol{L}^*$ already done for the single mode case are still valid: for this reason the stability analysis is carried out studying the unstable *growth time* rather than the *growth rate*, exactly as was done for the single mode analysis.

Exploiting the formal analogy with Eq. (4.40) for the single mode analysis, its easy to understand that relations (4.43), (4.44) are still valid for the case of multiple toroidal modes, but with a different meaning for the block matrices $\boldsymbol{R}_a^{-1}\boldsymbol{L}_{ai}$. Here, for a clear description, only the particularization of matrices (4.43) and (4.44) for two toroidal modes (n_1, n_2) are reported, and can be seen in Eqs. (4.80)-(4.81). The generalization to an arbitrary number of modes is straightforward. To write the matrix (4.80) with a slightly compact notation, the matrix $\boldsymbol{T}^{(n_i)}$ is introduced:

$$\boldsymbol{T}^{(n_i)} = \boldsymbol{P}_0^{(n_i)}\boldsymbol{Q}^{(n_i)}\boldsymbol{R}^{-1}$$

$$\boldsymbol{R}_a^{-1}\boldsymbol{L}_{a1} = \begin{bmatrix} \boldsymbol{R}^{-1}\boldsymbol{L} & \boldsymbol{R}^{-1}\boldsymbol{M}^{n_1} & \boldsymbol{R}^{-1}\overline{\boldsymbol{M}}^{n_1} & \boldsymbol{R}^{-1}\boldsymbol{M}^{n_2} & \boldsymbol{R}^{-1}\overline{\boldsymbol{M}}^{n_2} \\ \boldsymbol{T}^{n_1}\boldsymbol{L} - \boldsymbol{A}_1^{n_1}\boldsymbol{Q}^{n_1} & \boldsymbol{T}^{n_1}\boldsymbol{M}^{n_1} - \boldsymbol{B}_1^{n_1} & \boldsymbol{T}^{n_1}\overline{\boldsymbol{M}}^{n_1} & \boldsymbol{T}^{n_1}\overline{\boldsymbol{M}}^{n_2} & \boldsymbol{T}^{n_1}\overline{\boldsymbol{M}}^{n_2} \\ \overline{\boldsymbol{T}}^{n_1}\boldsymbol{L} - \overline{\boldsymbol{A}}_1^{n_1}\overline{\boldsymbol{Q}}^{n_1} & \overline{\boldsymbol{T}}^{n_1}\boldsymbol{M}^{n_1} & \overline{\boldsymbol{T}}^{n_1}\overline{\boldsymbol{M}}^{n_1} - \overline{\boldsymbol{B}}_1^{n_1} & \overline{\boldsymbol{T}}^{n_1}\boldsymbol{M}^{n_2} & \overline{\boldsymbol{T}}^{n_1}\overline{\boldsymbol{M}}^{n_2} \\ \boldsymbol{T}^{n_2}\boldsymbol{L} - \boldsymbol{A}_1^{n_2}\boldsymbol{Q}^{n_2} & \boldsymbol{T}^{n_2}\boldsymbol{M}^{n_1} & \boldsymbol{T}^{n_2}\overline{\boldsymbol{M}}^{n_1} & \boldsymbol{T}^{n_2}\boldsymbol{M}^{n_2} - \boldsymbol{B}_1^{n_2} & \boldsymbol{T}^{n_2}\overline{\boldsymbol{M}}^{n_2} \\ \overline{\boldsymbol{T}}^{n_2}\boldsymbol{L} - \boldsymbol{A}_1^{n_2}\boldsymbol{Q}^{n_2} & \overline{\boldsymbol{T}}^{n_2}\boldsymbol{M}^{n_1} & \overline{\boldsymbol{T}}^{n_2}\overline{\boldsymbol{M}}^{n_1} & \overline{\boldsymbol{T}}^{n_2}\boldsymbol{M}^{n_2} & \overline{\boldsymbol{T}}^{n_2}\overline{\boldsymbol{M}}^{n_2} - \overline{\boldsymbol{B}}_1^{n_2} \end{bmatrix} \tag{4.80}$$

$$\boldsymbol{R}_a^{-1}\boldsymbol{L}_{ai} = \begin{bmatrix} \boldsymbol{0} & & & \\ -\boldsymbol{A}_i^{n_1}\boldsymbol{Q}^{n_1} & \cdots & & \\ -\overline{\boldsymbol{A}}_i^{n_1}\overline{\boldsymbol{Q}}^{n_1} & \boldsymbol{B}_i^{n_1} & & \\ -\boldsymbol{A}_i^{n_2}\boldsymbol{Q}^{n_2} & & \overline{\boldsymbol{B}}_i^{n_1} & \\ -\overline{\boldsymbol{A}}_i^{n_2}\overline{\boldsymbol{Q}}^{n_2} & & & \boldsymbol{B}_i^{n_2} \\ & & & \overline{\boldsymbol{B}}_i^{n_2} \end{bmatrix} \tag{4.81}$$

Matrices (4.43) *and* (4.44) *for the multi-modal case, for two toroidal modes* (n_1, n_2).

It is useful to make some considerations about the number of DoF arising for CarMa-D system, related in particular with the number of toroidal modes considered. For static CarMa, the modelling of multiple toroidal modes would not make the number of DoF raising. Conversely, since the rational interpolation of plasma response matrix used in the CarMa-D, $2N$ equations should be added to the system (4.13) for the modal of N toroidal modes. This means that the number of DoF rises from $2k(M + N_{3D})$ for the single mode problem of Eq. (4.42) to $2k(2NM + N_{3D})$ for the multi-modal system. However, since $N_{3D} >> M$ for any devices and $M \approx N$ for RFPs [28, 29, 30] it follows that:

$$\frac{DoF_{CarMa-D}}{DoF_{CarMa}} = \frac{2k(2NM + N_{3D})}{N_{3D}} \approx 2k \tag{4.82}$$

thus CarMa-D has $2k$-times the number of DoF of static CarMa. As a matter of fact, this can be seen as a disadvantage of CarMa-D. Nevertheless, the actual reference quantity to understand the computational complexity of a model is the number of non-zeros. It can be proved that:

$$nnz_{CarMa-D} \approx nnz_{CarMa} \tag{4.83}$$

as was for the single mode analysis. This result will be shown for a real case in chapter 6.

4.5 Conclusions

The modelling of RWMs stability and control requires an accurate description of the three dimensional structures, such as the conducting wall and the feedback actuators. For this purpose, the static CarMa code has been developed. The assumptions made to couple the codes MARS and CARIDDI are that the plasma mass is disregarded, no plasma flow is present and no kinetic damping is taken into account. However, such assumption are, for some cases, too stringent: this happens if the mode evolves on a timescale much shorter than the wall time, if the toroidal rotation is present, or if appropriate kinetic damping model is required to describe the stabilizing effect given by the inherent energy dissipation inside the plasma.

For this reason, a new coupling strategy based on a *dynamic* plasma response model is presented. Starting from theoretical considerations, the dynamic plasma response has been approximated through suitable matrix-based Padé rational functions, providing a frequency dependent plasma response model. This model has been used to develop CarMa-D, a new cou-

pling strategy not depending on the aforementioned assumptions. This updated version overcomes certain limitations of the original computational model: in particular, (i) the massless assumption for the plasma is removed, allowing modeling of global modes growing from typical RWM regime to ideal-kink time scales; (ii) the effects of toroidal plasma flow and drift kinetic damping can be included into the new model, providing a powerful tool to study macroscopic phenomena where both the plasma dynamics and the 3D conducting structures play important roles (e.g. the resistive wall mode and the plasma response to ac resonant magnetic perturbations).

Additional effort has been made to include multiple toroidal modes in the mathematical description, to obtain a computational tool capable to take rigorously into account an arbitrary number of toroidal modes and their coupling in presence of three dimensional structures.

Moreover, some considerations in case of the static limit has been also done: it has been proved that, if the assumptions made for the static coupling scheme holds, CarMa-D recovers exactly the same eigenvalues of static CarMa.

Bibliography

[1] V. D. Pustovitov, "Plasma stability theory including the resistive wall effects," *Journal of Plasma Physics*, vol. 81, no. 6, 2015.

[2] A. B. Mikhailovskii, *Instabilities in a Confined Plasma*. Institute of Physics Publishing, 1998.

[3] M. S. Chu and M. Okabayashi, "Stabilization of the external kink and the resistive wall mode," *Plasma Physics and Controlled Fusion*, vol. 52, p. 123001, oct 2010.

[4] M. Chu, V. Chan, M. Chance, D. Edgell, A. Garofalo, A. Glasser, S. Guo, D. Humphreys, T. Jensen, J. Kim, R. L. Haye, L. Lao, G. Navratil, M. Okabayashi, F. Perkins, H. Reimerdes, H. S. John, E. Soon, E. Strait, A. Turnbull, M. Walker, and S. Wong, "Modelling of feedback and rotation stabilization of the resistive wall mode in tokamaks," *Nuclear Fusion*, vol. 43, pp. 196–201, feb 2003.

[5] E. J. Strait, J. M. Bialek, I. N. Bogatu, M. S. Chance, M. S. Chu, D. H. Edgell, A. M. Garofalo, G. L. Jackson, R. J. Jayakumar, T. H. Jensen, O. Katsuro-Hopkins, J. S. Kim, R. J. La Haye, L. L. Lao, M. A. Makowski, G. A. Navratil, M. Okabayashi, H. Reimerdes, J. T. Scoville,

A. D. Turnbull, and D. Team, "Resistive wall mode stabilization with internal feedback coils in DIII-D," *Physics of Plasmas*, vol. 11, no. 5, pp. 2505–2513, 2004.

[6] M. Okabayashi, J. Bialek, M. S. Chance, M. S. Chu, E. D. Fredrickson, A. M. Garofalo, R. Hatcher, T. H. Jensen, L. C. Johnson, R. J. L. Haye, G. A. Navratil, H. Reimerdes, J. T. Scoville, E. J. Strait, A. D. Turnbull, M. L. Walker, and the DIII–D Team, "Stabilization of the resistive wall mode in DIII–d by plasma rotation and magnetic feedback," *Plasma Physics and Controlled Fusion*, vol. 44, pp. B339–B355, nov 2002.

[7] A. Bondeson and D. J. Ward, "Stabilization of external modes in tokamaks by resistive walls and plasma rotation," *Phys. Rev. Lett.*, vol. 72, pp. 2709–2712, Apr 1994.

[8] A. M. Garofalo, E. J. Strait, L. C. Johnson, R. J. La Haye, E. A. Lazarus, G. A. Navratil, M. Okabayashi, J. T. Scoville, T. S. Taylor, and A. D. Turnbull, "Sustained stabilization of the resistive-wall mode by plasma rotation in the DIII-D tokamak," *Phys. Rev. Lett.*, vol. 89, p. 235001, Nov 2002.

[9] G. W. Hammett and F. W. Perkins, "Fluid moment models for Landau damping with application to the ion-temperature-gradient instability," *Phys. Rev. Lett.*, vol. 64, pp. 3019–3022, Jun 1990.

[10] A. Bondeson and M. S. Chu, "Inertia and ion Landau damping of low-frequency magnetohydrodynamical modes in tokamaks," *Physics of Plasmas*, vol. 3, no. 8, pp. 3013–3022, 1996.

[11] Y. Q. Liu, M. S. Chu, I. T. Chapman, and T. C. Hender, "Toroidal self-consistent modeling of drift kinetic effects on the resistive wall mode," *Physics of Plasmas*, vol. 15, no. 11, p. 112503, 2008.

[12] M. S. Chu, J. M. Greene, T. H. Jensen, R. L. Miller, A. Bondeson, R. W. Johnson, and M. E. Mauel, "Effect of toroidal plasma flow and flow shear on global magnetohydrodynamic MHD modes," *Physics of Plasmas*, vol. 2, no. 6, pp. 2236–2241, 1995.

[13] Y. Q. Liu, I. T. Chapman, M. S. Chu, H. Reimerdes, F. Villone, R. Albanese, G. Ambrosino, A. M. Garofalo, C. G. Gimblett, R. J. Hastie, T. C. Hender, G. L. Jackson, R. J. La Haye, M. Okabayashi, A. Pironti, A. Portone, G. Rubinacci, and E. J. Strait, "Progress in physics and control of the resistive wall mode in advanced tokamaks," *Physics of Plasmas*, vol. 16, no. 5, p. 056113, 2009.

[14] F. Villone and V. D. Pustovitov, "Skin effect modifications of the resistive wall mode dynamics in tokamaks," *Physics Letters A*, vol. 377, no. 39, pp. 2780 – 2784, 2013.

[15] Y. Q. Liu, "Constructing plasma response models from full toroidal magnetohydrodynamic computations," *Computer Physics Communications*, vol. 176, no. 3, pp. 161 – 169, 2007.

[16] Y. Q. Liu, A. Kirk, and E. Nardon, "Full toroidal plasma response to externally applied nonaxisymmetric magnetic fields," *Physics of Plasmas*, vol. 17, no. 12, p. 122502, 2010.

[17] Y. Q. Liu, R. Akers, I. Chapman, Y. Gribov, G. Hao, G. Huijsmans, A. Kirk, A. Loarte, S. Pinches, M. Reinke, D. Ryan, Y. Sun, and Z. Wang, "Modelling toroidal rotation damping in iter due to external 3D fields," *Nuclear Fusion*, vol. 55, p. 063027, 06 2015.

[18] A. Bondeson, G. Vlad, and H. Lütjens, "Resistive toroidal stability of internal kink modes in circular and shaped tokamaks," *Physics of Fluids B: Plasma Physics*, vol. 4, no. 7, pp. 1889–1900, 1992.

[19] Y. Q. Liu, R. Albanese, A. Portone, G. Rubinacci, and F. Villone, "An analytical demonstration of coupling schemes between magnetohydrodynamic codes and eddy current codes," *Physics of Plasmas*, vol. 15, no. 7, p. 072516, 2008.

[20] Y. Q. Liu and A. Bondeson, "Active feedback stabilization of toroidal external modes in tokamaks," *Phys. Rev. Lett.*, vol. 84, pp. 907–910, Jan 2000.

[21] A. Bondeson, Y. Q. Liu, C. Fransson, B. Lennartson, C. Breitholtz, and T. Taylor, "Active feedback stabilization of high beta modes in advanced tokamaks," *Nuclear Fusion*, vol. 41, pp. 455–463, apr 2001.

[22] Y. Q. Liu, M. S. Chu, A. M. Garofalo, R. J. La Haye, Y. Gribov, M. Gryaznevich, T. C. Hender, D. F. Howell, P. de Vries, M. Okabayashi, S. D. Pinches, H. Reimerdes, and E.-J. contributors, "Modeling of resistive wall mode and its control in experiments and ITER," *Physics of Plasmas*, vol. 13, no. 5, p. 056120, 2006.

[23] G. Baker and P. Graves-Morris, *Padé Approximants*. Cambridge University Press, 2010.

[24] W. Gautschi, "Norm estimates for inverses of Vandermonde matrices," *Numerische Mathematik*, vol. 23, pp. 337–347, Aug 1974.

[25] C. L. Lawson and R. J. Hanson, *Solving Least Squares Problem*. Prentice-Hall.

[26] G. Teschl, *Ordinary Differential Equations and Dynamical Systems*. Graduate studies in mathematics, American Mathematical Soc., 2012.

[27] M. Brookes, *The Matrix Reference Manual*. [online] http://www.ee.imperial.ac.uk/hp/staff/dmb/matrix/intro.html.

[28] P. R. Brunsell, D. Yadikin, D. Gregoratto, R. Paccagnella, T. Bolzonella, M. Cavinato, M. Cecconello, J. R. Drake, A. Luchetta, G. Manduchi, G. Marchiori, L. Marrelli, P. Martin, A. Masiello, F. Milani, S. Ortolani, G. Spizzo, and P. Zanca, "Feedback stabilization of multiple resistive wall modes," *Phys. Rev. Lett.*, vol. 93, p. 225001, Nov 2004.

[29] F. Villone, Y. Q. Liu, P. Roberto, T. Bolzonella, and G. Rubinacci, "Effects of three-dimensional electromagnetic structures on resistive-wall-mode stability of reversed field pinches," *Phys. Rev. Lett.*, vol. 100, p. 255005, 06 2008.

[30] F. Villone, M. Ariola, G. De Tommasi, Y. Liu, S. Mastrostefano, A. Pironti, and S. Ventre, "Multimodal RWM feedback control in ITER," *39th EPS Conference on Plasma Physics 2012, EPS 2012 and the 16th International Congress on Plasma Physics*, vol. 3, pp. 1374–1377, 01 2012.

5 | Validation of the CarMa-D model

Contents

In order to see if CarMa-D model is able to deal with plasma dynamics, considering also toroidal flow and kinetic damping physics, it has been tested with a reference benchmark problem to provide an idea of its effectiveness as well as to address its possible weaknesses. The benchmark case is the stability analysis of a plasma with circular cross section, already used to test the static CarMa code [1].

The main information are summarized in the Fig. 5.1. The plasma has a major radius of $R_0 = 2$m a minor radius of $a = 0.4$m, and the pressure and safety factor profiles are also reported in fig. 5.1. As shown, the circular plasma is enclosed by a coupling surface with circular poloidal trace placed between the plasma boundary and the circular resistive wall (Fig. 5.1). More details on the resistive wall, such as the wall time, will be given in Sec. 5.1.

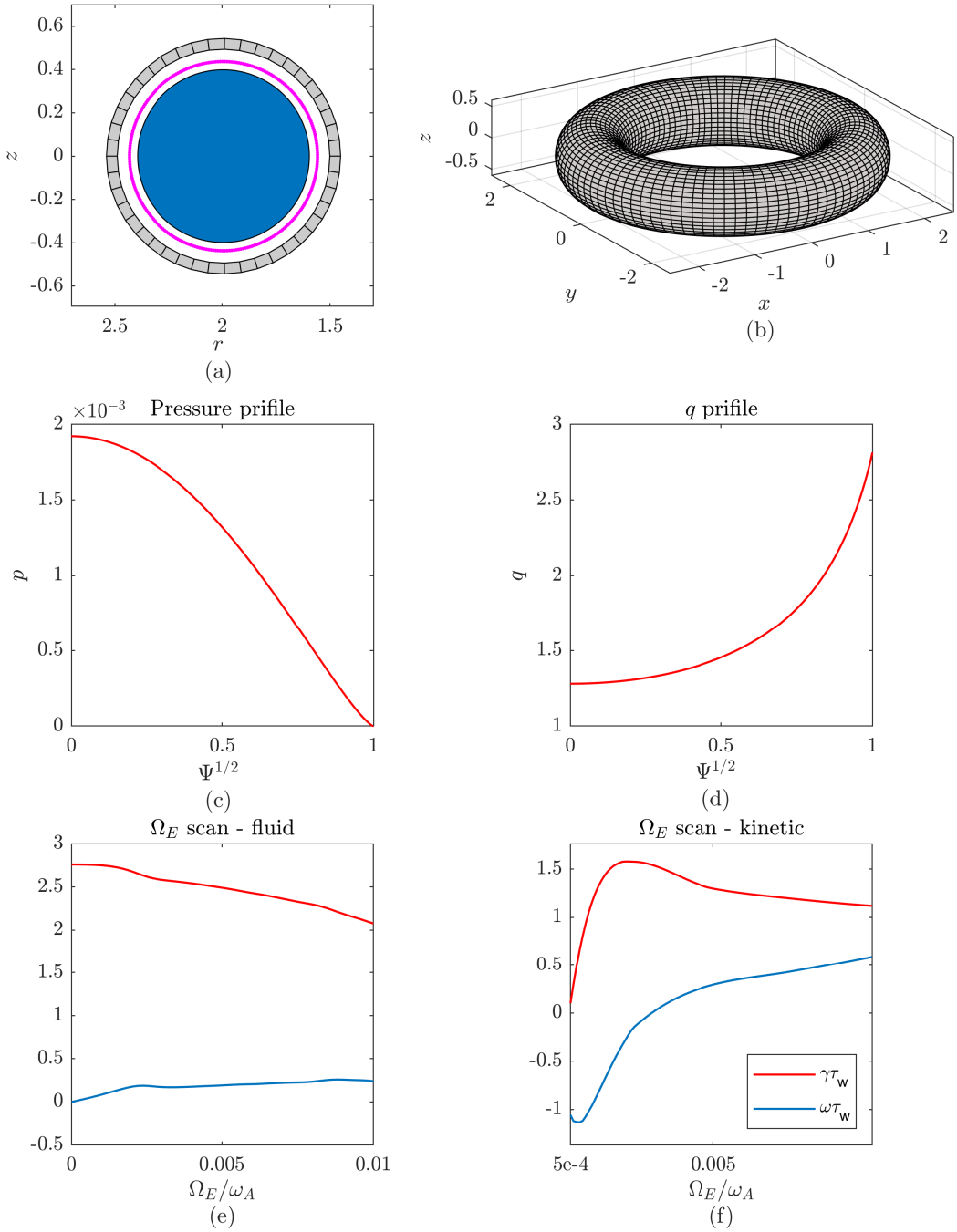

Figure 5.1: *Summary of the test case used in the validation part: (a) plasma cross-section, trace of the coupling surface and stabilizing wall; (b) 3-D view of the axisymmetric stabilizing wall; (c) p profile; (d) q profile; (e) - (f) real (red) and imaginary (blue) parts of the eigenvalue, normalized by the resistive wall time τ_W, for the two different damping mechanism considered (respectively sound wave damping and kinetic damping).*

To highlight the strength of CarMa-D, two different damping physics mechanism are used for the same equilibrium. At first, the parallel sound wave damping model is used, described in detail in [2]. This model includes, through a numerically adjustable coefficient, a viscous term in the momentum equation to represent parallel sound wave damping, which can be tuned varying the aforementioned coefficient. The second model is the MARS-K self consistent, full toroidal drift kinetic model [3], able to introduce kinetic effects in the plasma description. For both damping models, a scan of the mode eigenvalue are reported in Fig. 5.1 (e)-(f) (real and imaginary part, normalized by the wall time) for different values of normalized toroidal rotation Ω_E/ω_A, with ω_A Alfvén frequency. In these computations carried out with MARS-F and MARS-K, the toroidal rotation is assumed to be constant along the minor radius. These will be the reference results, to which the computations of CarMa-D will be compared.

For both the damping mechanisms, at first the rational approximation technique used in the new coupling strategy will be analyzed, to show its effectiveness to model frequency dependent plasma response. After this step, the validation of CarMa-D is performed exactly as done in [4], performing a scan of the wall resistivity η: in the limit of infinite resistivity, the no-wall growth rate of the ideal kink mode must be recovered, which has the same order of magnitude of Alfvén-like phenomena, and therefore strongly depends on the dynamical effects.

An important consideration can be done on the choice of the basis points $(s, \boldsymbol{P}(s))$ needed for the interpolation coefficients. Since $s = \sigma + i\omega$, in principle an infinite number of combinations of basis points are available: here, we have considered three different paths along the complex plane where the basis points are placed, named respectively *complex* ($s = \sigma + i\omega$, imposing $\sigma = \omega$ for the computations), *real* ($s = \sigma$) and *imaginary* ($s = i\omega$) cases. Fig. 5.2 shows these three sets of basis point on the complex plane. In the next part of the work also the comparison between these different choices of basis points has been done. The validation part has been devoted also to understand which set of basis points is the most suitable for this test case.

5.1 Model of the passive structures

A reliable model of RWMs dynamics requires an accurate description of the three dimensional conducting structures [5, 6]. Although CarMa is able, in principle, to model conductors of any shape and geometry, since the primary goal of this work is the validation of CarMa-D with MARS-K which assumes the axisymmetric wall, the wall model of Fig. 5.1 (b) is considered.

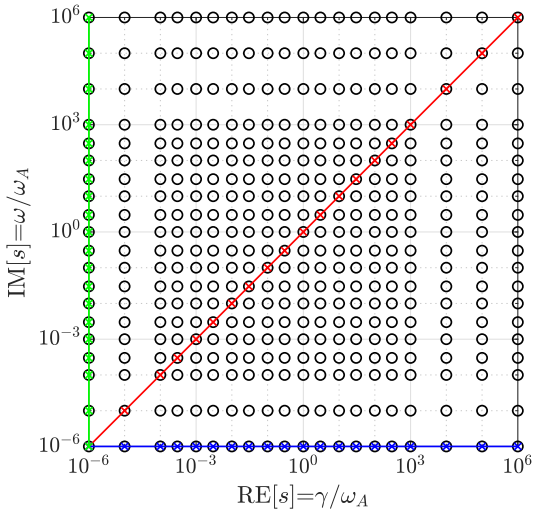

Figure 5.2: *View, on the complex plane, of the three sets of basis points used for the interpolation of plasma response: complex (red), real (blue), imaginary (green).*

The conducting wall used for this case has a circular shape with thickness $\delta = 5$mm, placed at minor radius $a_w = 1.3a$, and resistivity of $\eta = 6.5 \times 10^{-7}\Omega$m. The wall times for some toroidal modes, that is the slowest penetration time through the wall of a magnetic field perturbation with given n periodicity, is reported in Tab. 5.1. In Figs. 5.3 to 5.8 an overview of the image of the passive wall eigenvectors for different toroidal mode numbers: the corresponding eigenvalue is the wall time for that specific n.

	τ_w
$n = 0$	13.7ms
$n = 1$	4.7ms
$n = 2$	4.5ms

Table 5.1: *Wall times for different toroidal mode numbers.*

Since the equilibrium used as test case presents an unstable $n = 1$ instability, for the following part of the chapter the considered wall time used as a normalization factor is the one of the $n = 1$ passive eigenvector, that is $\tau_w = 4.7ms$.

It is worth noting that a precise simulation of the RWM stability problem should require an accurate model of also the resistive wall thickness, which can be done self-consistently by CarMa, without any artificial trick such as, for example, what was done with the VALEN code in [7]. Indeed, as was already mentioned in the introduction, recently was proven that [8, 9] for modes faster than conventional typical RWMs, the thin-wall approximation

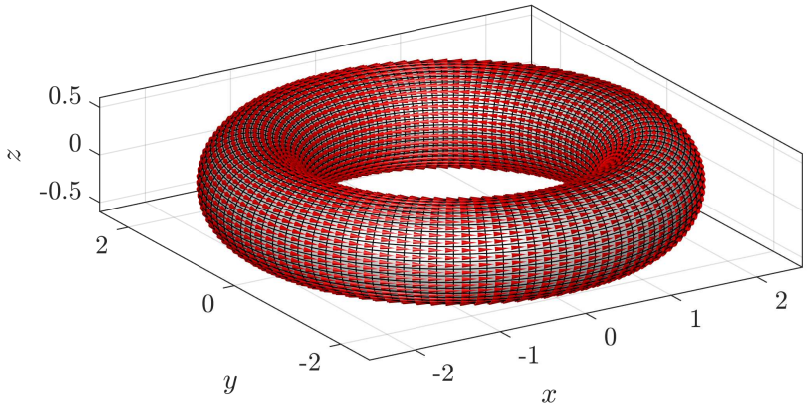

Figure 5.3: *Eddy current pattern related to the $n = 0$ slowest passive eigenvector.*

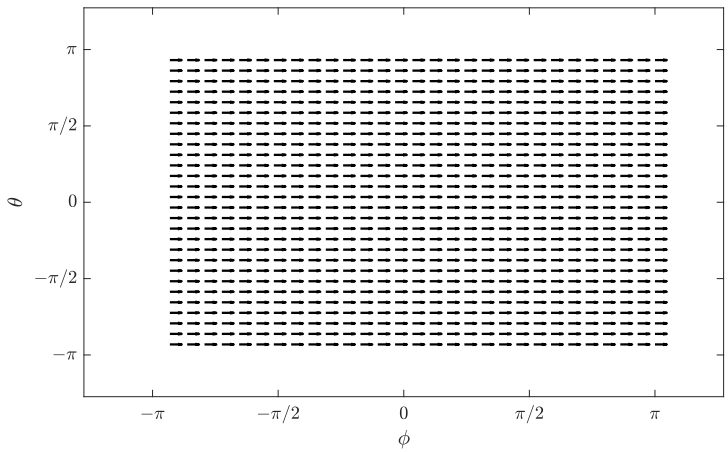

Figure 5.4: *Eddy current pattern related to the $n = 0$ slowest passive eigenvector (rectified view).*

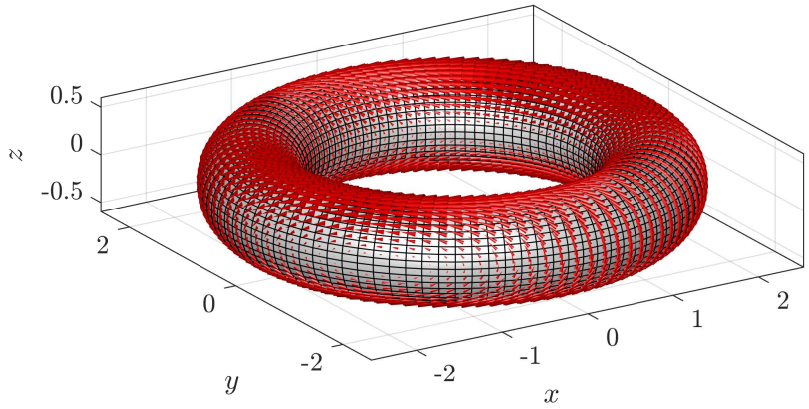

Figure 5.5: *Eddy current pattern related to the $n = 1$ slowest passive eigenvector.*

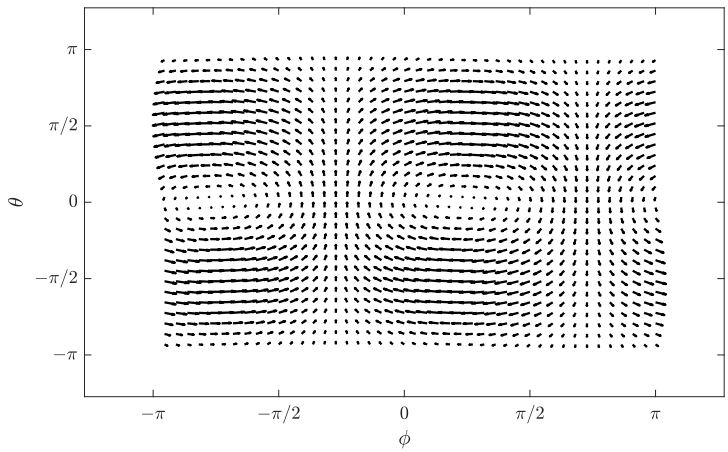

Figure 5.6: *Eddy current pattern related to the $n = 1$ slowest passive eigenvector (rectified view).*

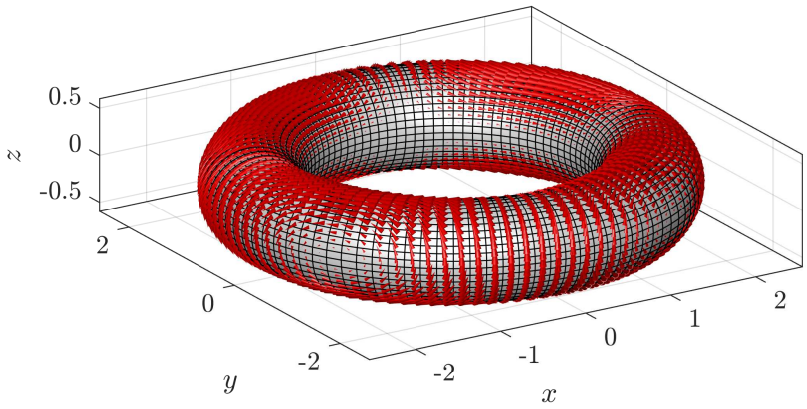

Figure 5.7: *Eddy current pattern related to the $n = 2$ slowest passive eigenvector.*

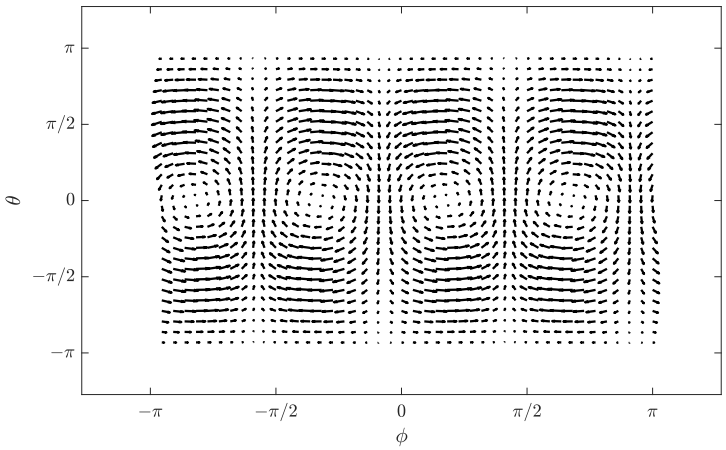

Figure 5.8: *Eddy current pattern related to the $n = 2$ slowest passive eigenvector (rectified view).*

can lead to inaccurate results because of the skin effect of the current induced into the wall. Since this occurs when the wall width and the penetration depth are comparable, it is clear that the number of mesh elements through the shell along the minor radius should be adequate to model the skin effect, especially because, in our analysis, the growth rate of the instability will vary continuously from the typical RWM to the Ideal Kink one. But, since MARS-K assumes the thin-wall approximation, only one mesh element along the shell thickness will be considered.

5.2 Sound wave damping model

In this section, the parallel sound wave damping model is considered. The behaviour of the mode eigenvalue versus the toroidal rotation can be seen in the bottom part of Fig. 5.1 (e). Before going further on with the validation part, it is useful to analyze the limitation of the static CarMa code.

5.2.1 Limitation of the static coupling strategy

The coupling procedure described in chapter 3 is based on the plasma response computation with MARS-F code, as described in section 3.3. This step is necessary to compute, with relations (3.14) and (3.19), the matrices $\boldsymbol{K}_\theta, \boldsymbol{K}_\phi, \boldsymbol{G}$. The matrices $\boldsymbol{K}_\theta, \boldsymbol{K}_\phi$ give, for a unitary magnetic perturbation normal to S_e, respectively the poloidal and toroidal components of the current density on S_e, and $\boldsymbol{G}$ gives the plasma magnetic field reaction $\boldsymbol{b}_N^{pla}$ normal to S_e.

The computation of $\boldsymbol{K}_\theta, \boldsymbol{K}_\phi, \boldsymbol{G}$ are performed starting from some suitable boundary conditions for $\boldsymbol{b}_N$ on S_e (see fig. 3.2). If this computation succeeds, starting from the *total* normal field perturbation $\boldsymbol{b}_N$ related to a certain RWM, and computed by MARS, one should recover the tangential field components $\boldsymbol{b}_{T,\theta}, \boldsymbol{b}_{T,\phi}$ related to this perturbation, and the normal field $\boldsymbol{b}_N^{pla}$ due to the plasma from these relations:

$$\boldsymbol{b}_{T,\theta} = \boldsymbol{K}_\theta \boldsymbol{b}_N \tag{5.1}$$

$$\boldsymbol{b}_{T,\phi} = \boldsymbol{K}_\phi \boldsymbol{b}_N \tag{5.2}$$

$$\boldsymbol{b}_N^{pla} = \boldsymbol{G}\boldsymbol{b}_N \tag{5.3}$$

Figure 5.9 shows a good agreement on the computation of both $\boldsymbol{b}_N^{pla} = \boldsymbol{G}\boldsymbol{b}_N$ and $\boldsymbol{b}_T = \boldsymbol{K}\boldsymbol{b}_N$.

The accuracy of these outcomes has an impact on the computation of matrix $\boldsymbol{W}$. As can be seen from Fig. 5.10, where both the Fourier harmonics

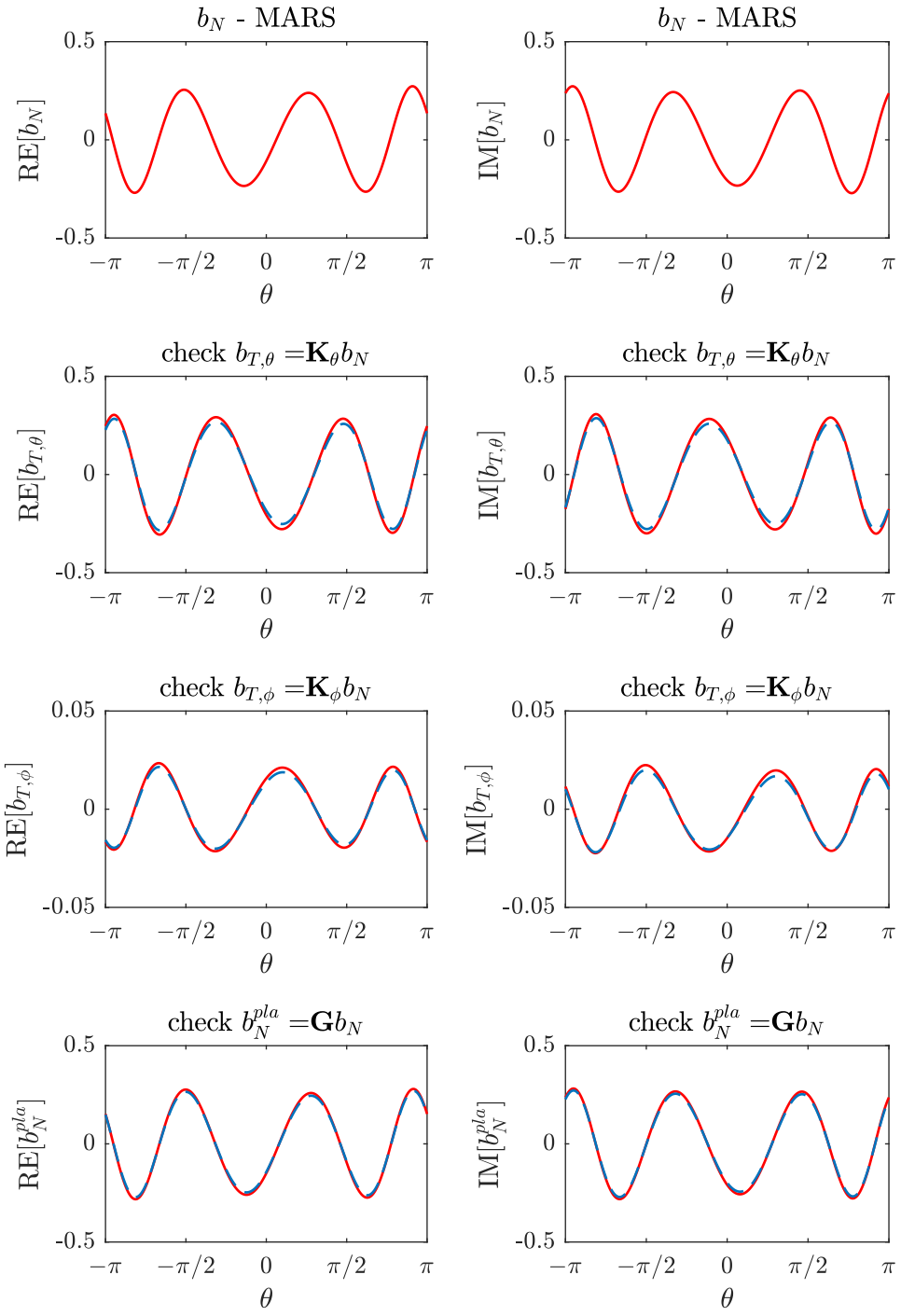

Figure 5.9: *The normal components given by MARS-F as input boundary conditions are shown in both real and imaginary part (top). Comparison between reference (red, MARS-F) and reconstructed (blue) magnetic field on the coupling surface (normal and tangential components).*

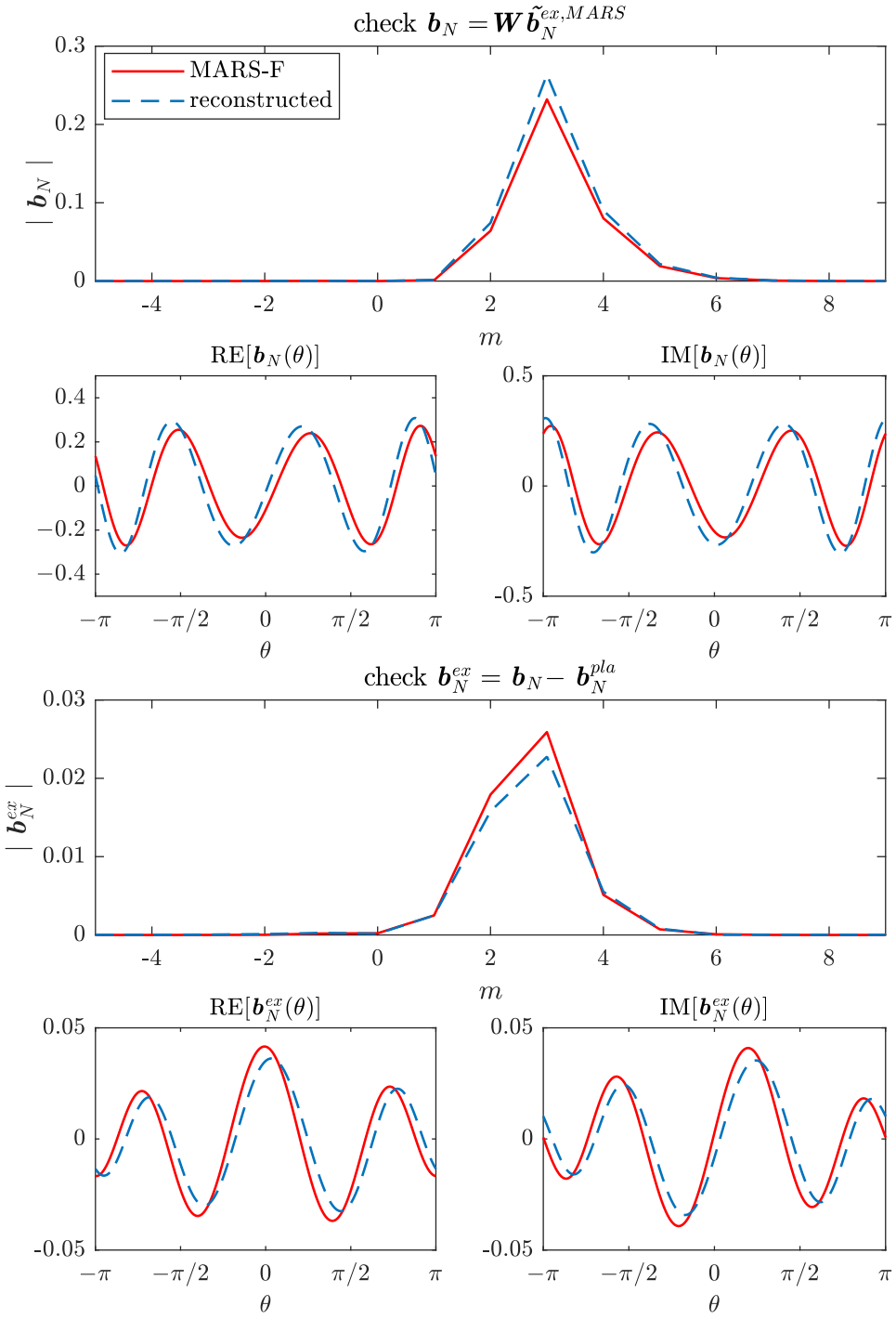

Figure 5.10: *Comparison between the total perturbed magnetic field* $\mathbf{b}_N$ *given by MARS-F (red) and the reconstructed with the matrix* $\boldsymbol{W}$*, as well as the comparison of the external field* $\mathbf{b}_N^{ex}$*.*

and the poloidal distribution is reported, there is a small discrepancy between the reference values from MARS (written as $\boldsymbol{b}_N^{ex,MARS}$) and the reconstructed quantities. In particular, if one tries to estimate the external contribution $\boldsymbol{b}_N^{ex}$ to the total perturbed magnetic field from the just computed $\boldsymbol{b}_N, \boldsymbol{b}_N^{pla}$, the results suffer of a small discrepancy. Some shrewdness can be done to improve the accuracy, such as, for example, improving the number of points of the coupling surface. However, in some cases the accuracy cannot be improved any more if the assumptions necessary for the static CarMa coupling are not satisfied: this happens in this case because toroidal rotation is considered.

These coupling matrices have been combined as described in chapter 3 to give rise to the static CarMa system, and have been used to analyze the stability of the circular plasma already presented. The recovered unstable eigenvalue is close to the reference one given by MARS-F, so the performances of static CarMa are acceptable:

	$\gamma\tau_w$
MARS-F	$2.08 + 0.24i$
CarMa	$2.05 + 0.23i$

Table 5.2: *Comparison between RWM growth rate given by MARS-F and by static CarMa for fluid model, for the toroidal rotation* $\Omega_E/\omega_A = 0.02$.

However, if we consider a much more resistive wall, i.e. the resistivity is increased by a factor of 10^5, any stabilizing effect vanishes, and the resulting instability is of the order of the no-wall ideal kink timescale. The static coupling procedure gives a static relation for the plasma response, therefore the growth rate of the mode has a linear dependance with the respect to the passive structures resistivity. For this reason, increasing the resistivity by the factor 10^5 gives a growth rate multiplied by the same factor. On the other hand, the mode growth rate should not raise that much, but is expected to saturate to the no-wall ideal kink growth rate:

	$\gamma\tau_w$
Mars-F	$123.8 + 42i$
CarMa	$(2.1 + 0.2i) \times 10^5$

Table 5.3: *Comparison between ideal kink growth rate given by MARS-F and by static CarMa for fluid model.*

5.2.2 Rational approximation of frequency dependent plasma response

Further considerations can be made with respect to the previous examples. In particular, with the static coupling procedure, the plasma response to external perturbation is assumed to be constant and equal to the one computed for vanishing frequency. In most realistic cases, where the mode growth rate has the same order of magnitude of the wall time, this assumption is still reasonable, but there are some cases in which this is too stringent.

For example, figure 5.11 shows the matrix $\boldsymbol{P}(s)$ computed for different frequencies of the magnetic perturbation. As already said, for a given Fourier spectrum of external magnetic field perturbation, and a given frequency, the matrix function $\boldsymbol{P}(s)$ gives the harmonics of plasma reaction in terms of equivalent current density on the coupling surface: as can be seen, the relation between these harmonics changes substantially with the frequency. We can also notice that there is a certain coupling between different poloidal harmonics for a given range of frequency. This is reasonable because the *aspect ratio* is large ($R_0/a = 5$). But as soon as the frequency increases, the matrix becomes mainly diagonal, ending up with only one dominant element, related to the poloidal harmonic $m = 1$, at high frequencies.

The behaviour of two main entries of $\boldsymbol{P}(s)$ are shown in fig. 5.12 in terms of $s = \sigma + i\omega$ along the complex plane to have a qualitative idea of the trend of $\boldsymbol{P}(s)$.

The limitations of the static coupling strategy can be overcome recalling a matrix-based rational approximation for the plasma response, as was presented in paragraph 4.2. Since two possibilities are available, that are to separately approximate $\boldsymbol{F}(s), \boldsymbol{W}(s)$ or to work directly with $\boldsymbol{P}(s)$, both the approaches have been investigated to understand which is the most reliable and accurate.

It is worth to remember that the approximating functions are matrix-based, meaning that the coefficients are $M \times M$ matrix. To have an idea of the quality of interpolation, the behaviour of the two main entries of $\boldsymbol{F}(s), \boldsymbol{W}(s)$ and $\boldsymbol{P}(s)$ are reported in Figs. 5.13 , 5.14, and 5.15. Since these matrices are mainly diagonal, these main entries belong to the diagonal: in particular, we will consider the entries related to harmonics $m = (3, -3)$ for $\boldsymbol{F}(s)$, $m = (0, 1)$ for $\boldsymbol{W}(s)$ and $m = (0, 3)$ for $\boldsymbol{P}(s)$. Figs. 5.13, 5.14 and 5.15 show these entries respectively for the three sets of basis points considered, to have a general idea of the performance related to each set.

For a given interpolation order k, the DoF for the interpolation on $\boldsymbol{F}(s), \boldsymbol{W}(s)$ are two times the DoF for $\boldsymbol{P}(s)$, because we have two times

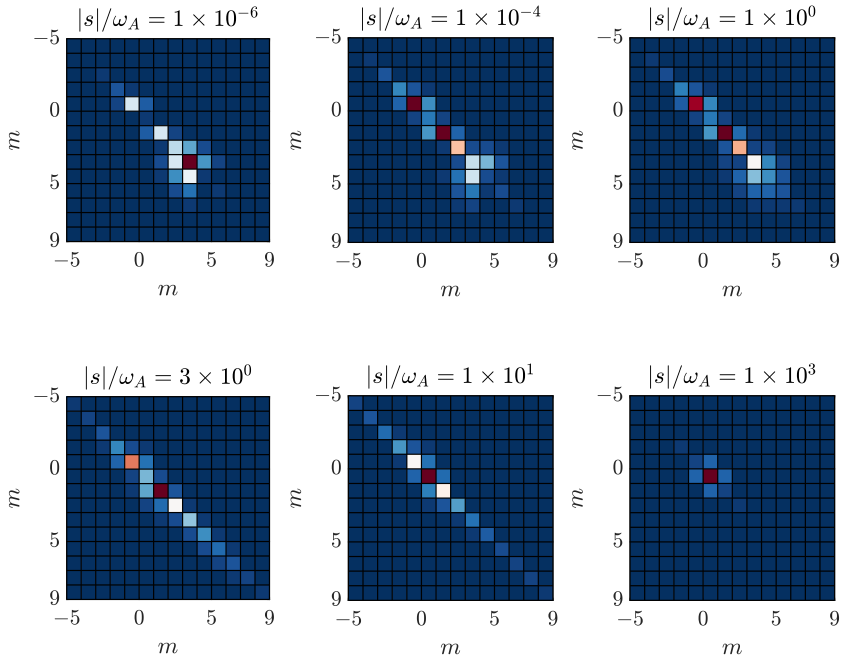

Figure 5.11: *Amplitude of $|\boldsymbol{P}(s)|$ at different values of Laplace variable s/ω_A.*

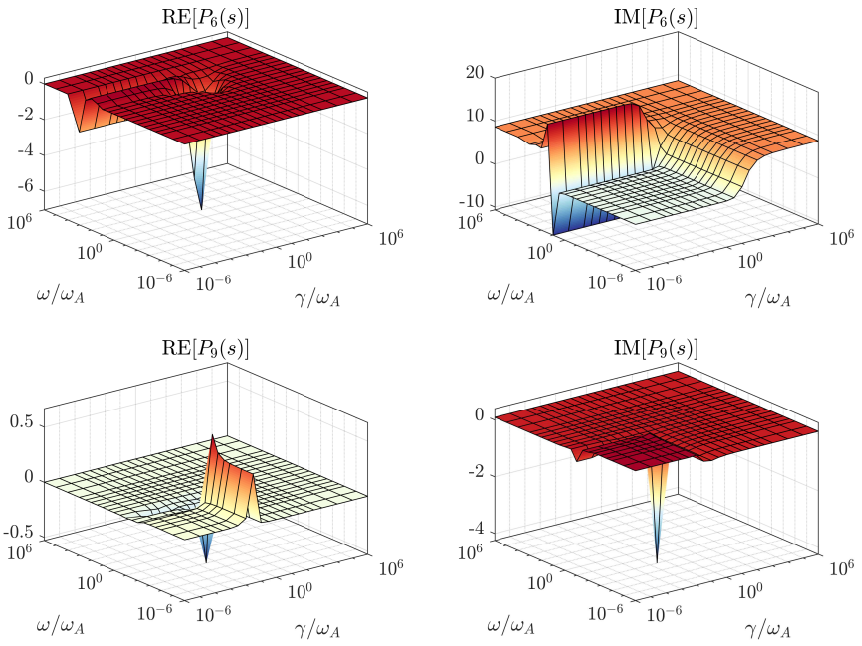

Figure 5.12: *behaviour of two of the greatest elements of $\boldsymbol{P}(s)$ along the complex plane.*

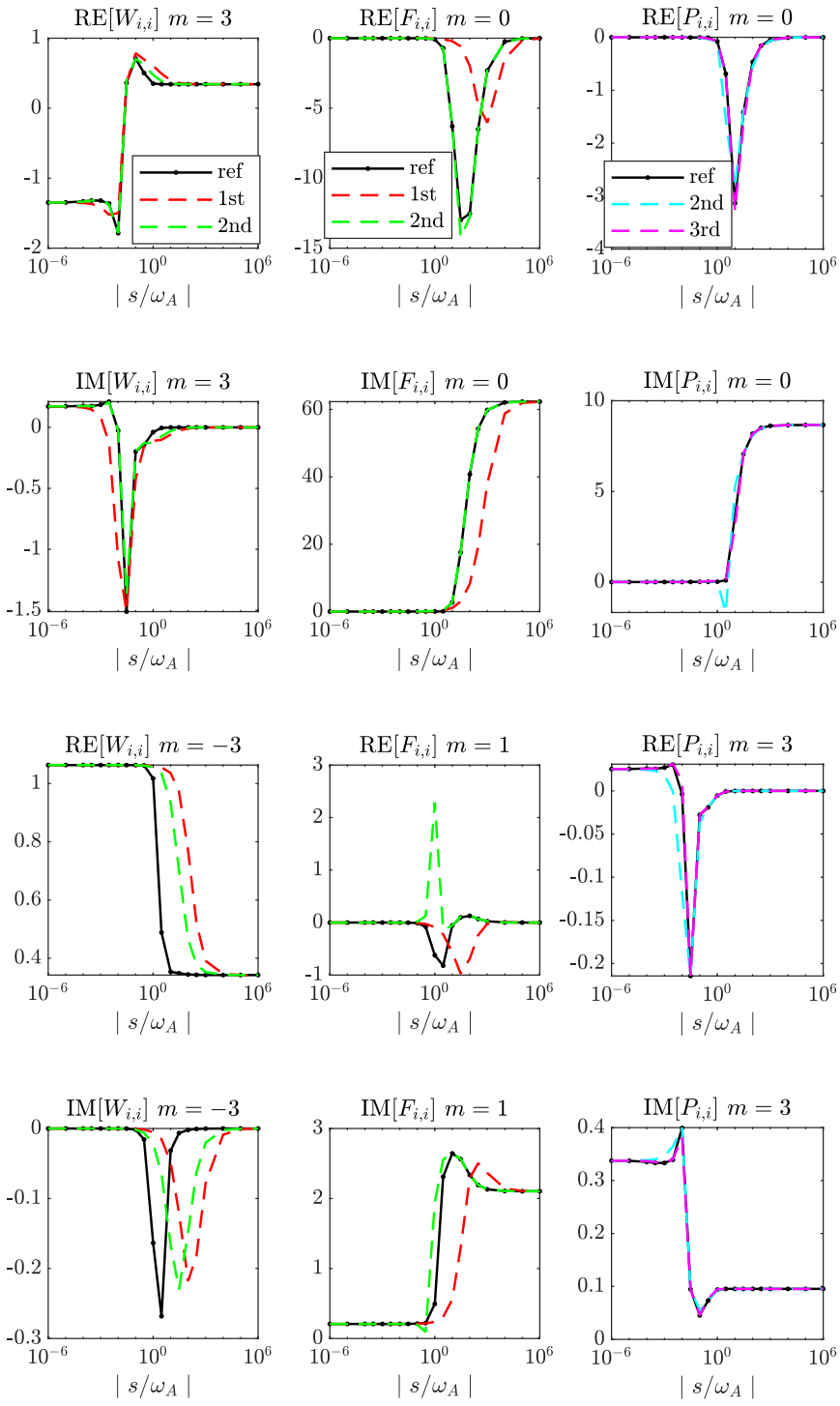

Figure 5.13: *Reference versus interpolated plasma response matrix for the two main entries of* $\boldsymbol{F}(s), \boldsymbol{W}(s)$ *(1st and 2nd degree interpolation) and* $\boldsymbol{P}(s)$ *(2nd and 3rd degree interpolation) for the* ***complex*** *set of basis points. Fluid case.*

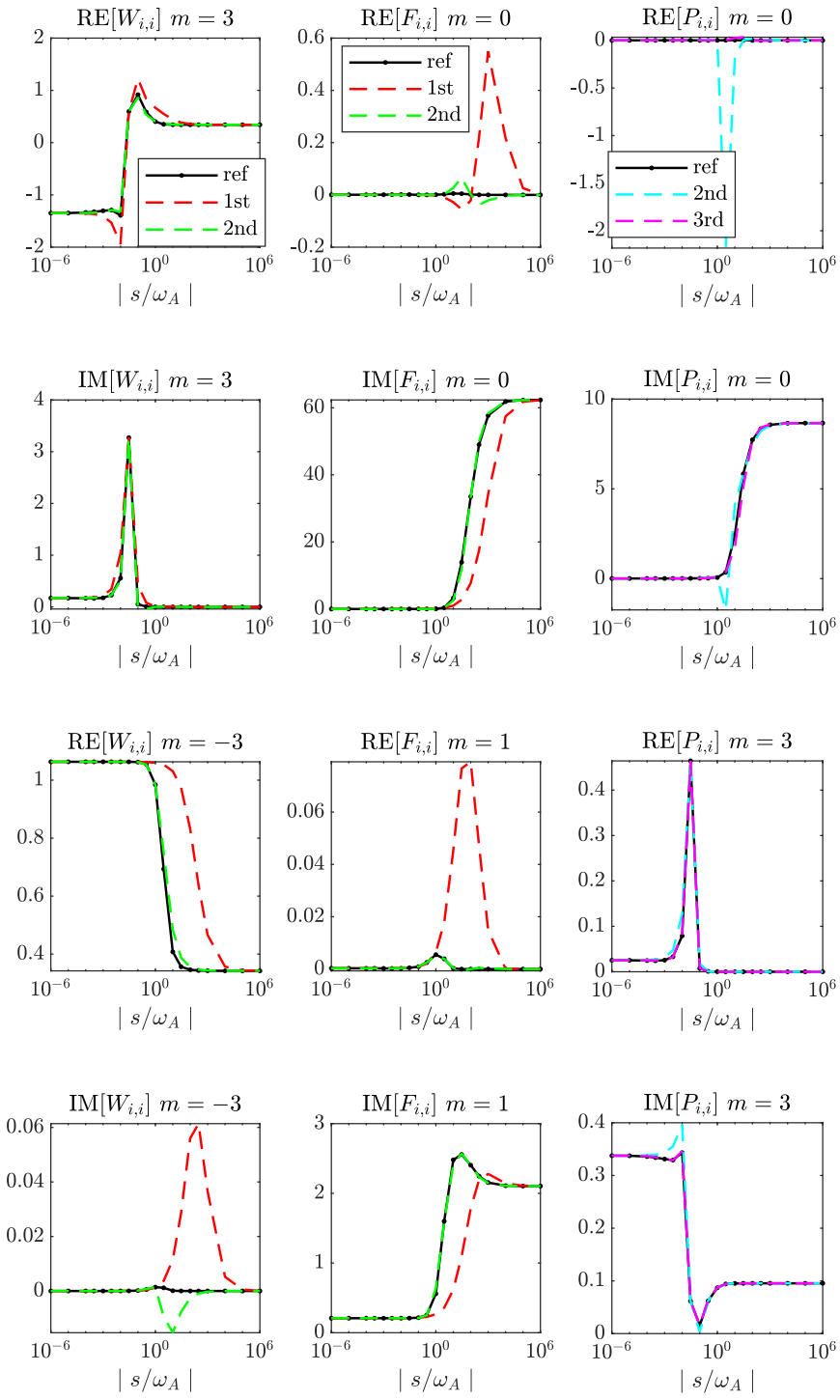

Figure 5.14: *Reference versus interpolated plasma response matrix for the two main entries of* $\boldsymbol{F}(s), \boldsymbol{W}(s)$ *(1st and 2nd degree interpolation) and* $\boldsymbol{P}(s)$ *(2nd and 3rd degree interpolation) for the* ***real*** *set of basis points. Fluid case.*

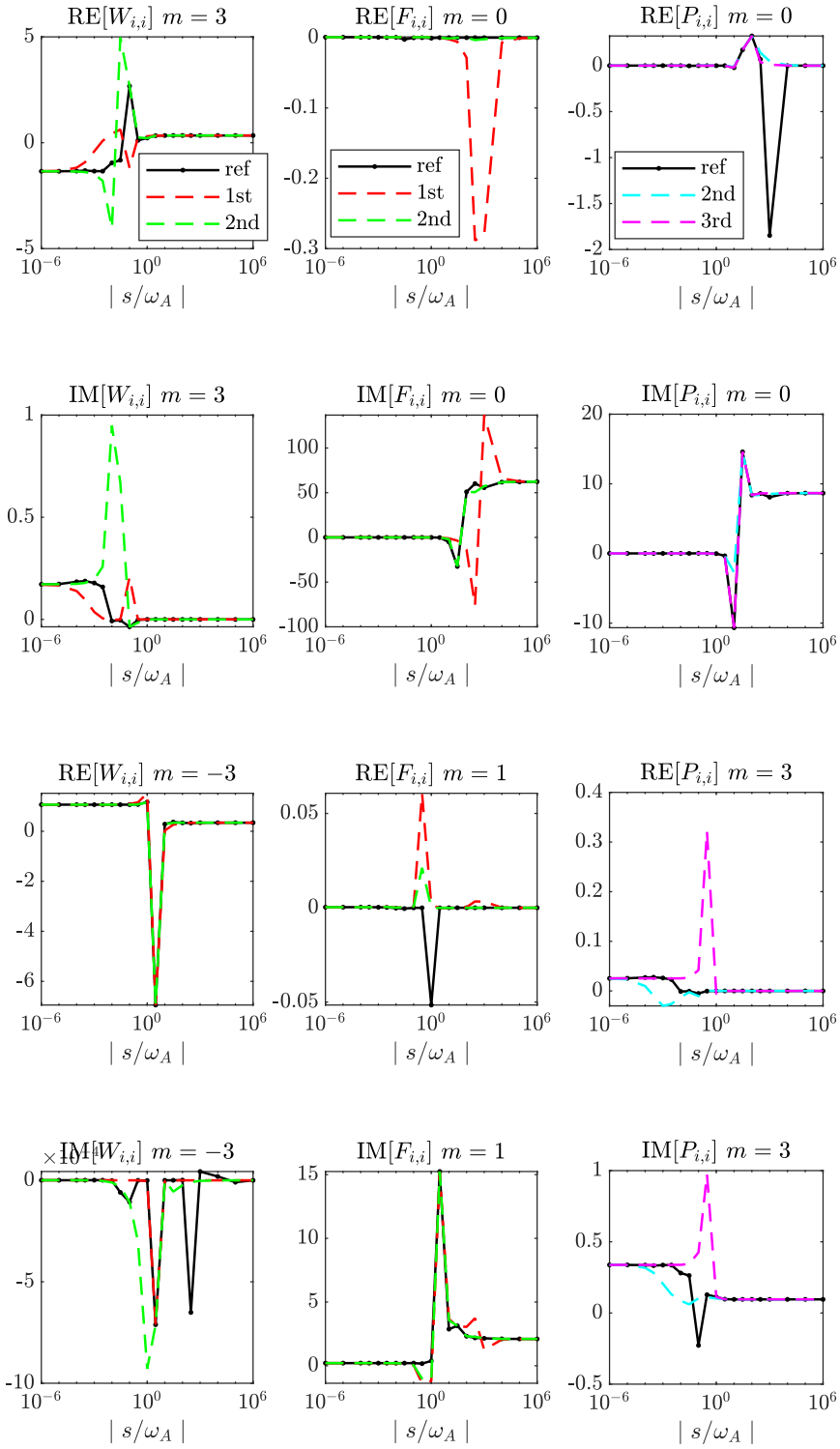

Figure 5.15: *Reference versus interpolated plasma response matrix for the two main entries of $\boldsymbol{F}(s), \boldsymbol{W}(s)$ (1st and 2nd degree interpolation) and $\boldsymbol{P}(s)$ (2nd and 3rd degree interpolation) for the **imaginary** set of basis points. Fluid case.*

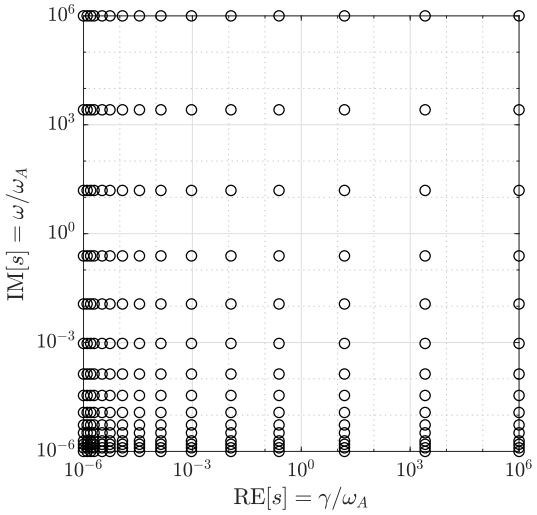

Figure 5.16: *View, on the complex plane, of the set of basis points used for the least-square approach-*

the number unknown coefficients. Taking this fact into account, it turned out that very good accuracy can be found, starting from data obtained from *complex* and *real* sets, with interpolation degree $k = 2$ for $\boldsymbol{F}(s), \boldsymbol{W}(s)$ separately and $k = 3$ for $\boldsymbol{P}(s)$. This can be seen in Figs. 5.13, 5.14. In addition to the chosen interpolation degree, also the lower degrees are shown in the figures. In particular, the case $k = 1$ for $\boldsymbol{F}(s), \boldsymbol{W}(s)$ was the fist improvement the static CraMa coupling strategy [4].

On the other hand, the *imaginary* set of data looks less approriate to this purpose, giving less accuracy in the interpolation. This can be explained considering the behaviour of the two sample entries of $\boldsymbol{P}(s)$ in Fig. 5.12 along the imaginary axis, the same reported in details in Fig. 5.15. The trend of the functions is much more complicated than the two previous cases, and it is reasonable that the interpolant of the same order should not be able to give a good approximation of this trend. Nonetheless, trying to use higher k can not improve the accuracy, because it would rise too much the ill-conditioning of Eq. (4.29).

As was said at the end of Sec. 4.2, another way to deal with this problem is choosing a number of basis points higher than the number of DoF, and use a regularization technique to find the solution. The first drawback of this approach is that no explicit constrain on the basis points can be imposed for the interpolating functions: in particular, this can be problematic for matching the static response (Eq. (4.22)), that can not be imposed explicitly. For this reason, the set of points on the complex plane shown in Fig. 5.16

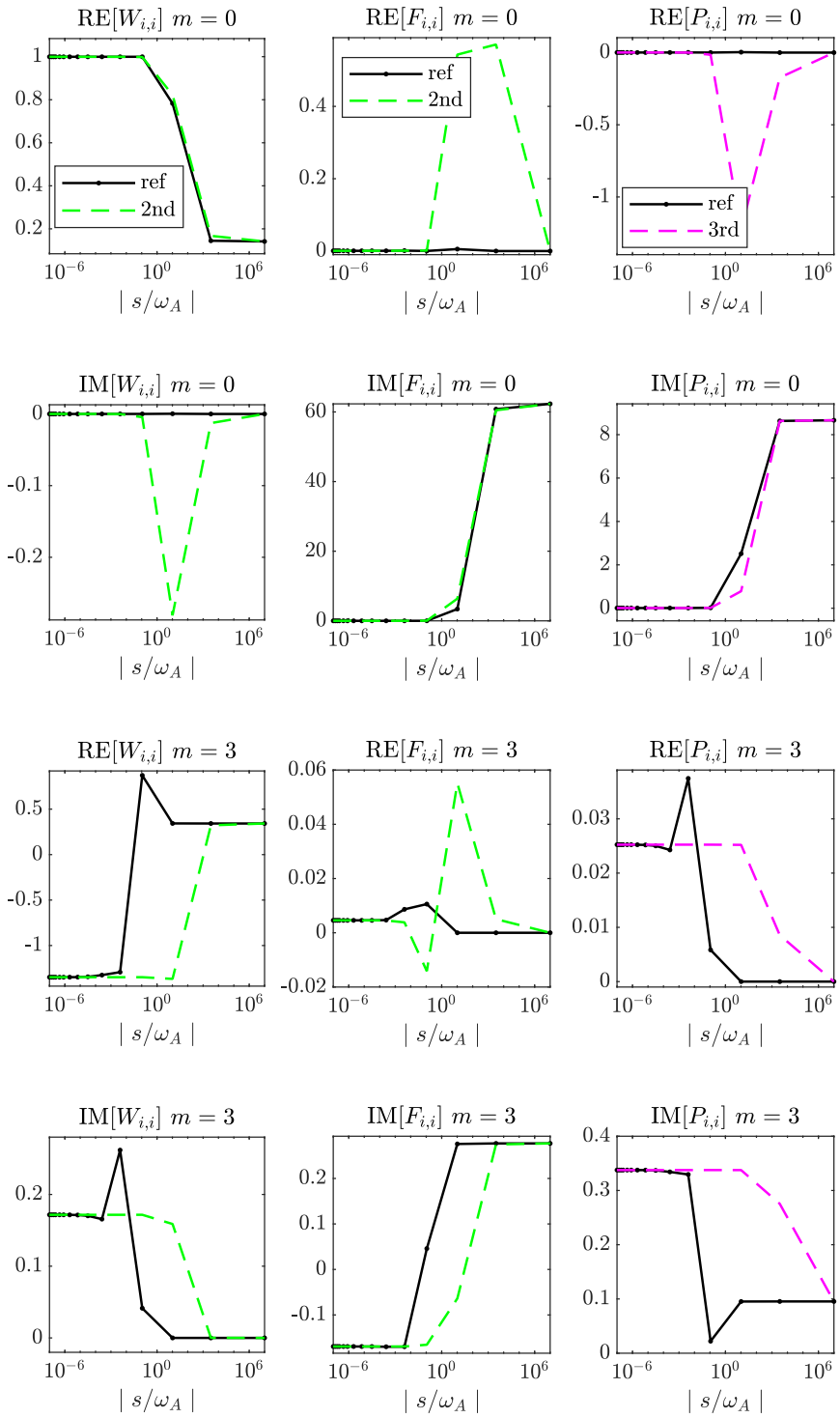

Figure 5.17: *Reference versus interpolated plasma response matrix for the two main entries of* $\boldsymbol{F}(s), \boldsymbol{W}(s)$ *(2nd degree interpolation) and* $\boldsymbol{P}(s)$ *(3rd degree interpolation) for the* ***least-square*** *approach.*

is used rather than the one already presented in Fig. 5.2. This should give more weight to the information close to $|s| = 0$, and try to match the static response without imposing the constrain explicitly.

The results, in the same format used for the previous cases, is reported in Fig. 5.17. In some cases the transfer function is well approximated by the interpolated one, but there is an evident worsening on the accuracy if compared with the previous cases. For this reason, only the higher interpolation degree are shown in the figure.

Since this last strategy is not effective for a proper interpolation, it will not be considered in the next part of the work.

5.2.3 Scan of conducting wall resistivity

To assess the capabilities of the CarMa-D model, we consider the circular equilibrium with the axisymmetric mesh shown in Fig. 5.1: the MHD model relies on the fluid description, therefore no kinetic effects are taken into account. In addition to this, the normalized toroidal rotation is $\Omega_E/\omega_A = 0.01$ and it is imposed to be constant along the radius.

The stability analysis of the mode is performed varying the resistivity of the wall η from $\eta/\eta_{ref} = 10^{-1}$ to $\eta/\eta_{ref} = 10^{6}$, with $\eta_{ref} = 6.5 \times 10^{-7}\Omega$m the reference value (fig. 5.18 shows the eddy current pattern for the case $\eta/\eta_{ref} = 1$). The more the wall resistivity is increased, the less stabilizing effect it has on the growing mode. In the limit of infinite resistivity, the stabilizing effect vanishes, and the mode growth rate should saturate to the no-wall ideal kink growth rate, as can be see in Fig. 5.19 (real and imaginary part are shown). The timescale of the instability has the same order of

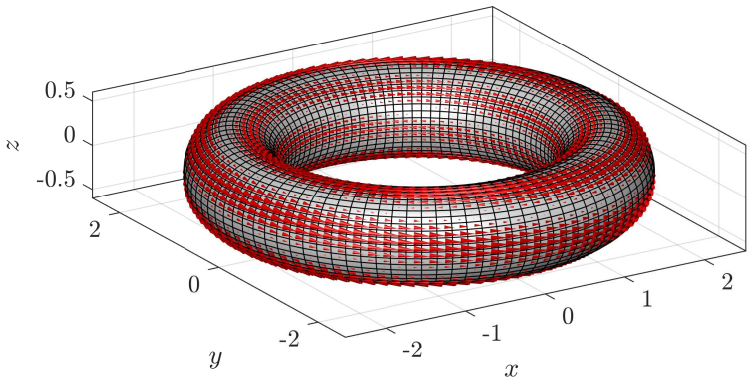

Figure 5.18: *Eddy current pattern related to the unstable eigenvector for the axisymmetric mesh. Fluid case with resistivity* $\eta/\eta_{ref} = 1$ *and toroidal rotation* $\Omega_E = \omega_A = 10^2$.

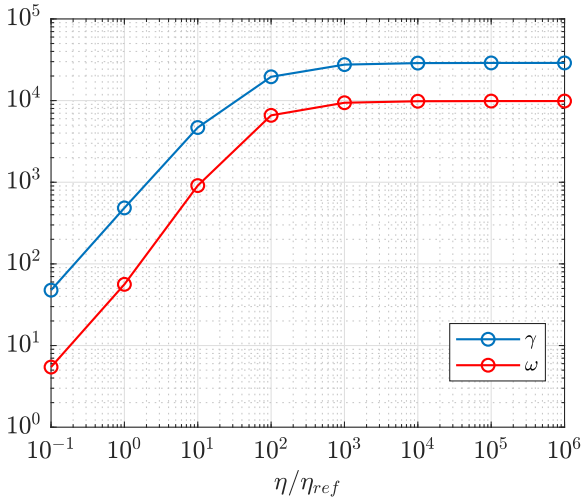

Figure 5.19: *Reference scan of wall resistivity for the fluid case with MARS-F: real part (blue) and imaginary part (red) of the eigenvalue.*

magnitude of Alfvén phenomena: within this regimes, the dynamical effect are not negligible, hence the mass-less approximation is no longer valid. The CarMa-D code should be able, in principle, to model plasma dynamics that occur in these regimes.

In the previous paragraph it has turned out that not all the sets of basis points are equally suitable to be used for a proper interpolation. In the next part of the work all the three sets of points have been considered, to have additional awareness of their strengths and weaknesses: in particular, Figs. 5.20-5.21 show the outcome for the *complex* set of basis points, Figs. 5.22 - 5.23 for the *real* set and Figs. 5.24 - 5.25 for the *imaginary* set. Logarithmic scale is used for all the figures.

In order to quantify the accuracy of the various sets of points, the percentage error has been defined as:

$$\epsilon_{\%} = 100 \, \frac{|(\gamma + i\omega) - (\gamma + i\omega)_{ref}|}{|(\gamma + i\omega)_{ref}|} \tag{5.4}$$

and summarized in fig. 5.26 for all the cases. Logarithmic scale is still used, and the colors are the same used for the previous figures.

It is clear, looking to the results, that the *imaginary* set of basis point is less suitable than the other sets. In particular, the most effective is the *real* set: this can be explained considering the fact that the real part of the unstable eigenvalue is an order of magnitude bigger than the imaginary part, as can be seen in Fig. 5.19, and choosing to interpolate the plasma response

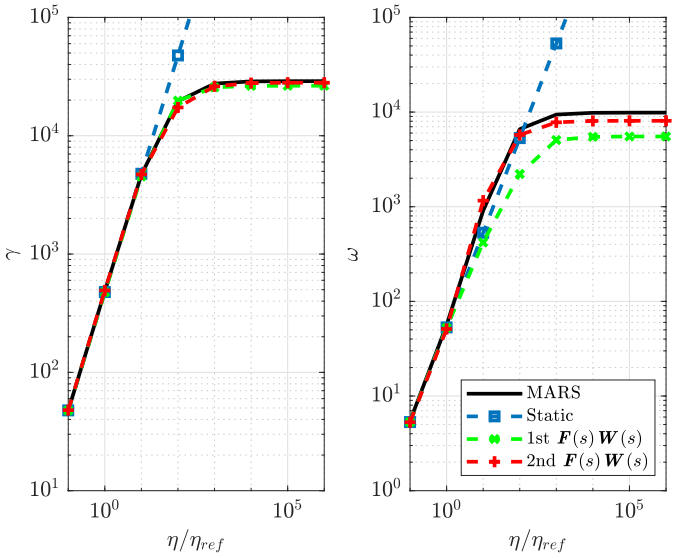

Figure 5.20: *Results of the scan of wall resistivity for the fluid case and the* ***complex*** *set of basis points: case of separate interpolation of* $\boldsymbol{F}(s)$ *and* $\boldsymbol{W}(s)$*. Real and imaginary part are shown in logarithmic scale.*

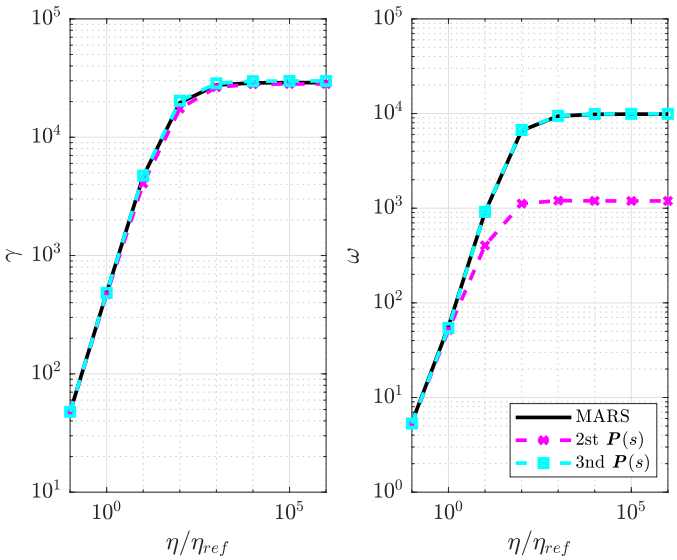

Figure 5.21: *Results of the scan of wall resistivity for the fluid case and the* ***complex*** *set of basis points: case of direct interpolation of* $\boldsymbol{P}(s)$*. Real and imaginary part are shown in logarithmic scale.*

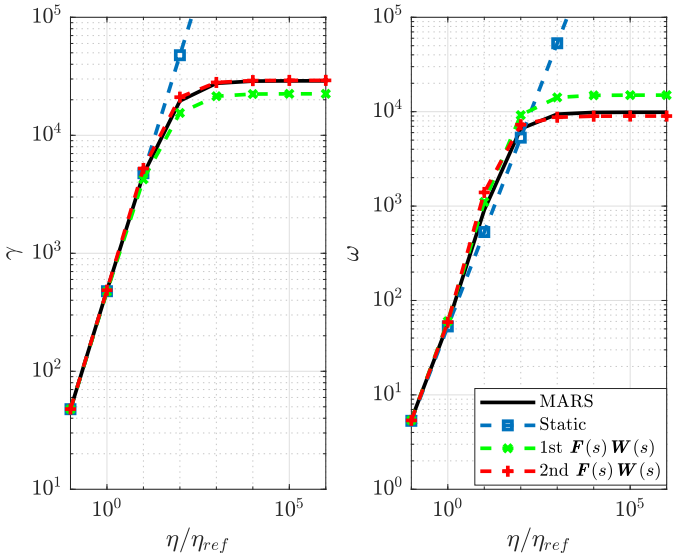

Figure 5.22: *Results of the scan of wall resistivity for the fluid case and the* ***real*** *set of basis points: case of separate interpolation of $\boldsymbol{F}(s)$ and $\boldsymbol{W}(s)$. Real and imaginary part are shown in logarithmic scale.*

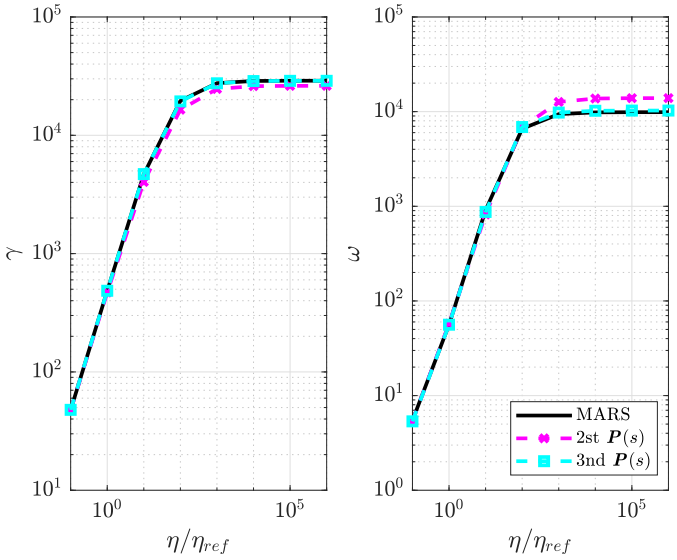

Figure 5.23: *Results of the scan of wall resistivity for the fluid case and the* ***real*** *set of basis points: case of direct interpolation of $\boldsymbol{P}(s)$. Real and imaginary part are shown in logarithmic scale.*

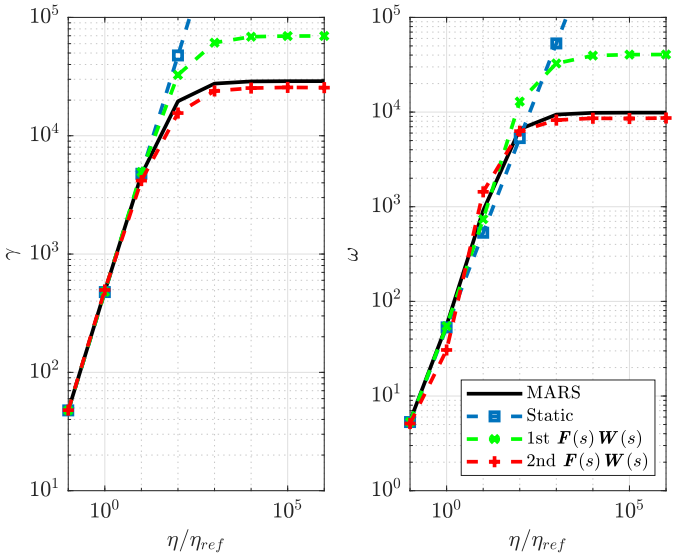

Figure 5.24: *Results of the scan of wall resistivity for the fluid case and the* ***imaginary*** *set of basis points: case of separate interpolation of* $\boldsymbol{F}(s)$ *and* $\boldsymbol{W}(s)$*. Real and imaginary part are shown in logarithmic scale.*

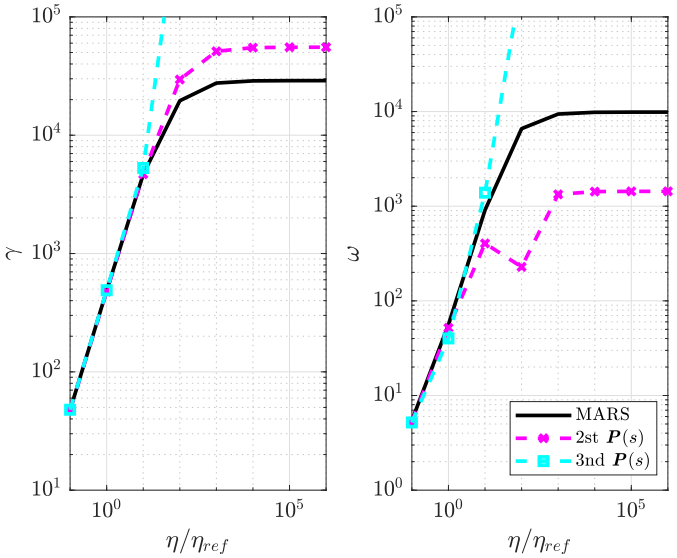

Figure 5.25: *Results of the scan of wall resistivity for the fluid case and the* ***imaginary*** *set of basis points: case of direct interpolation of* $\boldsymbol{P}(s)$*. Real and imaginary part are shown in logarithmic scale.*

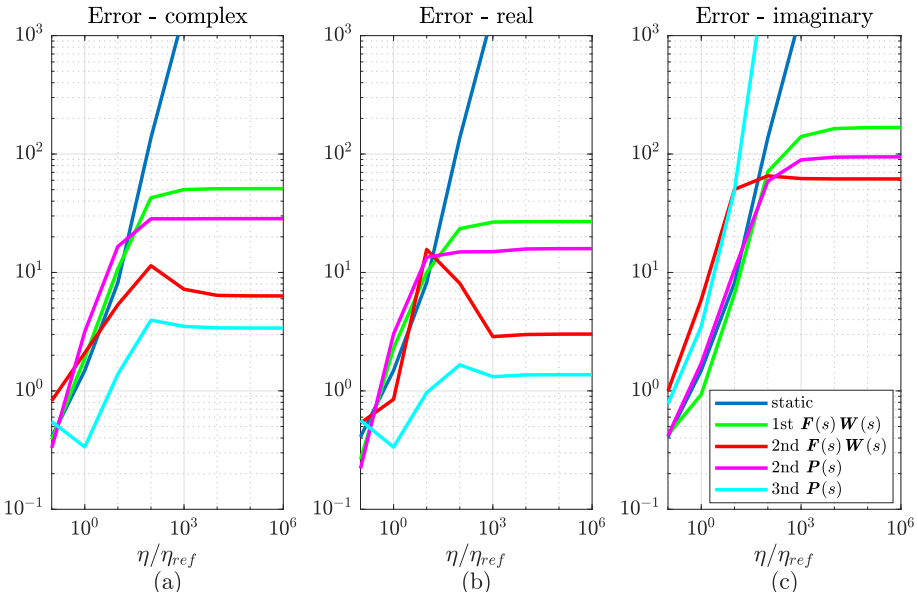

Figure 5.26: *Percentage errors of the scan of wall resistivity for all the sets of basis points for the fluid case. Logarithmic scale.*

along the real axis allows to obtain more information rather than the other choices of basis points.

In addition to this, interpolating directly the function $\boldsymbol{P}(s)$ gives much more accurate results that interpolating $\boldsymbol{F}(s), \boldsymbol{W}(s)$ separately. Specifically, the degree k for $\boldsymbol{P}(s)$ gives, for the real set of basis points, a percentage error always around 1% for all the range of resistivity.

On the other hand, from Fig. 5.26 the limitation of static CarMa is clearly pointed out: for lower values of resistivity ($\eta/\eta_{ref} < 10^1$), where the stabilizing effect of the wall is prominent, the error is less than 10%, meaning that the mass-less approximation holds and this approach is suitable to model instabilities of such timescale. But as soon as the resistivity increases, this approach is by far no longer suitable.

With the respect to the $k = 1$ degree interpolation on $\boldsymbol{F}(s), \boldsymbol{W}(s)$, we can see a considerable improvement with respect of static CarMa, but the results are still not satisfying. This fact agrees with the consideration pointed out in [10], and already presented in paragraph 4.2, that the system exhibits a second order dynamics. It is also true that the said proof is developed in cylindrical coordinates, but the aspect ratio of $R_0/a = 5$ for this case let this assumption to be reasonable.

Some of the results, for the real set of points, are also reported in table 5.4 to have a quantitative idea of CarMa-D accuracy.

	$\eta/\eta_{ref} = 1$	$\eta/\eta_{ref} = 10^5$
Mars	$2.08 + 0.24i$	$123.8 + 42.3i$
CarMa static	$2.05 + 0.23i$	$204776 + 22793i$
CarMa 1st ord. on $\boldsymbol{F}(s)\boldsymbol{W}(s)$	$2.03 + 0.26i$	$96.4 + 64.3i$
CarMa 2st ord. on $\boldsymbol{F}(s)\boldsymbol{W}(s)$	$2.10 + 0.25i$	$125.3 + 38.6i$
CarMa 3rd ord. on $\boldsymbol{P}(s)$	$2.08 + 0.24i$	$123.9 + 44.0i$

Table 5.4: *Growth rates for sound wave case with $\Omega_E/\omega_A = 1 \times 10^{-2}$ for two different wall resistivities.*

5.3 RWM with drift kinetic damping

In this section the self consistent, full toroidal drift kinetic model is considered as a benchmark problem. In this model, the damping effect is due to the mode resonance either with bounce motion of both passing and trapped thermal ions at fast plasma rotation, or with the magnetic precession drift of trapped thermal ions and electrons at slow plasma rotation [11, 3]. The same test case of Ref. [12] is used: only the precession drift resonances are considered, and the bounce resonances, as well as other physics such as the collisionality effects, are neglected. The validation of CarMa-D follows the same steps used in the previous section for the fluid damping model, but using the results from MARS-K as reference.

5.3.1 Rational approximation of frequency dependent plasma response

The outcomes of matrix-based approximation for $\boldsymbol{F}(s)$, $\boldsymbol{W}(s)$ and $\boldsymbol{P}(s)$ is shown, following the same methodology used for the fluid model, in Figs. 5.27, 5.28 and 5.29. for the three sets of basis points. The harmonic related to every shown entries is specified for each subplot.

Like the sound wave case, both real and complex sets of basis points give accurate results, but once again the real set is the more accurate. The trend of the plasma response matrix is much more complicated along the imaginary axis, requiring a higher number of DoF. Thus, also with the kinetic damping model the imaginary set of points is not a suitable choice.

The set of points shown in Fig. 5.16 has not been considered for this case, because, from the previous test, it has turned out to be very ineffective.

5.3.2 Scan of conducting wall resistivity

The same scan of wall resistivity performed for the fluid case is done, but including the kinetic damping physics in the plasma description. The refer-

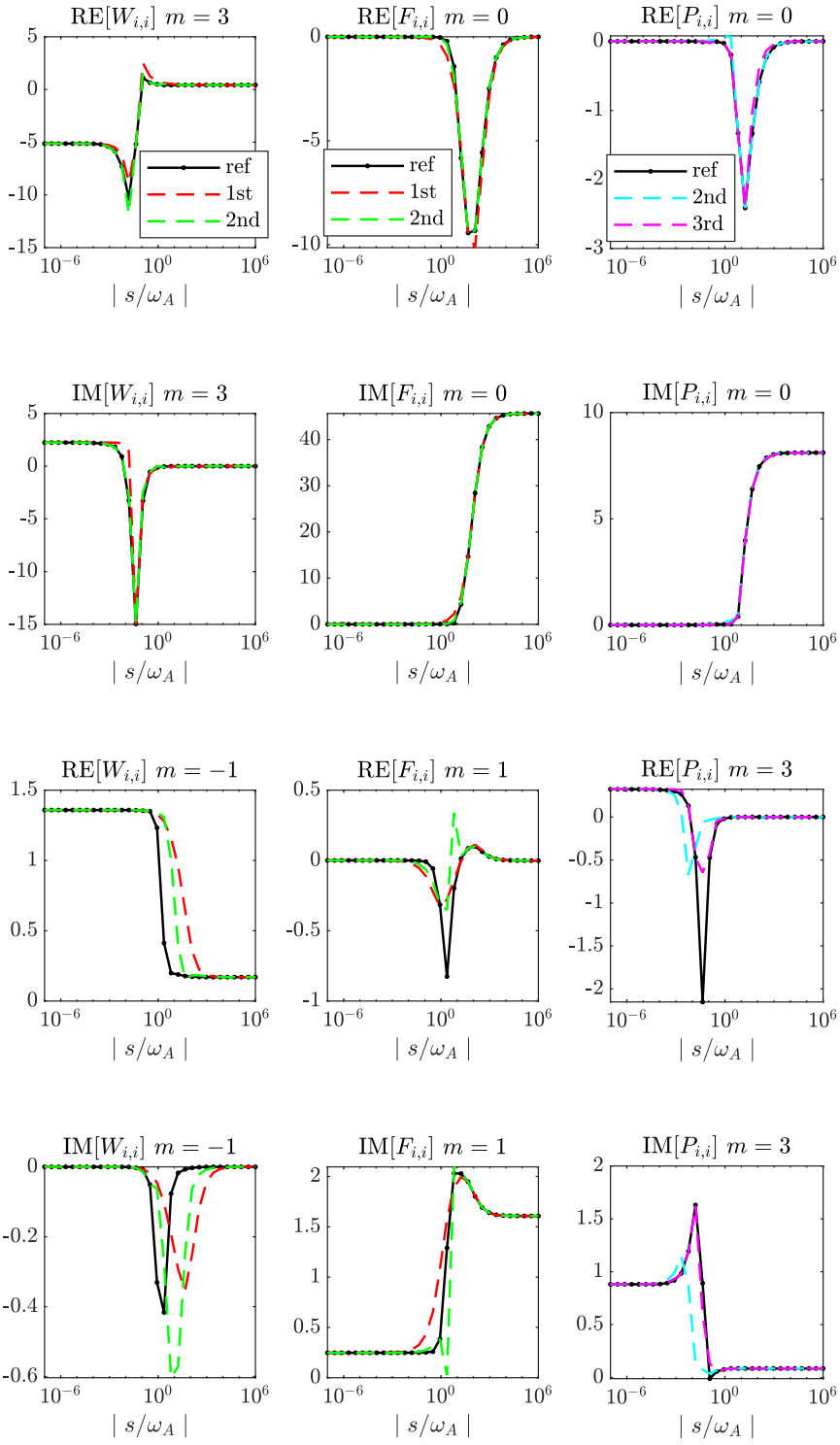

Figure 5.27: *Reference versus interpolated plasma response matrix for the two main entries of* $\boldsymbol{F}(s), \boldsymbol{W}(s)$ *(1st and 2nd degree interpolation) and* $\boldsymbol{P}(s)$ *(2nd and 3rd degree interpolation) for the* ***complex*** *set of basis points. Kinetic case.*

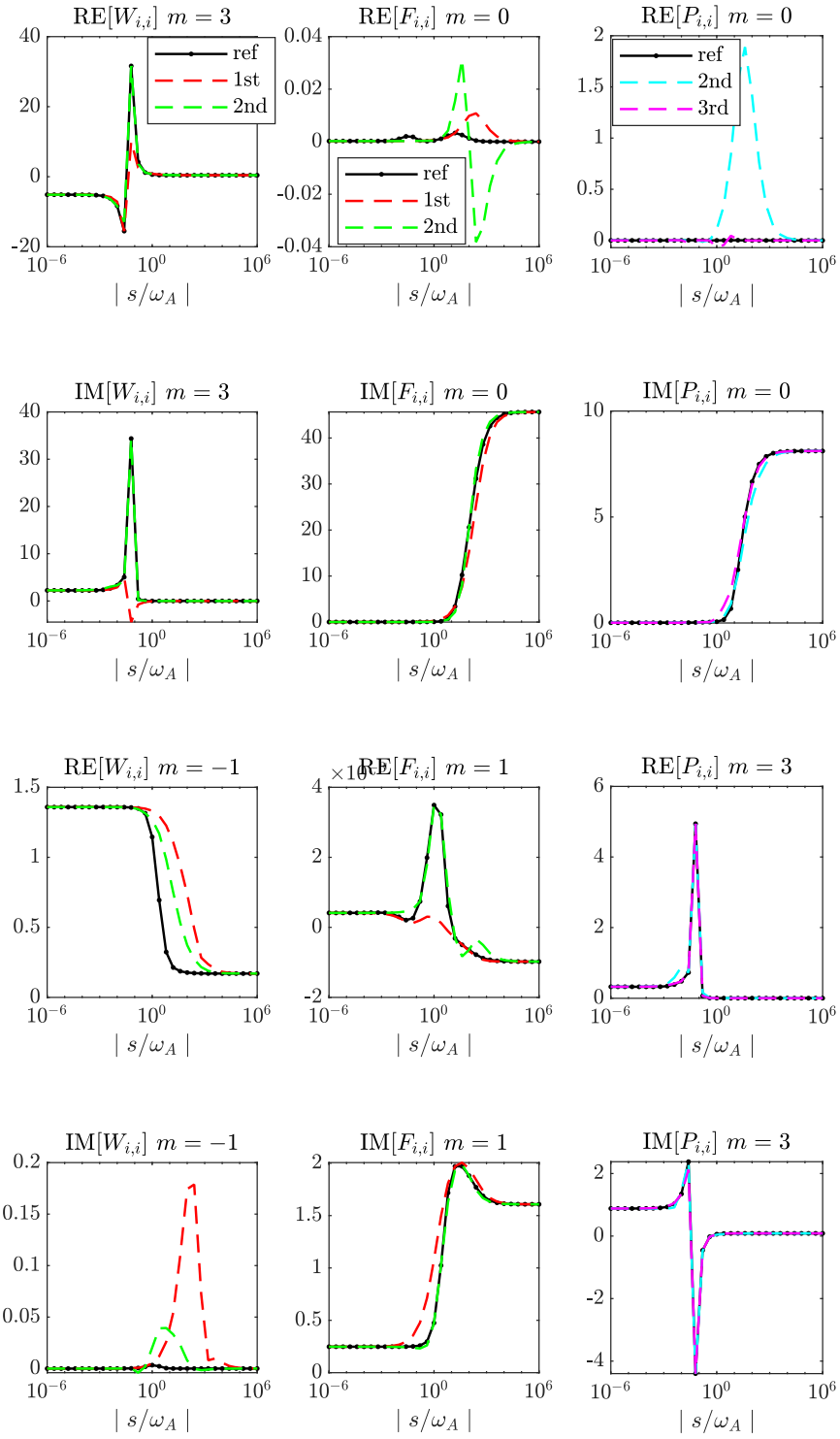

Figure 5.28: *Reference versus interpolated plasma response matrix for the two main entries of* $\boldsymbol{F}(s), \boldsymbol{W}(s)$ *(1st and 2nd degree interpolation) and* $\boldsymbol{P}(s)$ *(2nd and 3rd degree interpolation) for the* ***real*** *set of basis points. Kinetic case.*

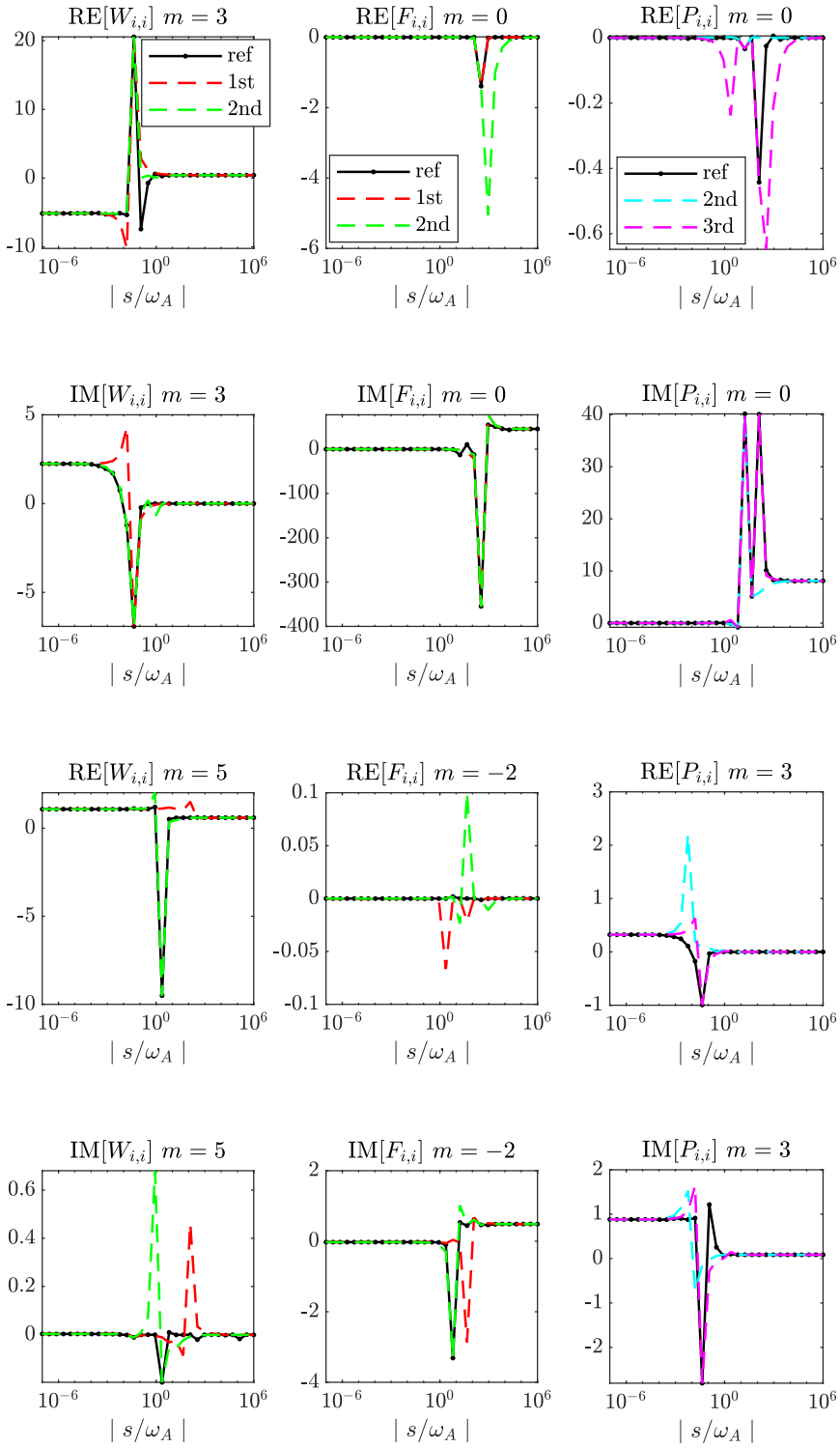

Figure 5.29: *Reference versus interpolated plasma response matrix for the two main entries of* $\boldsymbol{F}(s), \boldsymbol{W}(s)$ *(1st and 2nd degree interpolation) and* $\boldsymbol{P}(s)$ *(2nd and 3rd degree interpolation) for the* ***imaginary*** *set of basis points. Kinetic case.*

ence scan of wall resistivity for this case, performed with MARS-K, is shown in Fig. 5.30. The chosen value of toroidal rotation is $\Omega_E/\omega_A = 10^{-2}$. The benchmark results are shown from Figs. 5.31 to 5.36 with the same methodology of the previous case.

We can see from Figs. 5.34 and 5.37 (b) that the *real* set of basis point gives still the most accurate results. However, the effectiveness of interpolating directly $\boldsymbol{P}(s)$ rather than $\boldsymbol{F}(s), \boldsymbol{W}(s)$ separately seems no longer as clear as was for the previous benchmark case: this can be seen from fig. 5.37 (b), where both the cases gives an average error less than 5%. The interpolation of $\boldsymbol{F}(s), \boldsymbol{W}(s)$ (red curve) gives a narrow window of very good accuracy in the region of $\eta/\eta_{ref} \approx 10^1$, when the typical RWM regime is expected. On the other hand, the interpolation of $\boldsymbol{P}(s)$ is slightly less accurate in that region, but there is an overall accuracy which suggest more robustness for this approach.

Figure 5.38 compares of the eigenvectors, i.e. the spatial pattern of the eddy current induced by the unstable mode, with both poloidal and toroidal components computed by MARS-K and CarMa-D, assuming an interpolation degree of $k = 3$ for $\boldsymbol{P}(s)$ and the *real* set of basis points. Excellent agreement of the mode eigenfunction is obtained.

Some of the results, for the real set of points, are also reported in table 5.4 to have a quantitative idea of CarMa-D accuracy.

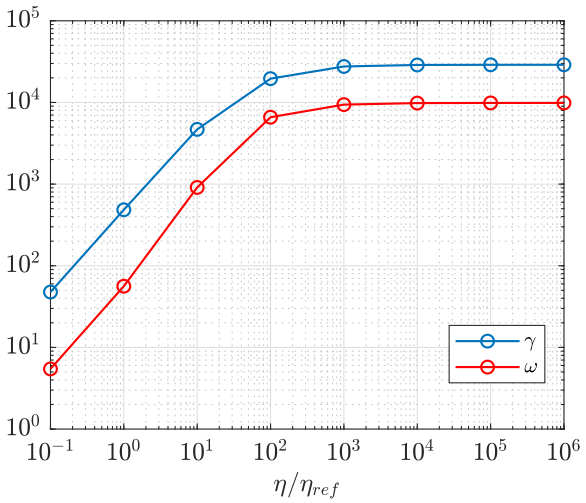

Figure 5.30: *Reference scan of wall resistivity for the kinetic case with MARS-K: real part (blue) and imaginary part (red) of the eigenvalue.*

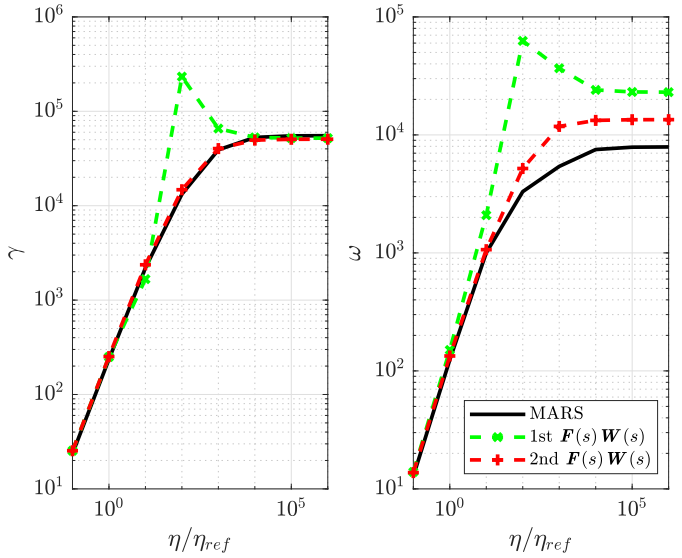

Figure 5.31: *Results of the scan of wall resistivity for the kinetic case and the* ***complex*** *set of basis points: case of separate interpolation of* $\boldsymbol{F}(s)$ *and* $\boldsymbol{W}(s)$*. Real and imaginary part are shown in logarithmic scale.*

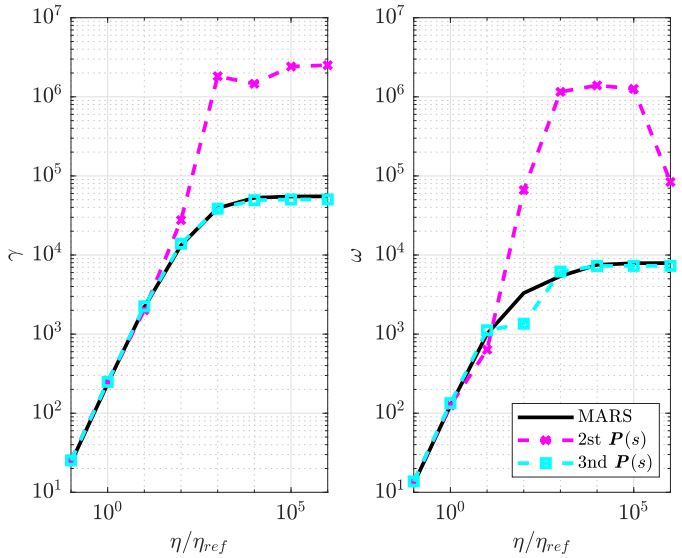

Figure 5.32: *Results of the scan of wall resistivity for the kinetic case and the* ***complex*** *set of basis points: case of direct interpolation of* $\boldsymbol{P}(s)$*. Real and imaginary part are shown in logarithmic scale.*

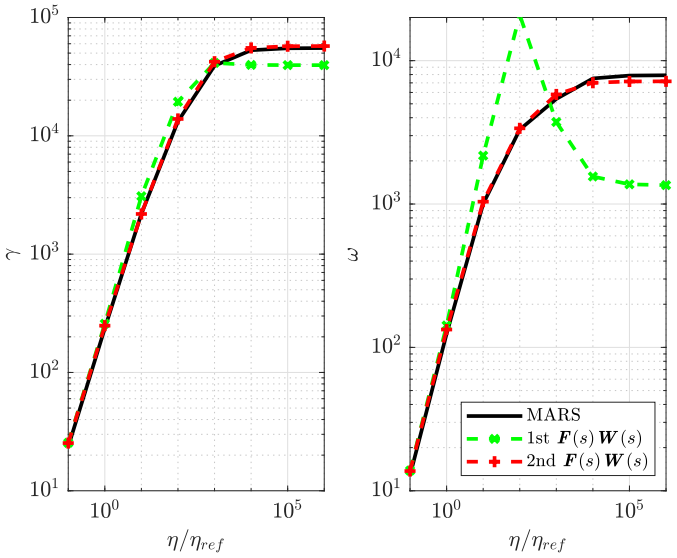

Figure 5.33: *Results of the scan of wall resistivity for the kinetic case and the* ***real*** *set of basis points: case of separate interpolation of* $\boldsymbol{F}(s)$ *and* $\boldsymbol{W}(s)$*. Real and imaginary part are shown in logarithmic scale.*

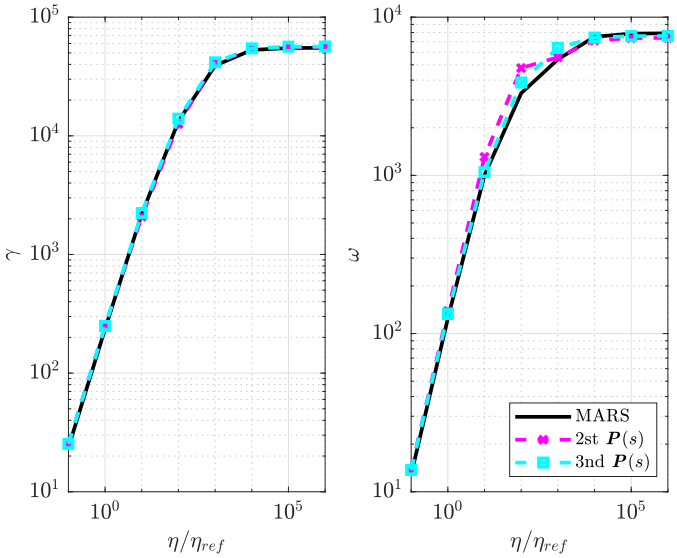

Figure 5.34: *Results of the scan of wall resistivity for the kinetic case and the* ***real*** *set of basis points: case of direct interpolation of* $\boldsymbol{P}(s)$*. Real and imaginary part are shown in logarithmic scale.*

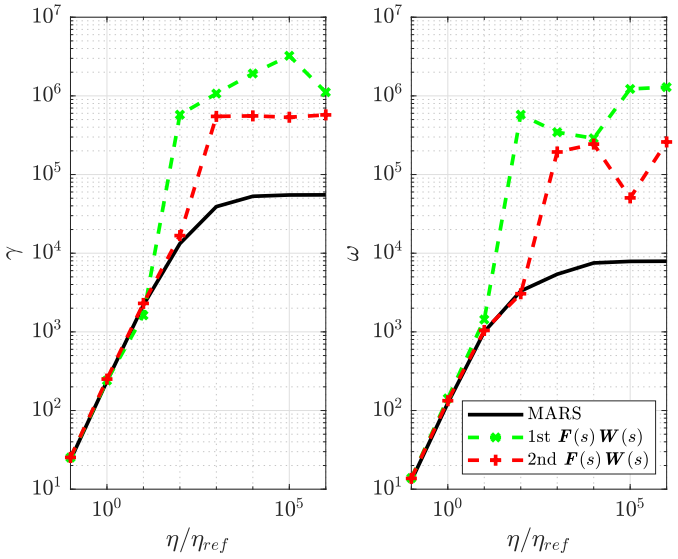

Figure 5.35: *Results of the scan of wall resistivity for the kinetic case and the* ***imaginary*** *set of basis points: case of separate interpolation of* $\boldsymbol{F}(s)$ *and* $\boldsymbol{W}(s)$*. Real and imaginary part are shown in logarithmic scale.*

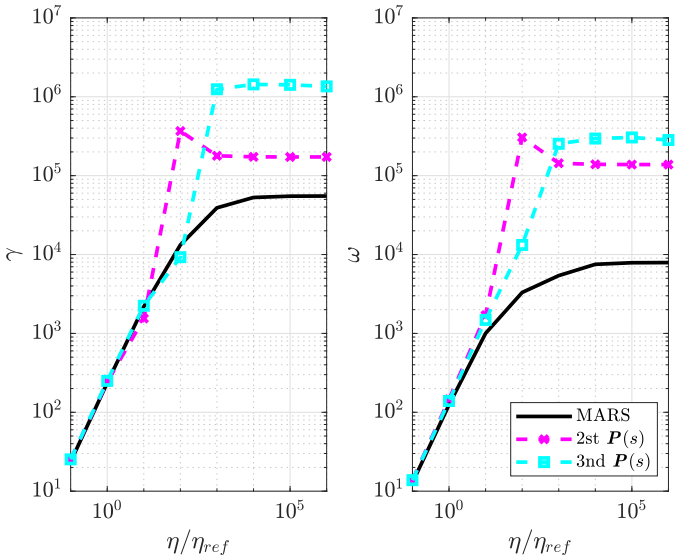

Figure 5.36: *Results of the scan of wall resistivity for the kinetic case and the* ***imaginary*** *set of basis points: case of direct interpolation of* $\boldsymbol{P}(s)$*. Real and imaginary part are shown in logarithmic scale.*

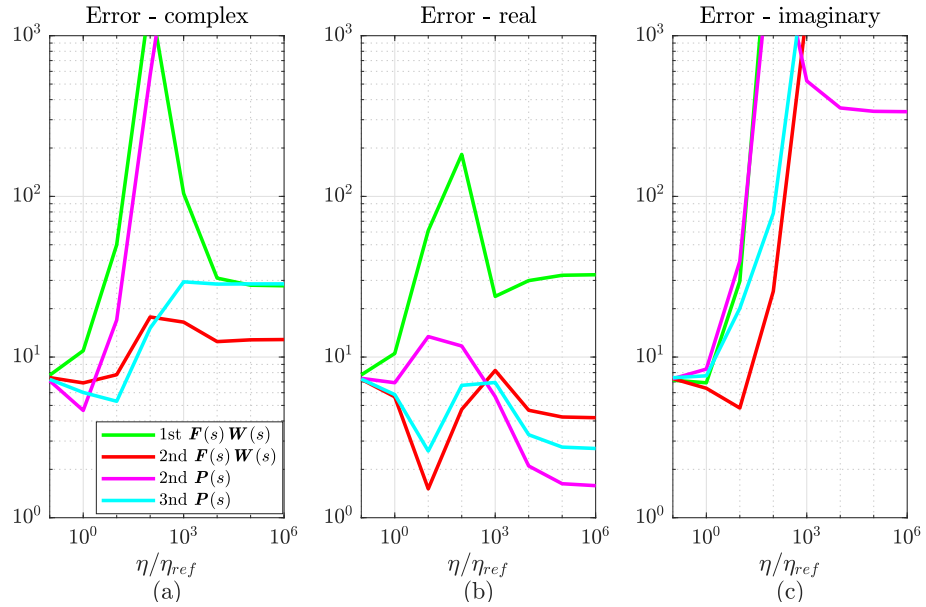

Figure 5.37: *Percentage errors of the scan of wall resistivity for all the sets of basis points for the kinetic case. Logarithmic scale.*

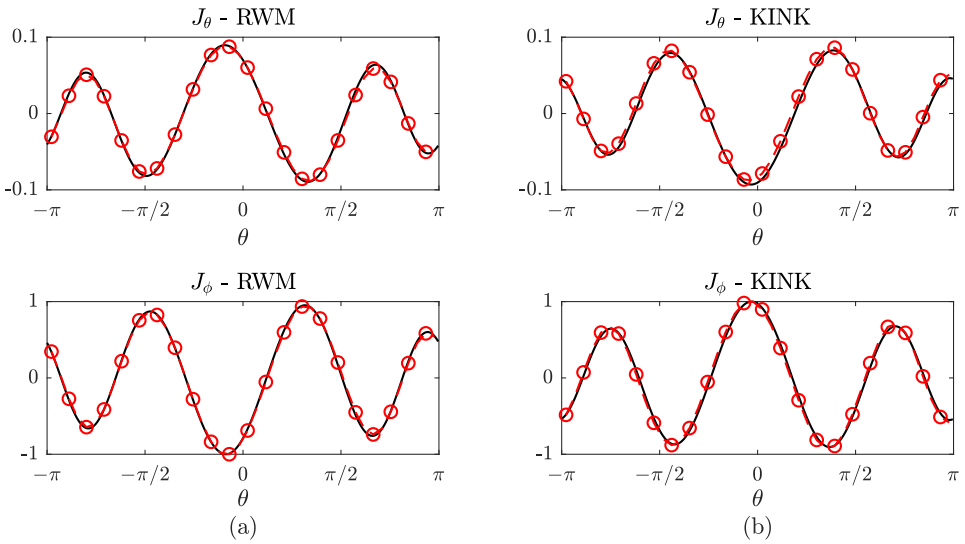

Figure 5.38: *Comparison of eigenvectors computed by MARS-K (black solid) and CarMa-D (red circles) for* 3*rd order interpolaion on* $\boldsymbol{P}(s)$ *and* real *set of basis points: standard RWM with* $\eta/\eta_{ref} = 1$ *(a) and Ideal Kink with* $\eta/\eta_{ref} = 10^5$ *(b).*

	$\eta/\eta_{ref} = 1$	$\eta/\eta_{ref} = 10^5$
Mars	$1.12 + 0.59i$	$260.5 + 37.3i$
CarMa static	$1.20 + 0.65i$	$120226 + 65324i$
CarMa 1st ord. on $\boldsymbol{F}(s)\boldsymbol{W}(s)$	$1.22 + 0.67i$	$187.7 - 6.5i$
CarMa 2st ord. on $\boldsymbol{F}(s)\boldsymbol{W}(s)$	$1.18 + 0.63i$	$271.1 + 34.0i$
CarMa 3rd ord. on $\boldsymbol{P}(s)$	$1.18 + 0.63i$	$267.6 + 36.0i$

Table 5.5: *Growth rates for drift kinetic case with $\Omega_E/\omega_A = 1 \times 10^{-2}$ for two different wall resistivities.*

5.3.3 Rotational stabilization of RWM at very low toroidal rotation

In the previous sections it has turned out that the *real* set of basis point gives much more accurate results if compared to the other sets, and the explanation of this accuracy is related to the fact that the real part of the unstable eigenvalue is much more greater than the imaginary part. To confirm this statement, another test case with very low toroidal flow is considered. We can see from Fig. 5.1 (f) that the kinetic effects (thermal particle precessional drift resonances with the mode in this case) occur strongly at very slow rotation frequency [13, 14, 3], providing an important stabilizing effect. Without going through a detailed investigation of various kinetic damping physics, it is interesting to see the effectiveness of CarMa and CarMa-D for this particular case, because, at $\Omega_E/\omega_A \approx 5 \times 10^{-4}$, we have $\omega >> \gamma$ (Fig. 5.1 (f)). If the previous assumption is correct, the imaginary set of basis points is expected to be the most desirable choice.

Table 5.6 shows that static CarMa erroneously predicts a stable mode, while CarMa-D is very accurate, showing the robustness of the approach. The imaginary data is slightly more precise than the real data (last row of Tab. 5.6), and this outcome verifies the conjecture that the choice of the basis points is related to the amplitude of the real/imaginary part of the eigenvalue. However, the real set of basis point gives still satisfying results.

It is worth nothing that static CarMa fails even if the mode is in the

	$\eta/\eta_{ref} = 1$
Mars	$0.31 - 1.12i$
CarMa static	$-0.08 - 0.98i$
CarMa 3rd ord. (real)	$0.26 - 1.06i$
CarMa 3rd ord. (imag)	$0.33 - 1.08i$

Table 5.6: *Growth rates for drift kinetic case with $\Omega_E/\omega_A \approx 5 \times 10^{-4}$ for two different values of wall resistivity.*

typical RWM regime, as discussed above, and the assumption of neglecting the plasma inertia should be valid. This suggests that the new CarMa-D model, based on the rational approximation of the plasma response, is able to deal with equilibria where the simultaneous stabilizing effect of plasma flow and kinetic damping are prominent.

5.3.4 Model of the 3-D passive structures

The capability of CarMa-D is further assessed by considering a 3-D model of the conducting structures. The 3-D geometry is obtained by opening a number of ports on the axisymmetric mesh already used for the previous cases. The mode is expected to be more unstable because of the holes [1, 12], and the aim of this benchmark activity is to understand how the effect of 3-D features affects CarMa and CarMa-D behaviour.

Figure 5.39 shows the same rotation scan already presented in Fig. 5.1 (f) for the kinetic case, but showing also the outcomes of CarMa-D both for the axisymmetric mesh and the 3D mesh, and of static CarMa. With the axisymmetric mesh (red), results given by CarMa-D agree well with the reference MARS-K data (black). The presence of holes in the wall leads to more unstable RWM: it is interesting to notice that CarMa-D (blue) gives less pessimistic results than static CarMa (green), especially for the case of $\Omega_E/\omega_A \approx 2.5 \times 10^{-3}$. Moreover, for a very low toroidal rotation $\Omega_E/\omega_A = 5 \times 10^{-4}$, the mode growth rate predicted by CarMa-D for the 3D mesh is the same of the axisymmetric case, because, being the mode growth rate very small, also the amplitude of the eddy current is small, giving a weak effect on the mode, and the geometry of the shell does not influence much the mode evolution. On the other hand, static CarMa erroneously predicts a stable mode. The imaginary part of the mode eigenvalue is not strongly affected by the 3D features of the geometry.

An example of the eddy current pattern induced by the unstable mode for the three-dimensional mesh and the case $\Omega_E/\omega_A = 10^{-2}$ is shown in Fig. 5.40, where the pattern modification due to the holes can be seen.

5.4 Numerical considerations

The mathematical model of CarMa-D suffers from the fact that the higher is the interpolation degree k, the higher is the number of DoF. This requires some considerations to show if this is a real drawback from the computational point of view. It was already mentioned that the number of non-zeros of CarMa and CarMa-D is almost unchanged: here we report the computational

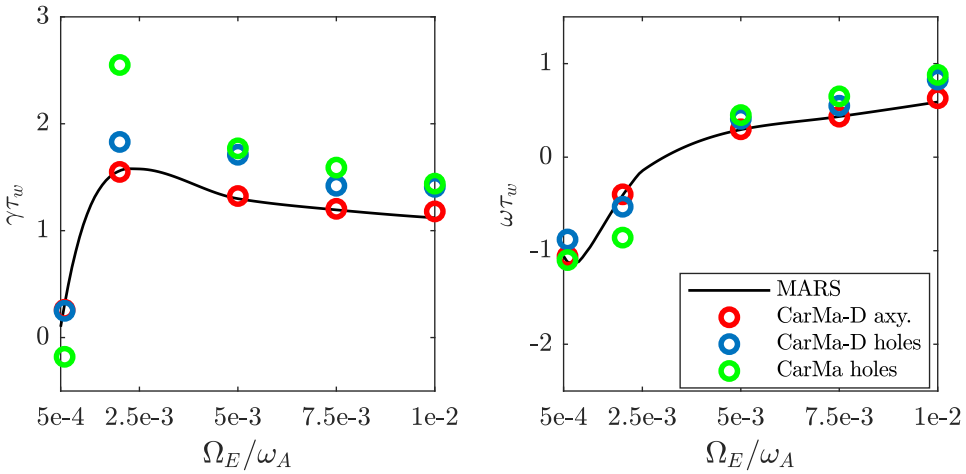

Figure 5.39: *Comparison of the mode eigenvalue, real (a) and imaginary (b) part, computed by MARS-K (black) for different values of toroidal rotation Ω_E/ω_A, with: CarMa-D and axisymmetric mesh (red), CarMa-D and 3D mesh (blue), static CarMa and 3D mesh (green).*

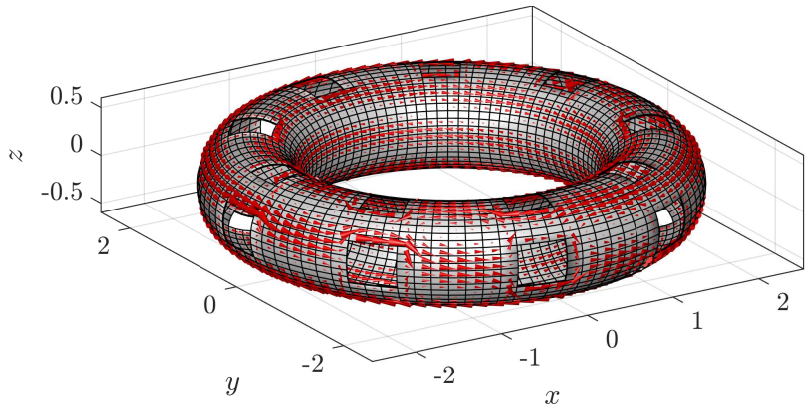

Figure 5.40: *Eddy current pattern related to the unstable mode for the 3-D mesh with holes. Kinetic case with resistivity $\eta/\eta_{ref} = 1$ and toroidal rotation $\Omega_E/\omega_A = 10^{-2}$.*

time to compute the LU decomposition of the system matrix, as well as the time required for a single step of the *inverse iteration scheme* for the computation of the mode eigenvalue, a method widely used in Magneto-Hydrodynamic stability analysis [15, 16]. All the computations have been performed on the same machine with Intel Core i7 2.80GHz and 16GB of Memory:

- static CarMa:
  - $nn = 2402$, $nnz = nn^2 \approx 6 \times 10^6$, sparsity factor $\alpha = nnz/nn^2 = 1$ (the matrix is full);
  - for inverse iteration: LU decomposition takes 0.2s, one step of inverse iteration takes 10ms;
- $\boldsymbol{F}(s)\boldsymbol{W}(s)$ 2nd ord:
  - $nn = 4864$, $nnz \approx 6 \times 10^6$, sparsity factor $\alpha = nnz/nn^2 = 0.25$;
  - for inverse iteration: LU decomposition takes 1.55s, one step of inverse iteration takes 11.3ms;
- $\boldsymbol{P}(s)$ 3rd ord:
  - $nn = 7251$, $nnz \approx 6 \times 10^6$, sparsity factor $\alpha = nnz/nn^2 = 0.11$;
  - for inverse iteration: LU decomposition takes 1.65s, one step of inverse iteration takes 11.8ms;
- $\boldsymbol{P}(s)$ 4th ord:
  - $nn = 9648$, $nnz \approx 6 \times 10^6$, sparsity fator $\alpha = nnz/nn^2 = 0.06$;
  - for inverse iteration: LU decomposition takes 1.7s, one step of inverse iteration takes 13ms;

We can note that, even if the number of non-zeros is practically unchanged, the LU decompositions for CarMa-D requires more time. This can be explained looking at Fig. 5.41, where the sparsity pattern for the $k = 3$ order interpolation of $\boldsymbol{P}(s)$ is reported. Such matrix is sparse, except for the dense square block on the upper left corner related to the static CarMa block $\boldsymbol{R}_a^{-1}\boldsymbol{L}_1$ in Eq. (4.42). Since we are dealing with a sparse matrix, a suitable sparse linear algebra toolbox should be used. However, these methods use the graph theory to minimize the so-called matrix *fill-in* [17], i.e. the entries that change from an initial zero to a non-zero value during the execution of an algorithm. It could happen that the very localized dense block does not allow to obtain the desirable performance gain that could be achieved

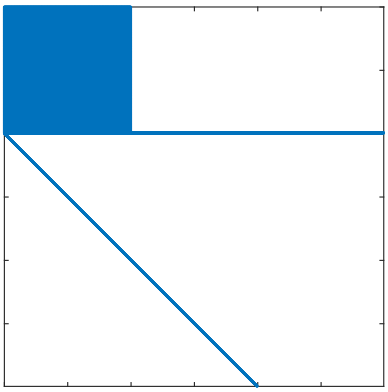

Figure 5.41: *Sparsity pattern of matrix* (4.42) *for interpolation degree* $k = 3$*. The matrix dimensions are* 7251×7251 *and the total number of non-zeros are* $\approx 6 \times 10^6$*.*

with a sparse matrix with the same number of non-zeros, but with a regular structure.

5.5 Conclusions

The CarMa-D code, whose mathematical model has been presented in the previous chapter, is applied to a reference test case in order to provide an idea of its effectiveness as well as to address its possible weaknesses. The test case used is a circular shaped plasma enclosed in an axi-symmetric conducting wall, already used to benchmark the static version of the code. For this purpose, two different damping physics mechanism are used for the same equilibrium: the parallel sound wave damping model and full toroidal drift kinetic model.

For both the damping mechanisms, the matrix-based rational approximation technique used in CarMa-D shows that a good accuracy can be reached interpolating the plasma response $\boldsymbol{P}(s)$ with a degree of $k = 3$. It turns out that, for this specific test case, the interpolation along the real axis of the complex plane gives results much more accurate than the other sets of basis points.

In addition to this, the performed scan of the resistivity η of the conducting wall in the range $\eta/\eta_{ref} = [10^{-1}, 10^6]$ underlines that, starting from the data interpolated along the real axis, the new dynamic model can recover the reference results provided by MARS-F/K with a percentage error less than 2% for the fluid model, and around 4% for the drift kinetic model. This is valid also for the ideal kink instability, for which the plasma inertia plays an essential role. It has also shown that the new CarMa-D model is able to

deal also with equilibria where the simultaneous effects of plasma flow and kinetic damping are prominent. In this case, the static CarMa model fails, recovering a stable mode.

An additional test example with 3-D mesh has been considered. The holes have a destabilizing effect, but it is very interesting to note that the inclusion of the drift kinetic damping effects in the model obtained by CarMa-D gives less pessimistic results than what gives the static CarMa.

Numerical consideration on the computational cost of CarMa-D with respect of CarMa are also reported, to understand how the computational complexity scales with the additional number of DoF required by CarMa-D.

Bibliography

[1] A. Portone, F. Villone, Y. Q. Liu, R. Albanese, and G. Rubinacci, "Linearly perturbed MHD equilibria and 3D eddy current coupling via the control surface method," *Plasma Physics and Controlled Fusion*, vol. 50, no. 8, p. 085004, 2008.

[2] Y. Q. Liu, A. Bondeson, C. M. Fransson, B. Lennartson, and C. Breitholtz, "Feedback stabilization of nonaxisymmetric resistive wall modes in tokamaks. i. electromagnetic model," *Physics of Plasmas*, vol. 7, no. 9, pp. 3681–3690, 2000.

[3] Y. Q. Liu, M. S. Chu, I. T. Chapman, and T. C. Hender, "Toroidal self-consistent modeling of drift kinetic effects on the resistive wall mode," *Physics of Plasmas*, vol. 15, no. 11, p. 112503, 2008.

[4] F. Villone and Y. Q. Liu, "Rwm analysis with 3d conductors, plasma flow and kinetic damping," vol. 33, pp. 61–64, 01 2009.

[5] F. Villone, Y. Q. Liu, P. Roberto, T. Bolzonella, and G. Rubinacci, "Effects of three-dimensional electromagnetic structures on resistive-wall-mode stability of reversed field pinches," *Phys. Rev. Lett.*, vol. 100, p. 255005, 06 2008.

[6] F. Villone, Y. Q. Liu, G. Rubinacci, and S. Ventre, "Effects of thick blanket modules on the resistive wall modes stability in ITER," *Nuclear Fusion*, vol. 50, p. 125011, nov 2010.

[7] J. Hanson, J. Bialek, F. Turco, J. King, G. Navratil, E. Strait, and A. Turnbull, "Validation of conducting wall models using magnetic measurements," *Nuclear Fusion*, vol. 56, p. 106022, aug 2016.

[8] V. D. Pustovitov, "Thick-wall effects in the theory of resistive wall modes," *Physics of Plasmas*, vol. 19, no. 6, p. 062503, 2012.

[9] F. Villone and V. D. Pustovitov, "Skin effect modifications of the resistive wall mode dynamics in tokamaks," *Physics Letters A*, vol. 377, no. 39, pp. 2780 – 2784, 2013.

[10] Y. Q. Liu, R. Albanese, A. Portone, G. Rubinacci, and F. Villone, "An analytical demonstration of coupling schemes between magnetohydrodynamic codes and eddy current codes," *Physics of Plasmas*, vol. 15, no. 7, p. 072516, 2008.

[11] Y. Q. Liu, M. S. Chu, C. Gimblett, and J. Hastie, "Magnetic drift kinetic damping of the resistive wall mode in large aspect ratio tokamaks," *Physics of Plasmas - PHYS PLASMAS*, vol. 15, 09 2008.

[12] Y. Q. Liu and F. Villone, "A rigorous approach to study kinetic and 3D effects on resistive wall mode," *Plasma Physics and Controlled Fusion*, vol. 51, p. 115008, oct 2009.

[13] B. Hu and R. Betti, "Resistive wall mode in collisionless quasistationary plasmas," *Phys. Rev. Lett.*, vol. 93, p. 105002, Sep 2004.

[14] B. Hu, R. Betti, and J. Manickam, "Application of the low-frequency energy principle to wall modes," *Physics of Plasmas*, vol. 12, no. 5, p. 057301, 2005.

[15] R. Gruber, F. Troyon, D. Berger, L. Bernard, S. Rousset, R. Schreiber, W. Kerner, W. Schneider, and K. Roberts, "Erato stability code," *Computer Physics Communications*, vol. 21, no. 3, pp. 323 – 371, 1981.

[16] A. Bondeson, G. Vlad, and H. Lütjens, "Computation of resistive instabilities in toroidal plasmas," *Proc. IAEA Technical Committee Meeting on Advances in Simulation and Modelling of Thermonuclear Plasmas*, 1993.

[17] Y. Saad, *Iterative Methods for Sparse Linear Systems: Second Edition*. Other Titles in Applied Mathematics, Society for Industrial and Applied Mathematics (SIAM, 3600 Market Street, Floor 6, Philadelphia, PA 19104), 2003.

6 RWMs analysis and control on JT-60SA high β scenario

Contents

6.1 Introduction

In the previous chapters, the new CarMa-D model has been at first presented, and then validated with a simple test problem obtained by considering a plasma with circular cross-section. CarMa-D has proven to be a reliable tool to study RWM analysis, able to deal with instabilities with non negligible dynamical effect and with the simultaneous combination of toroidal flow and kinetic damping. In particular, this latter feature of CarMa-D is a situation of particular interest, because of the strong stabilizing effect on the external

kink instabilities that occurs for certain values of toroidal flow if a kinetic-hybrid description of the plasma is used.

The validation with a circular plasma can be somehow optimistic and must be extended to more general cases, because a cross section of circular shape has a simple geometry if compared with those of real experiments. Indeed, it is well known that tokamak performances are substantially improved as the plasma cross section becomes more elongated [1]. Unlike the circular test case, this requires a higher number of Fourier harmonics to describe quantities in the poloidal plane. To assess how CarMa-D behaves when dealing with realistic devices, a test case has been taken from the forthcoming JT-60SA tokamak.

6.1.1 The JT-60SA experiment

The super-conducting fusion reactor Japan Torus Super Advanced (JT-60SA) [2, 3] is under construction in Naka, Japan, under the Satellite Tokamak Project (STP) of the Broader Approach (BA) agreement between European Union and Japan. The European Implementing Agency (EU-IA) is Fusion for Energy (F4E) and the Japanese Implementing Agency (JA-IA) is the Quantum and Radiological Science and Technology (QST). The aim of the project is to conduct supportive and complementary work for the ITER project towards supporting the basis for DEMO [4]. An overview of the device can be seen in Fig. 6.1.

One of the major objectives of the JT-60SA Project is to provide a research support for the ITER project, in order to accomplish the required technical goals. Since ITER is expected to operate with long pulses (300-500s) at Q=10 [5], many of critical issues need to be addressed. JT-60SA can operate in the ITER-like configuration inductive mode under the break-even-equivalent condition. This opens the possibility to investigate important problems, such as disruption avoidance and mitigation, ELM control for heat pulse reduction, heat load mitigation by radiative divertor and limitation of serious MHD instabilities.

The main parameters of JT-60SA are summarized in Tab. 6.1 [6, 7]. As can be seen, a significant amount of power is expected to be provided by heating and current drive systems, up to 41MW for 100s. In particular, the presence of off-axis Negative-NBI at 0.5 MeV and 10 MW power will allow current profile tailoring to operate at Advanced Tokamak scenarios, with fully non inductive current drive.

Whit these capabilities, JT-60SA device is expected to to explore ITER and DEMO relevant plasma regimes, in terms of non-dimensional param-

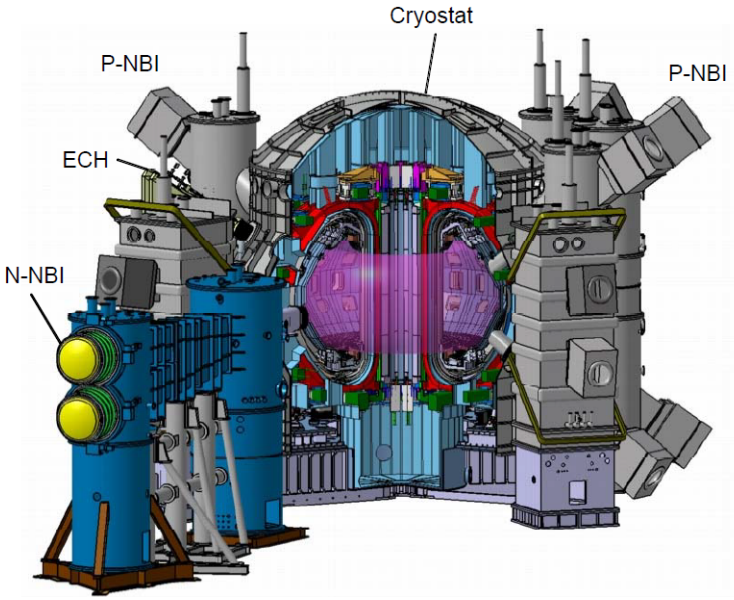

Figure 6.1: *Overview of JT-60SA.*

Toroidal field	2.25T
Plasma current	5.5MA
Major/minor radius	2.96/1.18m
Aspect ratio	2.5
Elongation	1.95
Triangularity	0.53
Plasma volume	$132m^2$
H&CD power (total)	41MW
N-NBI (500 keV)	10MW
P-NBI (85 keV)	24MW
ECRH (110, 138GHz)	7MW
Flat-top duration	100s

Table 6.1: *Nominal parameters of the JT-60SA tokamak.*

eters (such as normalized gyro radius ρ_p^*, normalized collisionality ν^* and normalized poloidal beta β_N) [6]. The steady-state operations require to maintain simultaneously high values of energy confinement, normalized beta β_N, bootstrap current fraction, normalized plasma density, and many other parameters. Such high performances have never been achieved, and one of the most important goals of JT-60SA is to reach and sustain such high performances. The first step is to expand the operational boundaries, exceeding the requirements for ITER. This means that, in terms of pressure limit, the device is expected to operate above the no-wall MHD stability limit, such as $\beta_N \approx 3 \div 5.5$. This is mandatory for an economically attractive compact DEMO device, but, on the other hand, leads the plasma to be subjected to global MHD instabilities.

6.1.2 Pressure driven kink instabilities in the Scenario 5 target plasma

In the following part of the work we turn attention to the stability analysis of Scenario 5 [6]. This scenario will establish the base for high β_N, fully non-inductive current drive operation on JT-60SA. As main features, it is characterized by reversed shear, plasma current $I_p = 2.3$MA, toroidal magnetic field $B_t = 1.72T$ and normalized beta $\beta_N = 4.3$.

The considered reference equilibrium is has been obtained with integrated modelling simulations performed with the CRONOS suite [8]. The scenario implemented in this work is a low power version of the Scenario 5, with 17MW from NBI and 7MW from ECRH, and $\beta_N \approx 3.6$. In Figs. 6.2a - 6.2b - 6.2c we show respectively the profiles of safety factor, pressure, and surface averaged current.

For the target plasma scenario, recent work has shown that $\beta_N \approx 3.6$ lies beyond the no wall limits for both the modes $n = 1$ and $n = 2$, because respectively of $\beta_N^{nw} = 1.9$ and $\beta_N^{nw} = 2.3$ [9]. The no-wall limits for these toroidal modes are shown in Fig 6.2d. This mean that the $n = 1$ is the most unstable mode for this equilibrium, but clearly both the modes require simultaneous feedback stabilization to allow the operations at the target value of β_N. In the next part of the chapter, CarMa-D will be used to assess this problem.

As a starting point, for the stability analysis the fluid model with no toroidal rotation is considered, while future effort will be oriented to include in the model drift-kinetic description of the plasma and toroidal rotation. Indeed, we consider first the assessment of the problem with the fluid damping model, and then providing a more physical and detailed description of the

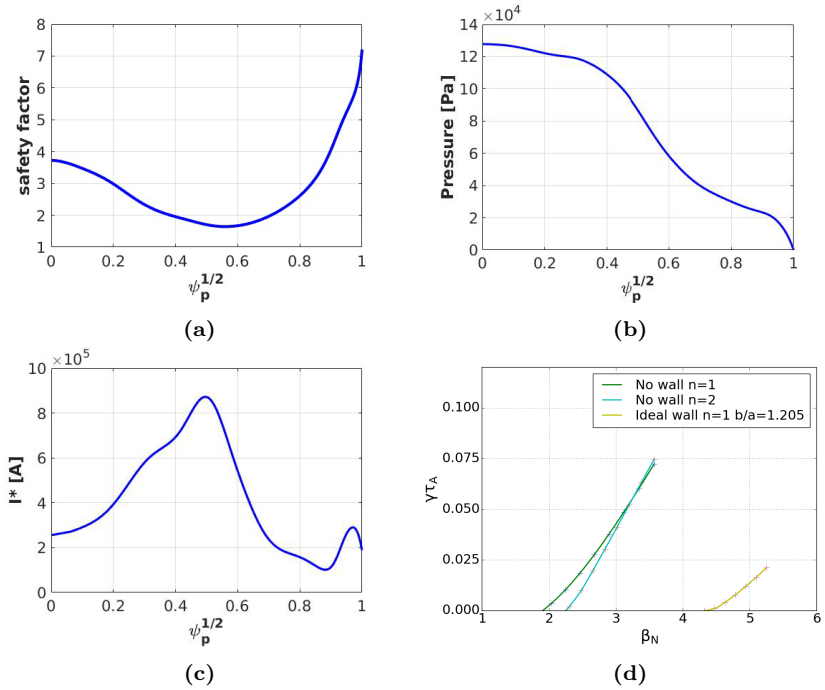

Figure 6.2: *View of the profiles of safety factor (a), pressure (b), and surface averaged current (c). Pressure scan for ideal kink mode (d). No-wall limits are shown for $n = 1$ and $n = 2$. Ideal-wall limit is calculated for n=1 and stabilizing plate position [9]*

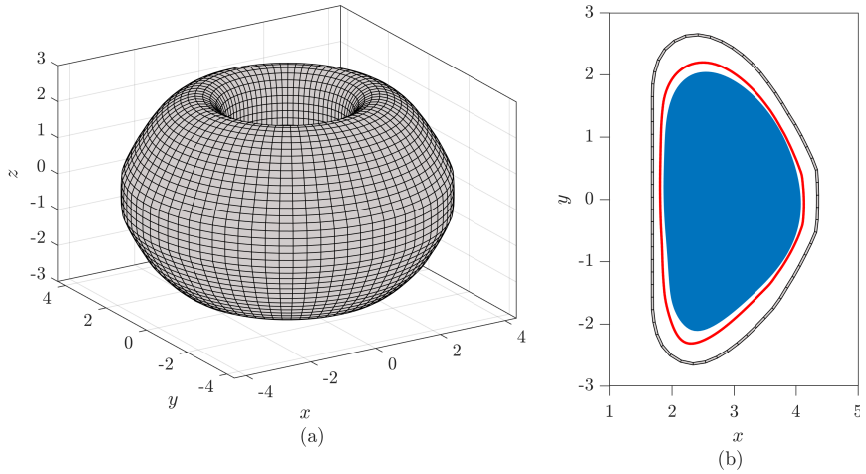

Figure 6.3: *Three-dimensional view of the axysimmetric mesh (a) and particular of the poloidal plane, with the coupling surface (red) and the plasma cross-section (blue).*

synergic effect of kinetic damping (viscosity [10], kinetic resonance with particle drift motion [11, 12, 13, 14]) and plasma rotation. As a matter of fact, these combined effects are expected to give a strong passive stabilization to the aforementioned instabilities [9].

On the other hand, this fluid description has already been used as starting point for stability analysis and feedback stabilization with the static CarMa model. In particular, in Ref. [15] the stability analysis of the $n = 1$ RWM is reported, at first with an axisymmetric mesh of the first wall, and then with a detailed 3-D mesh of the conducting structures. The same detailed mesh has been recently used also for preliminary study of multi-modal feedback controls of the $n = 1$ and $n = 2$ RWMs [16].

6.2 RWM stability analysis with axi-symmetric conducting structures

6.2.1 The conducting structures model

The first step to acquire confidence on CarMa-D results is to go through a preliminary validation with MARS results, as done for the circular equilibrium. For this reason, an axisymmetric mesh is required, which can be seen in Fig. 6.3a. Figure 6.3b shows also, in the poloidal plane, the coupling surface and the cross-section of the plasma equilibrium.

In order to characterize the passive structures, the penetration times for the slowest helical perturbations with $n = 0, 1, 2$ are reported in Tab. 6.2. Detailed views of the related image currents of the passive eigenvectors can be seen in Figs. 6.4 to 6.9.

For the same reasons already mentioned in section 5.1, only one mesh element along the shell thickness is considered.

	τ_w
$n = 0$	111.5mS
$n = 1$	84.4mS
$n = 2$	58.4mS

Table 6.2: *Wall times for different toroidal mode numbers.*

6.2.2 Notes on the static plasma response matrix

The highly elongated cross section (Fig 6.3b) of this equilibrium requires a broad spectrum of Fourier harmonics to decompose the quantities in the

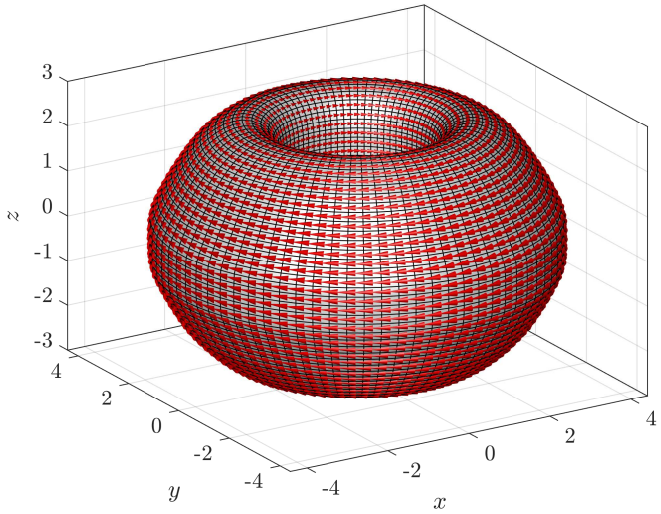

Figure 6.4: *Eddy current pattern related to the $n = 0$ slowest passive eigenvector.*

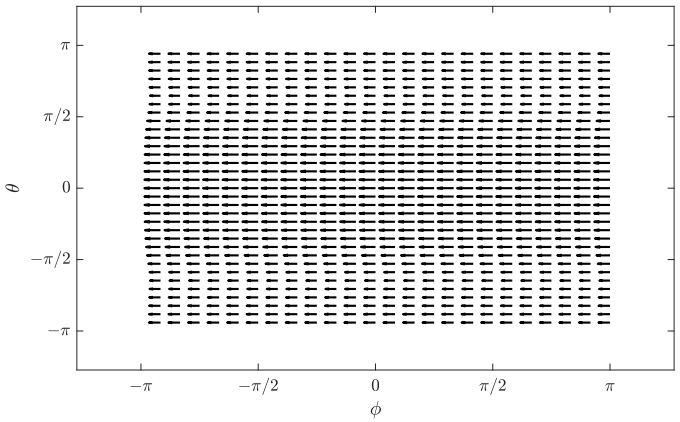

Figure 6.5: *Eddy current pattern related to the $n = 0$ slowest passive eigenvector (rectified view).*

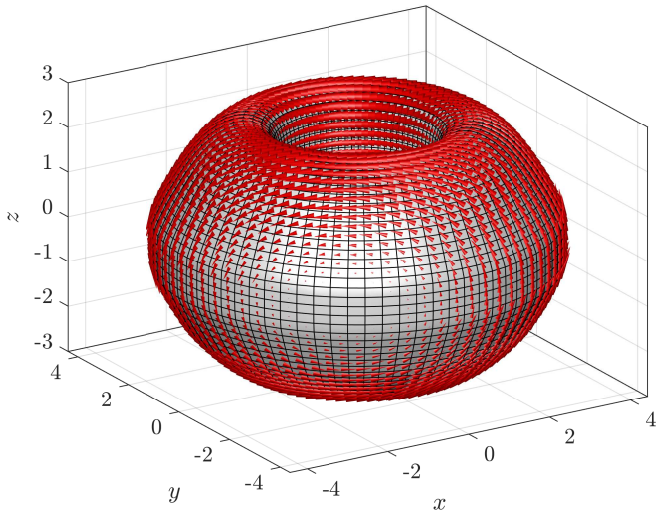

Figure 6.6: *Eddy current pattern related to the $n = 1$ slowest passive eigenvector.*

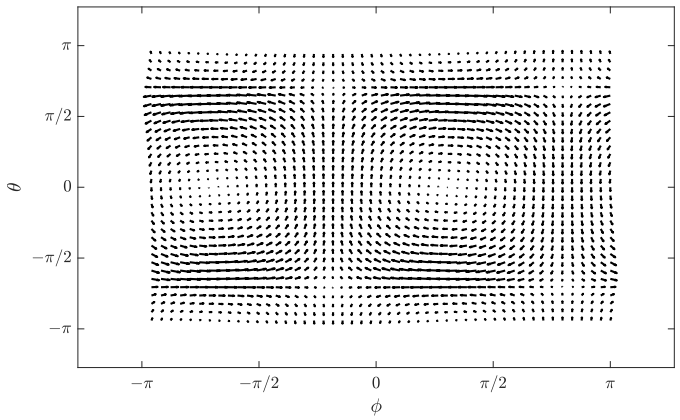

Figure 6.7: *Eddy current pattern related to the $n = 1$ slowest passive eigenvector (rectified view).*

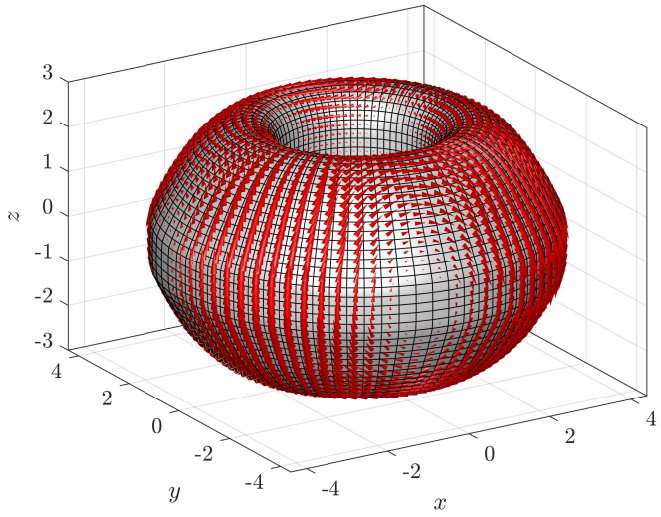

Figure 6.8: *Eddy current pattern related to the $n = 2$ slowest passive eigenvector.*

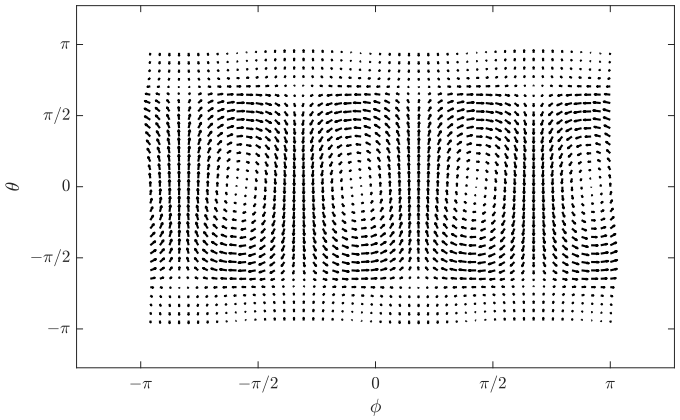

Figure 6.9: *Eddy current pattern related to the $n = 2$ slowest passive eigenvector (rectified view).*

poloidal plane. For this specific case, the chosen spectrum is $m \in [-9, 59]$. Figure 6.10 shows a convergence analysis of the real and imaginary part of the mode $n = 1$ growth rate as the number of harmonics M increases. The convergence is reached for $M = 60$ poloidal harmonics.

Increasing the dimension of the poloidal spectrum has several drawbacks, affecting in particular the computation of matrix $\boldsymbol{K}$ with Eq. (3.14), which is a very important step in the procedure, because it is used to compute $\boldsymbol{F}$ through Eq. (3.18), and $\boldsymbol{W}$ through Eq. (3.23).

The first drawback is that the MHD simulations with MARS require more computational resources, as well as more time, because the computational complexity for every single computation of Eqs. (3.12) scales with $\propto M^2$ [17]. Therefore, the entire procedure to compute the matrices $\boldsymbol{K}$ and $\tilde{\boldsymbol{K}}$ as Eqs. (3.14) - (3.15), where each one requires to solve M times the MHD equations in the domain bounded by the coupling surface, scales with $\propto 2M^3$. It is worth recalling that, for the matrix based rational interpolation, the computation of $\boldsymbol{K}$ should be repeated $N(2k+1)$ times, with k interpolation degree and N number of considered toroidal modes, causing a dramatic increase of the computational time.

The second drawback, which should be considered the most limiting one, is related to the ill-conditioning of the involved matrices. This is particularly problematic for the Eq. (3.14), which relies on the computation of $\boldsymbol{B}_N^{-1}$. This fact is particularly clear looking at the data shown in Figs. 6.11a to 6.11d, where the quantities involved in Eq. (3.14) are shown. This is the case of the $n = 1$ plasma response computation, but the same considerations hold for the $n = 2$ mode. The boundary conditions (BCs) on the normal field distributions, which have the same distribution already reported in Fig. 3.2, are shown as the columns of the matrix in Fig. 6.11a: this is the $M \times M$ matrix $\boldsymbol{B}_N$ built as Eq. (3.13). The same is done for $\boldsymbol{B}_T$ in Fig. 6.11b. It is clear that a narrow harmonic content of both the BCs and the resulting $\boldsymbol{B}_T$ is mainly centered around the harmonic $m = 0$. This means that the plasma response, described through $\boldsymbol{B}_T$, exhibits an harmonic content similar to that of the boundary conditions, meaning that the matrix $\boldsymbol{K}$ should be "mainly" diagonal (see Fig. 5.11; the structure of $\boldsymbol{P}$ is very close to the one of $\boldsymbol{K}$). In addition to this, the amplitudes of $\boldsymbol{B}_N$ and $\boldsymbol{B}_T$ elements are very close, requiring diagonal elements of the matrix $\boldsymbol{K}$ fo have almost unitary amplitude.

This is however in contrast with the matrix $\boldsymbol{K}$ shown in Fig. 6.11c, obtained performing the standard matrix inverse computation to get $\boldsymbol{B}_N^{-1}$. The structure of this matrix, which is not even close to diagonal, and the amplitude of the elements, are clearly not correct. On the other hand, performing

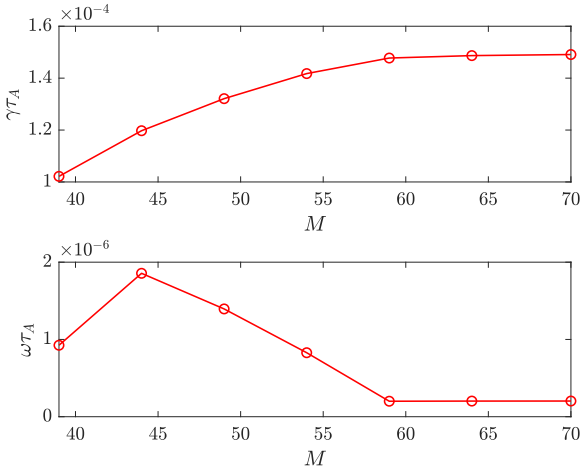

Figure 6.10: *Convergence of real and imaginary part of the eigenvalue, for the mode $n = 1$, as function of the total number of poloidal harmonics used for Fourier decomposition.*

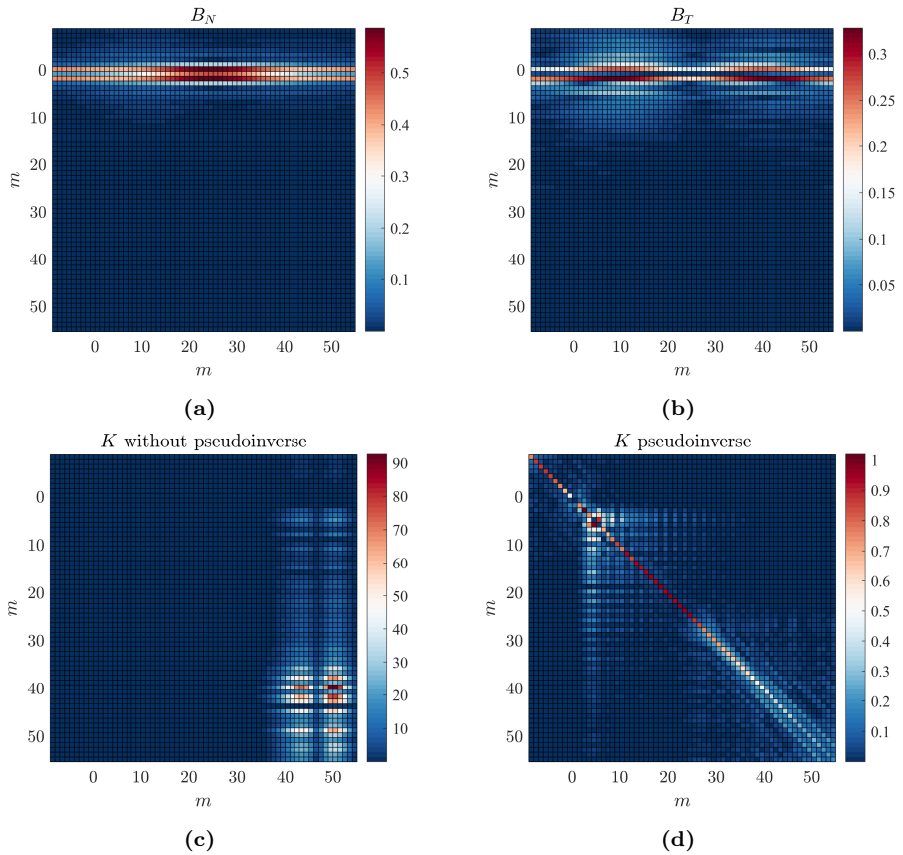

Figure 6.11: *Quantities involved in Eq. 3.14 for the $n = 1$ plasma response: input boundary conditions $\boldsymbol{B}_N$ (a), output $\boldsymbol{B}_T$ (b), and matrix $\boldsymbol{K}$ computed without pseudo-inverse (c) and with pseudo-inverse (d).*

the same computation with a regularization technique, such as the TSVD already reported in Eq. (4.31), leads to plausible results, as can be seen in Fig. 6.11d. Here the chosen truncation index is $t = 45$, meaning that the 45 singular values out of the total 65 have been retained in the computation. The value of the truncation index is linked to the extension of the noisy part of the matrix in Fig. 6.11d for higher harmonics (i.e. $m > 30$). The choice made here is a compromise, and has required the study of several cases.

It is worth noting that the aforementioned matrix $\boldsymbol{K}$ is the starting point of the entire mathematical structure of both static CarMa and CarMa-D. Failing the computation of this matrix would lead to inconsistent results also for the case of static CarMa. A proper derivation of this matrix is therefore mandatory, and one of the most important steps to take care about.

6.2.3 Stability analysis for toroidal modes $n = 1$ and $n = 2$

The CarMa-D multi-modal system, whose mathematical formulation has been developed in subsection 4.4.2, has been used for the stability analysis of the toroidal modes $n = 1$ and $n = 2$. The mode $n = 0$ has not been considered here, for a couple or reasons. The first one is more "practical", being the MARS code not able to treat easily the $n = 0$ component because, in the mathematical model, some quantities are divided by the toroidal mode number n. The response matrix for the case $n = 0$ has to be obtained exploiting other mathematical models, such as, for example, CREATE-L [18]. In addition to this, the mode $n = 0$ is expected to be weakly coupled to the other modes. This fact has already been presented in Ref. [19] for the ITER case, where the modes $n = 0$ and $n = 1$ are considered: the feedback strategy have been designed with two separate controllers, because the two modes are almost orthogonal.

For an axisymmetric mesh, the growth rates computed by MARS, and used as reference results, are reported in Tab. 6.3. For every toroidal mode number n, as expected, MARS-F recovers a couple of complex conjugate modes. This is due to the toroidal symmetry of the problem.

n	$\gamma\tau_w$	γ
1	$12.48 + 0.01i$	$1.39 \times 10^2 + 7i \times 10^{-2}$
	$12.48 - 0.01i$	$1.39 \times 10^2 - 7i \times 10^{-2}$
2	$10.57 + 0.22i$	$1.70 \times 10^2 + 3.52i$
	$10.57 - 0.22i$	$1.70 \times 10^2 - 3.52i$

Table 6.3: *Growth rates for the mode $n = 1, 2$ computed by MARS and normalized by the corresponding wall times.*

n	$\gamma\tau_w$	γ
1	$11.89 + 0.03i$	$1.410 \times 10^2 + 4.151i \times 10^{-1}$
	$11.89 - 0.03i$	$1.410 \times 10^2 - 4.154i \times 10^{-1}$
2	$10.17 + 0.50i$	$1.743 \times 10^2 + 8.494i$
	$10.17 - 0.50i$	$1.743 \times 10^2 - 8.494i$

Table 6.4: *Growth rates for the mode $n = 1$ and $n = 2$ computed by CarMa-D and normalized by the corresponding wall times.*

The CarMa-D model also recovers eigenvalues in pairs of complex conjugate modes, as was expected. All the unstable eigenvalues are shown in Tab. 6.4. The small discrepancy on the imaginary part of the $n = 1$ mode is due to the fact that the matrix (4.43) has complex entries, as was described in Sec. 4.4: with the new CarMa-D formulation it is no longer possible to simply add the contribution of different modes as done in Eqs. (3.43), and exploiting Eq. (3.44) to obtain real matrices. This would not be appreciable in infinite-precision arithmetics, but can be experienced here due to the finite precision of the geometry discretization. However, agreement with MARS-F results is accurate. The relative percentage error on the growth rate, and defined as Eq. (5.4) is around 4.5% for both the modes.

A 1-D quantitative comparison with the $n = 1$ and $n = 2$ eigenvectors computed by MARS-F is shown is Figs. 6.12a - 6.12b. Both the eigenvectors agree well with the reference. A possible explanation of the small discrep-

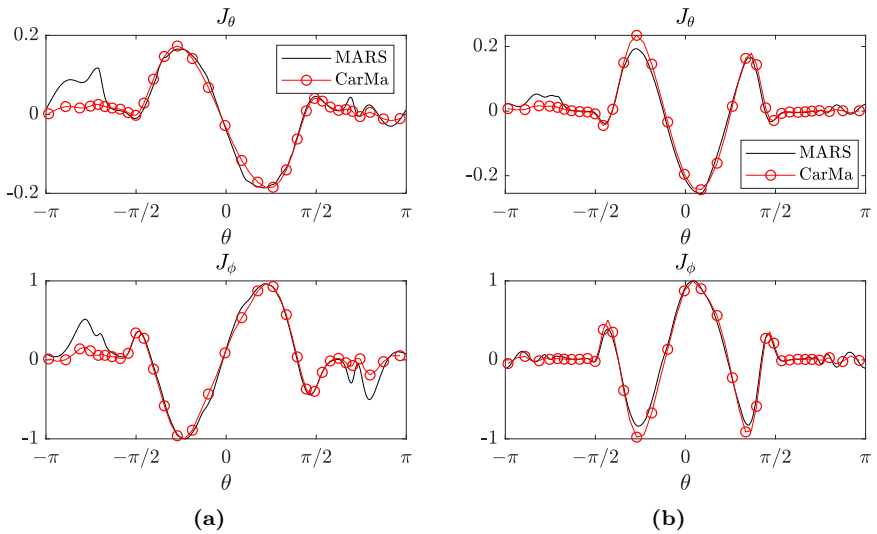

Figure 6.12: *Comparison of eigenvectors computed by MARS-K (black solid) and CarMa-D (red circles) for the modes $n = 1$ (a) and $n = 2$ (b).*

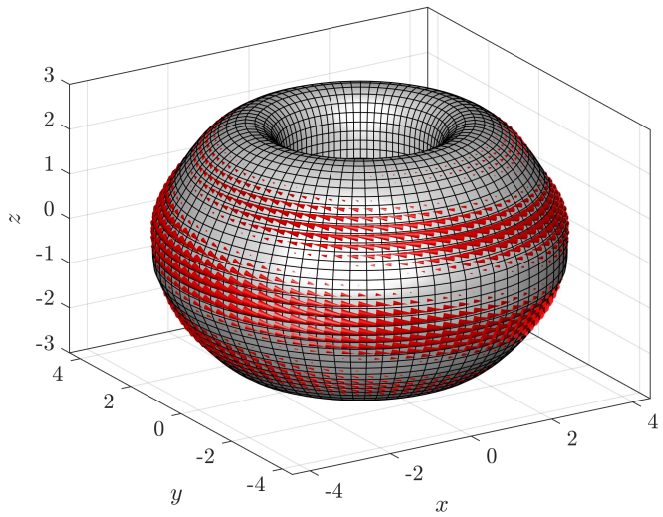

Figure 6.13: *Eddy current pattern related to the $n = 1$ unstable eigenvector.*

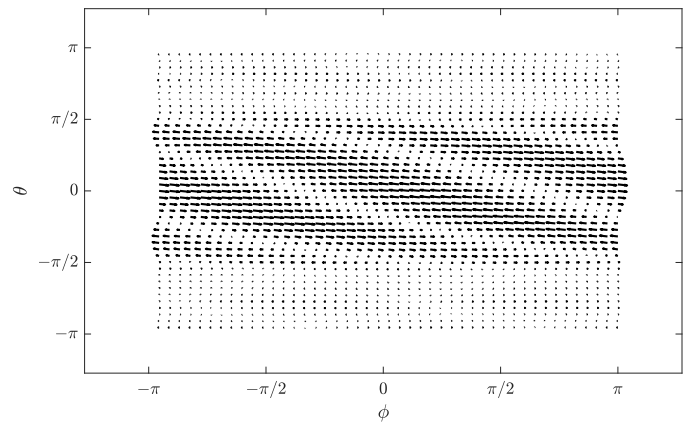

Figure 6.14: *Eddy current pattern related to the $n = 1$ unstable eigenvector (rectified view).*

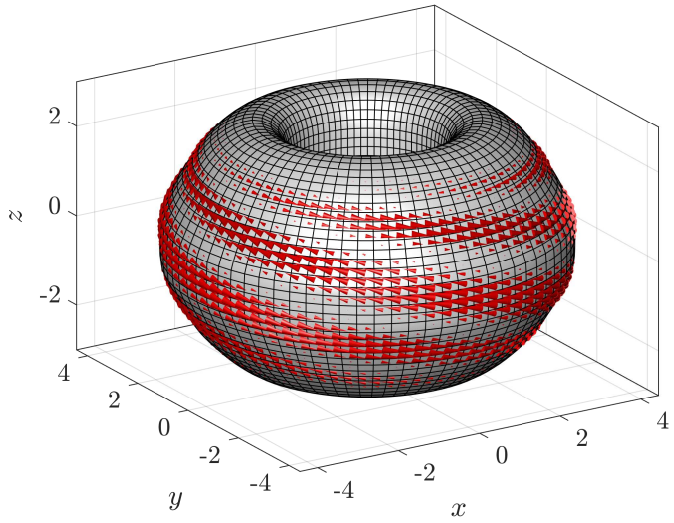

Figure 6.15: *Eddy current pattern related to the $n = 2$ unstable eigenvector*

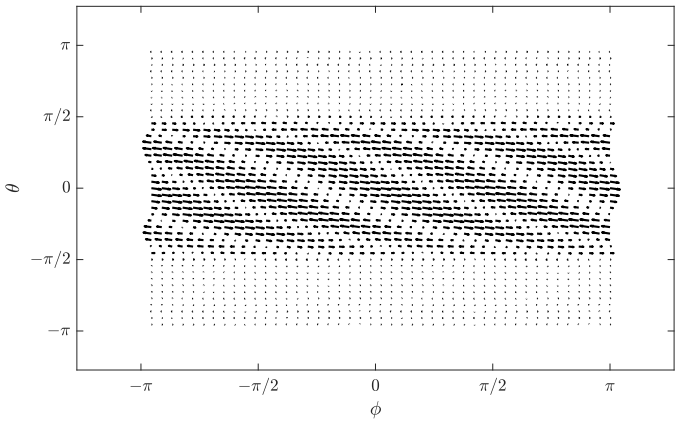

Figure 6.16: *Eddy current pattern related to the $n = 2$ unstable eigenvector (rectified view).*

ancy can be obtained remembering the regularization technique presented in subsection 6.2.2.

Figures 6.13 - 6.14 show the eddy current pattern related to the $n = 1$ unstable mode, both in 3-D view and for the rectified wall. For every toroidal mode number, only one unstable eigenvector is reported. The second eigenvector, related to the complex conjugate eigenvalue, is identical, but shifted of $\pi/2n$ in the toroidal direction [20, 21]. With respect to the circular case, due to the shape of the conducting structures the eddy current pattern is strongly localized in the Low Field Side (LFS). This fact can be due also to the lower aspect ratio ($R_0/a = 2.5$, Tab. 6.1). The same effect can be seen more prominent for the $n = 2$ mode in Figs. 6.15 - 6.16.

6.3 Effect of 3-D conducting structures on RWM stability

The previous section showed a preliminary analysis of the problem, considering an axisymmetric mesh, in order to benchmark CarMa-D with the MARS-F code. A more detailed model of the passive structures can be seen in Fig. 6.17: two stabilizing plates are (internal and external) are described in detail with holes and ports of the 3-D real geometry, while the vacuum vessels (internal and external) are described as axisymmetric walls. The frequency dependent plasma response model, tested in the previous subsection, is now used to study the effect of a more realistic mesh on the instabilities described above.

The axisymmetric mesh used to produce the results reported in subsection 6.2.3 was obtained by placing a closed conducting wall at the radial normalized position $r/a = 1.2$, where $a = 1.18$m is the minor radius (see Tab. 6.1). This position is close to the real radial position of the inner stabilizing plate, but, in the real geometry, the stabilizing plate is made of two layers very close to each other and not of a single close conducting wall. In addition, these plates have a finite poloidal extension, and do not completely surround the plasma. A detailed view of these structures on the poloidal plane, together with the trace of the coupling surface and the plasma cross-section, can be found in Fig. 6.18.

The case of a closed stabilizing plate without any hole is much more optimistic than the real geometry: the two modes are expected to be much more unstable than what was reported in Tab. 6.4, both for the reduced poloidal extension of the stabilizing plate, and because of the holes [22]. The effect of finite extension of the stabilizing plates was already pointed out

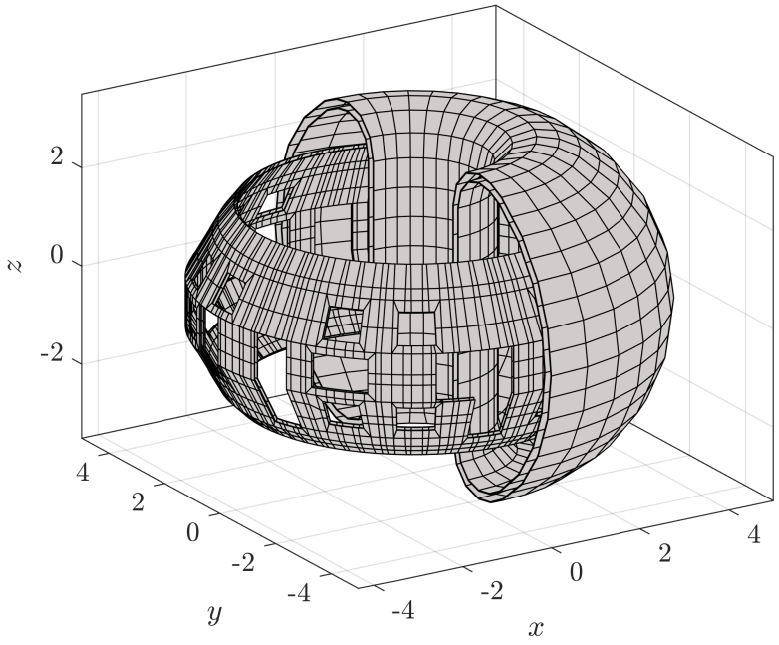

Figure 6.17: *View of the 3-D passive structures. The external vacuum vessels have been represented partially to show the stabilizing plates.*

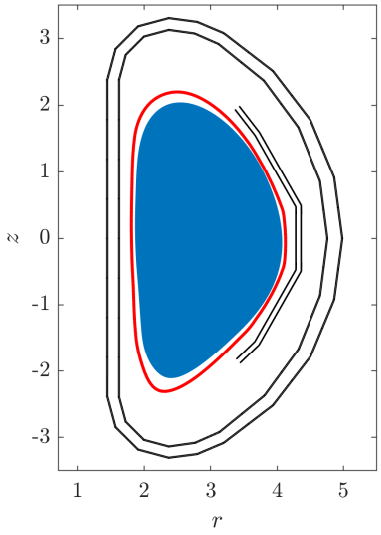

Figure 6.18: *View, in the poloidal plane, of the two nested vacuum vessels as well as the two stabilizing plates. The trace of the coupling surface (red) and the plasma cross-section (blue) are also represented.*

in Ref. [15], where the growth rate obtained with a closed axisymmetric stabilizing plate was approximately $\gamma\tau_W \approx 6$, while using a detailed model of the stabilizing plate led to a growth rate $\gamma\tau_W > 100$.

The presence of the holes in the stabilizing plates makes the passive wall model no longer axisymmetric. The eigenvalues therefore are no longer expected to be in complex conjugate pairs. This happens because the toroidal symmetry is broken, giving rise to four unstable modes, each with a peculiar eigenvector pattern. In addition to this, a non negligible toroidal mode coupling is expected [22], because of the broken symmetry. To evaluate how strong the mode coupling is, both the mono-modal (one mode at time) and the multi-modal analysis has been performed.

The results of this analysis are reported in Tab. 6.5. It is worth noting that, since the configuration is no longer axisymmetric, in principle the wall time for a given n cannot be defined as the decay time of the slowest passive eigenvector with that n periodicity, as done in subsection 6.2.1 for the axisymmetric case. However, the comparison between the obtained growth rates and the wall times in Tab. 5.1 is still useful to have an intuitive idea of the how much more unstable the modes are with respect to the axisymmetric configuration.

The holes have a strong effect in breaking the symmetry of the wall, and this can be understood from two different considerations. At first, the breaking of symmetry leads to breaking also the degeneracy of the spectrum, whose eigenvalues are no longer complex conjugate, and are not even close to each others as in the case of a slight modification of toroidal symmetry [22]. Moreover, the toroidal asymmetry is pointed out by the difference between the mono-modal and the multi-modal responses, showing the strong coupling between different n's that occurs for 3-D wall, even in case of linear MHD [23]. This is due to the fact that, when a mode with a single n interact with a 3-D wall, the eigenvector has not a single n periodicity, but spurious components with different n arise. This spurious spectrum is related to the 3-D

	mono-modal		multi-modal	
n	γ	$\gamma\tau_W$	γ	$\gamma\tau_W$
1	1.81×10^3	152.7	1.95×10^3	164.6
	1.01×10^3	85.2	1.02×10^3	86.1
2	1.36×10^3	79.8	1.33×10^3	77.7
	9.52×10^2	55.6	9.24×10^2	54.0

Table 6.5: *Growth rates of the unstable modes for the 3-D mesh, mono-modal and multi-modal analysis.*

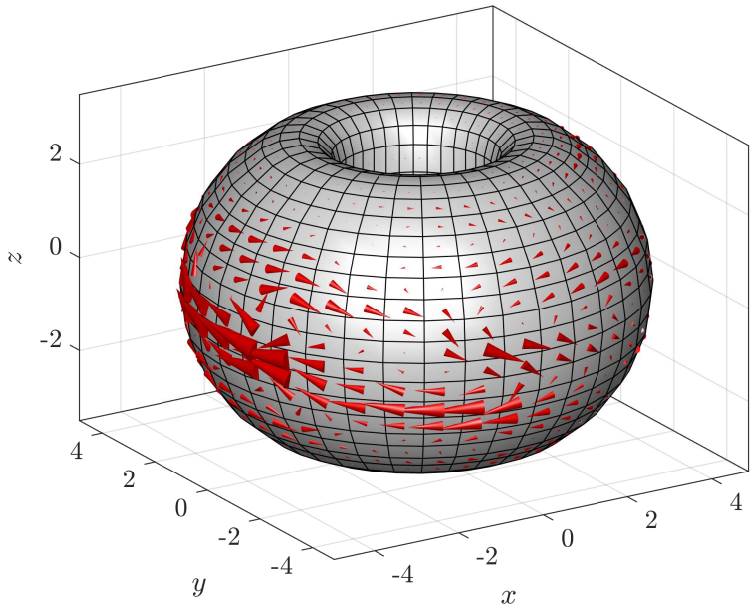

Figure 6.19: *Eddy current pattern related to one of the unstable eigenvectors on the inner vacuum vessel.*

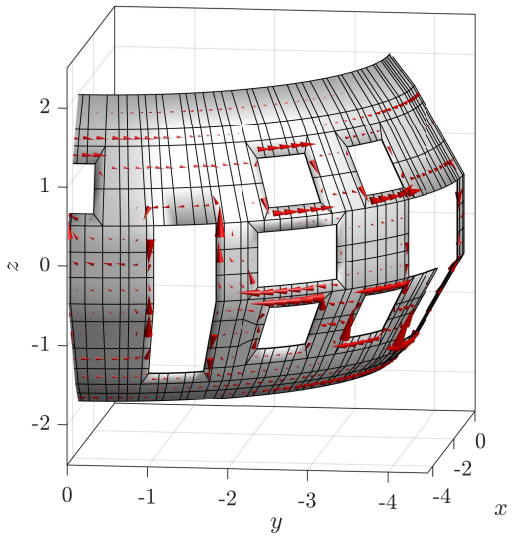

Figure 6.20: *Detailed view of the mode structure in the inner stabilizing plate.*

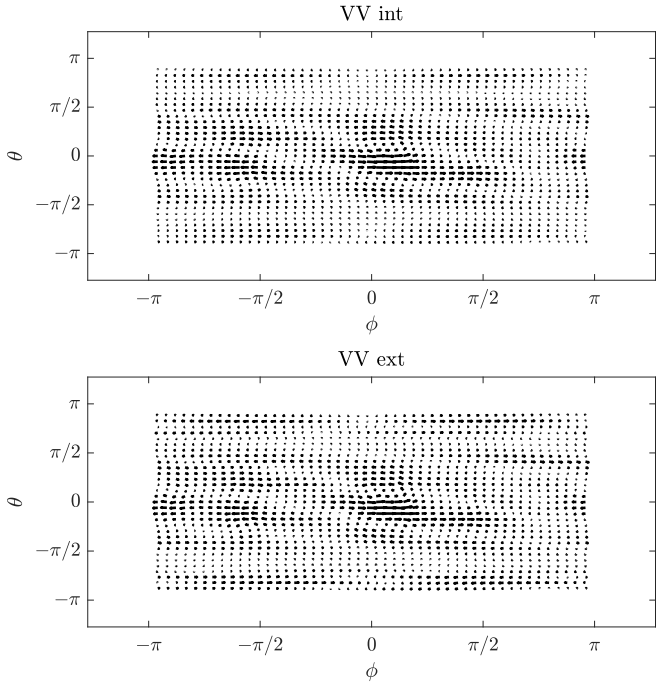

Figure 6.21: *Eddy current pattern related to the most unstable $n = 1$ eigenvector on vacuum vessels.*

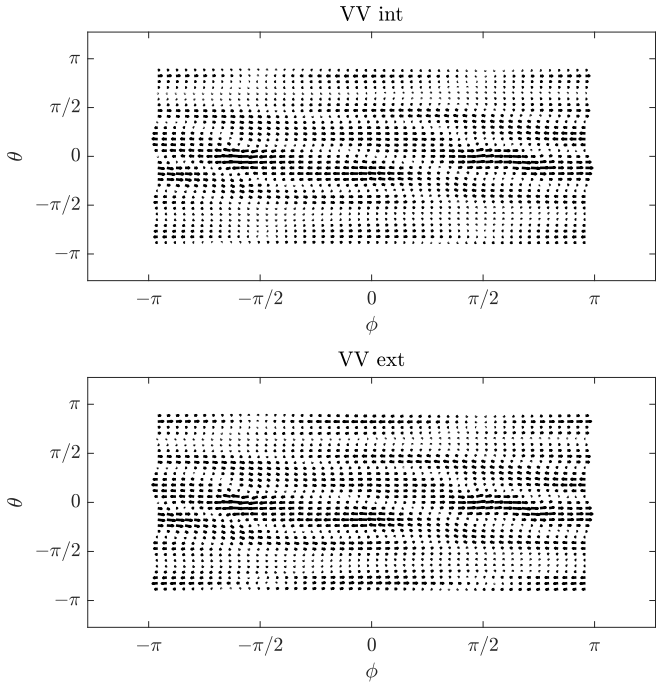

Figure 6.22: *Eddy current pattern related to the least unstable $n = 1$ eigenvector on vacuum vessels.*

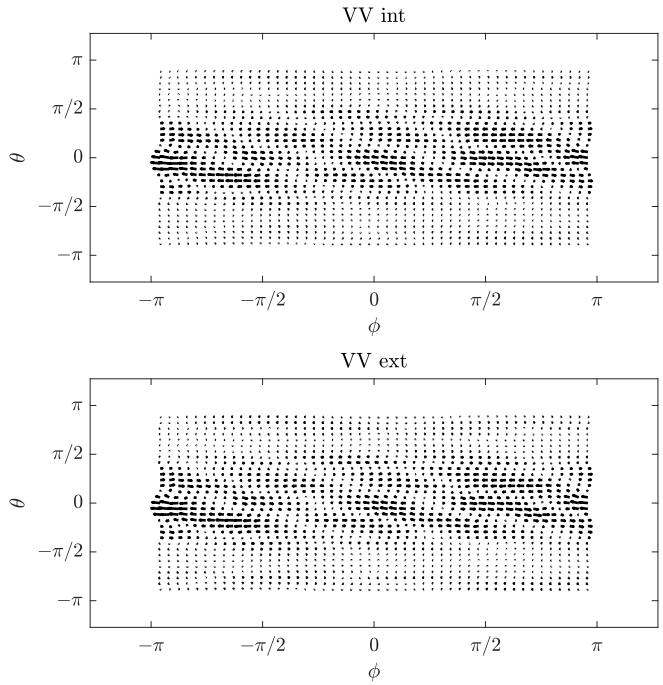

Figure 6.23: *Eddy current pattern related to most unstable $n = 2$ eigenvector on vacuum vessels.*

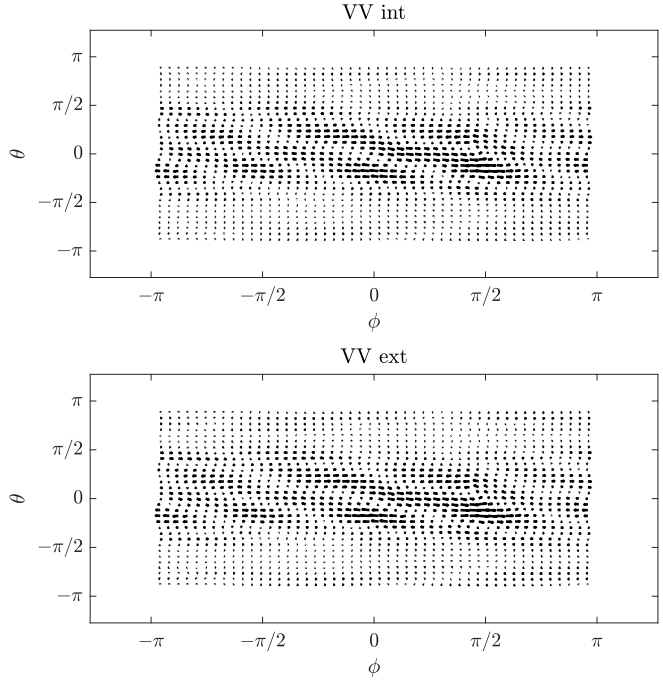

Figure 6.24: *Eddy current pattern related to the least unstable $n = 2$ eigenvector on vacuum vessels.*

geometry. For this reason, the $n = 1$ mode in axi-symmetric geometry would no longer have the same periodicity if a 3-D wall is considered, but would be characterized by a certain spectrum, whose spurious toroidal components would combine with the components of the same n's related to the other modes involved. This effect is particularly noticeable in this case through the difference between the mono-modal and the multi-modal responses

Figure 6.19 shows the eigenvector related to the first unstable eigenvalue on the inner vacuum vessel, which is the closest to the stabilizing plates. The eddy current pattern is not as clean as the axisymmetric case shown in 6.13 - 6.15, even if the vacuum vessel is symmetric. This is due to the proximity effect of the stabilizing plates. The current showing in the stabilizing plates can be seen in detail in Fig. 6.20.

Figures from 6.21 to 6.24 show a rectified view of the eddy current induced by the four unstable modes in both the stabilizing plates, following the same order of Tab. 6.5. Clearly, a pure toroidal periodicity cannot be seen. A predominant $n = 1$ component for eigenvectors of Figs. 6.21 - 6.22, and $n = 2$ component for eigenvectors of Figs. 6.23 - 6.24, can be identified instead.

6.4 Future work: combining active and passive stabilization

The stability analysis carried out in Sec. 6.3 for the 3-D passive structures suggest that strong stabilization is required for these modes. This stabilization can be reached following multiple approaches, combining active and passive strategies.

A RWM feedback control system is expected to be implemented in JT-60SA, thanks to the presence of a dedicated set of active coils designed for this specific task. These coils are organized in three toroidal arrays, each one with six coils, which will be placed around some holes of the stabilizing plate. Figure 6.25 shows the geometry of the coil system and its position with respect to the stabilizing plate. Dedicated modelling activities have already been performed, including the realistic 3-D geometry of the passive structures [15], as well as a preliminary assessment of the feedback system design for the simultaneous stabilization of the modes $n = 1$ and $n = 2$ with a proportional controller [16].

On the other hand, passive stabilization usually arises from the combination of toroidal flow and different kinetic damping mechanisms, such as viscosity [10] and kinetic resonance with the particles drift motions [11, 24, 25].

The latter is due to the Landau resonance, through which the energy associated with the mode is transferred to the particles.

For the case of JT-60SA Scenario 5, the effect of passive stabilization is pointed out in both Figs. 6.26a - 6.26b. In particular, Fig. 6.26a shows the mode growth rate as the factor α_D is increased, in absence of toroidal rotation. The factor α_D multiplies the off-axis elements of the pressure tensor in the MHD equation solved by MARS-K, and this scan describes a smooth transition from the fluid ($\alpha_D = 0$) to the drift-kinetic description ($\alpha_D = 1$), showing a stabilizing effect even if no rotation is present. On the other hand, Fig. 6.26b shows the scan of toroidal rotation for the target plasma and three re-scaled versions of the same equilibrium, but with increasing β_N. It can be noted that, for low rotation, the stabilization due to the resonance with thermal ions precession drift is effective, leading to a strong effect on the cases with higher β_N. In particular, when the stabilization is stronger ($\Omega/\omega_A \approx 0.01$), the normalized growth rate is $\gamma\tau_W \approx 1$, which is one order of magnitude less than what is obtained for the fluid case (see Tab. 6.4). All these results came from MARS-K simulations, thus a closed axisymmetric wall at $r/a = 1.2$ is used.

Taking advantage of these considerations, future developments for what concerns control techniques will be oriented to the combinations of both active and passive stabilizing effects [26, 27]. The CarMa-D model is a suitable choice to be used for this purpose, because it is able to rigorously include in the model the effects of toroidal plasma flow and drift kinetic damping.

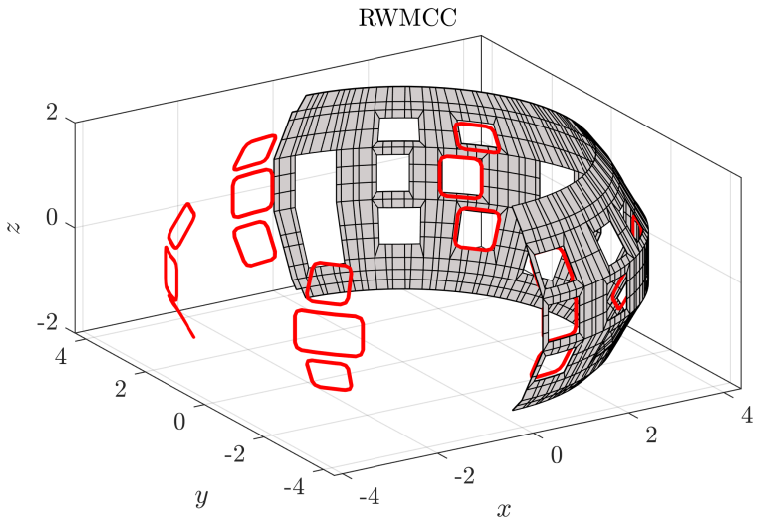

Figure 6.25: *3-D representation of the stabilizing plate and the three toroidal arrays of RWM control coils (RWMCC).*

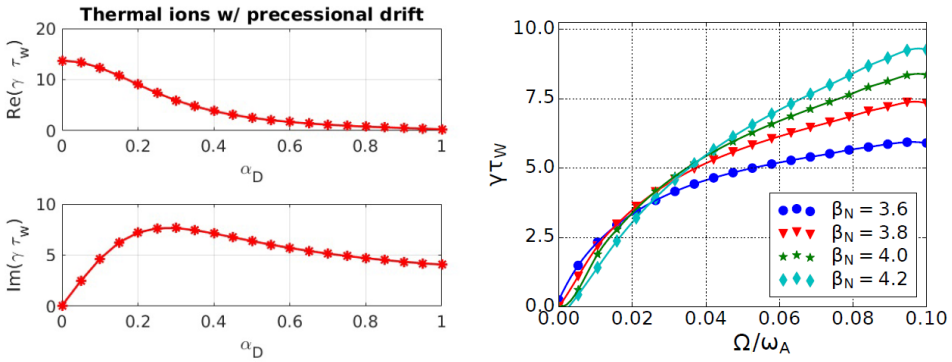

Figure 6.26: *Contribution of the kinetic effects to stabilization: scan of the drift kinetic contributions (a) and scan of toroidal rotation for four different values of β_N for the target plasma (figures from [9]).*

This strength point can be combined together with CarMa-D capability of modelling in a detailed way the active/passive conductors, oriented to the development of a more reliable and effective control strategy.

6.5 Conclusions

The super-conducting fusion reactor Japan Torus Super Advanced (JT-60SA) is being built in Naka, Japan, under the Broader Approach (BA) agreement between European Union and Japan. JT-60SA has the purpose of conducting supportive and complementary work for the ITER project, and to support the basis for DEMO development.

The device will be equipped with a dedicated set of active coils designed for RWM feedback control, opening the possibility to develop a control system aimed to the limitation of serious MHD instabilities. In particular, future effort for what concerns control techniques will be oriented in the combinations of both active and passive stabilizing effects. Thus, in order to make such control system effective, accurate modelling should be performed for both modelling in detail the active/passive conductors, and exploit an accurate description of the combined effect of drift-kinetic damping and toroidal rotation.

For this reason, CarMa-D model has been used to perform preliminary studies on Resistive Wall Modes stability of both the toroidal modes $n = 1$ and $n = 2$. For this part, plasma damping mechanisms rely in fluid description, and no toroidal flow is considered. The first part of the work was a preliminary validation, considering a simplified axisymmetric mesh of the

conducting structures, in order to use MARS-F results as reference. This step has allowed to gain confidence on the capability of the model.

The second part of the work has involved the realistic geometry of the stabilizing plates, with a detailed study of the effects of this 3-D geometry on the stability of both the $n = 1$ and $n = 2$ RWMs. It has turned out that the modes growth rates rise of one order of magnitude if the realistic 3-D geometry of the stabilizing plates is considered. This outcome is a further motivation on the need of an effective stabilization of this kind of instabilities.

The results have shown that additional effort is needed, in particular to include in the model also toroidal flow together with drift-kinetic description of the plasma. This is expected to take advantage of both passive and active stabilization. In the previous chapter, the CarMa-D code has proven to be a valid choice for this purpose.

Bibliography

[1] J. P. Freidberg, A. Cerfon, and J. P. Lee, "Tokamak elongation – how much is too much? part 1. theory," *Journal of Plasma Physics*, vol. 81, no. 6, p. 515810607, 2015.

[2] S. Ishida, P. Barabaschi, and Y. Kamada, "Overview of the JT-60SA project," *Nuclear Fusion*, vol. 51, p. 094018, aug 2011.

[3] Y. Kamada, P. Barabaschi, and S. Ishida, "Progress of the JT-60SA project," *Nuclear Fusion*, vol. 53, p. 104010, sep 2013.

[4] P. Barabaschi, Y. Kamada, and H. Shirai, "Progress of the JT-60SA project," *Nuclear Fusion*, vol. 59, p. 112005, jun 2019.

[5] ITER Physics Basis Editors and ITER Physics Expert Group Chairs an Co-Chairs and ITER Joint Central Team and Physics Unit, "Chapter 1: Overview and summary," *Nuclear Fusion*, vol. 39, pp. 2137–2174, dec 1999.

[6] "JT-60SA research plan," 2018. `www.jt60sa.org/pdfs/JT-60SA_Res_Plan.pdf`.

[7] G. Giruzzi et al., "Physics and operation oriented activities in preparation of the JT-60SA tokamak exploitation," *Nuclear Fusion*, vol. 57, p. 085001, jul 2017.

[8] J.F. Artaud et al., "The CRONOS suite of codes for integrated tokamak modelling," *Nuclear Fusion*, vol. 50, p. 043001, mar 2010.

[9] L. Pigatto, N. Aiba, T. Bolzonella, N. Hayashi, M. Honda, Y. Q. Liu, G. Marchiori, S. Mastrostefano, G. Matsunaga, M. Takechi, and F. Villone, "Resistive wall mode physics and control challenges in JT-60SA high β_n scenarios," *Nuclear Fusion*, 2019.

[10] A. Bondeson and D. J. Ward, "Stabilization of external modes in tokamaks by resistive walls and plasma rotation," *Phys. Rev. Lett.*, vol. 72, pp. 2709–2712, Apr 1994.

[11] B. Hu and R. Betti, "Resistive wall mode in collisionless quasistationary plasmas," *Phys. Rev. Lett.*, vol. 93, p. 105002, Sep 2004.

[12] Y. Q. Liu, M. S. Chu, I. T. Chapman, and T. C. Hender, "Toroidal self-consistent modeling of drift kinetic effects on the resistive wall mode," *Physics of Plasmas*, vol. 15, no. 11, p. 112503, 2008.

[13] Y. Q. Liu, I. T. Chapman, J. P. Graves, G. Z. Hao, Z. R. Wang, J. E. Menard, M. Okabayashi, E. J. Strait, and A. Turnbull, "Non-perturbative modelling of energetic particle effects on resistive wall mode: Anisotropy and finite orbit width," *Physics of Plasmas*, vol. 21, no. 5, p. 056105, 2014.

[14] M. Takechi, G. Matsunaga, N. Aiba, T. Fujita, T. Ozeki, Y. Koide, Y. Sakamoto, G. Kurita, A. Isayama, and Y. Kamada, "Identification of a low plasma-rotation threshold for stabilization of the resistive-wall mode," *Phys. Rev. Lett.*, vol. 98, p. 055002, Feb 2007.

[15] S. Mastrostefano, P. Bettini, T. Bolzonella, M. F. Palumbo, Y. Q. Liu, G. Matsunaga, R. Specogna, M. Takechi, and F. Villone, "Three-dimensional analysis of JT-60SA conducting structures in view of RWM control," *Fusion Engineering and Design*, vol. 96-97, pp. 659 – 663, 2015. Proceedings of the 28th Symposium On Fusion Technology (SOFT-28).

[16] L. Pigatto, P. Bettini, T. Bolzonella, M. Bonotto, Y. Q. Liu, G. Marchiori, and M. Takechi, "Modelling multi-modal resistive wall mode feedback control in JT-60SA perspective high β scenarios," pp. 46th EPS Conference on Plasma Physics – 8 – 12 July 2019.

[17] D. Liu and A. Bondeson, "Improved poloidal convergence of the mars code for MHD stability analysis," *Computer Physics Communications*, vol. 116, no. 1, pp. 55 – 64, 1999.

[18] R. Albanese and F. Villone, "The linearized CREATE-L plasma response model for the control of current, position and shape in tokamaks," *Nuclear Fusion*, vol. 38, pp. 723–738, may 1998.

[19] M. Ariola, G. D. Tommasi, A. Pironti, and F. Villone, "Control of resistive wall modes in tokamak plasmas," *Control Engineering Practice*, vol. 24, pp. 15 – 24, 2014.

[20] A. Portone, F. Villone, Y. Q. Liu, R. Albanese, and G. Rubinacci, "Linearly perturbed MHD equilibria and 3D eddy current coupling via the control surface method," *Plasma Physics and Controlled Fusion*, vol. 50, no. 8, p. 085004, 2008.

[21] F. Villone, M. Ariola, G. De Tommasi, Y. Liu, S. Mastrostefano, A. Pironti, and S. Ventre, "Multimodal RWM feedback control in ITER," *39th EPS Conference on Plasma Physics 2012, EPS 2012 and the 16th International Congress on Plasma Physics*, vol. 3, pp. 1374–1377, 01 2012.

[22] F. Villone, Y. Q. Liu, P. Roberto, T. Bolzonella, and G. Rubinacci, "Effects of three-dimensional electromagnetic structures on resistive-wall-mode stability of reversed field pinches," *Phys. Rev. Lett.*, vol. 100, p. 255005, 06 2008.

[23] R. Fitzpatrick, "Effect of a nonuniform resistive wall on the stability of tokamak plasmas," *Physics of Plasmas*, vol. 1, no. 9, pp. 2931–2939, 1994.

[24] I. T. Chapman, C. G. Gimblett, M. P. Gryaznevich, T. C. Hender, D. F. Howell, Y. Q. Liu, and S. D. Pinches, "Stability of the resistive wall mode in JET," *Plasma Physics and Controlled Fusion*, vol. 51, p. 055015, mar 2009.

[25] J. W. Berkery, S. A. Sabbagh, H. Reimerdes, R. Betti, B. Hu, R. E. Bell, S. P. Gerhardt, J. Manickam, and M. Podestà, "The role of kinetic effects, including plasma rotation and energetic particles, in resistive wall mode stability," *Physics of Plasmas*, vol. 17, no. 8, p. 082504, 2010.

[26] G. Xia, Y. Liu, and Y. Q. Liu, "Synergetic effects of magnetic feedback and plasma flow on resistive wall mode stability in tokamaks," *Plasma Physics and Controlled Fusion*, vol. 56, p. 095009, jul 2014.

[27] G. Xia, Y. Q. Liu, Y. Liu, G. Hao, and L. Li, "Stabilization of resistive wall modes in tokamaks by drift kinetic effects combined with magnetic feedback," *Nuclear Fusion*, vol. 55, p. 093007, jul 2015.

7 Further development: multi-modal RWM active control

Contents

The results presented in the previous chapter made clear that the need of a synergic integration of passive and active stabilizations is expected to play a crucial role in present and future devices, in order to overcome the limitations imposed by the Resistive Wall Modes and reach operational conditions viable for fully non-inductive scenarios. For this purpose, CarMa-D is a suitable choice, because it has proven to be an accurate and reliable tool to model RWM dynamics, even if the simultaneous effects of plasma dynamics, toroidal flow and kinetic damping are prominent.

Whit the aim of developing a model-based feedback control system, the formalism of state-space representation is a powerful tool. This procedure has been done for many devices using the static CarMa code [1, 2, 3], because it allows to write straightforwardly the state-space model starting from the modified RL equation [4]. Unfortunately, this is no longer possible if CarMa-D modified RL equation is used, i.e. Eq. (4.39), because the matrix $\boldsymbol{L}^*$ is rank-deficient. This particular feature was already treated is Sec. 4.3 with the aim of stability analysis through eigenvalues computation, and the proposed solution is well suited for that specific purpose.

In this chapter, it is shown how CarMa-D RL system of equation can be written in a state-space form only by performing algebraic manipulations and arrangements of the block matrices.

7.1 State-Space representation of a Linear Time Invariant system

In mathematical physics, analytical mechanics and control theory, a *state-space representation* means that a dynamical system is described by means of a particular vector space of state variables. The arising *state-space model* represents a physical system in which the inputs, outputs and states variables are related by a system of first-order differential equations [5]. In addition to this, if the dynamical system is linear, which is the case studied in this work, the resulting differential equations may be written in matrix form. Then a significant algebraization of general system theory can be exploited, and this is one of the strength points of the state-space approach, providing a favorable and compact way to model and analyze systems with multiple inputs and outputs (MIMO systems).

A state-space model of a linear, time invariant (LTI) dynamical system is usually written as:

$$\frac{d\boldsymbol{x}(t)}{dt} = \boldsymbol{A}\boldsymbol{x}(t) + \boldsymbol{B}\boldsymbol{u}(t) \tag{7.1}$$

$$\boldsymbol{y}(t) = \boldsymbol{C}\boldsymbol{x}(t) + \boldsymbol{D}\boldsymbol{u}(t) \tag{7.2}$$

where $\boldsymbol{x}(t)$ is the state vector, $\boldsymbol{u}(t), \boldsymbol{y}(t)$ are respectively the input and output vectors, and $\boldsymbol{A}, \boldsymbol{B}, \boldsymbol{C}, \boldsymbol{D}$ are the matrices of the system.

The state space representation works in time domain, as opposed to the transfer function method which works in the Laplace domain. However, there is a straightforward connections between the two methods, that can be underlined by taking the Laplace transform of Eq. (7.1), leading to:

$$\boldsymbol{X}(s) = (\boldsymbol{E}s - \boldsymbol{A})^{-1}\boldsymbol{x}(0) + (\boldsymbol{E}s - \boldsymbol{A})^{-1}\boldsymbol{B}\boldsymbol{U}(s) \tag{7.3}$$

where $\boldsymbol{E}$ is the identity matrix and $\boldsymbol{x}(0)$ are the initial conditions. Taking the Laplace transform also of Eq. (7.2) and considering Eq. (7.3) we obtain:

$$\boldsymbol{Y}(s) = \boldsymbol{C}\big[(\boldsymbol{E}s - \boldsymbol{A})^{-1}\boldsymbol{x}(0) + (\boldsymbol{E}s - \boldsymbol{A})^{-1}\boldsymbol{B}\boldsymbol{U}(s)\big] + \boldsymbol{D}\boldsymbol{U}(s) \tag{7.4}$$

The state space representation is of remarkable interest when a model-based feedback controller is required, such as PID controllers, Pole placement method, Linear Quadratic Regulator (LQR), and many others, especially for MIMO systems.

7.2 State-Space representation of CarMa-D system

As was already said, the CarMa-D modified RL equation (4.39) is not suitable to be written directly in a state space form, due to the fact that the system matrix $\boldsymbol{L^*}$ is rank-deficient. To understand this fact it is necessary to look at the structure of the blocks of $\boldsymbol{L^*}$. In order to make the description more clear, relations (4.13), (4.36) and (4.39) from Chap. 4 are repeated in the following. Specifically, system (4.13) shows the equations for the eddy currents and for the plasma response external perturbations, assuming vanishing initial conditions for the current such as $\boldsymbol{i}(t=0)=0$. This gives the starting point of the development of CarMa-D coupling strategy:

$$\begin{cases} s\boldsymbol{L}\boldsymbol{i} + \boldsymbol{R}\boldsymbol{i} + s\boldsymbol{M}\boldsymbol{j}_{eq} = \boldsymbol{D}\boldsymbol{v} \\ \boldsymbol{b}_N = \boldsymbol{W}(s)\boldsymbol{b}_N^{ex} = \boldsymbol{W}(s)\boldsymbol{Q}\boldsymbol{i} \\ \boldsymbol{j}_{eq} = \boldsymbol{F}(s)\boldsymbol{b}_N \end{cases} \tag{7.5}$$

Then, by considering the Padé approximation defined as Eq. (4.17), one can write the, kth order system of linear differential equations defined as (4.36):

$$\begin{aligned} s^k \begin{bmatrix} \boldsymbol{0} & \boldsymbol{0} \\ -\boldsymbol{A}_k\boldsymbol{Q} & \boldsymbol{B}_k \end{bmatrix} \begin{bmatrix} \boldsymbol{i} \\ \boldsymbol{j}_{eq} \end{bmatrix} + ... + s^i \begin{bmatrix} \boldsymbol{0} & \boldsymbol{0} \\ -\boldsymbol{A}_i\boldsymbol{Q} & \boldsymbol{B}_i \end{bmatrix} \begin{bmatrix} \boldsymbol{i} \\ \boldsymbol{j}_{eq} \end{bmatrix} + ... \\ + s \begin{bmatrix} \boldsymbol{L} & \boldsymbol{M} \\ -\boldsymbol{A}_1\boldsymbol{Q} & \boldsymbol{B}_1 \end{bmatrix} \begin{bmatrix} \boldsymbol{i} \\ \boldsymbol{j}_{eq} \end{bmatrix} + \begin{bmatrix} \boldsymbol{R} & \boldsymbol{0} \\ -\boldsymbol{P}_0\boldsymbol{Q} & \boldsymbol{E} \end{bmatrix} \begin{bmatrix} \boldsymbol{i} \\ \boldsymbol{j}_{eq} \end{bmatrix} = \begin{bmatrix} \boldsymbol{D}\boldsymbol{v} \\ \boldsymbol{0} \end{bmatrix} \end{aligned} \tag{7.6}$$

and with the change of variable defined as (4.38) the modified RL equation can be obtained:

$$s \begin{bmatrix} \boldsymbol{E} & & & \\ & \boldsymbol{E} & & \\ & & \ddots & \\ & & & \boldsymbol{L}_k \end{bmatrix} \begin{bmatrix} \boldsymbol{x} \\ \boldsymbol{y}_1 \\ \vdots \\ \boldsymbol{y}_{k-1} \end{bmatrix} + \begin{bmatrix} \boldsymbol{0} & -\boldsymbol{E} & & \\ & \boldsymbol{0} & \ddots & \\ & & \ddots & -\boldsymbol{E} \\ \boldsymbol{R}_a & \boldsymbol{L}_1 & \cdots & \boldsymbol{L}_{ak-1} \end{bmatrix} \begin{bmatrix} \boldsymbol{x} \\ \boldsymbol{y}_1 \\ \vdots \\ \boldsymbol{y}_{k-1} \end{bmatrix} = \begin{bmatrix} \boldsymbol{u} \\ \boldsymbol{0} \\ \vdots \\ \boldsymbol{0} \end{bmatrix} \tag{7.7}$$

If the block matrix $\boldsymbol{L}_{ak}$ is now considered, we see from Eq. (7.6) that:

$$\boldsymbol{L}_{ak} = \begin{bmatrix} \boldsymbol{0} & \boldsymbol{0} \\ -\boldsymbol{A}_k\boldsymbol{Q} & \boldsymbol{B}_k \end{bmatrix} \tag{7.8}$$

meaning that the system is a Differential-Algebraic system of Equations

(DAE) [6]: it contains both differential equations and algebraic equations. This particularly occurs because, in general, the degree of the differential equations of the system is not the same, but some equations have a lower order than others. Here the first block of equations, which is related to the eddy currents, have a first order dynamic; on the other hand, the second block of equations, related to the rational interpolation of plasma response matrices, has an *kth* order dynamic which depends on the interpolation degree.

For the purpose of the stability analysis, the rank deficiency of $\boldsymbol{L}^*$ has been treated looking for the growth time of the instability, rather than for the growth rate, and inverting the matrix $\boldsymbol{R}^*$ to obtain the matrix (4.42). On the other hand, if the State-Space system is needed, system (4.40) should be suitably rearranged. To achieve this goal, we write $\boldsymbol{L}^*$ showing explicitly the structure of $\boldsymbol{L}_{ak}$:

$$\boldsymbol{L}^* = \begin{bmatrix} \boldsymbol{E} & & & \\ & \boldsymbol{E} & & \\ & & \ddots & \\ & & & \begin{bmatrix} \mathbf{0} & \mathbf{0} \\ -\boldsymbol{A}_k\boldsymbol{Q} & \boldsymbol{B}_k \end{bmatrix} \end{bmatrix}$$

the second-last block row of the matrix $\boldsymbol{L}^*$ is all zero. This fact can be exploited to partition and permutate the second-last block row with the last one, doing the same procedure with the block columns:

$$\boldsymbol{L}^* = \left[\begin{array}{ccc|c} \boldsymbol{E} & & & \\ & \boldsymbol{E} & & \\ & & \ddots & \\ & & \mathbf{0} & \mathbf{0} \\ \hline & & -\boldsymbol{A}_k\boldsymbol{Q} & \boldsymbol{B}_k \end{array}\right] \tag{7.9}$$

$$\Rightarrow \left[\begin{array}{ccc|c} \boldsymbol{E} & & & \\ & \boldsymbol{E} & & \\ & & \ddots & \\ & & \boldsymbol{B}_k & -\boldsymbol{A}_k\boldsymbol{Q} \\ \hline & & \mathbf{0} & \mathbf{0} \end{array}\right] = \begin{bmatrix} \boldsymbol{L}^*_{11} & \boldsymbol{L}^*_{12} \\ \boldsymbol{L}^*_{21} & \boldsymbol{L}^*_{22} \end{bmatrix} \tag{7.10}$$

The sub-matrices $\boldsymbol{A}_{11}, \boldsymbol{A}_{12}, \boldsymbol{A}_{21}, \boldsymbol{A}_{22}$ are then defined. The same manipula-

tion is done to the $\boldsymbol{R}^*$ matrix:

$$\boldsymbol{R}^* = \left[\begin{array}{cccc|c} & & \ddots & & \\ & & & -\boldsymbol{E} & \\ & & & & -\boldsymbol{E} \\ \boldsymbol{R} & \boldsymbol{0} & \dots & \boldsymbol{L} & \boldsymbol{M} \\ \hline -\boldsymbol{P}_0\boldsymbol{Q} & \boldsymbol{E} & \dots & -\boldsymbol{A}_1\boldsymbol{Q} & \boldsymbol{B}_1 \end{array}\right] \tag{7.11}$$

$$\Rightarrow \left[\begin{array}{cccc|c} & & \ddots & & \\ & & & -\boldsymbol{E} & \\ & & & & -\boldsymbol{E} \\ -\boldsymbol{P}_0\boldsymbol{Q} & \boldsymbol{E} & \dots & \boldsymbol{B}_1 & -\boldsymbol{A}_1\boldsymbol{Q} \\ \hline \boldsymbol{R} & \boldsymbol{0} & \dots & \boldsymbol{M} & \boldsymbol{L} \end{array}\right] = \begin{bmatrix} \boldsymbol{R}^*_{11} & \boldsymbol{R}^*_{12} \\ \boldsymbol{R}^*_{21} & \boldsymbol{R}^*_{22} \end{bmatrix} \tag{7.12}$$

and finally also to the rows of the vector of unknowns and to the source term:

$$\boldsymbol{y}^* = \begin{bmatrix} \boldsymbol{y}^*_1 \\ \boldsymbol{y}^*_2 \end{bmatrix} \qquad \boldsymbol{u}^* = \begin{bmatrix} \boldsymbol{u}^*_1 \\ \boldsymbol{0} \end{bmatrix} \tag{7.13}$$

With this partition, and noting that $\boldsymbol{L}^*_{21} = \boldsymbol{0},\ \boldsymbol{L}^*_{22} = \boldsymbol{0}$ from Eq. (7.10), it follows that system (4.39) can be written as:

$$s\begin{bmatrix} \boldsymbol{L}^*_{11} & \boldsymbol{L}^*_{12} \\ \boldsymbol{0} & \boldsymbol{0} \end{bmatrix}\begin{bmatrix} \boldsymbol{y}^*_1 \\ \boldsymbol{y}^*_2 \end{bmatrix} + \begin{bmatrix} \boldsymbol{R}^*_{11} & \boldsymbol{R}^*_{12} \\ \boldsymbol{R}^*_{21} & \boldsymbol{R}^*_{22} \end{bmatrix}\begin{bmatrix} \boldsymbol{y}^*_1 \\ \boldsymbol{y}^*_2 \end{bmatrix} = \begin{bmatrix} \boldsymbol{u}^*_1 \\ \boldsymbol{0} \end{bmatrix} \tag{7.14}$$

Now, with this arrangement, matrix $\boldsymbol{L}^*_{11}$ has full rank, as can be seen in Eq. (7.10). Equation (7.14) is then written as two separate systems of equations, one of first-order differential equations, and the other one of algebraic equations. The second system can be solved with respect of $\boldsymbol{y}_2$ thanks to the fact that $\boldsymbol{L}^*_{21} = \boldsymbol{L}^*_{22} = \boldsymbol{0}$:

$$s\boldsymbol{L}^*_{11}\boldsymbol{y}_1 + s\boldsymbol{L}^*_{12}\boldsymbol{y}^*_2 + \boldsymbol{R}^*_{11}\boldsymbol{y}^*_1 + \boldsymbol{R}^*_{12}\boldsymbol{y}^*_2 = \boldsymbol{u}^*_1 \tag{7.15}$$

$$\boldsymbol{R}^*_{21}\boldsymbol{y}^*_1 + s\boldsymbol{R}^*_{22}\boldsymbol{y}^*_2 = \boldsymbol{0} \tag{7.16}$$

From Eq. (7.16) it follows that:

$$\boldsymbol{y}^*_2 = -(\boldsymbol{R}^*_{22})^{-1}\boldsymbol{R}^*_{21}\boldsymbol{y}^*_1 \tag{7.17}$$

and by inserting $\boldsymbol{y}_2$ into Eq. (7.15):

$$s\boldsymbol{L}^*_{11}\boldsymbol{y}^*_1 - s\boldsymbol{L}^*_{12}(\boldsymbol{R}^*_{22})^{-1}\boldsymbol{R}^*_{21}\boldsymbol{y}^*_1 + \boldsymbol{R}^*_{11}\boldsymbol{y}^*_1 - \boldsymbol{R}^*_{12}(\boldsymbol{R}^*_{22})^{-1}\boldsymbol{R}^*_{21}\boldsymbol{y}^*_1 = \boldsymbol{u}^*_1 \tag{7.18}$$

with the following redefinitions:

$$s\underbrace{\left[\boldsymbol{L}_{11}^{*}-\boldsymbol{L}_{12}^{*}(\boldsymbol{R}_{22}^{*})^{-1}\boldsymbol{R}_{21}^{*}\right]}_{\boldsymbol{L}_{SS}}\boldsymbol{y}_{1}^{*}+\underbrace{\left[\boldsymbol{R}_{11}^{*}\boldsymbol{y}_{1}^{*}-\boldsymbol{R}_{12}^{*}(\boldsymbol{R}_{22}^{*})^{-1}\boldsymbol{R}_{21}^{*}\right]}_{\boldsymbol{R}_{SS}}\boldsymbol{y}_{1}^{*}=\boldsymbol{u}_{1}^{*} \quad (7.19)$$

it follows directly:

$$\boldsymbol{A}^{*}=-\boldsymbol{L}_{SS}^{-1}\boldsymbol{R}_{SS} \quad (7.20)$$

$$\boldsymbol{B}^{*}=\boldsymbol{L}_{SS}^{-1} \quad (7.21)$$

where $\boldsymbol{A}^{*}, \boldsymbol{B}^{*}$ are the matrices of the dynamic equation of the State-Space system for the CarMa-D model. In particular, with this procedure the matrix $\boldsymbol{A}^{*}$ has full rank. These matrices are formally equivalent to those of Eq. (3.48), but with a higher number of states to model plasma dynamics. It can be proved that the eigenvalues of $\boldsymbol{A}^{*}$ are exactly the inverse of the growth times given by Eq. (4.42).

Equation (3.49) can be obtained by composing the matrix $\boldsymbol{C}^{*}$ as:

$$\boldsymbol{C}^{*}=\begin{bmatrix}\boldsymbol{C} & & & \\ & \mathbf{0} & & \\ & & \ddots & \\ & & & \mathbf{0}\end{bmatrix} \quad (7.22)$$

where $\boldsymbol{C}$ is the same of Eq. (3.49). Now, going back to the time domain we obtain the desired state-space system:

$$\frac{d\boldsymbol{y}_{1}^{*}(t)}{dt}=\boldsymbol{A}^{*}\boldsymbol{y}_{1}^{*}(t)+\boldsymbol{B}^{*}\boldsymbol{u}_{1}^{*}(t) \quad (7.23)$$

$$\boldsymbol{b}(t)=\boldsymbol{C}^{*}\boldsymbol{y}_{1}^{*}(t) \quad (7.24)$$

where the outputs $\boldsymbol{b}(t)$ are the magnetic field perturbations at given spatial points around the torus.

7.3 Conclusions

The work presented in the previous section opens the possibility to use CarMa-D model for control oriented purposes. A schematic overview of the feedback control principle can be seen in Fig. 7.1. Here, the input quantity $\boldsymbol{r}(t)$ is regulated through a negative feedback by a general controller. The regulation is related to the output signal of the system in a real time framework.

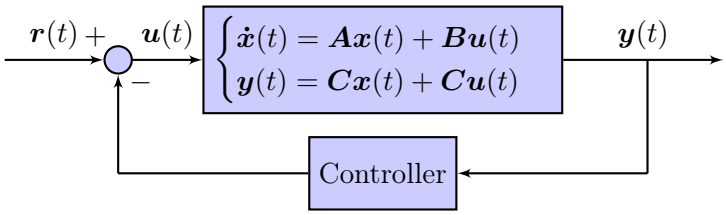

Figure 7.1: *Schematic view of a feedback control.*

CarMa-D has been proved, through the validation work carried out in the previous chapters, to be effective and reliable in every analyzed case. It has shown capable to deal with such instabilities out of the capabilities of static CarMa, giving very satisfactory results. In addition to this, CarMa-D system lends itself to a state-space representation through suitable algebraic manipulations. For this reason CarMa-D should be preferred for the design of model-based control system rather than static CarMa.

Additional work will be done in order to obtain the CarMa-D state space for the multi-modal RWM feedback stabilization of the $n = 1$ and $n = 2$ RWM for JT-60SA. This can be considered a natural extension of the stability analysis presented in Chap. 6.

Further discussions should be done concerning the higher number of DoF of CarMa-D. In this particular case, the high number of DoF are related both to the complexity and level of detail required by the 3D mesh to ensure the desired precision, and also for the change of variables defined in Eq. (4.38) to obtain a first order system. It follows that this high number of DoF are required, and cannot be cut down upstream. A possible solution of the high number of DoF can be the use of a Model Order Reduction technique. Many Model Order Reduction techniques have been developed in last decades, in order to model the system behavior only by considering a small group of dominant modes for the evolution of the system. The strategy to do this is peculiar of each method. The main MOR techniques are optimal Hankel-norm approximation [7], Balanced Truncation [8], Selective Modal Analysis [9], Proper Orthogonal Decomposition [10], and Krylov subspace method [11].

Recently Krylov subspace method has been used to cut down the computational complexity of a state-space model for the eddy current computation in large-scale fusion devices [12]. This strategy has proven to be effective for such particular problem, because the number of DoF was cut down of almost a factor of 100. For this reason, further effort will be devoted to implement Krylov subspace MOR technique to the CarMa-D state space model, and exploit the low-order system for the control oriented modelling activities.

Bibliography

[1] G. Marchiori, M. Baruzzo, T. Bolzonella, Y. Q. Liu, A. Soppelsa, and F. Villone, "Dynamic simulator of RWM control for fusion devices: Modelling and experimental validation on RFX-mod," *Nuclear Fusion*, vol. 52, p. 023020, 01 2012.

[2] F. Villone, M. Ariola, G. De Tommasi, Y. Liu, S. Mastrostefano, A. Pironti, and S. Ventre, "Multimodal RWM feedback control in ITER," *39th EPS Conference on Plasma Physics 2012, EPS 2012 and the 16th International Congress on Plasma Physics*, vol. 3, pp. 1374–1377, 01 2012.

[3] L. Pigatto, P. Bettini, T. Bolzonella, M. Bonotto, Y. Q. Liu, G. Marchiori, and M. Takechi, "Modelling multi-modal resistive wall mode feedback control in JT-60SA perspective high β scenarios," pp. 46th EPS Conference on Plasma Physics – 8 – 12 July 2019.

[4] A. Portone, F. Villone, Y. Q. Liu, R. Albanese, and G. Rubinacci, "Linearly perturbed MHD equilibria and 3D eddy current coupling via the control surface method," *Plasma Physics and Controlled Fusion*, vol. 50, no. 8, p. 085004, 2008.

[5] G. Marchesini and E. Fornasini, *Appunti di teoria dei sistemi*. Libreria Progetto, 1983.

[6] T. R. Achim Ilchmann, *Surveys in Differential-Algebraic Equations II*. Springer, 2014.

[7] D. Kumar and S. Nagar, "Model reduction by extended minimal degree optimal Hankel norm approximation," *Applied Mathematical Modelling*, vol. 38, no. 11, pp. 2922 – 2933, 2014.

[8] S. Gugercin and A. C. Antoulas, "A survey of model reduction by balanced truncation and some new results," *International Journal of Control*, vol. 77, no. 8, pp. 748–766, 2004.

[9] A. Cenedese, M. Fagherazzi, and P. Bettini, "A novel application of selective modal analysis to large-scale electromagnetic devices," *IEEE Transactions on Magnetics*, vol. 52, pp. 1–4, March 2016.

[10] K. Willcox and J. Peraire, "Balanced model reduction via the proper orthogonal decomposition," *Aiaa Journal - AIAA J*, vol. 40, pp. 2323–2330, 11 2002.

[11] Z. Bai, "Krylov subspace techniques for reduced-order modeling of large-scale dynamical systems," *Applied Numerical Mathematics*, vol. 43, no. 1, pp. 9 – 44, 2002. 19th Dundee Biennial Conference on Numerical Analysis.

[12] M. Bonotto, P. Bettini, and A. Cenedese, "Model-order reduction of large-scale state-space models in fusion machines via Krylov methods," *IEEE Transactions on Magnetics*, vol. 53, pp. 1–4, June 2017.

8 Conclusions and further work

In this thesis, CarMa-D, an improved version of the CarMa code, is presented. This upgraded version of the code is capable of self-consistently take into account, in addition to the three dimensional conducting structures, also plasma mass, toroidal rotation and kinetic damping physics for the study of Resistive Wall Modes stability. The improvement of CarMa coupling strategy to model all these phenomena provides a computational tool which can be considered the state of the art of the RWMs modelling for stability analysis and active stabilization in presence of 3-D conducting structures.

CarMa-D has been presented in the first part of the work. The new coupling strategy relies on a *matrix-based Padé rational approximation* to model the frequency dependent plasma response. Starting from this point, the original coupling strategy is completely reformulated, leading finally to a modified RL equation formally equivalent to the static case, but able to take into account the plasma dynamics in the RWMs stability analysis. In addition to this, the mathematical model is further generalized to take into account an arbitrary amount of toroidal mode numbers (*multi-modal* CarMa-D).

CarMa-D has been extensively tested against a tokamak plasma with a circular cross-section, and surrounded by a resistive wall with a coherent shape. The testing activity follows different steps, in order to assess CarMa-D reliability and robustness. Two different damping physics models have been considered, (i) the parallel sound wave damping and (ii) the self-consistent, full toroidal drift kinetic model; different values of toroidal rotation have been considered for both cases. For the analyzed cases, it has been shown that the Padé rational approximation is able to model the plasma dynamics in a very accurate way, and the resulting CarMa-D successfully deals with equilibria where the simultaneous effects of plasma dynamics, toroidal flow and kinetic damping are prominent.

CarMa-D has also been used to study RWM stability on the JT-60SA device, involving a realistic geometrical description of the stabilizing plates.

A detailed study of the effects of this 3-D geometry on the stability of both the toroidal modes $n = 1$ and $n = 2$ has been performed. It has turned out that growth rate of the modes increase of one order of magnitude if the realistic 3-D geometry of the stabilizing plates is considered instead of a simple shell, enclosing the plasma completely. In addition to this, a noticeable toroidal mode coupling appears due to the holes and ports present in the real geometry. These results provide further motivation regarding the need of an effective stabilization.

Finally, additional effort has been made to write the CarMa-D mathematical model in a way suitable to be casted as a state-space representation. This is a crucial step needed to exploit CarMa-D features in a model-based feedback control strategy. Unlikely the original CarMa, CarMa-D cannot be written straightforwardly in a state-space form, due to the new matrix-based coupling strategy. However, this goal is achieved simply through an algebraic manipulation of the system matrices, without any simplifying assumption.

Further work will concern the application of CarMa-D to several cases of interest, such as, for example, additional work related to JT-60SA and the application to ITER, both concerning the stability analysis as well as the design and the implementation of a model-based feedback controller.

A | Formulas for F(s) e W(s)

For the case of rational interpolation of $\boldsymbol{F}(s), \boldsymbol{W}(s)$ separately, the derivation of eq. (4.37) follows the same steps done for interpolation of $\boldsymbol{P}(s)$. Using eqs. (4.15),(4.16) in the system of equations (4.13) leads to:

$$\begin{cases} s\boldsymbol{L}\boldsymbol{i} + \boldsymbol{R}\boldsymbol{i} + s\boldsymbol{M}\boldsymbol{j}_{eq} = \boldsymbol{D}\boldsymbol{v} \\ \boldsymbol{b}_N = \left(\sum_i s^i \boldsymbol{B}_i\right)^{-1} \left(\sum_i s^i \boldsymbol{A}_i\right) \boldsymbol{Q}\boldsymbol{i} \\ \boldsymbol{j}_{eq} = \left(\sum_i s^i \boldsymbol{D}_i\right)^{-1} \left(\sum_i s^i \boldsymbol{C}_i\right) \boldsymbol{b}_N \end{cases} \tag{A.1}$$

this system of equations can be written as a *kth* order system of differential equations defining the block matrices $\boldsymbol{L}_{ia}$ and $\boldsymbol{R}_a$ exactly as was already done for the previous case, but with sligthly different meaning:

$$\begin{aligned} & s^k \underbrace{\begin{bmatrix} \boldsymbol{0} & \boldsymbol{0} & \boldsymbol{0} \\ -\boldsymbol{A}_k\boldsymbol{Q} & \boldsymbol{0} & \boldsymbol{B}_k \\ \boldsymbol{0} & \boldsymbol{D}_k & -\boldsymbol{C}_k \end{bmatrix}}_{\boldsymbol{L}_{ak}} \underbrace{\begin{bmatrix} \boldsymbol{i} \\ \boldsymbol{b}_N \\ \boldsymbol{j}_{eq} \end{bmatrix}}_{\boldsymbol{x}} + \ldots + s^i \underbrace{\begin{bmatrix} \boldsymbol{0} & \boldsymbol{0} & \boldsymbol{0} \\ -\boldsymbol{A}_i\boldsymbol{Q} & \boldsymbol{0} & \boldsymbol{B}_i \\ \boldsymbol{0} & \boldsymbol{D}_i & -\boldsymbol{C}_i \end{bmatrix}}_{\boldsymbol{L}_{ai}} \begin{bmatrix} \boldsymbol{i} \\ \boldsymbol{b}_N \\ \boldsymbol{j}_{eq} \end{bmatrix} + \ldots \\ & + s \underbrace{\begin{bmatrix} \boldsymbol{L} & \boldsymbol{M} & \boldsymbol{0} \\ -\boldsymbol{A}_1\boldsymbol{Q} & \boldsymbol{0} & \boldsymbol{B}_1 \\ \boldsymbol{0} & \boldsymbol{D}_1 & -\boldsymbol{C}_1 \end{bmatrix}}_{\boldsymbol{L}_{a1}} \begin{bmatrix} \boldsymbol{i} \\ \boldsymbol{b}_N \\ \boldsymbol{j}_{eq} \end{bmatrix} + \underbrace{\begin{bmatrix} \boldsymbol{R} & \boldsymbol{0} & \boldsymbol{0} \\ -\boldsymbol{W}_0\boldsymbol{Q} & \boldsymbol{0} & \boldsymbol{E} \\ \boldsymbol{0} & \boldsymbol{E} & -\boldsymbol{F}_0 \end{bmatrix}}_{\boldsymbol{R}_a} \begin{bmatrix} \boldsymbol{i} \\ \boldsymbol{b}_N \\ \boldsymbol{j}_{eq} \end{bmatrix} = \underbrace{\begin{bmatrix} \boldsymbol{D}\boldsymbol{v} \\ 0 \\ 0 \end{bmatrix}}_{\boldsymbol{u}} \end{aligned} \tag{A.2}$$

This system of differential equations can be straightforwardly written as eq. (4.37), and consequently leads to (4.40). The same considerations lead exactly to (4.42), where the block matrices are now:

$$\boldsymbol{R}_a^{-1}\boldsymbol{L}_{a1} = \begin{bmatrix} \boldsymbol{R}^{-1}\boldsymbol{L} & \boldsymbol{R}^{-1}\boldsymbol{M} & \boldsymbol{0} \\ \boldsymbol{F}_0\boldsymbol{W}_0\boldsymbol{Q}\boldsymbol{R}^{-1}\boldsymbol{L} - \boldsymbol{F}_0\boldsymbol{A}_1\boldsymbol{Q} & \boldsymbol{F}_0\boldsymbol{W}_0\boldsymbol{Q}\boldsymbol{R}^{-1}\boldsymbol{M} + \boldsymbol{D}_1 & \boldsymbol{F}_0\boldsymbol{B}_1 - \boldsymbol{C}_1 \\ \boldsymbol{W}_0\boldsymbol{Q}\boldsymbol{R}^{-1}\boldsymbol{L} - \boldsymbol{A}_1\boldsymbol{Q} & \boldsymbol{W}_0\boldsymbol{Q}\boldsymbol{R}^{-1}\boldsymbol{M} & \boldsymbol{B}_1 \end{bmatrix} \tag{A.3}$$

$$\boldsymbol{R}_a^{-1}\boldsymbol{L}_{ai} = \begin{bmatrix} \mathbf{0} & \mathbf{0} & \mathbf{0} \\ -\boldsymbol{F}_0\boldsymbol{A}_i\boldsymbol{Q} & \boldsymbol{D}_i & \boldsymbol{F}_0\boldsymbol{B}_i - \boldsymbol{C}_i \\ -\boldsymbol{A}_2\boldsymbol{Q} & \mathbf{0} & \boldsymbol{B}_i \end{bmatrix} \tag{A.4}$$

Acknowledgments

These three years of my Ph.D. have been a quite long journey, and have seen several people taking part in different ways. All deserve to be acknowledged.

At first, the main acknowledgements must be addressed to my supervisor, Prof. Fabio Villone, for several reasons. Thank to his guidance, I have been inspired and motivated to grow up from the scientific point of view. This is, in my opinion, the most important goal I have achieved during this Ph.D.. In addition to this, the work itself I have developed comes from his proposal, and was carried out exploiting many helps and hints obtained from our discussions. There are additional reasons, such as the consistent amount of time I have been hosted in Naples, the effort spent reviewing the chapters of this thesis, and many others.

I would like to deeply acknowledge also Dr. Yueqiang Liu, for his continuous support obtained in these three years. Dr. Liu's help has been fundamental to gain experience and improve my interest in numerical physics, to patiently clarifying my doubts, and to discuss new ideas concerning the development of this work. The 6 months I spent in San Diego, under his hospitality, have been an incredible possibility to grow up and to open my mind.

I have to acknowledge also Prof. Paolo Bettini, at first for supervising an important part of the work done in these years, not only during my Ph.D., but also during both my master thesis and the following research grant. It was following his suggestion that I decided to undertake this career.

Other people have actively contributed to the development of this work. First of all, I would like to thank Leonardo Pigatto, for his help with the MARS code and for the useful discussions on many topics. Lots of useful discussions have been made also with Domenico Abate, who I deeply acknowledge.

My family has played a crucial role in all my life, and not only during these last three years. I would like to deeply acknowledge ar first my parents Claudio and Marina, for their complete support they are giving me: to always believe in me, from the very beginning of my life. I would like to acknowledge also my sister Chiara, wishing for her the same (and more) exciting experience I have had in these years.

To conclude, a special thank goes to my special girlfriend, Giulia, for being always at my side and a constant support in any situation, for believing in me, for giving me motivation for constantly improving myself, and really for too many reasons to be reported. I wish I am for her, and will be, as helpful as she is for me, not only during her Ph.D., but for everything in her

life.

Additional acknowledgements goes to all my colleagues, for sharing good and bad times during these three years.